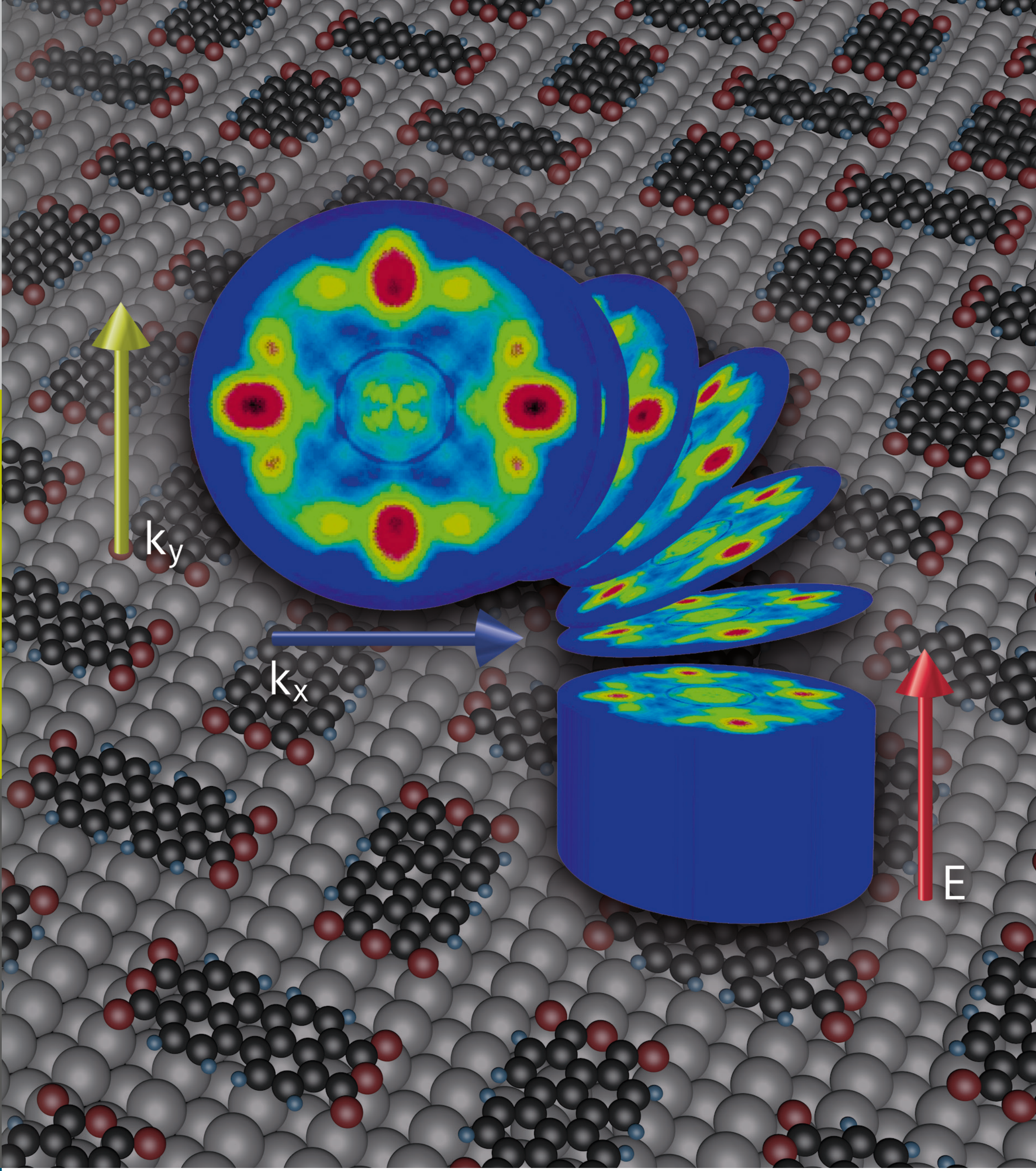

Member of the Helmholtz Association

Interacting Interactions: A Study on the Interplay of Molecule-Molecule and Molecule-Substrate Interactions at Metal-Organic Interfaces

Martin Willenbockel

JÜLICH
FORSCHUNGSZENTRUM

Interacting Interactions: A Study on the Interplay of Molecule-Molecule and Molecule-Substrate Interactions at Metal-Organic Interfaces

Von der Fakultät für Mathematik, Informatik und Naturwissenschaften
der RWTH Aachen University zur Erlangung des akademischen Grades
eines Doktors der Naturwissenschaften genehmigte Dissertation.

vorgelegt von

Diplom-Physiker

Martin Willenbockel

aus Soltau

Berichter: Universitätsprofessor Dr. F. S. Tautz
Universitätsprofessorin Dr. P. Tegeder

Tag der mündlichen Prüfung: 27. November 2014

Diese Dissertation ist auf den Internetseiten der Hochschulbibliothek
online verfügbar.

Forschungszentrum Jülich GmbH
Peter Grünberg Institut (PGI)
Functional Nanostructures at Surfaces (PGI-3)

Interacting Interactions: A Study on the Interplay of Molecule-Molecule and Molecule-Substrate Interactions at Metal-Organic Interfaces

Martin Willenbockel

Schriften des Forschungszentrums Jülich
Reihe Schlüsseltechnologien / Key Technologies Band / Volume 99

ISSN 1866-1807 ISBN 978-3-95806-018-0

Bibliographic information published by the Deutsche Nationalbibliothek.
The Deutsche Nationalbibliothek lists this publication in the Deutsche
Nationalbibliografie; detailed bibliographic data are available in the
Internet at http://dnb.d-nb.de.

Publisher and Distributor: Forschungszentrum Jülich GmbH
Zentralbibliothek
52425 Jülich
Tel: +49 2461 61-5368
Fax: +49 2461 61-6103
Email: zb-publikation@fz-juelich.de
www.fz-juelich.de/zb

Cover Design: Grafische Medien, Forschungszentrum Jülich GmbH

Printer: Grafische Medien, Forschungszentrum Jülich GmbH

Copyright: Forschungszentrum Jülich 2014

Schriften des Forschungszentrums Jülich
Reihe Schlüsseltechnologien / Key Technologies, Band / Volume 99

D 82 (Diss. RWTH Aachen University, 2014)

ISSN 1866-1807
ISBN 978-3-95806-018-0

The complete volume is freely available on the Internet on the Jülicher Open Access Server (JuSER)
at www.fz-juelich.de/zb/openaccess.

Neither this book nor any part of it may be reproduced or transmitted in any form or by any
means, electronic or mechanical, including photocopying, microfilming, and recording, or by any
information storage and retrieval system, without permission in writing from the publisher.

Acknowledgements

The realization of this thesis and the presented projects would have not been possible without fruitful collaborations and the support and contribution of many other people. Therefore, I would like to take this oppertunity to express my gratitude.

First of all I like to thank Professor Stefan Tautz for having confidence in me and providing the opportunity to carry out my PhD work in his group. Despite his tough time schedule there was always the possibility for inspiring discussions with him. His interest in my research ideas and results was always an important source of motivation.

I like to thank Professor Petra Tegeder (Universität Heidelberg) for taking her time to co-referee my thesis and for the joint project on azobenzene and benzene, where special thanks go to Christopher Bronner, Michael Schulze, Stephan Stremlau and Dr. Erwan Varene for our joint beam time at the ESRF. Furthermore, I thank Professor Karsten Reuter and Dr. Reinhard Maurer (Technische Universität München) for their support of the project from the theory side. For the joint research on PTCDA/Ag(100), which led to my first beam time experience, I thank Professor Moritz Sokolowski and Oliver Bauer (Rheinische Friedrich-Wilhelms-Universität Bonn). Completing the list of ESRF beam times I thank Professor Steven L. Tait (Indiana University Bloomington) and Dr. Sebastian M. Stepanow (ETH Zurich) for the collaboration on the TPA experiments. All successfull beam times would not have been possible without the support by the ESRF staff, namely Dr. Jörg Zegenhagen, Dr. Blanka Detlefs and Dr. Julien Duvernay.

For the BESSY beam times on the PTCDA/Ag experiments I thank Professor Michael G. Ramsey and Dr. Georg Koller (Karl Franzens Universität Graz) for their collaboration, and Eva M. Reinisch, Thomas Ules, and Hannes Offenbacher for turning it into unforgettable Berlin experiences. Furthermore the theory support of the projects by Professor Peter Puschnig and Daniel Lüftner (Karl Franzens Universität Graz) is gratefully acknowledged.

I also like to thank my colleagues from the PGI-3 at the Forschungszentrum Jülich, especially Dr. Serguei Soubatch for his friendly guidance and support, Benjamin Stadtmüller for his patience, the anytime possibility to distract him from his work, and all the time spent together on beam times. Giuseppe Mercurio, Mirko Müller, Taner Esat, and Jessica Sforzini for our nice office atmosphere, Dr. Francois Bocquet and Dr. Tomoki Sueyoshi for the joint lab experience, Sonja Schröder, Hubertus Junker, and Norman Fournier for many discussions about the really important topics and all other colleagues for creating a warm and welcoming working atmosphere.

My thanks also go to all my friends, especially Carola, Anja, Falk, Raphael, Sandra, Jan, and Sebastian, and my parents Gisela and Otto and my sister Verena for their unlimited support through all this time.

Abstract

In this work a surface science study on metal-organic interfaces is presented to resolve their geometric and electronic properties and study the interplay of molecule-molecule and molecule-substrate interactions. The organic molecules benzene, azobenzene, 3,4,9,10-perylenetetracarboxylic acid dianhydride (PTCDA), and terephthalic acid (TPA) are deposited on low index Ag and Cu surfaces to form monolayer and sub-monolayer structures which are investigated by normal incidence X-ray standing waves and angle resolved photoemission spectroscopy, which leads to several surprising findings.

Investigating the adsorption of benzene, we find it physisorbed in a flat geometry for benzene on Ag(111). Enhancing the molecule-substrate interaction by exchanging Ag(111) with the stronger interacting Cu(111) is expected to simply lower the adsorption height. However, we find flat molecules at an elevated adsorption height for benzene/Cu(111), which seem to be stabilized via intermolecular interactions due to the coexistence with upright standing benzene molecules.

The interplay of molecule-molecule and molecule-substrate interactions is further explored on a metal-organic network formed by codeposition of TPA and Fe atoms on Cu(100). The coordination of TPA molecules by the Fe atoms reduces the TPA-substrate interaction. An additional sitespecific adsorption of oxygen again alters this balance.

In case of PTCDA a comprehensive study for its adsorption on low index Ag surfaces is presented. From linking the geometric and electronic stucture properties, it is understood that the electron density spill-out of the surface and its uptake by the adsorbing molecule is a decisive molecule-substrate interaction channel. This explains the finding that the resulting binding energies of the lowest unoccupied molecular orbital (LUMO) as well as the adsorption height of PTCDA on Ag are determined by the work function.

Moving to the archetypal molecular switch azobenzene, which is studied on Cu(111), three different azobenzene monolayer phases which are formed along with a coverage dependent dissociation of the molecule are revealed. The higher the density of molecules get, the stronger molecule-molecule interactions become and force the molecule to bend. However, its strong molecule-substrate bond prevents a conformational change and the resulting stress ultimately leads to a dissociation.

The surprising results of this work show that the understanding of interactions at metal-organic interfaces is still only rudimentary and stress the importance of further fundamental research.

List of Acronyms

ARPES	angle resolved photoelectron spectroscopy
BW	brickwall
CBE	constant binding energy
COP	commensurate ordered phase
DFT	density functional theory
DP	disordered phase
EDC	energy distribution curve
EELS	electron energy loss spectroscopy
FWHM	full width at half maximum
HB	herringbone
HOMO	highest occupied molecular orbital
LEED	low energy electron diffraction
LUMO	lowest unoccupied molecular orbital
MLP	multilayer phase
NEXAFS	near edge X-ray absorption fine structure spectroscopy
NIXSW	normal incidence X-ray standing waves
PDOS	projected density of states
PLP	point-on-line phase
PTCDA	3,4,9,10-perylenetetracarboxylic acid dianhydride
STM	scanning tunneling microscopy
STS	scanning tunneling spectroscopy

TPA	terephthalic acid
TPD	temperature programmed desorption
UHV	ultra-high vacuum
UPS	ultraviolet photoelectron spectroscopy
vdW	van der Waals
XPS	X-ray photoelectron spectroscopy
XSW	X-ray standing waves
2PPE	two photon photoemission spectroscopy

Contents

1 Introduction 1

2 Methods 5
- 2.1 Introduction 5
- 2.2 Photoelectron spectroscopy 5
- 2.3 Angle resolved photoelectron spectroscopy 8
- 2.4 X-Ray standing waves 10
- 2.5 Experimental setups 16
  - 2.5.1 ARPES 16
  - 2.5.2 XSW 17

3 Benzene on Ag(111) and Cu(111) 19
- 3.1 Introduction 19
- 3.2 Benzene on Ag(111) 20
  - 3.2.1 Introduction 20
  - 3.2.2 Experimental details 21
  - 3.2.3 X-ray induced changes 22
  - 3.2.4 Coverage estimation 25
  - 3.2.5 XSW results 27
  - 3.2.6 Conclusion 29
- 3.3 Benzene on Cu(111) 33
  - 3.3.1 Introduction 33
  - 3.3.2 Experimental details 34
  - 3.3.3 Beam damage 35
  - 3.3.4 Coverage estimation 36
  - 3.3.5 XSW analysis 37
  - 3.3.6 LEED 43
  - 3.3.7 Conclusion 44
- 3.4 Summary 48

4 **Azobenzene Cu(111)** 49

4.1 Introduction . . . 49
4.2 Submonolayer coverage regime . . . 50
  4.2.1 LEED results . . . 50
  4.2.2 XPS model . . . 51
  4.2.3 XSW analysis . . . 53
4.3 Ordered point-on-line phase . . . 57
  4.3.1 LEED results . . . 57
  4.3.2 XPS Model . . . 58
  4.3.3 XSW analysis . . . 60
4.4 Ordered commensurate phase . . . 65
  4.4.1 LEED results . . . 65
  4.4.2 XPS model . . . 67
  4.4.3 XSW analysis . . . 67
4.5 Multilayer . . . 74
  4.5.1 XPS models . . . 74
  4.5.2 Coverage estimation . . . 75
  4.5.3 XSW results . . . 78
4.6 Discussion . . . 83
  4.6.1 Introduction . . . 83
  4.6.2 Distortion of azobenzene for the DP . . . 83
  4.6.3 Coverage dependent dissociation . . . 87
  4.6.4 Ordered lateral structures . . . 91
4.7 Conclusion . . . 94

5 **Geometric and electronic structure of PTCDA on low index Ag surfaces** 99

5.1 Introduction: An attempt of a comprehensive view . . . 99
5.2 Lateral structures of PTCDA on Ag(111) and Ag(100) . . . 101
5.3 Lateral structures of PTCDA/Ag(110) . . . 102
5.4 Vertical structure of PTCDA/Ag(100) . . . 104
  5.4.1 Introduction . . . 104
  5.4.2 Experimental details . . . 105
  5.4.3 Coverage estimation . . . 106
  5.4.4 PTCDA/Ag(100) - C1s results . . . 108
  5.4.5 PTCDA/Ag(100) - O1s results . . . 114
  5.4.6 Adsorption site determination for PTCDA/Ag(100) . . . 119

5.4.7 PTCDA/Ag(100) - Substrate results 123
5.4.8 Discussion 124
5.5 A/B split for PTCDA/Ag(110) 132
5.5.1 Introduction 132
5.5.2 Results 133
5.5.3 Discussion 136
5.6 Energy level alignment of LUMO and HOMO in PTCDA/Ag 140
5.6.1 Introdction 140
5.6.2 Experimental results 141
5.6.3 Discussion 142
5.7 Native order of stronger bound molecular Orbitals 148
5.7.1 Introduction 148
5.7.2 Results 149
5.7.3 Discussion 153
5.8 Summary 155

6 TPA:Fe/Cu(100) - A metal organic network 157
6.1 Introduction 157
6.2 Experimental 158
6.3 O1s results 161
6.4 Fe results 166
6.5 C1s results 172
6.6 Oxygen dosing on TPA:Fe/Cu(100) 178
6.7 Conclusions 182

7 Summary 187

A Appendix 191

Bibliography 225

1 Introduction

A major challenge of todays society is the development of ideas and technology for the electrical power supply in the future. The ever increasing number of electronic devices in all aspects of life and the goal to become independent of fossil fuel and nuclear power emphasizes the need to invent new concepts and solutions. In this framework the development of organic electronic devices plays an important role, because the use of organic semiconductors instead of the inorganic Si based technology promises a major advantage: energy efficiency. This is illustrated by a competition between humans and the '*IBM Watson*' super computer [1] in the famous quiz show '*Jeopardy!*'. While the computer could beat its human competitors in a very human-like task, it required more than 2 MW to challenge the human brain, which consumes just about 25 W. This example shows the potential of energy efficincy in the use of organic materials instead of common technology and it emphasizes the need to explore and understand the fundamental processes far beyond the present use of organic semiconductors in devices like organic light emitting diodes [2].

Before one can design novel concepts and tailor the properties of organic devices by changes of the molecular constituents, the principles of their functionality and the elementary processes behind must be understood in detail. Furthermore, interfaces between different materials can be expected to be crucial parts of each device with an important impact on the properties. For example metal-organic interfaces may even govern the performance characteristics due to their influence on the geometric and electronic structure of the organic layer [3]. To understand how the properties of molecules are affected by a metal surface we study the interwined intermolecular and molecule-substrate interactions of metals and molecules on representative metal-organic interfaces on a fundamental level.

A sensitive gauge for the metal-organic interaction is the adsorption distance between surface and molecule. This parameter can be directly accessed by (normal incidence) X-ray standing wave ((NI)XSW) experiments [4, 5]. Because an important feature of organic semiconductor molecules is an aromatic backbone, benzene as smallest representative of the class of aromatic molecules, hence in some manner a building block of more extended systems, is an important candidate for our study. To this end the adsorption geometry of benzene on Ag(111) and Cu(111) is studied by NIXSW in chap. 3, demonstrating the influence of the substrate by large differences in the structure formation at both interfaces.

One of the molecules interesting for organic electronics and in possession of a large aromatic backbone is 3,4,9,10-perylenetetracarboxylic acid dianhydride (PTCDA). It attracted great research interest over the last two decades (e.g. compare ref. [6]), therefore a wealth of data for various PTCDA/metal combinations is already available. Here the focus lies on the PTCDA adsorption on low index Ag surfaces, which offers a variety of different geometric structures and electronic properties. The relatively new orbital tomography approach [7–9], which is based on angle resolved photoemission spectroscopy (ARPES) experiments but succeeds in the differentiation of data from differently aligned molecules on the surface, is employed to gain insight in the delicate balance of molecule-molecule and molecule-substrate interactions and reveals the crucial role of the work function in the energy level alignment process.

The influence of molecule-substrate interactions on the functionality of molecules is studied on the example of the archetypal molecular switch azobenzene. Upon adsorption of the molecule onto surfaces, the switching ability is often quenched [10, 11]. Therefore, one needs to investigate the adsorption process to understand the reason for the quenching to be able to develop strategies which preserve the switching functionality upon adsorption. In chap. 4 the azobenzene/Cu(111) system is studied by means of NIXSW and a detailed picture of the adsorption geometry is presented. Furthermore a phase change is observed depending on the surface coverage. The phase change could be traced back to a dissociation of the azobenzene molecule, similar to the case of azobenzene/TiO_2 [12] and it seems reasonable that the switching of the molecule might be prevented, because it dissociates before a conformational change is completed.

Finally, the controlled arrangement of structures due to the self assembly of adsorbates, the so called bottom-up approach [13] is focused. A famous class of systems forming nanopatterned surfaces in self organisation, which could host functional molecules in a next step, are metal-organic networks [14]. By the co-deposition of molecules and metals, regular structures are formed through the coordination of the molecules around the metal centers. By the coadsorption of terephthalic acid (TPA) and Fe atoms a well known representative of this metal-organic networks is formed [15, 16]. Even without additional guest molecules the system represents a highly ordered array of magnetically active centers in form of the Fe atoms and the direction of their easy magnetization axis can be tuned by site selective oxygen adsorption [17]. In chap. 6 TPA:Fe/Cu(100) before and after oxygen adsorption is investigated by NIXSW and the interplay in the Fe-TPA, TPA-substrate and Fe-substrate bonding is illuminated.

2 Methods

2.1 Introduction

The following chapters introduce the methods employed for the data acquisition used in this work. The first section will introduce the photoemission process in general to prepare the explanation of the specialized variants of angle resolved photoelectron spectroscopy and the X-ray standing wave technique. Finally the experimental setups are described briefly.

2.2 Photoelectron spectroscopy

We make use of the processes happening upon light shining on matter. If the energy of the electromagnetic wave is high enough, the interaction with matter can lead to the emission of electrons (so called photoelectrons) which can be detected by a spectrometer. The basic phenomenon is called the photoelectric effect which was explained by Einstein [18] after it had been experimentally observed by Hertz [19] and Hallwachs [20]. Today the spectroscopy of photoelectrons is a well-established technique in surface science to investigate the electronic properties of materials. The reason is its intrinsic surface sensitivity due to the limited escape depth of the photoelectrons. The kinetic energy of the photoelectron (E_{kin}) is calculated as

$$E_{\mathrm{kin}} = h\nu - E_{\mathrm{B}} - \Phi, \tag{2.1}$$

with E_{B} being the binding energy and Φ being the potential difference between sample and spectrometer and the spectrometer workfunction. With lab sources photon energies ($h\nu$) of up to roughly 1500 eV are commonly used and therefore photoelectrons may feature inelastic mean free paths of the order of 20 Å [21]. Of course, the detailed escape depth depends on the material under investigation. The use of high energy photons of several keV has only recently become possible for photoelectron spectroscopy, because spectrometers had to be developed for high kinetic energy photoelectrons. Nowadays such hard X-ray photoemission experiments are possible at specialized beamlines on synchrotron sources around the world and allow the application of photoemission to study bulk properties due to the enhanced escape depth [22]. In general the main usage still divides into two areas: First the investigation of valence states with low binding energies by using rather low photon energies ($E_{h\nu} < 100\,\mathrm{eV}$), which is called ultraviolet photoelectron spectroscopy (UPS), and the investigation of core levels, which is called X-ray photoelectron spectroscopy (XPS) and usually employs higher photon energies ($E_{h\nu} > 100\,\mathrm{eV}$). In all cases the monochromaticity of the light is very important for a defined relation between E_{kin} and E_{B} which can be deduced directly from eq. (2.1).

We now turn to the mathematical description of the photoemission process. However, the theoretical introduction of the photoemission spectroscopy presented here will be restricted to the very basics and is following reference [23] which offers a far more detailed description of its theory and applications. Before the photoemission process takes place our system is in its initial state i with the wavefunction $\Psi_i(N)$, where N is the number of electrons. After the photoemission we have the final state f with the corresponding wavefunction $\Psi_f(N)$. The light is described by a photon field with the vector potential $\boldsymbol{A}$. In the time dependent pertubation theory the transition probability per time can now be described by Fermi's Golden Rule

$$w \propto \frac{2\pi}{\hbar} \left|\langle\Psi_f|\,\Delta\,|\Psi_i\rangle\right|^2 \delta(E_f - E_i - h\nu) \tag{2.2}$$

with E_i and E_f being the energies of the initial and final states and Δ the pertubation operator. In the Coulomb gauge the scalar potential of the photon field becomes zero and the relation $\nabla \cdot \mathbf{A} = 0$ is valid. If one further neglects two photon processes, the pertubation operator has the form

$$\Delta = \frac{e}{mc}\boldsymbol{A} \cdot \boldsymbol{p} \tag{2.3}$$

with $\boldsymbol{p}$ being the momentum operator $\boldsymbol{p} = i\hbar\nabla$ of the photoelectron. Assuming that the wavelength of the light is much larger than the interatomic distances (dipole approximation), we can take the vector potential of the light field as constant ($\boldsymbol{A} =$

$\boldsymbol{A}_0$) and reach the equation

$$w \propto \frac{2\pi e}{mc\hbar} \left|\langle\Psi_f|\, \boldsymbol{A}_0 \cdot \boldsymbol{p}\, |\Psi_i\rangle\right|^2 \delta(E_f - E_i - h\nu). \tag{2.4}$$

At this point one can introduce the so called frozen approximation which is based on the assumption that only the photoelectron changes its state, while the other $N-1$ electrons of the system stay unperturbed. If we separate the photoelectron in the initial and final state wavefunctions, we get

$$\Psi_i(N) = \widehat{C}\psi_{i,\mathbf{k}}\Psi^{\mathbf{k}}_{i,\mathrm{R}}(N-1) \tag{2.5}$$

$$\Psi_f(N) = \widehat{C}\psi_{f,E_{\mathrm{kin}}}\Psi^{\mathbf{k}}_{f,\mathrm{R}}(N-1) \tag{2.6}$$

with $\widehat{C}$ being the proper antisymmetrizing operator and R indicating 'remaining'. If we use these wavefunctions for the matrix element in eq. (2.4), we find the expression

$$\langle\Psi_f|\, \boldsymbol{A}_0 \cdot \boldsymbol{p}\, |\Psi_i\rangle = \langle\psi_{f,E_{\mathrm{kin}}}|\, \boldsymbol{A}_0 \cdot \boldsymbol{p}\, |\psi_{i,\mathbf{k}}\rangle \left\langle\Psi^{\mathbf{k}}_{f,\mathrm{R}}(N-1)|\Psi^{\mathbf{k}}_{i,\mathrm{R}}(N-1)\right\rangle, \tag{2.7}$$

which consists of a one electron matrix element and the $(N-1)$ electron overlap integral. In the frozen approximation the overlap integral will be one, because we use $\Psi^{\mathbf{k}}_{f,\mathrm{R}}(N-1) = \Psi^{\mathbf{k}}_{i,\mathrm{R}}(N-1)$. Then only the one-electron matrix element is left as transition matrix element between the initial and the final state and therefore eq. (2.2) in the frozen approximation becomes

$$w \propto \frac{2e\pi}{mc\hbar} \left|\langle\psi_{f,E_{\mathrm{kin}}}|\, \boldsymbol{A}_0 \cdot \boldsymbol{p}\, |\psi_{i,\mathbf{k}}\rangle\right|^2 \delta(E_f - E_i - h\nu). \tag{2.8}$$

This approximation is useful, but the binding energies calculated in the frozen approximation will be obviously wrong, because it is neglecting any charge reorganisation upon the creation of a photohole. However, such reorganisation will especially appear in the presence of surfaces and polarizable molecules and hence the orbital binding energies would need corrections. Further detailed information on the topic can be found in standard textbooks about photoemission such as ref. [23].

2.3 Angle resolved photoelectron spectroscopy

In the general approach of an angle integrated UPS experiment one measures the intensity of photoelectrons depending on the binding energy, which results in the so called energy distribution curve (EDC). Hence, in case of metal-organic interfaces, in an EDC the energy position of the corresponding molecular orbitals will appear as peaks on top of the signature from the metal bands. To assign these features and to understand which peak represents which orbital one can only compare the experimental data with calculations. However, the angular emission pattern of the photoelectrons is not homogeneous and strongly orbital dependent, therefore allowing their unambiguous discrimination. The angle resolved photoelectron spectroscopy (ARPES) is already used to map out bandstructures or surface states [23], but a rather new approach is used for the identification of molecular orbitals in large organic molecules.

Recently Puschnig *et al.* [7, 8] demonstrated that even a rather simple approximation on the theoretical side is sufficient to calculate the orbital dependent angular photoelectron emission pattern well enough to identify even overlapping orbitals in the experimental data. The approximation uses the so-called plane wave approximation [24] in which the final state of the photoelectron is described by a plane wave. This changes eq. (2.8) to

$$w \propto \left| \left\langle e^{i\vec{k}\vec{r}} \right| \boldsymbol{A}_0 \cdot \boldsymbol{p} \left| \psi_{\mathbf{k}} \right\rangle \right|^2 \delta(E_f - E_i - h\nu) \tag{2.9}$$

and therefore the angle dependent intensity $I(E_B, \phi, \theta)$ of the orbitals is proportional to the Fourier transform of the initial state wavefunction $\tilde{\psi}_{\mathbf{k}}$:

$$I(E_B, \phi, \theta) \propto w \propto \left| \left\langle e^{i\vec{k}\vec{r}} \right| \boldsymbol{A}_0 \cdot \boldsymbol{p} \left| \psi_{\mathbf{k}} \right\rangle \right|^2 \propto |\boldsymbol{A}_0 \boldsymbol{k}|^2 \cdot \left| \tilde{\psi}_{\mathbf{k}} \right|^2 . \tag{2.10}$$

For large organic molecules it was shown that the Fourier transforms of their gas phase wavefunction can be used to identify the corresponding molecular orbitals at metal organic interfaces [7, 8, 25].

One can go one step further and apply the technique of orbital tomography. Tomography usually describes a technique where sections of a 3D object are imaged. In our case the object is a 3D datacube $I(k_x, k_y, E_\mathrm{B})$ of the ARPES intensity with k_x and k_y being the conserved parallel momentum components of the photoelectron and E_B its binding energy. As shown in Fig. 2.1a the tomographic sections of our 3D object are

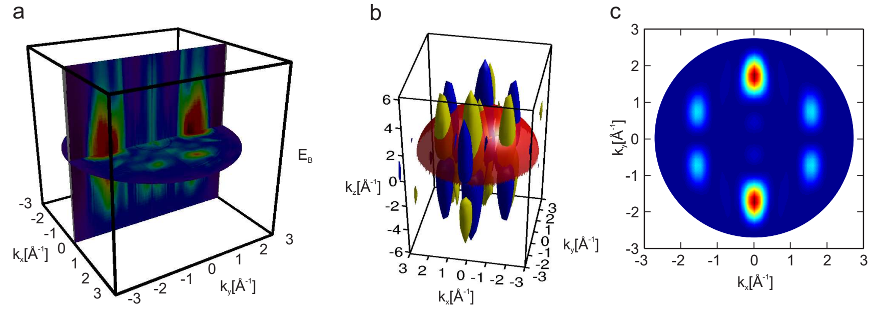

Figure 2.1: (a) Experimental datacube $I(k_x, k_y, E_\mathrm{B})$ as schematic false colour plot. For the orbital tomography slices of constant binding energy are extracted and the resulting $I(k_x, k_y)$ CBE map is fitted by theoretical CBE maps of contributing orbitals. (b) Fourier transform of the molecular orbital with the hemispherical cut to extract the calculated CBE map which is shown in panel c. The figure is done by D. Lüftner, KFU Graz. (c) Calculated CBE map for the LUMO of PTCDA. The calculations were done by D. Lüftner and P. Puschnig, KFU Graz.

slices through the datacube at constant binding energy (CBE) and therefore called CBE maps. The datacube is deconvoluted section-by-section into the contributions of individual orbitals. In this way the orbital tomography allows to unambiguously assign in energy overlapping orbitals [7–9, 25–27].

Technically, density functional theory (DFT) is used to calculate the gas phase wavefunction of a certain orbital, which is then Fourier transformed. To create a 2D map which corresponds to the experimental CBE maps, the projection of a hemispherical cut along $|\mathbf{k}| = \sqrt{(\frac{2m}{\hbar^2}) \cdot E_\mathrm{kin}}$ is extracted as shown in Fig. 2.1b, because k_x and k_y of the photoelectron are conserved in the photoemission process and hence k_z is adjusted such that $E_\mathrm{kin} = \mathrm{const}$. The resulting calculated CBE maps look like the example shown in Fig. 2.1c for the PTCDA lowest unoccupied molecular orbital (LUMO). A direct comparison of the CBE map with the experimental data is already useful for energetically well separated orbitals, but in case of orbitals closely spread in energy, the method of orbital tomography uses a fitting routine to match the experimental CBE map by a linear combination of several theoretical CBE maps following the minimization of

$$\chi^2 = \int\int dk_x dk_y \left[I(k_x, k_y, E_\mathrm{B}) - \sum_i a_i(E_\mathrm{B}) \phi_i(k_x, k_y) \right]^2 . \qquad (2.11)$$

The $I(k_x, k_y, E_\mathrm{B})$ is the intensity from the experimental data and the $\phi_i(k_x, k_y)$ are the calculated CBE maps. The $a_i(E_\mathrm{B})$ are the fitting parameters. If the binding energy of the orbital is sufficiently separated from the Fermi edge, and hence its intensity contribution is not convoluted with the Fermi function, these parameters actually represent the projected density of states (PDOS) of the corresponding orbital. In this way the PDOS can be accessed experimentally, which is a unique and powerfull property of the orbital tomography approach.

It should be noted that one can argue about the general applicability of the orbital tomography, because the plane wave approximation leading to the theoretical CBE maps does not consider any scattering, the wavefunctions are calculated from gas phase molecules in the one-electron picture and the substrate is completely neglected. While the substrate can be introduced by including experimental data of the clean surface into the fitting routine [9], it is true that the theoretical CBE maps represent a somewhat artifical basis set which is then used to fit the experimental data. However, if understood as a projection of the experimental data onto an arbitrary basis set, the method is analogue to the theoretical procedure to obtain the PDOS and the result shows that CBE maps calculated in the described way are indeed a good choice as a basis. Further details about this method can be found in ref. [7–9] and it is applied in this work in chapter 5. It should be noted that, bringing orbital tomography to the next level, the direct reconstruction of real space wavefunctions from experimental CBE maps, despite the lack of phase information, was recently accomplished [28].

2.4 X-Ray standing waves

The X-ray standing waves (XSW) method is used to directly determine the adsorption height of adsorbates in an experiment. It is described in detail in ref. [4, 5, 29] and only a brief introduction will be given here.

The prerequisits for this method are a tunable monochromatized photon source in the range of a few keV and therefore a suitable synchrotron beamline, together with a sample that features a distinct lattice spacing such as a single crystal, and a vertically well defined interface. The method is based on the interference between an incoming photon beam with the electric field $\mathscr{E}_0 = E_0 e^{-2\pi i \vec{k}_0 \vec{r}}$ and its reflected wave $\mathscr{E}_H = E_H e^{-2\pi i \vec{k}_H \vec{r}}$. For the Bragg reflection from the (hkl) plane of the sample, $2\pi \vec{H} = \vec{k}_H - \vec{k}_0$ must be the reciprocal lattice vector with length $\left| \vec{H}_{hkl} \right| = \frac{1}{d_{hkl}}$, where d_{hkl} is the real space distance between lattice planes. Because both waves are coherent, they interfere with each other and form a standing wave field with the intensity

$$I = \left| E_0 e^{-2\pi i \vec{k}_0 \vec{r}} + E_H e^{-2\pi i \vec{k}_H \vec{r}} \right|^2 = |E_0|^2 \left| 1 + \frac{E_H}{E_0} e^{-2\pi i \vec{H} \vec{r}}. \right|^2 \tag{2.12}$$

If we define z to be the vertical distance between the point $\vec{r}$ and the lattice plane, we can therefore write $\vec{H} \cdot \vec{r} = \frac{z}{d_{hkl}}$. Furthermore, the amplitude of the standing wave can be expressed as

$$\frac{E_H}{E_0} = \sqrt{R} e^{i\phi} \tag{2.13}$$

with the reflectivity $R = \left| \frac{E_H}{E_0} \right|^2$ and the phase relationship ϕ between incoming and reflected wave. This changes eq. (2.12) to

$$I = \left| E_0 e^{-2\pi i \vec{k}_0 \vec{r}} + E_H e^{-2\pi i \vec{k}_H \vec{r}} \right|^2 = |E_0|^2 \left| 1 + \sqrt{R} e^{i\phi} e^{-2\pi i \frac{z}{d_{hkl}}} \right|^2. \tag{2.14}$$

and we find for the X-ray intensity (for $|E_0|^2 = 1$)

$$I = 1 + R + 2\sqrt{R} \cos(\phi - 2\pi \frac{z}{d_{hkl}}). \tag{2.15}$$

From Bragg's law

$$\lambda_{\mathrm{Bragg}} = 2 d_{hkl} \sin\theta \tag{2.16}$$

one would only expect a defined photon energy $E_{\mathrm{Bragg}} = \frac{hc}{\lambda_{\mathrm{Bragg}}}$ to be suited to create this standing wave, but from the dynamic scattering theory, which takes into account multiple scattering events, it follows that a finite energy range exists where constructive interference (Bragg reflection) takes place and therefore a standing wave field is generated. The reflectivity curve with nonvanishing R in this energy range is called Darwin curve. When the photon energy is varied through the range of the Darwin curve the phase ϕ changes from $\phi = \pi$ for $h\nu \ll E_{\mathrm{Bragg}}$ to $\phi = 0$ for $h\nu \gg E_{\mathrm{Bragg}}$. Hence, the nodes and antinodes of the standing wave field are shifted by half the lattice spacing during the energy scan.

With the standing wave field present at our sample, we can now use XPS as a detection method. Alternative methods which detect flourescence or Auger electron signals are also possible, but with XPS we get the surface sensitivity we want and furthermore a chemical sensitivity, because one can distinguish not only different elements, but also the same element in different chemical environments in XPS spectra.

If we imagine an atom at a position $\vec{r}$ above the surface, its integrated photoelectron signal, the so-called photoelectron yield Y, is proportional to the X-ray intensity ($Y \propto I$) and we can directly use eq. (2.15) to fit the yield profile $Y(h\nu)$ and extract z, the distance above the Bragg plane of the atom at position $\vec{r}$. It should be mentioned that z is only the adsorption height d_c modulo the Bragg plane distance

$$z = d_\mathrm{c} \bmod d_{hkl} \tag{2.17}$$

and therefore the real adsorption height

$$d_\mathrm{c} = z + n \cdot d_{hkl}, n \in \mathbb{N}_0 \tag{2.18}$$

is ambiguous, but there is usually only one physically meaningful result.

However, the example of a single atom is very artificial, because in the real experiment there will always be an ensemble of N atoms which will therefore show a certain z distribution instead of a single distance. To account for this, we introduce the distribution of adsorbers

$$f(z) = \frac{1}{N} \sum_{i=1}^{N} \delta(z - z_i) \tag{2.19}$$

which fulfills the normalization $\int_0^{d_{hkl}} f(z)dz = 1$. This changes eq. (2.15) to

$$I = 1 + R + 2\sqrt{R} \int_0^{d_{hkl}} f(z) \cos(\phi - 2\pi \frac{z}{d_{hkl}})dz. \tag{2.20}$$

If we define two parameters, the coherent fraction $F_\mathrm{c}^i = \frac{1}{N}$ of the individual atoms and their coherent position $P_\mathrm{c}^i = \frac{z_i}{d_{hkl}}$, eq. (2.20) can be written as

$$I = 1 + R + 2\sqrt{R} \cdot \sum_{i=1}^{N} F_\mathrm{c}^i \cos\left(\phi - 2\pi \cdot P_\mathrm{c}^i\right). \tag{2.21}$$

If P_c^i and F_c^i are interpreted as phase and amplitude of the Fourier vector

$$\tilde{f}_{\vec{H}}^i = F_\mathrm{c}^i \exp\left(2\pi i P_\mathrm{c}^i\right), \tag{2.22}$$

we find for the Fourier transform of the distribution $f(z)$

$$\sum_{i=1}^{N} \tilde{f}_{\vec{H}}^i = F_\mathrm{c} \exp\left(2\pi i P_\mathrm{c}\right), \tag{2.23}$$

and hence

$$I = 1 + R + 2\sqrt{R} \cdot F_\mathrm{c} \cos\left(\phi - 2\pi \cdot P_\mathrm{c}\right) \tag{2.24}$$

with F_c being the coherent fraction and P_c the coherent position of the ensemble. The P_c describes the mean height of the atoms in fractions of the Bragg plane distance from the next Bragg plane. Hence the P_c can have values between 0 and 1 and suffers from the ambiguity discussed above for z with

$$d_\mathrm{c} = (P_\mathrm{c} + n) \cdot d_{hkl}, n \in \mathbb{N}_0. \tag{2.25}$$

It should be noted that this means for the adsorption height $d_\mathrm{c}(P_\mathrm{c})$ that $d_\mathrm{c}(0) = d_\mathrm{c}(1)$. The F_c describes the distribution of atoms among the Bragg plane distance. It can vary between 0 and 1, where a F_c of 1 means perfect order, while a homogeneous distribution leads to a F_c of 0. For the presentation of the results a polar plot with the F_c as radius and the P_c as angle is very useful, because it contains the ambiguity of P_c and the correct vector sum following eq. (2.23). In Fig. 2.2a such a plot, which is called Argand diagram, is shown, where two adsorption sites exist and the individual results (F_c^1, P_c^1, blue) and (F_c^2, P_c^2, red) are used to construct the ensemble result (F_c, P_c, green). For reasons of simplicity the site population is assumed to be

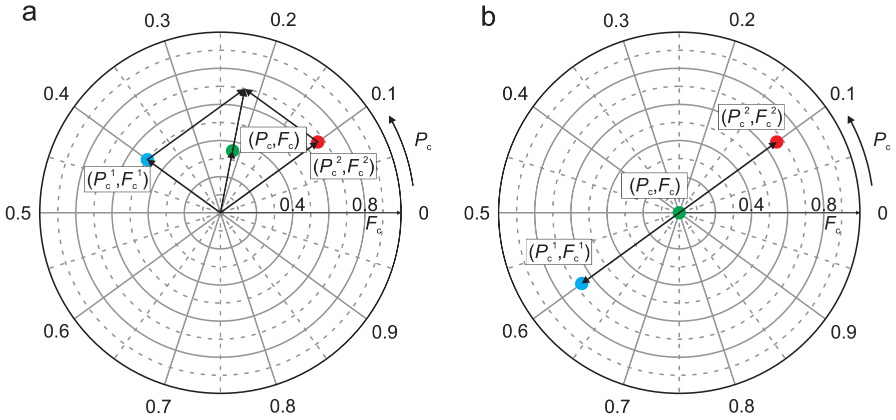

Figure 2.2: Two Argand diagrams are shown to visualize the use of P_c and F_c as Fourier components. In these polar plots P_c acts as the angle parameter and F_c is the radius. This intrinsically fulfills the requirement $0 \equiv 1$ for P_c. In panel a the vector sum of the red and the blue lead to the green result, assuming that the population of red and blue is equal. In panel b the red and blue results differ by a P_c of 0.5 and therefore their mean value (green) has a F_c of 0, rendering its P_c meaningless despite the well defined results for red and blue.

equal for this example, else the vectors have to be summed with their corresponding weights.

In Fig. 2.2b the same principle is depicted but for the special case of $|P_\mathrm{c}^2 - P_\mathrm{c}^1| = 0.5$ and $F_\mathrm{c}^1 = F_\mathrm{c}^2$. Because these positions (red, blue) are opposite in the Argand diagram, the sum vector (green) yields $F_\mathrm{c} = 0$ rendering the P_c meaningless despite the well defined individual results for red and blue. Therefore the interpretation of F_c as a measure of the order has to be done very carefully.

As long as all atoms of the measured ensemble are situated in the same Bragg spacing the calculation of their mean adsorption height is simply following eq. (2.25). However, there are cases like tilted molecules or multilayers where the distribution of atoms crosses one or more Bragg planes, and hence leads to a discontinuity in the P_c, rendering the simple calculation of d_c from eq. (2.25) erroneous. In fact, complicated adsorption geometries may prevent the calculation of d_c from the XSW results. In such cases the XSW results of all possible geometries must be simulated, because the calculation of F_c and P_c from a known real space distribution of atoms is always possible, and the correct configuration has to be selected by comparison to the experiment. This means both parameters P_c and F_c are necessary to resolve the correct d_c. A detailed investigation of this issue is presented by Mercurio *et al.* [30] and the simulation of XSW results to match the experimental data is used in this work in sec. 3.3 and chap. 4.

It was already mentioned that the value of F_c should not exceed 1. However, values above this threshold are indeed extracted from the fitting routine in several cases throughout this work. Such artificial values for F_c might arise because the dipole approximation is not valid anymore. The wavelenght of the X-ray beam is in fact of the order of the inter atomic distances, and therefore the vector potential of the light field cannot be treated as constant, but its direction becomes important. This leads to a different angle dependence of the emitted photoelectrons for the incoming and the reflected waves, and hence the electron yield becomes dependent on the angle between incoming photon beam and analyser. Fortunately, it turns out that such corrections are not necessary for an angle of 90° between incoming photon beam and analyser, which is the geometry used for the XSW experiments presented here. Detailed information about this issue can be found in ref. [31, 32] and the determination of non dipolar corrections especially in the case of wide analyzer acceptance angles is subject of ongoing research. Exactly this acceptance angle issue could lead to necessary corrections in our case (and hence raw values of F_c above 1), but because no correction scheme is available so far, no corrections are applied.

2.5 Experimental setups

2.5.1 ARPES

The tomographic ARPES experiments were carried out at room temperature under ultra-high vacuum (UHV) conditions with a base pressure $p < 2 \times 10^{-9}$ mbar at the Beamline U125/2-SGM BESSY II storage ring with the toroidal analyzer endstation. In our tomographic ARPES experiments the samples are illuminated under an incident angle of $\alpha = 40°$ with respect to the surface normal and only the intensity of forward emitted photoelectrons is later used for the analysis, to fulfill the condition of a small angle between the polarization vector of the incoming photons and the direction of the emitted electrons, which is a prerequisite for the applicability of the plane wave approximation [7]. The analyzer allows the simultaneous detection of photoelectrons emitted with with kinetic energy differences up to 2 eV and polar angles (ϕ) between ±80°. Hence, photoelectrons of all polar angles are collected without the need of a sample tilt, which would be necessary in the case of an analyser with a smaller acceptance angle. This enables the measurement without any change of the incident light polarisation in respect to the surface normal. To collect photoelectrons in the full hemisphere above the sample surface, the sample is rotated around its surface normal (azimuthal rotation around θ) in steps of 1°. Symmetries of the system are employed to reduce the necessary rotation to 90°, 120° or 180° respectively. While this has the drawback that the full electron emission is not measured in one shot like in a microscope approach [26, 33], it has the advantage that the angle between the polarization vector of the incoming photons and the direction of the emitted photoelectrons in the resulting data set is independent of the azimuthal angle. For more details on the toroidal analyzer see ref. [34]. The obtained angle dependent data is transformed into (k_x, k_y) reciprocal space coordinates by

$$k_x = \sqrt{\frac{2m_e}{\hbar^2} E_{\text{kin}}} \sin(\theta) \cos(\phi) \tag{2.26}$$

$$k_y = \sqrt{\frac{2m_e}{\hbar^2} E_{\text{kin}}} \sin(\theta) \sin(\phi) \tag{2.27}$$

to allow a direct comparison with the calculated CBE maps and the fitting routine for the orbital tomography as described above.

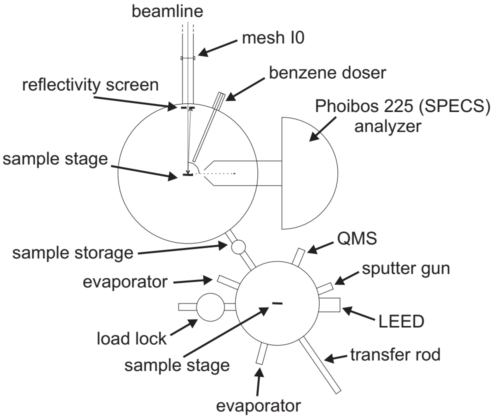

Figure 2.3: Sketch of the experimental UHV chamber system at ID 32 at the ESRF Grenoble. It consists of two main parts: First the analysis chamber (top part of the figure) equipped with an electron analyzer (Phoibos 225, SPECS), a coolable sample stage which allows for precise sample positioning, a reflectivity screen to record the intensity of the reflected beam, the beamline connection, the mesh I0 to measure incoming beam intensity and the benzene doser. Second the preparation chamber (bottom part of the figure) equipped with a sample storage, evaporators, a load lock, the transfer system, a LEED, a sputter gun and a QMS

2.5.2 XSW

All XSW experiments were performed at the UHV endstation at beamline ID 32 at the European Synchrotron Radiation Facility (ESRF) Grenoble. A sketch of the two-chamber system is presented in Fig. 2.3. For the detection of the photoelectrons a hemispherical electron analyzer is used (Phoibos 225, SPECS) which has an acceptance angle of ±17° and is equipped with a delay line detector. For residual gas analysis and evaporator flux control a mass spectrometer is employed. A LEED unit allows for surface characterization in the preparation chamber. It should be noted that, while the sample can be cooled by liquid helium down to 60 K during the XSW experiments, in the preparation chamber only liquid nitrogen cooling is available and the sample transfer cannot be cooled. Therefore the benzene/metal systems discussed in sec. 3 were prepared directly in the analysis chamber.

The data evaluation is done in a two step process. First, the XPS datasets are fitted in *CasaXPS* [35] to extract the electron yields of the corresponding photoemission lines for each photon energy, and second the yield profiles are fitted with *Torricelli* [36–38] to find the resulting P_c and F_c and hence the adsorption height d_c. The errors given for P_c, F_c and hence d_c are statistical errors and are calculated following Mercurio *et al.* [39], which is briefly introduced in the following.

First the errors of the photoelectron intensities which are extracted from each individual XPS spectrum of an XSW data set are calculated. Based on the assumption that the noise of the XPS spectra follows Poisson statistics, a Monte Carlo algorithm calculates 400 synthetic spectra with random noise from the XPS model of the experimental data. The deviation of the fitting parameter, i.e. the intensity, between those synthetic spectra is therefore only based on the statistical noise. Hence it can be used to calculate the statistical error δY of the integrated intensity of each component in the XPS model for each XPS spectrum in the XSW data set. The calculation is done within the *CasaXPS* [35] software. In a second step this error values δY are taken into account within the fitting algorithm for the yield curves in *Torricelli* [36–38] to produce an error value $\delta P_{\mathrm{c},i}$ and $\delta F_{\mathrm{c},i}$ of each dataset i. To calculate the error of the mean value for a number of k datasets the following two possibilities are computed. First the mean value of the corresponding errors of the single datasets

$$\delta F_{\mathrm{c}} = \frac{1}{k}\sum_{i=1}^{k}\delta F_{\mathrm{c},i} \tag{2.28}$$

$$\delta P_{\mathrm{c}} = \frac{1}{k}\sum_{i=1}^{k}\delta P_{\mathrm{c},i} \tag{2.29}$$

and second the standard deviation of P_{c} and F_{c}

$$\delta F_{\mathrm{c}}^{\mathrm{stdev}} = \sqrt{\frac{1}{k-1}\sum_{i=1}^{k}(F_{\mathrm{c},i}-F_{\mathrm{c}})^2} \tag{2.30}$$

$$\delta P_{\mathrm{c}}^{\mathrm{stdev}} = \sqrt{\frac{1}{k-1}\sum_{i=1}^{k}(P_{\mathrm{c},i}-P_{\mathrm{c}})^2} \tag{2.31}$$

with $P_{\mathrm{c},i}$ and $F_{\mathrm{c},i}$ being the results of the individual dataset i. The larger of δF_{c} or $\delta F_{\mathrm{c}}^{\mathrm{stdev}}$ and δP_{c} or $\delta P_{\mathrm{c}}^{\mathrm{stdev}}$ is finally given as error.

3 Benzene on Ag(111) and Cu(111)

3.1 Introduction

Studying the behaviour of benzene (C_6H_6) seems to be a natural step in the investigation of aromatic molecules as it is the smalles possible molecule of this class (see Fig. 3.1 for a sketch of the molecule). In the framework of metal organic interfaces aromatic molecules are important because of their semiconducting properties. Additionally it turns out that their π-system opens an important bonding channel for the molecule-metal interaction [3, 6, 40]. Therefore the understanding of the adsorption behaviour of the smallest building block of such aromatic backbones is of great interest.

Here XSW experiments are presented which measure the adsorption height of benzene on Ag(111) and Cu(111) which can be used as a gauge for the interaction strenght between molecule and substrate in these systems. It turns out that the situation on Ag(111) as the less reactive surface is very much as expected. We find a flat adsorption geometry and a distance of $3.04 \pm 0.02\,\text{Å}$ between molecule and surface. Hence we conlclude that the molecules are weakly physisorbed. However, for Cu(111) a coexistence of two molecular geometries is found. Some are adsorbing flat as in the Ag(111) case but others are tilted by $70 \pm 20°$. Due to this mixture the adsorption height of the flat molecules is enhanced to $3.55 \pm 0.02\,\text{Å}$ although Cu(111) is in general expected to be more reactive.

In the following the benzene/Ag(111) case will be discussed in detail first and the second part of the chapter focuses on the benzene/Cu(111) system. The experiments were done in collaboration with the group of Prof. Petra Tegeder (Universität Heidelberg).

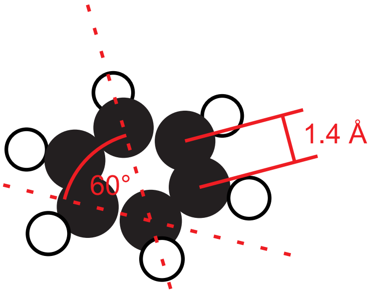

Figure 3.1: Sketch of the benzene molecule (C_6H_6) with the carbons depicted in black and the hydrogens in white. All carbons are equivalent with a C-C distance of 1.4 Å and consequently 120° bond angles.

3.2 Benzene on Ag(111)

3.2.1 Introduction

In contrast to the adsorption of benzene on transition metals (see ref. [41] and references therein), where studies are motivated by the catalytic activity of the surfaces, the benzene adsorption on Ag(111) in the submonolayer coverage regime is expected to show only a weak molecule surface interaction. Indeed, inverse photoemission spectroscopy experiments find the benzene monolayer to be physisorbed on Ag(111) [42] which is supported by the electron energy loss spectroscopy (EELS) finding that the vibrational modes of the molecule stay very similar to the liquid phase upon adsorption on Ag(111) [43]. Another indicator is the desorption temperature of 220 K gained from temperature programmed desorption (TPD) experiments [44, 45], which revealed a desorption energy of 50 kJ/mol to 55 kJ/mol [45]. No decomposition of benzene is observed from the TPD experiments, only if the molecules are exposed to an electron beam before, a dehydrogenation is seen [44]. The adsorption geometry is consistently revealed to be flat lying from near edge X-ray absorption fine structure spectroscopy (NEXAFS) [46], ARPES [47], Raman spectroscopy [48], and EELS [43]. Laterally a 3 × 3 superstructure is reported for the monolayer from LEED experiments [42, 47, 49], but other structures seem to exist, depending on the deposited amount of benzene [49, 50]. From symmetry reductions the adsorption site is determined to be a 3-fold hollow site observed in ARPES [47], Raman spectroscopy [48], and EELS [43], as a $C_{3v}(\sigma_d)$ symmetry is identified. However, TPD experiments indicate the coexistence of two slightly different species on the surface and hence suggest the presence of molecules in $C_{3v}(\sigma_d)$ and $C_{3v}(\sigma_v)$ symmetries

Parameter	XSW data set acquisition	Off-Bragg XPS
ΔE_{photon}	8 eV	
E_{photon}		2620 eV
# of XPS spectra	22	
repeats	1	2
pass energy	100 eV	100 eV
ΔE_{kin}	0.2 eV	0.1 eV
dwell time	0.2 s	0.2 s

Table 3.1: Acquisition parameters used for the XSW data sets and off-Bragg XPS spectra.

[45]. For workfunction changes upon benzene deposition of a monolayer, values of $\Delta\phi = -0.3\,\text{eV}$ [47] and $\Delta\phi = -0.7\,\text{eV}$ [44] are given.

Benzene adsorption on Ag(111) in the submonolayer coverage regime is expected to be a model system in the way that the interaction of the smallest aromatic molecule on a weakly interacting surface is investigated. Therefore theoretical approaches, which respond to the challenge to include dispersive van-der-Waals interactions into the calculation to allow the precise prediction of adsorption geometries and energies for the adsorption of organic molecules on metal surfaces, can be benchmarked on the benzene/Ag(111) interface. Recent adsorption heights reported from DFT studies are 2.93 Å [51] and 3.1 Å [52]. In this context the experimental investigation of the adsorption height of benzene/Ag(111) is a valuable tool to prove the theoretical predictions and to learn about the interaction strength between small aromatic building blocks and metal surfaces.

3.2.2 Experimental details

The experiments were preformed during a beamtime at ID 32 of the ESRF Synchrotron on the UHV system described in sec. 2.5.2. During the same beamtime the XSW experiments for benzene/Cu(111) presented later in this chapter and azobenzene/Cu(111) described in sec. 4 were carried out. The Ag(111) crystal was cleaned by repeated Ar^+ ion sputtering and annealing cycles. The benzene dosing took part in the analysis chamber, as a non-cooled sample transfer would lead to the desorption of benzene [45]. Before the dosing step the benzene was purified through several freeze-pump-thaw cycles. During the deposition and the measurement the sample temperature was kept below 80 K. The Bragg energy for the (111) reflection of Ag is found at $E_{\mathrm{photon}} \approx 2636\,\mathrm{eV}$ and the lattice spacing is $d_{\mathrm{Ag}(111)} = 2.36\,\text{Å}$. Off-Bragg XPS spectra, i.e. XPS spectra taken at a photon energy well separated from the Bragg condition, are taken at $E_{\mathrm{photon}} = 2620\,\mathrm{eV}$. The corresponding analyzer settings for XSW data sets and off-Bragg XPS spectra are listed in Table 3.1. The benzene/Ag(111) sample was independently prepared four times. Preparations are referred to as 1 to 4 in chronological order.

3.2.3 X-ray induced changes

In the field of metal-organic interfaces one should always keep in mind that the structures under investigation might be changed by the measurement process. In our case we have to consider that the molecules might be prone to structural changes due to the exposure to the X-ray beam, because such beam damage was explicitly reported for benzene/Ag(111) from investigations with electron diffraction and UV light [44]. One can easily imagine that bond breaking may occur within the molecules or the molecule-surface interaction is altered. Therefore, we must carefully check our spectra for time dependent changes and their relation to the X-ray exposure.

Unfortunately, benzene/Ag(111) turns out to be quite sensitive to X-ray exposure, which limits the life time of each spot on the sample available for our experiments. In Fig. 3.2 a time dependent off-Bragg XPS measurement at $E_{\mathrm{photon}} = 2620\,\mathrm{eV}$ for the C1s line on benzene/Ag(111) is shown and a clear change with time is visible. After roughly 15 min a peak shift is observed together with a broadening. This trend is continued and after 30 min we make two observations: First, the centre of the C1s peak shifted by 200 meV to lower binding energy and, second, the shift is more pronounced on the low than on the high binding energy side, therefore leading to a peak broadening. It should be noted that an intensity loss is not observed. The mechanism behind the observed shift is not clear, but the exposure to the X-ray beam can be identified to be the crucial time parameter for the observed change, because no changes are observed without beam exposure. Therefore, we have to restrict our measurement times to below 15 min. Unfortunately, for preparation 1 each spot was irradiated for 30 min during the XSW measurements, rendering this preparation meaningless for our evaluation. For preparations 2 to 4 the exposure time was restricted to 15 min and therefore one can expect the data to be reliable.

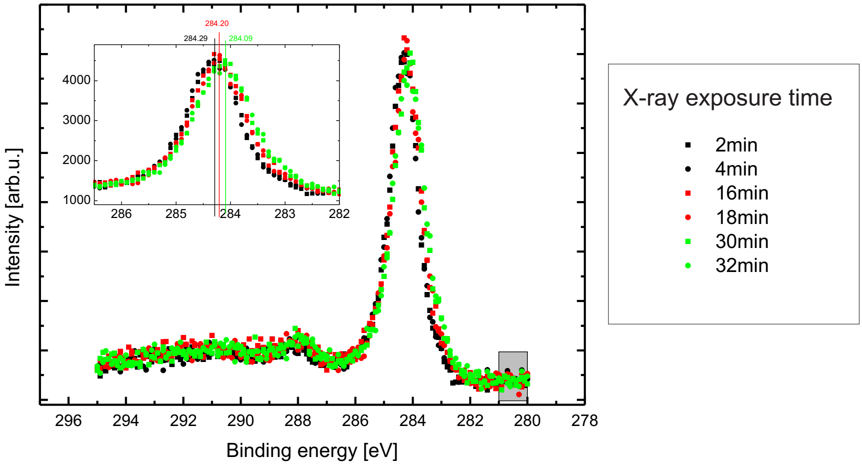

Figure 3.2: Off-Bragg XPS spectra at $E_{\text{photon}} = 2620\,\text{eV}$ of the C1s signal for Bz/Ag(111) to visualize beam induced changes. The spectra show a time dependent change of the peak-position, starting at 284.3 eV (black) changing to 284.2 eV (red) and further to 284.1 eV (green). The overall shift is 200 meV. Besides the centre position also the width is changed. The difference is more prominent on the low binding energy side. The reason for this change is the X-ray exposure time given in the top right corner for all spectra. All spectra were normalized to the mean value of the Ag background in the interval [280 eV,281 eV] which is indicated by a grey box.

However, the single XPS spectra of the XSW scans show that already after 8 min first changes can be observed. Therefore, we have to conclude that the local intensity enhancement due to the standing wave field accelerates the X-ray induced changes which where already observed in the off-Bragg XPS (see Fig. 3.2). The situation for the XSW scan is depicted in Fig. 3.3. In this case the XPS peak is modeled by two components constrained in position, width and relativ intensity and the agreement between fit and data is very good in the beginning of the 22 XPS spectra for this XSW datapoint. However after spectrum 11 and hence an exposure time of 8 min, one can clearly observe a disagreement between the envelope (red) and the datapoints (black circles) which stems from a shift of the experimental data. This shift continues until the last XPS spectrum. The observed movement is not a standing wave effect, as this could change the shape of a multicomponent peak but not its overall position.

While the observed changes in the XPS do not necessarily mean that the vertical height of the adsorbate changes, we cannot exclude an influence. Anyway, we have to accept the compromise of a minimum time of 15 min to be able to perform a full XSW scan and that a XPS model featuring components with fixed positions and

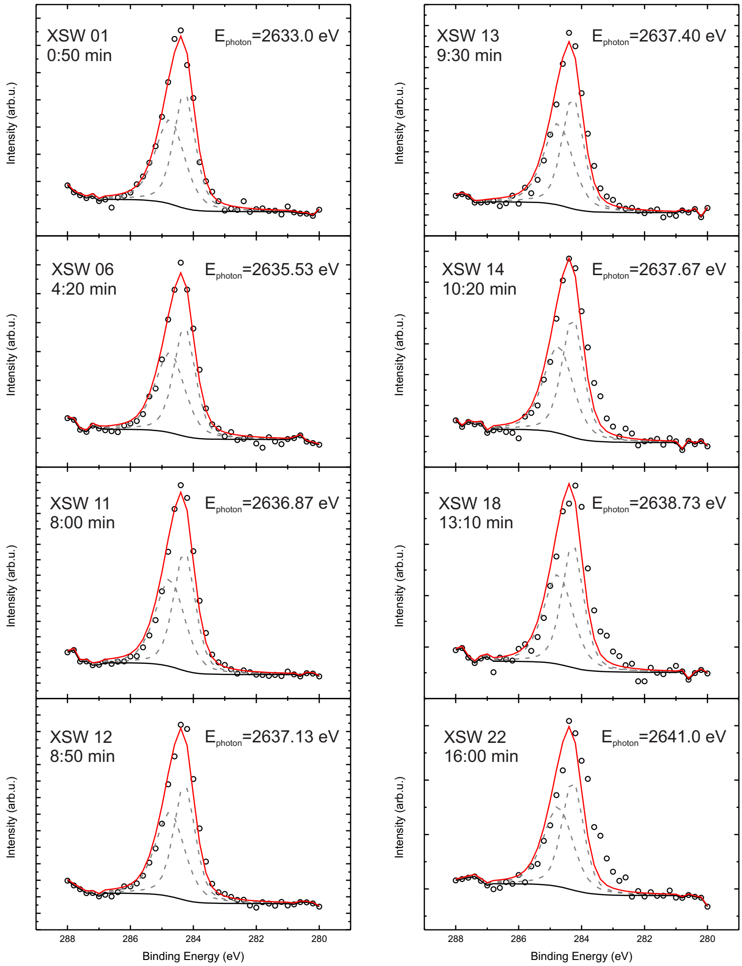

Figure 3.3: On individual XPS spectra of a XSW measurement of preparation 2 the enhanced beam damage during the XSW measurement is depicted. The XSW data set consists of 22 consecutive XPS spectra of which eight are shown in this figure starting with the first (01) at the top left and ending with the last (22) at the bottom right. All spectra show the raw data (open circles), the background (black line) two components (dashed grey lines) and the resulting envelope (red line). From spectrum 11 on the consistence of raw data and envelope clearly gets worse due to a shift of the C1s peak. The components cannot follow the shift as they are constrained in position, width and relative intensity. The effect is similar to the beam damage observed from XPS as shown in Fig. 3.2.

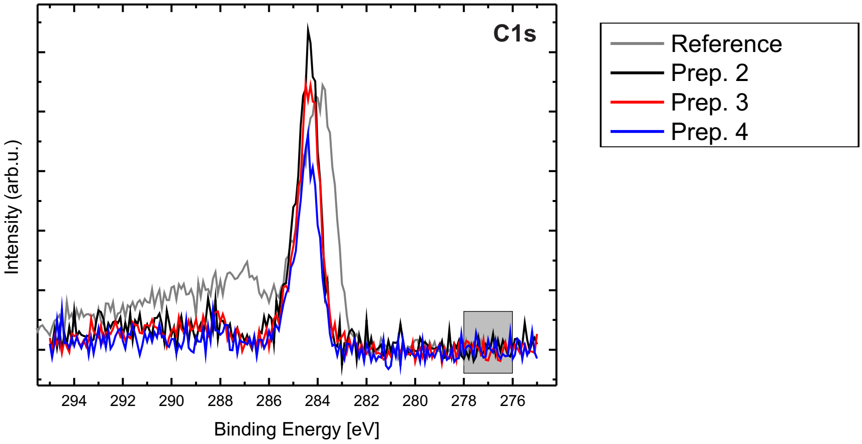

Figure 3.4: Off-Bragg XPS spectra at $E_{\text{photon}} = 2620\,\text{eV}$ of the C1s signal used for the coverage estimation for preparation 2 (black), 3 (red) and 4 (blue) together with a C1s reference spectrum of a PTCDA/Ag(111) monolayer [53] (grey) measured at $E_{\text{photon}} = 2633\,\text{eV}$. While the benzene specra can be directly compared the PTCDA spectrum is not corrected for the different carbon density on the surface. In Table 3.2 the intensities are tabulated together with the corrected PTCDA intensity as reference. All spectra were normalized to the mean value of the Ag background in the interval [276 eV,278 eV] which is indicated by a grey box.

widths cannot fit our XSW data. Hence, we cannot use a multi-component model in our analysis, but we can only use the full intensity of the C1s signal after background subtraction. Luckily no hint of components with independent intensity variations is seen in the data, which means that the full intensity of the C1s signal can be expected to reflect the adsorption height correctly. This absence of multiple adsorption heights is in agreement with the expectation of flat adsorbing benzene molecules raised by previous studies about benzene on Ag(111) [43, 46].

3.2.4 Coverage estimation

An inportant piece of information about our benzene/Ag(111) layer is the coverage. For the XSW experiments a sub-monolayer coverage is advisable, since this excludes the possibility of second layer molecules which could falsify the results. We use XPS to determine the coverage of our sample by comparing the C1s intensity to a reference spectrum.

In Fig. 3.4 a XPS spectrum is shown for preparations 2-4 in comparison with a reference spectrum of 1 ML of PTCDA/Ag(111)[53]. All spectra are normalized to

Preparation	Intensity [arb. u.]	Coverage [monolayer of 3 × 3 phase]
Reference	3100	1.00
Prep. 2	3600	1.16
Prep. 3	3600	1.16
Prep. 4	2000	0.65

Table 3.2: Coverage estimation results of benzene/Ag(111) compared to the reference of a monolayer of PTCDA/Ag(111)[53]. The values are taken from the XPS spectra shown in Fig. 3.4 and the PTCDA intensity was corrected by the different surface density to serve as a reference.

the Ag background signal on the low binding energy side to ensure that the ratio of intensities reflects the ratio of carbon atoms. To calculate the coverage one has to take into account the unit cell area as well as the number of carbon atoms per unit cell. In the case of PTCDA/Ag(111) the unit cell covers an area of $239\,\text{Å}^2$ and contains 48 carbon atoms [54]. Unfortunately, for benzene the situation is not that clear. In the literature a 3 × 3 unit cell is reported [47, 49], containing one benzene molecule and therefore six carbon atoms. Although it seems as if there are additional monolayer phases with different densities possible [49, 50], there is no detailed LEED study available on these phases and we could not do LEED on our sample to confirm the 3 × 3 structure, because the benzene desorbed during the non-cooled transfer (see sec. 2.5.2). Therefore, we *assume* a 3 × 3 unit cell for the benzene layer which leads to a unit cell size of $65\,\text{Å}^2$. From the PTCDA/Ag(111) spectrum we get an intensity of 6700 arb u and therefore a monolayer of benzene should yield an intensity of 3100 arb u . The intensities and coverages for preparation 2-4 are tabulated in Table 3.2

From this coverage estimation we can derive two important things. First, we see that our coverages are around the expected value of a monolayer and, second, we have data sets from two significantly different coverages. The fact that preparation 2 and 3 show more than one monolayer coverage should not be taken too seriously, because later we will see that the results from preparation 2 to 4 are in very good agreement, suggesting that in all cases the same structure, at least from the vertical point of view, was investigated. Therefore, we can be confident that all preparations yield molecules in the first layer only. However, the density may be higher than one molecule per 3 × 3 unit cell.

	XSW Dataset #	F_c	P_c	d_c [Å]
Preparation 2	079	0.89(3)	0.29(0)	
	080	0.94(5)	0.29(1)	
Preparation 3	083	0.84(5)	0.29(1)	
	084	0.88(5)	0.29(1)	
	085	0.87(5)	0.29(1)	
	086	0.84(4)	0.30(0)	
Preparation 4	088	0.95(6)	0.29(1)	
	089	0.85(7)	0.29(1)	
	090	0.85(5)	0.29(1)	
mean value		0.88(5)	0.29(1)	3.04(2)

Table 3.3: Results of the XSW analysis for benzene/Ag(111). The adsorption height is calculated following eq. (2.25) with the Ag(111) lattice distance of $d_{\mathrm{Ag}(111)} = 2.36$ Å and $n = 1$. No preparation dependence can be observed. The results are visualized in the Argand diagram in Fig. 3.6. Errors are calculated following sec. 2.5.2

3.2.5 XSW results

We now turn to the XSW evaluation. This is a three-step process. First, a XPS fitting model is developed, using off-Bragg XPS spectra to deconvolute the possibly many components in the spectrum. In this step information about the stoichiometry and the number of chemically different atoms of the same species have to be considered to be reflected in the model. Furthermore, a suitable background is chosen to substract the contribution of the multiple scattered electrons which mainly stem from the metal sample, i.e. Ag in this case.

After a suitable XPS model is developed, it has to be transferred from the off-Bragg XPS to the XSW data set, which typically consists of 20-30 XPS spectra taken consecutively with a photon energy variation of ±4 eV around the Bragg energy. In this second step the relative positions of all components and their widths are fixed. Relative intensities are fixed for peaks which stem from the same atom, i.e. a main peak and its sattelite, but are free to change between peaks of different origin in terms of adsorption position. The absolute energy position of the components is fixed for each XSW data set separately by fitting its first spectrum, which is typically still more than 3 eV off the Bragg energy. Afterwards the complete data set is fitted and the integrated intensity of each component as well as the integrated intensity of the complete spectrum after background subtraction are extracted. All data processing of the first two steps is done in *CasaXPS* [35]. Note that due to the above mentioned X-ray induced changes, we only evaluate the full intensity of the XPS spectra after background subtraction without any component model in the

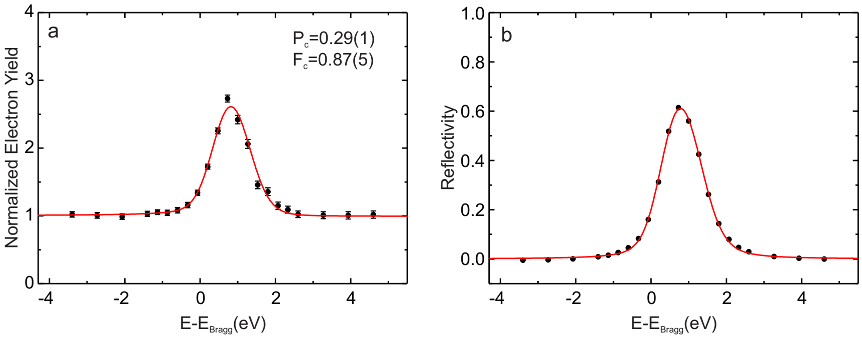

Figure 3.5: Example for an electron yield (a) and a reflectivity fit (b) for benzene/-Ag(111). The displayed data belongs to XSW data set 085 and the x-axis displays the photon energy relativ to the Bragg energy of $E_{\mathrm{Bragg}} = 2636.2\,\mathrm{eV}$.

case of benzene/Ag(111).

The third and last step is the XSW yield fit by using the *Torricelli* [36–38] software. First, the corresponding reflectivity exemplary shown in Fig. 3.5a and second the electron yield curve shown in Fig. 3.5b are fitted to gain the F_c and P_c of the XSW data set. More details on the XSW method and the calculation of the errors can be found in sec. 2.4 and sec. 2.5.2.

For benzene/Ag(111) the data of preparation 1 is disregarded due to too long measurement time and the associated changes induced in the layer by the X-ray beam. Additionally, we faced a temperature drift of our sample and therefore a Bragg plane distance change during the first XSW data set of each preparation. This leaves us with overall nine valid XSW data sets for benzene/Ag(111). These data sets and the corresponding XSW results are shown in Table 3.3 and visualized in Fig. 3.6.

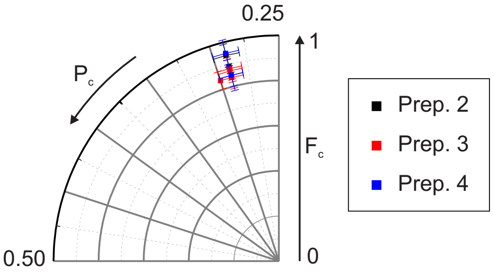

Figure 3.6: Argand diagram visualizing the results for benzene/Ag(111) for preparations 2 (black), 3 (red) and 4 (blue) (see Table 3.3). The data spread is very low and no preparation dependence is observed.

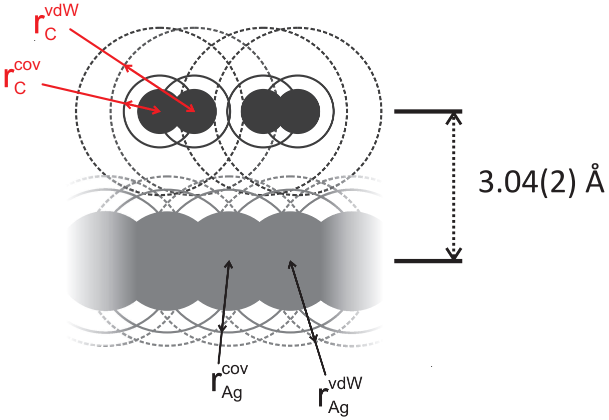

Figure 3.7: Vertical adsorption geometry of benzene/Ag(111). The filled circles represent the carbon (black) and silver (grey) positions. The solid cirles represent the covalent ($r_{\mathrm{Ag}}^{\mathrm{cov}} = 1.45\,\text{Å}$, $r_{\mathrm{C}}^{\mathrm{cov}} = 0.73\,\text{Å}$)[55] and the dashed lines the vdW bonding radii ($r_{\mathrm{Ag}}^{\mathrm{vdW}} = 1.72\,\text{Å}, r_{\mathrm{C}}^{\mathrm{vdW}} = 1.77\,\text{Å}$) [56]. The small overlap of the vdW radii of silver and carbon of 0.45 Å suggests that benzene is only physisorbed on Ag(111).

We find values for F_{c} in the range 0.84 ± 0.05 to 0.95 ± 0.06, with a mean value of 0.88 ± 0.05, along with a P_{c} of 0.29 ± 0.01, resulting in an adsorption height of $3.04 \pm 0.02\,\text{Å}$. It should be noted that no dependency on the preparation is observed, neither for the F_{c} nor the P_{c} results. The high F_{c} shows that the vertical spread among the carbon atoms must be small. This confirms the flat adsorption geometry of benzene on the surface in agreement with literature [43, 46] and the submonolayer coverages of our preparations. Furthermore, it indicates that only one benzene species exists on Ag(111), at least from the vertical geometry point of view. This result should not be mistaken to contradict the literature suggesting different lateral adsorption sites, as these may lead only to a negligible variation in the vertical height of the adsorbed molecules [45]. The height value of $3.04 \pm 0.02\,\text{Å}$ is in agreement with the finding that benzene is mainly physisorbed on Ag(111) [42, 43], because the sum of the van der Waals (vdW) radii [56] of C (1.77 Å) and Ag (1.72 Å) is larger by only 0.45 Å than the adsorption height (covalent radii [55] are well separated), which is sketched in Fig. 3.7.

3.2.6 Conclusion

The investigation of benzene on Ag(111) confirms the flat adsorption geometry of the monolayer which is reported in literature [43, 46–48] and extends the characterization of the system by the accurate determination of the adsorption height of 3.04 ± 0.02 Å. If we understand this height as a reference for the physisorption of aromatic molecules one would expect several trends: First, a more extended aromatic system, i.e. a larger aromatic molecule, should show a lower adsorption height due to the enhanced interaction which stems from the higher density of carbons per surface area of a molecular layer on one hand and non-additive contributions to the polarizability [57] on the other hand. Second, the presence of functional groups is likely to lead to a lower adsorption height, because possible chemical interaction channels may increase the molecule-metal interaction. Third, any molecule-molecule interactions is likely to lead to an increase in adsorption height, as they may compete with the molecule-surface interaction.

The height of a molecule with an extended aromatic backbone is measured with pentacene ($C_{22}H_{14}$), which is found to adsorb at 2.98 Å on Ag(111) for a coverage of 0.5 monolayer [58]. The finding agrees well with the expectation of benzene to represent a prototype aromatic building block and extended aromatic systems to be adsorbed at smaller distance. However, the adsorption height of pentacene increases to 3.12 Å when the coverage is increased to 0.75 monolayers [58], which can be rationalized by the argument of increasing molecule-molecule interactions and hence a weaker molecule-metal bond. Both height values refer to the room temperature liquid-like phase of pentacene.

For the case of phenyl rings with additional chemical interaction channels, azobenzene ($C_{12}H_{10}N_2$) is a suitable candidate, where two phenyl rings are connected by an ($-N \equiv N-$) azo-bridge. Its adsorption on Ag(111) shows a vertical distance of 2.97 ± 0.05 Å between the azo-bridge and Ag surface [30, 59]. As expected, this is lower than the adsorption height of benzene/Ag(111). However, it is difficult to compare these two cases, because on one hand the van-der-Waals radius of 1.60 Å for N [56] is 0.17 Å smaller than for C, which would overcompensate the observed difference, but on the other hand molecule-molecule interactions seem to play an important role in the measured phase as a twisting of the phenyl rings is observed [30, 59], bringing the rather large adsorption height in line with the expectation.

For PTCDA ($C_{24}H_8O_6$), a molecule with an aromatic perylene backbone and functional carboxylic endgroups, an adsorption height of 2.86 ± 0.01 Å is found [60, 61]. This agrees well with the expectation that its extended backbone and the functional groups lead to a smaller vertical adsorption distance than the 3.04 ± 0.02 Å of benzene/Ag(111). Furthermore the low temperature phase of PTCDA/Ag(111) is found to adsorb even lower at 2.80 ± 0.02 Å, which is attributed to reduced molecule-molecule interactions, because the molecules are more isolated in this phase [62]. However, in chapter 5 we will see that another crucial parameter to determine the PTCDA adsorption height on Ag surfaces is its charge uptake by the molecule. Another large organic molecule which has attracted much scientific interest is Copper-Pthalocyanine (CuPc, $C_{32}H_{18}N_8$), which is adsorbing at a distance of 3.08 ± 0.02 Å on Ag(111) for a coverage of 1 monolayer [63]. Surprisingly this value is higher than the benzene/Ag(111) distance. An observed coverage dependence of the adsorption height [63] suggests an important influence of molecule-molecule interactions to contribute to this result. Even more interesting than the homomolecular phases is the result for a mixture of CuPc and PTCDA molecules on Ag(111). If the molecules are mixed within the monolayer with a ratio of 1:1, the CuPc is slightly shifting downwards to 3.04 ± 0.02 Å while the PTCDA is moved up by 0.14 Å to 3.00 ± 0.02 Å and the process behind this change is a charge redistribution at the plane between surface and adsorbates [64] which again stresses the important link between the charge distribution and the adsorption height, which we will investigate on the example of PTCDA in chapter 5.

This last example shows that the complexity in the interplay of competing mechanisms, which in the end determine the adsorption height, is too large to be solely explained on the basis of an elementary building block like the simple aromatic molecule benzene. A larger database of molecular data is needed to allow better predictions for yet unknown systems. However, it should be noted that besides the variety of the molecules also the surface differences have to be considered. For example PTCDA/Au(111) shows an adsorption height of 3.27 ± 0.02 Å which results in an overlap of carbon and metal vdW radii of only 0.14 Å [61] which is less than the overlap of 0.45 Å observed for benzene/Ag(111), therefore showing that the reference height of for a weakly interacting system gained from benzene adsorption here, is a reference for Ag(111) but the comparison to adsorption on other surfaces is difficult.

An alternative solution to increase the predictive power for the behaviour of molecule-metal interfaces is the implementation of reliable calculations. This challenging task is taken up by many research groups by the development of density functional theory (DFT) calculations, where the incorporation of vdW forces is an ongoing challenge. The role of a very small, and hence computational less expensive, prototype and reference point for physisorption like benzene on a not reconstructing surface like Ag(111) is therefore an interesting reference point for the theory developement. The adsorption height for benzene/Ag(111) predicted by Ruiz *et al.* by the vdW-surf method, which extends disperion corrected DFT [65] by the inclusion of screening [51] is 2.93 Å and therefore at the edge of their claimed accuracy of 0.1 Å [51] while Chwee and Sullivan predict 3.1 Å using the framework of dispersion corrected Kohn-Sham DFT, including dispersive effects following the method of Becke and Johnson [52, 66]. Hence the agreement between experiment and theory is already very good, however it is shown that finite temperature effects should be included into the calculations to improve the accuracy of the prediction, which is not yet done for benzene/Ag(111) [59].

3.3 Benzene on Cu(111)

3.3.1 Introduction

To compare the situation of the benzene adsorption on Ag(111) as described in the above chapter to the situation for a more reactive surface, the adsorption of benzene on Cu(111) was investigated. By changing from Ag to Cu one would expect a lower adsorption height for the benzene molecule, as the copper atoms are smaller ($r_{\mathrm{Cu}}^{\mathrm{vdW}} = 1.4$, $r_{\mathrm{Ag}}^{\mathrm{vdW}} = 1.72$ [56]) and the reactivity is expected to be higher.

For very low coverages low temperature scanning tunneling microscopy (STM) experiments show a step edge decoration of benzene on Cu(111) with a coexisting 2D gas phase on the terraces [67–69] and the preferred adsorption on steps and defects is confirmed by a TPD study on the flat Cu(111) in comparison to vicinal surfaces [70]. For higher coverages, the enhanced stability of benzene adsorbed at steps is still visible in TPD experiments in an extended tail up to 300 K of the desorption spectra, while the monolayer desorption peak is found at 225 K [70–72]. The density of the benzene layer varies with the coverage, and even coexisting domains of different density are observed by STM [73].

The adsorption of the first layer molecules is reported to be flat from NEXAFS and EELS experiments [71], while the second layer is tilted according to NEXAFS and two photon photoelectron spectroscopy (2PPE) [71, 72]. However, in the coverage calibration of the second layer and hence the density of tilted molecules, results for work function change and TPD do not agree [71, 72]. For the electronic structure IPES measurements reveal the first affinity level of the adsorbed benzene far above the Fermi edge at 4.6 ± 0.1 eV for a 2 ± 1 monolayer thick benzene film on Cu(111) [74], hence the nature of benzene bonding to Cu(111) can be expected to be physisorption. Contradicting 2PPE experiments which claimed to find a partially filled benzene LUMO for the monolayer [75] can be disregarded, because recent publications suggest that the observed state stems from a broadening of the surface state instead [76]. DFT calculations are in line with the interpretation of physisorption and predict adsorption heights of 3.0 Å [52] and 2.68 Å [51].

Contrary to the expectation from literature of a result for benzene on Cu(111) similar to benzene on Ag(111), the experiments presented here show significant differences with a rather surprising outcome. Annealing of the layer reveals a stability that is unexpected from the desorption temperatures reported by TPD in literature [71, 72]. A

Parameter	XSW Preparation 1	XSW Preparation 3	Off-Bragg XPS
ΔE_{photon}	8 eV	8 eV	
E_{photon}			2960 eV
# of XPS spectra	26	24	
repeats	1	1	2
pass energy	100 eV	100 eV	100 eV
ΔE_{kin}	0.25 eV	0.1 eV	0.1 eV
dwell time	0.2 s	0.2 s	0.2 s

Table 3.4: Acquisition parameters used for the XSW data sets and off-Bragg XPS spectra in the benzene/Cu(111) experiments.

clear LEED pattern is observed and allows the identification of a small unit cell which indicates the presence of tilted molecules in the monolayer, because the footprint of flat benzene molecules is larger than the unit cell dimensions. However, at the same time XSW experiments indicate the existence of flat molecules, therefore leading to the conclusion that we face a coexistence of tilted and flat adsorbing molecules already for the submonolayer of benzene on Cu(111).

3.3.2 Experimental details

The experiments were performed during the same beamtime at the beamline ID 32 of the ESRF as the benzene/Ag(111) measurements described above (see sec. 3.2) and the azobenzene experiments described later in this work (see sec. 4). Therefore, the chamber was in the same state as described in sec. 3.2.2 and the preparation followed the same procedure, with keeping the sample below 80 K during deposition and measurement. The Cu(111) crystal was cleaned by subsequent Ar^+ ion sputtering and annealing cycles. The Bragg energy for the (111) reflection of Cu is found at $E_{\text{photon}} \approx 2977\,\text{eV}$ and the lattice spacing is $d_{\text{Cu(111)}} = 2.09\,\text{Å}$. Off-Bragg XPS spectra are taken at $E_{\text{photon}} = 2960\,\text{eV}$. The corresponding analyzer settings for XSW data sets and off-Bragg XPS spectra are listed in Table 3.4. In our experiments we measured XSW on 4 preparations of benzene on Cu(111), where the 3rd preparation results from the 2nd preparation by an additional adsorption step. LEED and annealing was only done on the 1st preparation. Between the 3rd and the 4th preparation, the measurements of benzene on Ag(111) took place (see section 3.2), and hence the photon energy of the beamline had to be readjusted from the Ag(111) to the Cu(111) Bragg condition ($\Delta_E \approx 340\,\text{eV}$) prior to preparation 4.

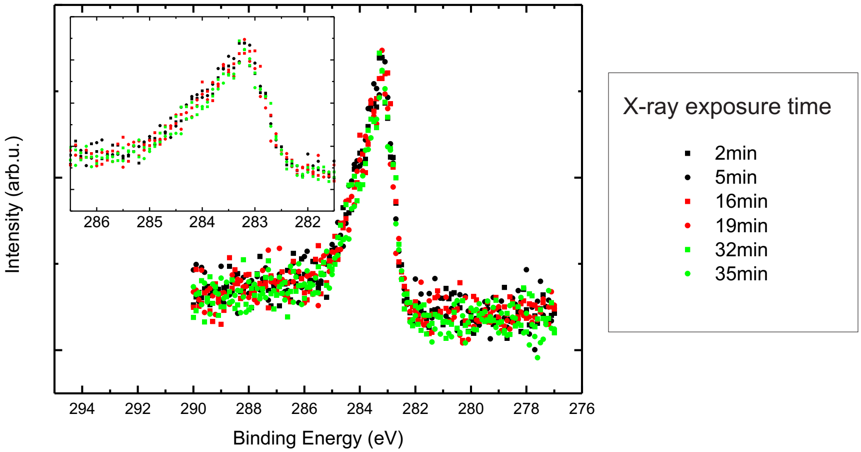

Figure 3.8: Off-Bragg XPS spectra at $E_{photon} = 2960\,\mathrm{eV}$ of the C1s signal for Bz/Cu(111) to observe possible exposure time related changes. In contrast to benzene/Ag(111) (see Fig. 3.2) the spectra show no time dependent behaviour within the measured time of 35 min. The exposure times are given at the top right corner.

3.3.3 Beam damage

As illustrated by the benzene adsorption on Ag(111) (see sec. 3.2), the issue of beam induced changes of our sample has to be adressed prior to the XSW data evaluation.

To this end XPS spectra of the C1s feature were recorded for 35 min with with the off-Bragg photon energy of $E_{\mathrm{photon}} = 2960\,\mathrm{eV}$, but no time dependent change could be observed. Representative spectra are depicted in Fig. 3.8. The XSW experiments were recorded with only 20 min per XSW data point and therefore we can exclude beam induced influences on our XSW results in this case. Apparently, benzene is more stable on Cu(111) than on Ag(111). Possible reasons for this will be discussed at the end of the chapter.

However, the data evaluation revealed a systematic problem of preparation 4, rendering this data set unreliable for the analysis. All reflectivities and yield curves of this preparation show a tilted baseline as it is shown in Fig. 3.9. As mentioned before, the difference towards the earlier preparations is the beamline condition, because the photon energy was moved for the measurements on Ag(111) in between. It appears that the beam was not sufficiently set after changing back to the Cu(111) Bragg condition and therefore we observe a problem with the intensity normalization here. It should be mentioned that the result of the XSW analysis does not deviate

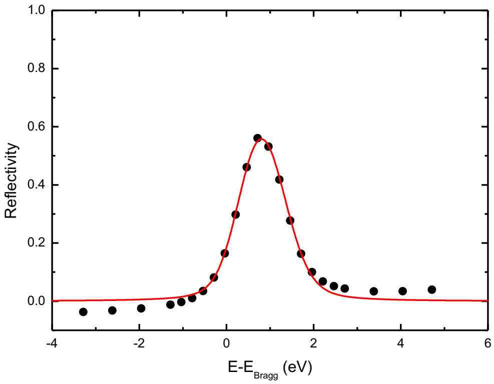

Figure 3.9: Exemplary reflectivity curve of preparation 4. The experimental data shows a clear tilt of the baseline which is a consequence of a normalization error due to an unstable beam. Therefore the results from this preparation are discarded.

from the other preparations, but nevertheless preparation 4 is discarded due to its tilted baseline.

3.3.4 Coverage estimation

Excluding preparation 4 leaves us with three preparations for the data analysis. The next step is the coverage estimation of these data sets. In this context it should be recalled that preparation 3 resulted from 2 by additional deposition.

The coverage is estimated by comparing the C1s intensity of off-Bragg XPS spectra of each preparation as shown in Fig. 3.10. All spectra are normalized to the low binding energy side background.

Preparation 1 yields the highest signal and therefore its integrated area is defined as 1. For preparation 2 this leads to a value of 0.27 and for preparation 3 of 0.48. The

Preparation	Intensity [arb. u.]	relative coverage
Prep. 1	1684	1.00
Prep. 2	459	0.27
Prep. 3	812	0.48

Table 3.5: Results of the relative coverage estimation for benzene/Cu(111) based on the intensities of the normalized off-Bragg XPS spectra shown in Fig. 3.10. Preparation 1 is found to yield the highest coverage with twice as much material as preparation 3. The deposition onto preparation 2 which lead to preparation 3 approximately doubled the amount of benzene adsorbed on the surface.

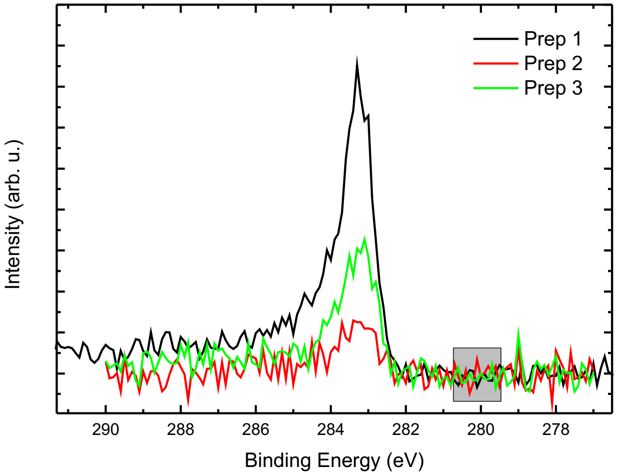

Figure 3.10: The graph shows normalized off-Bragg XPS spectra ($E_{\text{photon}} = 2960\,\text{eV}$) of the C1s signal for Bz/Cu(111) from preparations 1 (black), 2 (red) and 3 (green), to compare their coverages. Clearly preparation 1 yields the highest coverage while 2 has a lower one than 3 as preparation 3 is done by dosing more material onto preparation 2. The quantitative estimation leads to the numbers given in Table 3.5. The normalization of all spectra was done in the low binding energy range indicated by the grey box.

values are summarized in Table 3.5. Unfortunately, the poor signal-to-noise ratio for preparation 2 does not allow reasonable fitting of its XSW data sets. A rough analysis shows no differences to preparations 1 and 3 and therefore we only discuss the data of these preparations in more detail from now on.

3.3.5 XSW analysis

To answer the question whether a detailed fitting model is needed to do the XSW analysis in case of benzene/Cu(111), we analyze the XPS spectra of a XSW data set. In Fig. 3.11 a few XPS spectra from the data set C1s058 are depicted. A peak at a binding energy of 283.2 eV is clearly visible in all spectra and we can observe the intensity change of the Cu background as well. In addition to this, on the high binding energy side of that clear peak another component exists with a different intensity variation. Therefore, we cannot treat this shoulder as a satellite but we have to separate the contributions of the independent XSW components. Hence, in contrast to benzene/Ag(111), we clearly need a dedicated XPS model for our XSW analysis.

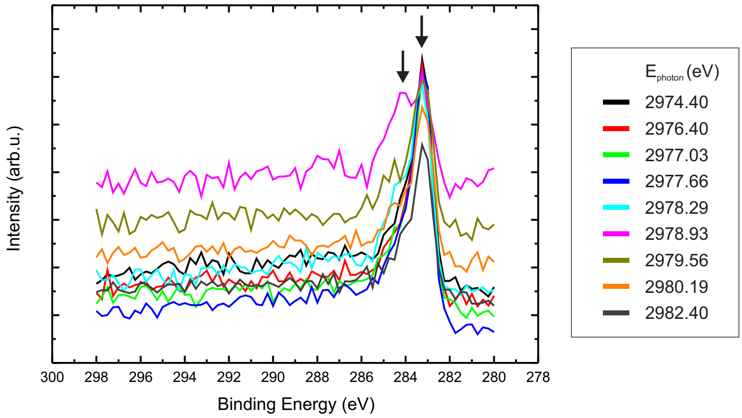

Figure 3.11: Representative XPS spectra from the XSW data set 058 (Preparation 1). Each color represents the C1s XPS spectrum at a different photon energy during the XSW measurement. Two independent XSW components are clearly present (marked by arrows). Therefore the shoulder on the carbon peak cannot (only) be explained by satellites. The behaviour is not restricted to preparation 1 but observed in all XSW spectra for benzene/Cu(111) and makes a dedicated XPS model (see Fig. 3.12) mandatory for a meaningful XSW analysis.

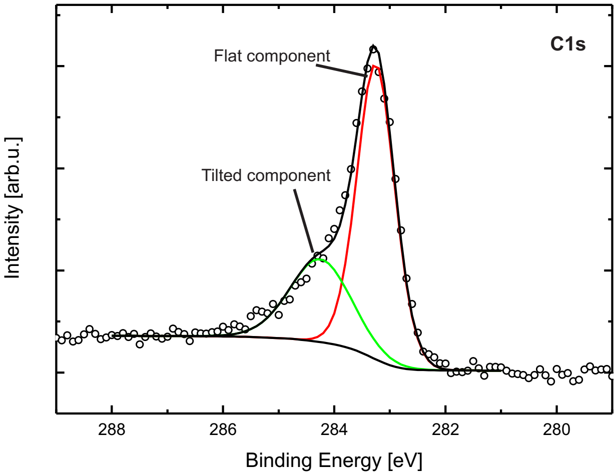

Figure 3.12: Sum of 3 off-Bragg XPS spectra, taken at $E_{\text{photon}} = 2960\,\text{eV}$ of the C1s region for benzene/Cu(111) to derive a model for the XSW analysis. A two component model was chosen as the quality of the single XSW spectra asks for a simple model, although a third component could increase the fitting quality on the high binding energy side. Furthermore, the position of the tilted component (green) was extracted from single XPS spectra of the XSW data sets where the peak is more pronounced in comparison to the flat component (red) (see Fig. 3.11). The shown spectrum is a sum of 3 normalized XPS spectra to get better statistics. They were taken at different positions on the sample during preparation 1.

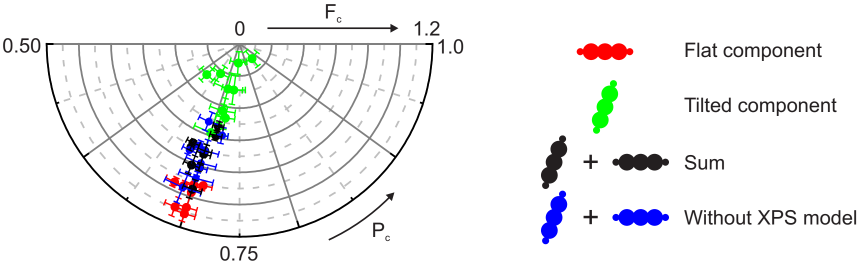

Figure 3.13: Argand diagram displaying the results of the XSW analysis for benzene/-Cu(111). The datapoints of the flat component (red) are found at very high F_c (note that the scale goes up to 1.2) while the tilted component (green) is found at rather low F_c. The P_c is identical for both components. Hence the sum (black) is at the same P_c with the F_c in between the components and it is in good agreement with the result for the full intensity after background subtraction (blue).

Unfortunately, the measurement time for the XSW data set is restricted to prevent beam damage and hence the noise in these spectra is quite high, as can be seen in Fig. 3.11. Therefore, a compromise between accuracy and simplicity has to be made for the fitting model. The result is shown in Fig. 3.12 for a sum of three normalized off-Bragg XPS spectra taken on preparation 1. Only two components, named flat and tilted, are featured, although the fit is not perfect on the high binding energy side and would need an additional satellite to be improved. However, such a model was tested for the XSW analysis and discarded, because the high noise level in the XSW spectra asks for a simple model. The binding energies of the flat and tilted components are found to be 283.2 eV and 284.2 eV, respectively. It must be noted that the relative binding energies of the components are not derived from the off-Bragg XPS, but from XPS spectra within an XSW dataset where the tilted component is enhanced in comparison to the flat component and therefore allows a more precise determination of its binding energy position.

The model shown in Fig. 3.12 is employed for all data sets of preparations 1 and 3, and fitted following the XSW fitting routine explained in sec. 3.2.5, leading to several interesting results. These results shall be discussed along the Argand diagram in Fig. 3.13 which visualizes the resulting P_c and F_c. Exemplary reflectivity and yield curves of the XSW analysis are shown in Fig. 3.14. First, we look at the results for the full intensity after background subtraction (blue dots), ignoring our fitting model. We find a position of $P_\mathrm{c} = 0.70 \pm 0.02$ and a mean F_c of 0.74 ± 0.14. The result seems to be very clear at first glance, featuring rather flat benzene molecules at an adsorption height of 3.55 ± 0.02 Å. However, this adsorption height is unexpectedly large. In fact, it is not only larger than the benzene-Ag distance of 3.04 ± 0.02 Å

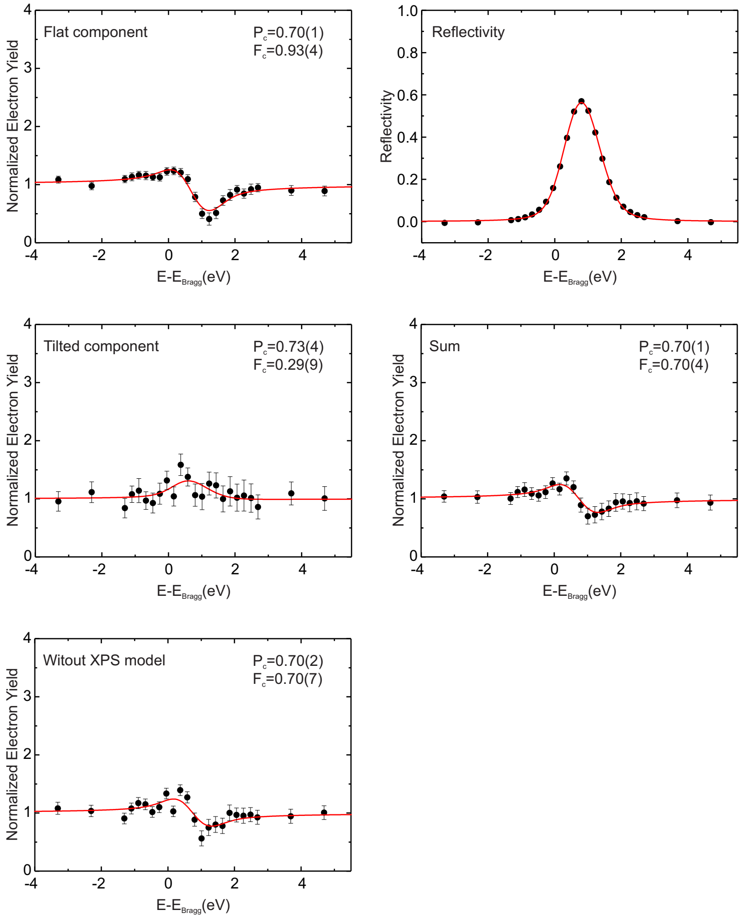

Figure 3.14: Yield curves of XSW data set C1s064 ater employing the XPS model shwon in ig. 3.12 for the XSW fitting. The corresponding reflectivity curve is shown as well. The results of all XSW data sets are given in Table 3.6.

reported in the previous chapter. 3.2, but also larger than the sum of the vdW radii of Cu (1.4 Å) and C (1.77 Å) [56]. These results could indicate either of the following two possibilities: First, a multilayer or second, tilted molecules are present, which can still provide the relatively high F_c of 0.74 ± 0.14.

Before we turn to a detailed discussion of these possibilities, we have to consider the fitting result from the two-component XPS model. The quality of the fit is fine, as the sum of the components (black dots) reproduces the result of the full intensity after background subtraction. The two components (red and green dots) however show another surprising result, they both yield a similar P_c (0.70 ± 0.01 and 0.72 ± 0.07, respectively) but with a very high F_c of 0.99 ± 0.08 for the flat (red dots) and a rather low F_c of 0.31 ± 0.16 for the tilted component (green dots). In case of the flat component the F_c of several data sets even exeeds 1.0 which is the limit for a fit with a physical meaning. The artificially enhanced F_c most probably results from the necessity to apply nondipolar corrections. However, as discussed in sec. 2.4 a distinct correction scheme based on analyzer position and acceptance angle is not yet available and therefore the data shown is always uncorrected.

Independent from this problem such high F_c values can only be explained by a very well defined adsorption height. In the case of benzene this leads to the conclusion that molecules adsorb flat, in agreement with the literature [71]. However, we still observe a tilted component with a F_c of 0.31 ± 0.16. Such a low value can be rationalized in two ways, as already mentioned in sec. 2.4: Either a vertically disordered species is present, or the result stems from a sum of positions, each maybe well defined and featuring a high F_c but with opposite directions in the Argand diagram, similar to the example of the extreme case of F_c=0 described in sec. 2.4. This second case could be realized for benzene by tilted or even upright standing molecules. From the LEED data we will see that such tilted adsorption can indeed be expected, although we have carried out our experiments on a film with a submonolayer coverage.

It should be noted that the possibilities of CO adsorption or graphene formation can be ruled out. While such effects could lead to a C1s signature with a high F_c in the XSW analysis, no O1s intensity is observed in the XPS experiments and the employed temperatures are insufficient for the formation of graphene on Cu(111) from benzene, which would require annealing above 1000 K [77].

		Preparation 1				Preparation 3						
Component		C1s056	C1s058	C1s059	C1s063	C1s064	C1s065	C1s066	C1s068	C1s069	mean value	ads. height[Å]
Flat	P_c	0.70(0)	0.68(1)	0.69(0)	0.70(1)	0.70(1)	0.70(1)	0.69(1)	0.70(1)	0.71(1)	0.70(1)	3.55(2)
component	F_c	0.97(2)	0.95(3)	0.95(3)	1.11(5)	0.93(4)	0.92(4)	1.09(6)	1.07(6)	0.91(3)	0.99(8)	
Tilted	P_c	0.72(2)	0.66(4)	0.62(3)	0.70(3)	0.73(4)	0.86(7)	0.71(3)	0.71(5)	0.74(7)	0.72(7)	4.64(15)
component	F_c	0.47(7)	0.22(5)	0.28(5)	0.58(12)	0.29(9)	0.12(6)	0.43(8)	0.29(10)	0.12(7)	0.31(16)	
Sum	P_c	0.70(0)	0.68(1)	0.68(0)	0.70(1)	0.70(1)	0.71(1)	0.69(1)	0.70(1)	0.71(1)	0.70(1)	3.55(2)
	F_c	0.81(2)	0.68(2)	0.71(2)	0.95(6)	0.70(4)	0.59(3)	0.81(6)	0.72(6)	0.53(3)	0.72(12)	
Without	P_c	0.70(1)	0.69(1)	0.68(1)	0.69(2)	0.70(2)	0.69(2)	0.70(2)	0.70(2)	0.72(1)	0.70(2)	3.55(4)
XPS model	F_c	0.81(3)	0.68(3)	0.73(3)	0.96(10)	0.70(7)	0.52(6)	0.88(8)	0.78(8)	0.58(5)	0.74(14)	

Table 3.6: Results of the XSW analysis for benzene/Cu(111). The components show the same P_c and only differ in their F_c but this does not neccessarily indicate indentical adsorption heights. The tilted component represents molecules which are crossing the bragg planes and therefore the calculation of the height from the P_c gets more complicated (see sec. 2.4). Flat and tilted component refers to the components of the fitting model as it is shown in Fig. 3.12 while the sum describes the analysis of their summed up intensities and without XPS model is the outcome of an XSW analysis without components and only background subtraction. The good agreement between sum and region indicates that a meaningful XPS model was used.

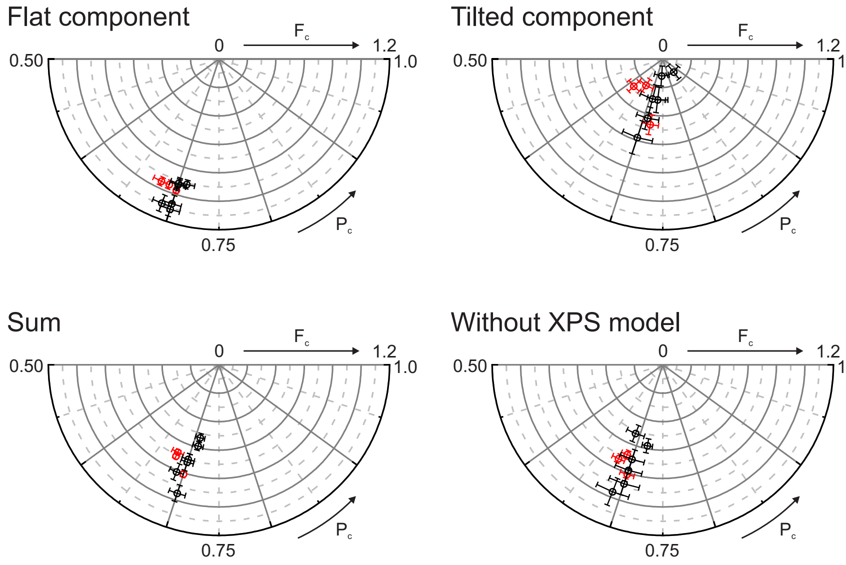

Figure 3.15: To visualize possible preparation dependent effects of the results from Table 3.6 the data points are plotted into four Argand diagrams. We see that preparation 1 (red) and 2 (black) are in agreement in all cases and no preparation dependence is found.

3.3.6 LEED

Now we turn to the information which can be extracted from LEED measurements on the benzene/Cu(111) film. LEED measurements were only performed on the first preparation. Therefore, the question if all preparations are the same or if we have to consider preparation-dependent results becomes important. In Fig. 3.15 the XSW results are color coded according to the preparation. No systematic difference between the results of preparation 1 (red) and preparation 3 (black) is discernable in any of the Argand diagrams. Therefore, LEED measurements on preparation 1 are well-suited to represent the situations in the other preparations as well.

The LEED pattern which is observed for benzene/Cu(111) is shown in Fig. 3.16, together with a LEED pattern simulation (red dots) done with *Spotplotter* [78]. The resulting unit cell matrix is $\begin{pmatrix} 4 & 0 \\ 1 & 2 \end{pmatrix}$. The real space unit cell of this commensurate structure is depicted in Fig. 3.16. It should be noted that the LEED pattern could be measured even after annealing up to 210 K, which should be in the desorption regime for the monolayer as determined by TPD [71, 72]. However, no difference could be

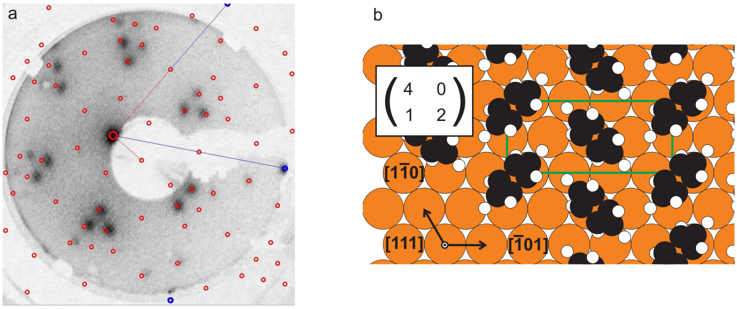

Figure 3.16: In panel (a) the commensurate LEED pattern of benzene/Cu(111) is shown together with an overlayed simulation performed by *Spotplotter* [78]. In the simulation, small red circles mark the superstructure, the big red circle the (00), and blue circles the substrate spots. Thin lines indicate the substrate (blue) and the superstructure (red) reciprocal unit cell vectors. The observed mismatch between LEED picture and simulation, especially present in the left part of the picture, is a technical artifact and originates from the distortion of the LEED image. The resulting real space unit cell is indicated in the picture in panel (b) by a green rectangle and its matrix is shown in the top left corner. Such a small unit cell can only exist if the benzene molecules are tilted. The tilt angle of 70° is extracted from the XSW analysis of component two. Flat benzene molecules would not fit in the unit cell and therefore they are expected to form disordered arrangements which are therefore not recognized in the LEED image.

noted neither from the LEED nor from XSW or XPS experiments upon annealing. The discovered unit cell is too small to comprise flat lying benzene molecules. Therefore we have to assume tilted ones. The internal structure of the unit cell as well as the adsorption sites of the molecules are still unknown, but from the size one could expect a filling of two molecules per unit cell. The unit cell area is $0.455\,\mathrm{nm}^2$ and this leads to a density of $4.4\,\mathrm{nm}^{-2}$ for the benzene molecules. Compared to Dougherty *et al.* [73] this density is very high because they obviously only observed flat lying benzene domains in their STM measurements.

3.3.7 Conclusion

The experimental results for benzene on Cu(111) indicate a surprisingly complicated situation. The XSW experiments show two species of carbons, one well ordered (large F_c), the other with low F_c, but both with essentially the same P_c. LEED shows a commensurate structure with a relatively small unit cell which only tilted molecules can form. Both experiments, LEED and XSW, show a higher stability of the benzene layer against annealing than it is expected from the literature by TPD

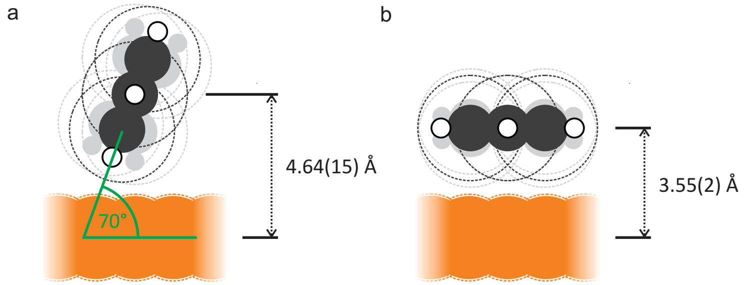

Figure 3.17: Side view of the benzene adsorption geometry for the 70 ± 20° tilted (a) and the flat (b) adsorbing species. The adsorption heights of 4.64 ± 0.15 Å and 3.55 ± 0.02 Å, and the tilt angles are the result of the XSW data evaluation (numbers are given in Table 3.6). The Cu surface layer is depicted in orange, carbon atoms are drawn in black and Hydrogen as open circles. Spheres mark the corresponding covalent ($r_{\mathrm{Cu}}^{\mathrm{cov}} = 1.32$ Å, $r_{\mathrm{C}}^{\mathrm{cov}} = 0.73$ Å, $r_{\mathrm{H}}^{\mathrm{cov}} = 0.31$ Å) [55] and dashed circles the vdW radii ($r_{\mathrm{Cu}}^{\mathrm{vdW}} = 1.4$ Å, $r_{\mathrm{C}}^{\mathrm{vdW}} = 1.77$ Å) [56]. The vdW radii of the H atoms ($r_{\mathrm{H}}^{\mathrm{vdW}} = 1.00$ Å)[56] are not displayed for simplicity. Shadowed molecular outlines in the background display the possible deviation due to the error of the angle of 20° for the tilted and 10° for the flat species.

experiments [71, 72].

To merge everything into one picture, we will start with the tilted molecules first. The LEED experiments are very clear regarding the unit cell and therefore this is a strong indication for the existence of tilted molecules. If these tilted molecules were in the second layer on top of flat lying benzene, which does not form a long range ordered superstructure, a commensurate registry between the tilted layer and the Cu substrate would be a surprising coincidence. Hence, the commensurability of the structure strongly suggests that these tilted molecules are in contact with the Cu surface and do not represent the upright standing second layer reported in the literature [71, 72]. As the LEED shows only one structure, the other species which is present on the surface must be expected to form a disordered layer or a dilute gas phase.

If we now take into account our XSW results, we can immediately identify the low fraction tilted component with the upright molecules. However, this complicates the interpretation of the P_{c} for this component, because an upright standing benzene is actually larger than the Bragg-spacing of 2.09 Å and therefore we have to take into account the Bragg-plane crossing of the molecule. As mentioned in in sec. 2.4 this prevents an easy calculation of the adsorption height from the P_{c} and simulations have to be carried out to find the correct structure matching the experimental results. While the vertical position of the centre and its error are derived from the P_{c}, the tilt angle and its corresponding error stems from the F_c and the steric hindrance known from the unit cell size. A detailed description on the problems due to Bragg-plane crossing in XSW experiments can be found in refs. [30, 36]. In the present case we find that the P_c and F_c measured in the experiment can be mimicked by a tilt of $70 \pm 20°$ between the molecular and the surface plane with the adsorption height of the centre of the molecule at 4.64 ± 0.15 Å. This consequently leads to a distance of 2.61 ± 0.45 Å between the surface and the closest hydrogens. In Fig. 3.17a a sideview of this adsorption model is depicted.

While this molecule explains the tilted component, we still have to consider the XSW data of the flat component. The high F_c is a clear sign for a flat adsorption with a tilt of less than 10°, and therefore we can straightforwardly get the adsorption height of 3.55 ± 0.02 Å from the P_c, which leads to the adsorption picture shown in Fig. 3.17b. This height is unexpectedly large if we had flat molecules only, recalling that the height for flat benzene on Ag(111) is only 3.04 ± 0.02 Å and DFT predicts adsorption heights of 3.0 Å [52] and 2.68 Å [51]. Therefore, an intermolecular interaction between tilted and flat molecules can be expected, lifting the flat molecules from the Cu surface. The large adsorbate surface distance and hence the decoupling of these molecules from the surface rationalizes why the flat adsorbing molecules do not form an ordered superstructure.

To quantify the average ratio between flat and tilted molecules we make use of the vector sum explained in sec. 2.4 (eq. (2.24)). We know the experimental result for the sum as well as each component and can therefore deduce their population. In this case it is even easier as differences in the P_c are negligible and we can simply calculate the relative presence on the surface from the F_c. The tilted component shows a mean F_c of 0.31 ± 0.16, the flat molecules feature a F_c of 0.99 ± 0.08 and the sum has a F_c of 0.72 ± 0.12 as can be seen from Table 3.6. Hence the ratio of tilted molecules to flat molecules calculates to 2:3. The explanation of an intermolecular interaction as driving force behind the enhanced height of the flat molecules requires all flat molecules to be in the vicinity of tilted ones. Compact domains of both species would therefore disagree with this picture and flat molecules decorating the border of compact islands of tilted molecules can not fulfill the necessary population ratio. Because the island size of tilted molecules is still large enough to observe sharp spots in the LEED pattern a dendritic growth as sketched in Fig. 3.18 is expected. However, this is pure speculation and should be clarified by microscopy experiments like STM.

Furthermore, it is interesting to note that the structure of the tilted molecules is

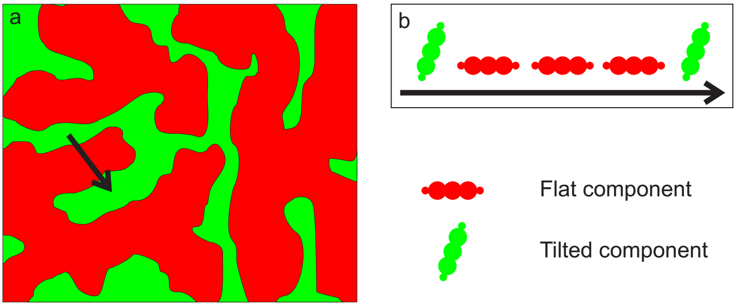

Figure 3.18: (a) Schematic picture of a dendritic mixture of flat (red area) and tilted (green area) molecules. The black arrow marks the position of the sideview depicted in panel (b), where the flat (red) and tilted (green) molecules are sketched.

commensurate, although their adsorption height is quite large, pointing to an interesting balance of molecule-molecule and molecule-substrate interactions. Compared to benzene/Ag(111) the layer is more stable against thermal desorption as well as X-ray induced changes. The finding of a higher stability for benzene/Cu(111) than benzene/Ag(111) agrees well with the trend of adsorption energy predicted by DFT ($E_{\mathrm{ads}}^{\mathrm{Ag}} = 0.81\,\mathrm{eV}$, $E_{\mathrm{ads}}^{\mathrm{Cu}} = 0.91\,\mathrm{eV}$)[51] and may be a result of the differences in polarizability of the surface. Hence, the larger adsorption height does not necessarily introduce an overall weaker interaction with the surface in this case, but the opposite is true. Furthermore, it should be noted that no sign for a substrate relaxation is found in an XSW measurement on the Cu2p signal, but unfortunately this measurement was done on preparation 4, which is excluded from the analysis due to the tilted baseline described in sec. 3.3.3.

In general the results obtained from the structural investigation of the benzene/-Cu(111) system are very interesting, because they reveal a new phase with a coexistence of flat and tilted molecules in the first layer of the adsorbate. Until now, tilted molecules were only reported for the second layer [71, 72], which raises the question if indeed a new phase is observed here, or if the interpretation of the tilted molecules forming on top of a closed layer of flat molecules in the literature is incorrect. On the other hand, such behaviour of first layer molecules was not found in recent STM experiments [73], because the formation might be very dependent on the preparation procedure. For future experiments a dedicated temperature and coverage dependent study of benzene/Cu(111) seems promising to unravel the driving forces behind this interesting structure formation and may reveal the responsible intermolecular interactions. Furthermore, an investigation of the different electronic properties of the flat and tilted molecules will give an insight into the bonding mechanism and possible charge transfers.

3.4 Summary

In this chapter the results for the XSW investigation of the adsorption systems of benzene/Ag(111) and benzene/Cu(111) were presented and surprising differences are revealed. While the benzene/Ag(111) system follows the expectations from former experiments [43, 46–48] and theoretical predictions [51, 52] with flat adsorbing molecules at a height of 3.04 ± 0.02 Å, the benzene/Cu(111) system turns out to be more complicated. Already for submonolayer coverages tilted molecules are observed in coexistence with flat molecules. This coexistence leads to an interestingly high adsorption distance for the flat molecules which points at strong intermolecular influences on the structural organization of the benzene layer. However, the molecule-substrate interaction is still very important, which is reflected by the commensurate registry of the tilted molecules. The final result is a system of $70 \pm 20°$ tilted molecules with an adsorption at 4.64 ± 0.15 Å and flat molecules at 3.55 ± 0.02 Å. While the benzene/Ag(111) appears solved and well understood, for benzene/-Cu(111) further experiments should be performed to investigate details of the electronic properties and driving forces of this structure formation.

4 Azobenzene Cu(111)

4.1 Introduction

After the investigation of benzene in sec. 3 we turn to the structurally more complex molecule azobenzene. It consists of two phenyl rings which are linked by a double bonded nitrogen pair as shown in Fig. 4.1. Simply speaking, we investigate now a dimer of benzene which features an additional reaction center in form of the nitrogens. Azobenzene is a molecule which was already studied in the 19th century due to its wide range of derivatives which are used as dyes for example [79]. Nowadays it is a promising candidate for the miniaturization of logic cicuits in the bottom-up approach, as the molecule in the gas phase and in solution is known to feature a *trans* and a *cis* state as shown in Fig. 4.1. The state of the molecule can be changeded by exposure to UV light (*trans* to *cis*) or visible light (*cis* to *trans*), making azobenzene an archetypal molecular switch. Upon adsorption, new surface mediated switching channels may occur [80], but in general the reversible switching capability is quenched if azobenzene is adsorbed on metal surfaces, and can only be preserved if the molecule is electronically decoupled [10, 11]. Hence, many experiments focus on the interaction of azobenzene derivatives with the weakly interacting Au(111) surface, where STM and light induced switching of adsorbed molecules is

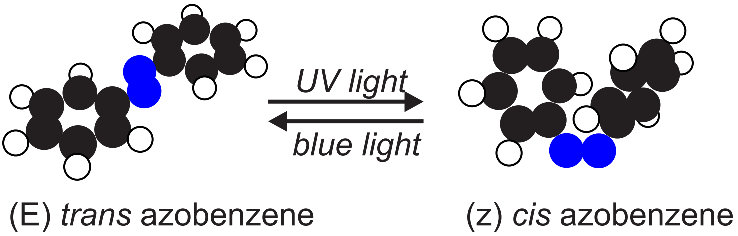

Figure 4.1: *trans* (left) and *cis* (right) configuration of azobenzene. In the gas phase the molecule can be switched from its *trans* to the *cis* state by UV light and vice versa by blue light.

indeed observed [10, 11, 81–85]. However, a more detailed knowledge of the adsorption processes of azobenzene is neccessary to understand the prerequisites to obtain an azobenzene interface on more reactive surfaces that allows the switching process and is suitable to be integrated into devices like memories on the molecular scale.

In the following a XSW study of adsorbed azobenzene on Cu(111) is reported. Dependent on the preparation parameters, namely coverage and annealing process, three submonolayer phases are identified. We find a disordered low coverage phase followed by an intermediate coincident structure, a commensurate ordered phase, and finally an ordered multilayer. The XSW results allow for a detailed analysis of the intramolecular geometries and reveal not only distortions, but even a bond breaking of the azobridge and hence the formation of phenyl nitrene in the dense monolayer structure. The dissociation is driven by the azobenzene coverage, similar to what was observed for azobenzene/TiO_2 [12, 86]. The comparison to the bahaviour of azobenzene/Ag(111) [59], where no dissociation occurs, allows to identify the N-substrate bond strength as decisive parameter that determines whether the molecule will undergo a dissociation upon coverage increase. Furthermore, the formed phenyl nitrene species in surface contact might serve as a buffer layer for additional azobenzene and therefore allow the formation of only weakly coupled azobenzene layers on top which may preserve their switching abilities. The experiments were done in collaboration with the group of Prof. Petra Tegeder (Universität Heidelberg).

4.2 Submonolayer coverage regime

4.2.1 LEED results

All experiments were done at the beamline ID32 of the ESRF Grenoble synchrotron using the UHV vessel described in chapter 2.5.2. The azobenzene was evaporated from a homemade Knudsen cell at room temperature and the photoemission experiments were done at a sample temperature of 60 K. In this section we focus on a submonolayer phase which was prepared by an azobenzene deposition time of 15 s onto the sample held at 300 K. The resulting LEED image shows no spots but a hexagonal shaped background intensity as it is seen in Fig. 4.2. In sec. 4.3 we will see that this hexagonal background evolves into a clear LEED pattern. However,

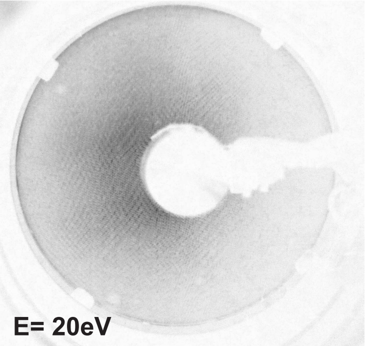

Figure 4.2: LEED picture of the DP of azobenzene on Cu(111). No spots are visible but a hexagonal shaped background intensity is identified to be characteristic for this phase.

for the moment we can only conclude that there is no long range order present within the molecular layer and therefore we will call this phase the *disordered phase* (DP).

4.2.2 XPS model

Turning to the XSW analysis of the DP we need to find proper XPS models to evaluate data sets for the C1s and N1s photoelectron signals. The acquisition parameters for the XSW and XPS spectra are given in Table 4.1. We find a very simple N1s spectrum which yields only one component at a binding energy of 397.8 eV (Fig. 4.3) which is named DP component. This is a more comfortable situation compared to

Parameter	XSW data set acquisition		Off-Bragg XPS	
	N1s	C1s	N1s	C1s
ΔE_{photon}	8 eV	8 eV		
E_{photon}			2960 eV	2960 eV
# of XPS spectra	17	17		
repeats	1	1	11	7
pass energy	100 eV	100 eV	100 eV	100 eV
ΔE_{kin}	0.2 eV	0.25 eV	0.1 eV	0.1 eV
dwell time	0.3 s	0.2 s	0.2 s	0.2 s

Table 4.1: Acquisition parameters used for the XSW data sets and off-Bragg XPS spectra for the DP. The Bragg energy for the (111) reflection of Cu is found at $E_{\text{photon}} \approx 2977\,\text{eV}$ and the lattice spacing is $d_{\text{Cu(111)}} = 2.09\,\text{Å}$.

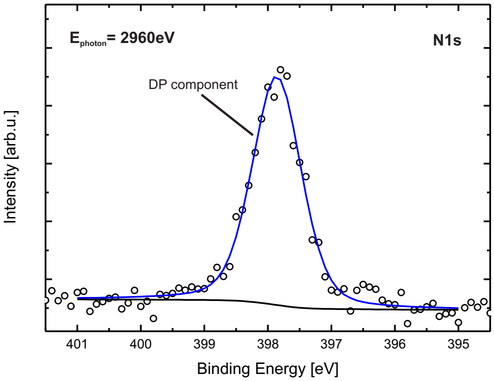

Figure 4.3: Off-Bragg XPS spectrum ($E_{\text{photon}} = 2960\,\text{eV}$) for the N1s emission of the DP. The XSW fitting model contains only the DP component shown in blue located at 397.8 eV. A shirley background is subtracted shown in black, to account for the Cu background intensity.

an analysis of azobenzene on Ag(111) done by Mercurio *et al.* [59] where the N1s signal was masked by a Ag plasmon.

In the C1s case we find a peak at a binding energy of 284.0 eV and a tail of satellites at higher binding energies, as depicted in Fig. 4.4. A shoulder is visible at the high binding energy flank of the peak, which can be fitted by a component at 284.9 eV (coloured in green in Fig. 4.4). It is known from XSW experi-

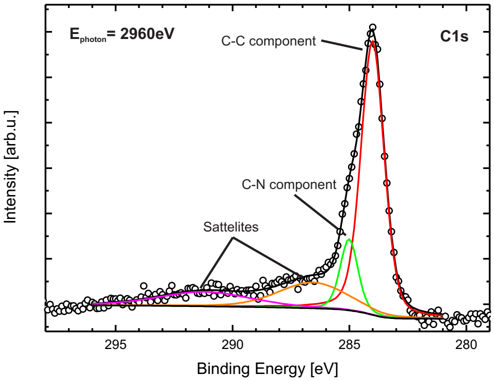

Figure 4.4: Off-Bragg XPS spectrum ($E_{\text{photon}} = 2960\,\text{eV}$) for the C1s emission of the DP. In contrast to N1s (see Fig. 4.3) the XSW fitting model contains several components. The C-C component (red) at 284.0 eV represents the carbons which only bind to other carbons while the C-N component (green) at 284.9 eV represents the carbons bonded to nitrogen. In the high binding energy tail two satellites (orange and pink) are identified. A shirley background (black) is subtracted to account for the background intensity.

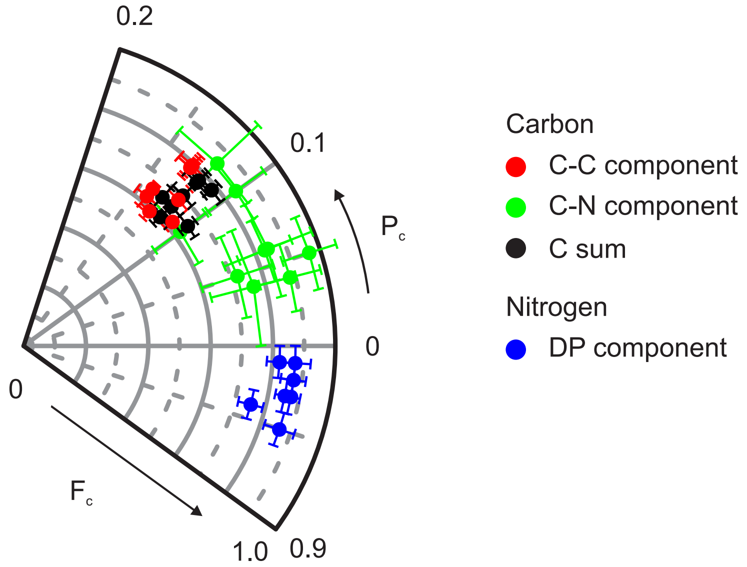

Figure 4.5: Results of the XSW analysis for the submonolayer azobenzene on Cu(111) depicted in an Argand diagram. The results for nitrogen from the N1s spectra are shown in blue, the results for carbon are shown in black, red and green. The red (C-C component) and green (C-N component) data points refer to the corresponding components of the XPS model shown in Fig. 4.4, the black datapoints represent the sum of both components. All values are tabulated in Table 4.2 for C1s and Table 4.3 for N1s.

ments on CuPc/Ag(111)[53] that such a shoulder can be attributed to the nitrogen bonding carbons (C-N) and hence we name it C-N component, while the main peak represents all carbon bound carbons and is therefore named C-C component (coloured in red in Fig. 4.4). This leads to an expected intensity ratio of 1:5 for $I_{(C-N)} : I_{(C-C)}$ from the stoichiometry of the molecule, which is indeed fulfilled in the XPS model.

4.2.3 XSW analysis

The XPS models developed in the last section are used to perform the XSW analysis following the procedure described in sec. 3.2. The *Torricelli* [36–38] software is employed to perform the electron yield data fit introduced in sec. 2.4. Exemplary electron yield curves are depicted in Fig. 4.6 for C1s and Fig. 4.7 for N1s and all results are plotted in the Argand diagram shown in Fig. 4.5. In the figure the N1s results are depicted in blue. We find a mean F_c of 0.84 ± 0.04 and a mean P_c

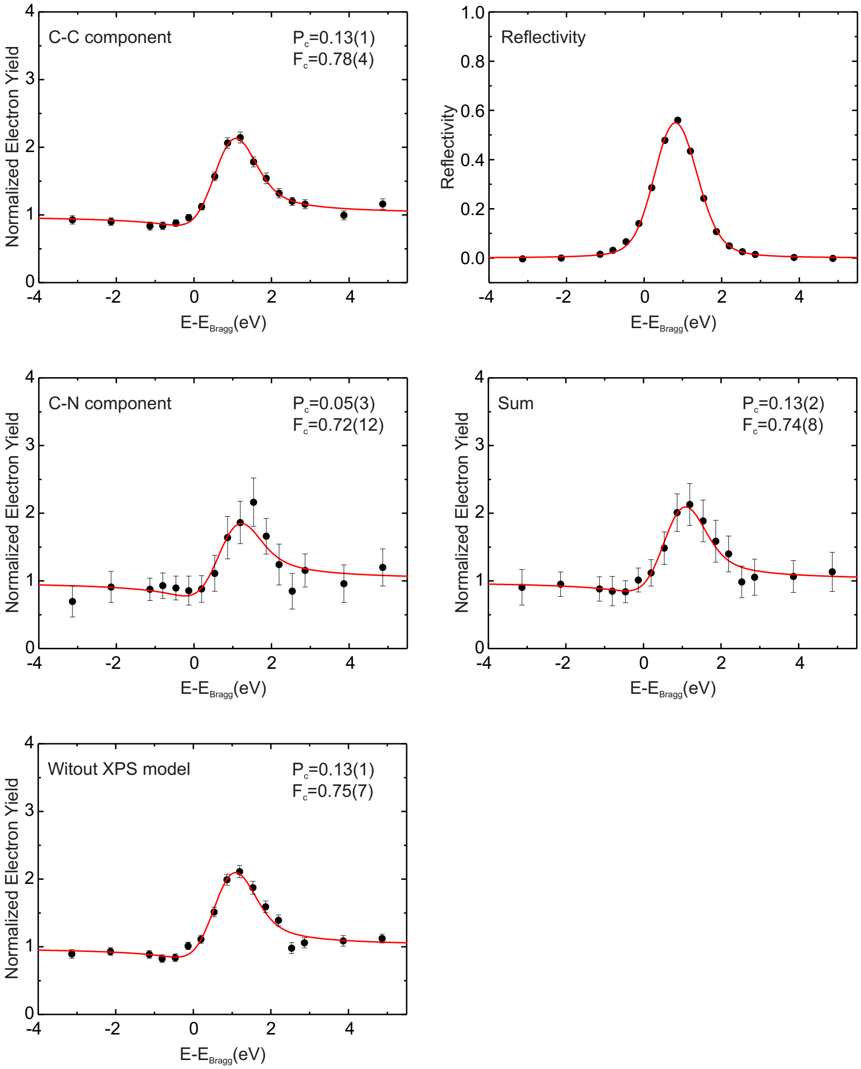

Figure 4.6: Exemplary electron yield curves from the C1s XSW fit using the XPS model depicted in Fig. 4.4. The displayed data belongs to XSW data set C1s047. The x-axis displays the photon energy relativ to the Bragg energy. The results of all C1s data sets are summarized in Table 4.2.

Component		Preparation 1				Preparation 2						
		C1s031	C1s034	C1s035	C1s040	C1s043	C1s045	C1s047	C1s049	C1s051	mean value	d_c [Å]
C-C	P_c	0.12(1)	0.14(0)	0.14(1)	0.11(1)	0.13(1)	0.13(1)	0.13(1)	0.13(1)	0.13(1)	0.13(1)	2.36(2)
	F_c	0.68(5)	0.65(2)	0.62(4)	0.62(3)	0.59(3)	0.79(4)	0.78(4)	0.78(3)	0.78(4)	0.70(8)	
C-N	P_c	0.12(3)	0.04(4)	0.10(2)	0.06(3)	0.10(3)	0.04(2)	0.05(3)	0.05(2)	0.06(2)	0.07(3)	2.23(6)
	F_c	0.85(18)	0.76(14)	0.84(11)	0.84(15)	0.62(10)	0.88(10)	0.72(12)	0.96(9)	0.83(9)	0.80(12)	
Sum	P_c	0.09(2)	0.11(1)	0.09(2)	0.07(1)	0.11(1)	0.11(1)	0.13(2)	0.12(1)	0.12(1)	0.11(2)	2.32(4)
	F_c	0.68(7)	0.63(4)	0.53(6)	0.63(5)	0.64(5)	0.81(6)	0.74(8)	0.83(6)	0.78(6)	0.69(10)	
Without XPS model	P_c	0.08(2)	0.11(1)	0.09(2)	0.08(2)	0.10(1)	0.12(1)	0.13(1)	0.12(1)	0.11(1)	0.11(2)	2.32(4)
	F_c	0.67(8)	0.62(4)	0.52(6)	0.64(5)	0.62(5)	0.81(6)	0.75(7)	0.82(6)	0.76(6)	0.69(10)	

Table 4.2: Results of the XSW analysis for the C1s data from two preparations of the DP. The XSW analysis is based on the model shown in Fig. 4.4 and distinguishes two carbon components, namely only carbon binding carbons (C-C component) and nitrogen bonding carbons (C-N component). These results are visualized in the Argand diagram in Fig. 4.5. Furthermore the results for the sum of all components (including satellites) and the fit without XPS model are given. The adsorption height d_c is calculated according to eq. (2.25) with $n = 1$ and $d_{\mathrm{Cu}(111)} = 2.09$ Å.

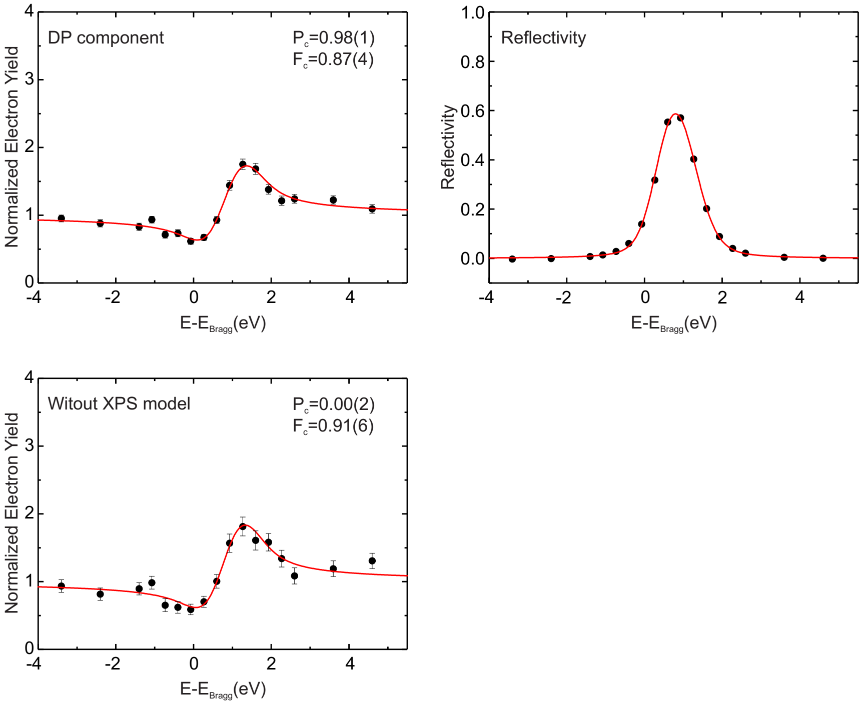

Figure 4.7: Exemplary electron yield curves from the N1s XSW fit using the XPS model depicted in Fig. 4.3. The displayed data belongs to XSW data set N1s046. The x-axis displays the photon energy relativ to the Bragg energy of. The results of all N1s data sets are summarized in Table 4.3.

	XSW Dataset	F_c	P_c	ads. height [Å]
Preparation 1	N1s030	0.86(5)	0.95(1)	
	N1s032	0.87(5)	0.99(1)	
	N1s033	0.87(3)	0.97(1)	
Preparation 2	N1s044	0.75(4)	0.96(1)	
	N1s046	0.87(4)	0.98(1)	
	N1s048	0.85(3)	0.97(1)	
	N1s052	0.82(4)	0.99(1)	
mean value		0.84(4)	0.97(1)	2.02(2)

Table 4.3: Results of the XSW analysis for N1s from two preparations of the DP. The results are visualized in the Argand diagram in Fig. 4.5 and were extracted by an XSW evaluation using the one component model shown in Fig. 4.3.

of 0.97 ± 0.01 which corresponds to a vertical adsorption height of 2.02 ± 0.02 Å. For C1s we can distinguish the (C-N, green) from the (C-C, red) carbons as it was described earlier and obtain a F_c of 0.80 ± 0.12 and a P_c of 0.07 ± 0.03 for the (C-N), and a F_c of 0.70 ± 0.08 and a P_c of 0.13 ± 0.01 for the (C-C). The results are consistent with the structural model of the molecule, because we find a slightly lower F_c for the (C-C) carbons than the (C-N) carbons, as their signal results from different carbons in the phenyl ring which have slightly different vertical positions. Furthermore, the vertical heights are calculated to 2.23 ± 0.06 Å (C-N) and 2.36 ± 0.02 Å (C-C), showing that the nitrogen bonded carbons are closer to the nitrogen, as expected. The scattering of the results in the Argand plot (Fig. 4.5) shows a very good agreement of all nitrogen and (C-C) results, only three (C-N) data points are diverging towards the (C-C) results, which shows that the discrimination of the signals did not work as well in these cases. All numbers for the results of each valid data set taken in the experiment and depicted in Fig. 4.5 are given in Table 4.2 for C1s and Table 4.3 for N1s. The resulting adsorption geometry of the molecule is discussed later in sec. 4.6.

4.3 Ordered point-on-line phase

4.3.1 LEED results

For longer deposition times in comparison to the preparation of the DP, a different structure is observed by LEED. In this experiment the deposition was done in two steps of 11 s and 30 s deposition time. The resulting LEED pattern is depicted in Fig. 4.8a. The observed pattern reminds one of the hexagonal shape observed for the DP (see Fig. 4.2), but now we find several clearly distinguishable LEED spots at these positions.

The software *Spotplotter* [78] is used to determine the unit cell of this structure by comparison to a simulated pattern. The LEED picture overlayed with the simulated pattern is shown in Fig. 4.8b and the resulting super structure matrix is

$$\begin{pmatrix} 2.9 & 0 \\ 0.7 & 5 \end{pmatrix} \tag{4.1}$$

The agreement between simulation and experiment is very good and we note that the first column of the matrix consists of non-integer numbers, while the second column

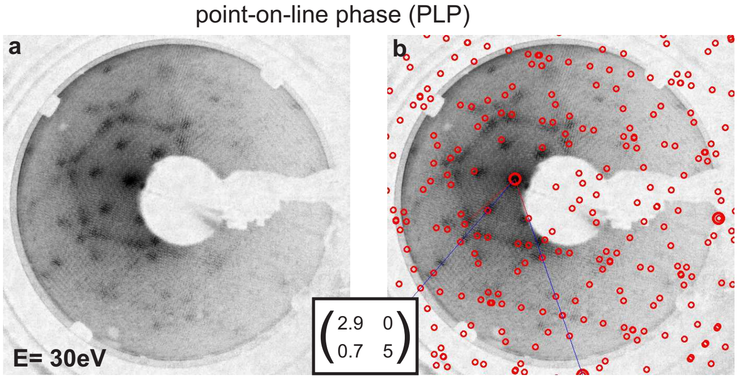

Figure 4.8: Panel (a) shows a LEED picture of the PLP taken at an energy of 30 eV. It shows a clear hexagonal structure of spots. In panel (b) the same picture is shown with a simulated LEED pattern on top corresponding to the given point-on-line coincident superstructure matrix. Due to this matrix the phase is named *point-on-line phase* (PLP). The LEED simulation is done with *Spotplotter* [78].

shows integers. This means the structure is not commensurate, but all superstructure vectors point on grid lines of the substrate lattice. Such a superstructure is called point-on-line coincident [87], hence we will call this phase the *point-on-line phase* (PLP).

4.3.2 XPS Model

Upon inspection of the XPS spectra for the PLP (all XPS and XSW acquisition parameters are given in Table 4.4), one finds that the difference to the DP is reflected by the photoemission data as well. In the N1s spectrum shown in Fig. 4.9 the peak observed for the DP at 397.8 eV is still visible but another component, named COP component, at 396.3 eV has evolved and actually dominates the spectrum. Due to the difference of 1.5 eV the peaks are well separated and each is fitted by only one component.

In case of the C1s spectrum the change is not that obvious, because the peak shape stays the same within our accuracy. However, the C-C component is slightly shifted by 0.3 eV to a binding energy of 283.7 eV and the C-N component by 0.2 eV to 284.7 eV. Since we can identify different species in the N1s spectrum, we can as well expect more components for C1s, but unfortunately they differ too little to be separated. The satellite structure is similar to the DP case, too.

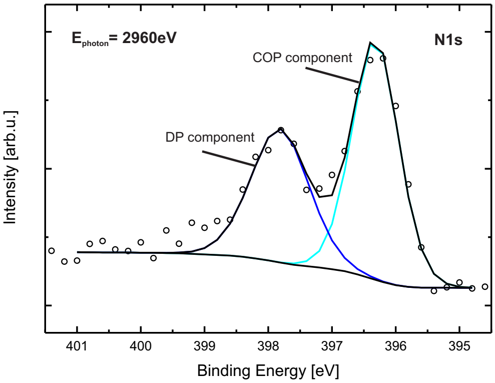

Figure 4.9: Off-Bragg XPS spectrum ($E_{\text{photon}} = 2960\,\text{eV}$) of the N1s region for the PLP. Two peaks are visible each fitted with one component. The DP component at 397.8 eV (dark blue) is already known from the DP (see Fig. 4.3) but at 396.3 eV a new feature appeared (light blue), which is named COP component. This new peak will later be identified as a signature of the dissociated phenyl nitrene species.

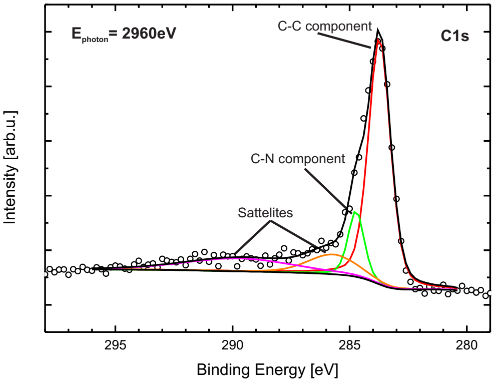

Figure 4.10: Off-Bragg XPS spectrum ($E_{\text{photon}} = 2960\,\text{eV}$) visualizing the XSW fitting model for C1s for the PLP. In general the spectrum looks like the one of the DP in Fig. 4.4 but peaks are slightly shifted. The C-C component (red) is now at 283.7 eV and the C-N component (green) at 284.7 eV. However a distinct new feature as it appeared in the N1s spectrum (see Fig. 4.9) is not visible.

Parameter	XSW data set acquisition		Off-Bragg XPS	
	N1s	C1s	N1s	C1s
$\Delta E_{\mathrm{photon}}$	8 eV	8 eV		
E_{photon}			2960 eV	2960 eV
# of XPS spectra	24	24		
repeats	1	1	5	2
pass energy	100 eV	100 eV	100 eV	100 eV
ΔE_{kin}	0.2 eV	0.25 eV	0.2 eV	0.2 eV
dwell time	0.3 s	0.2 s	0.2 s	0.2 s

Table 4.4: Acquisition parameters used for the XSW data sets and off-Bragg XPS spectra for the PLP. The Bragg energy for the (111) reflection of Cu is found at $E_{\mathrm{photon}} \approx 2977\,\mathrm{eV}$ and the lattice spacing is $d_{\mathrm{Cu(111)}} = 2.09\,\text{Å}$.

4.3.3 XSW analysis

The N1s and C1s XPS models are employed to fit the XSW data sets of the PLP. Exemplary yields are shown in Fig. 4.12 and Fig. 4.11, respectively. The results are depicted in the Argand diagram in Fig. 4.13. Unfortunately, we have only two data sets for the C1s level and all results have to be assessed carefully, because beam damage problems similar to the ones reported in the previous chapter for benzene/Ag(111) (see sec. 3.2.3) have been observed. In case of the N1s DP component at 397.8 eV (dark blue) the numbers agree very well with our expectations already known from the DP, since its mean F_c of 0.55 ± 0.11 and P_c of 0.92 ± 0.02

Component		C1s023	C1s025	mean value	ads. height[Å]
C-C component	P_c	0.32(1)	0.29(1)	0.31(2)	-
	F_c	0.44(2)	0.27(2)	0.35(12)	
C-N component	P_c	0.15(1)	0.14(2)	0.15(2)	-
	F_c	0.99(8)	0.40(5)	0.69(42)	
Sum	P_c	0.27(1)	0.27(1)	0.27(1)	-
	F_c	0.40(3)	0.22(3)	0.31(13)	
Without XPS model	P_c	0.28(1)	0.28(1)	0.28(1)	-
	F_c	0.39(3)	0.22(3)	0.31(12)	

Table 4.5: Results of the XSW analysis for the C1s data of the PLP. Unfortunately we have only two data points available, rendering the mean value prone to a large error bar in the F_c. The results are obtained by using the C1s model from Fig. 4.10 for the XSW analysis and are depicted in the Argand diagram in Fig. 4.13. Adsorption heights cannot be calculated, because the signal is a mixture of DP molecules (flat) and COP molecules, which later turns out to be upright standing phenyl nitrene after azobenzene dissociation. Hence, the phenyl ring is crossing the Bragg plane, complicating the interpretation of the data as explained in sec. 2.4.

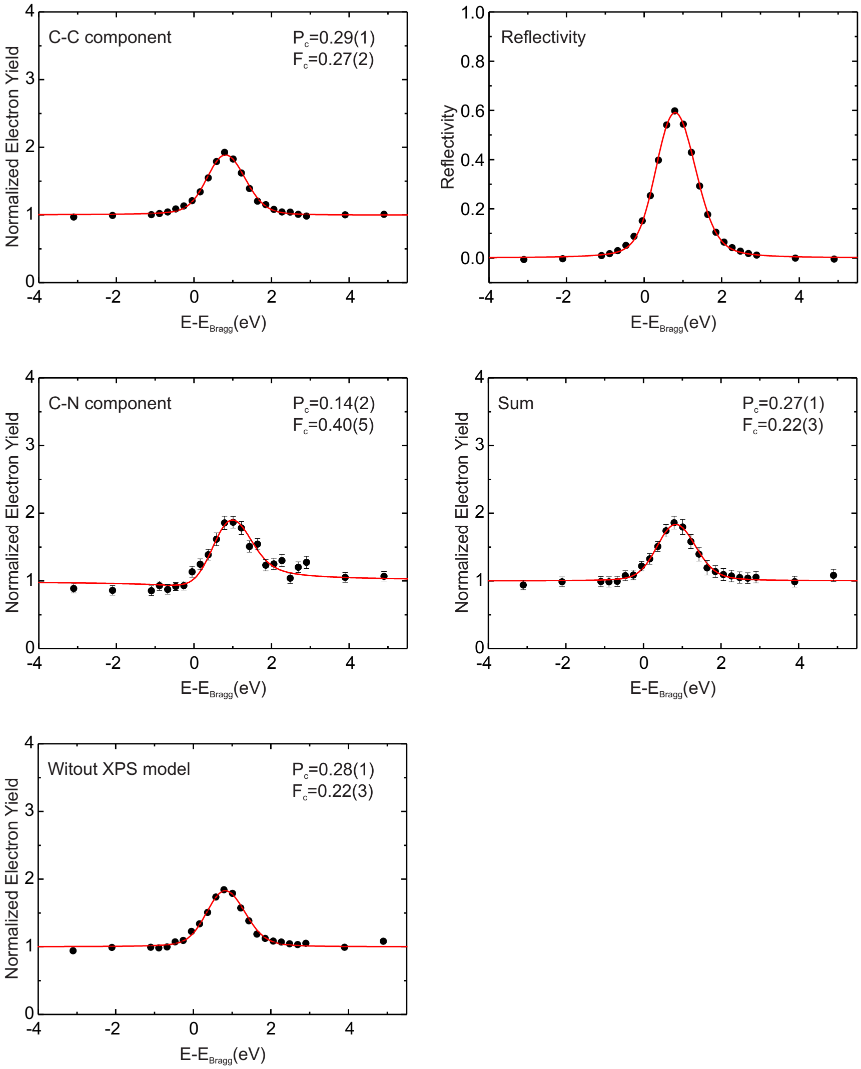

Figure 4.11: Exemplary electron yield curves from the C1s XSW fit using the XPS model depicted in Fig. 4.10. The displayed data belongs to XSW data set C1s025. The x-axis displays the photon energy relativ to the Bragg energy. The results of all C1s data sets are summarized in Table 4.5.

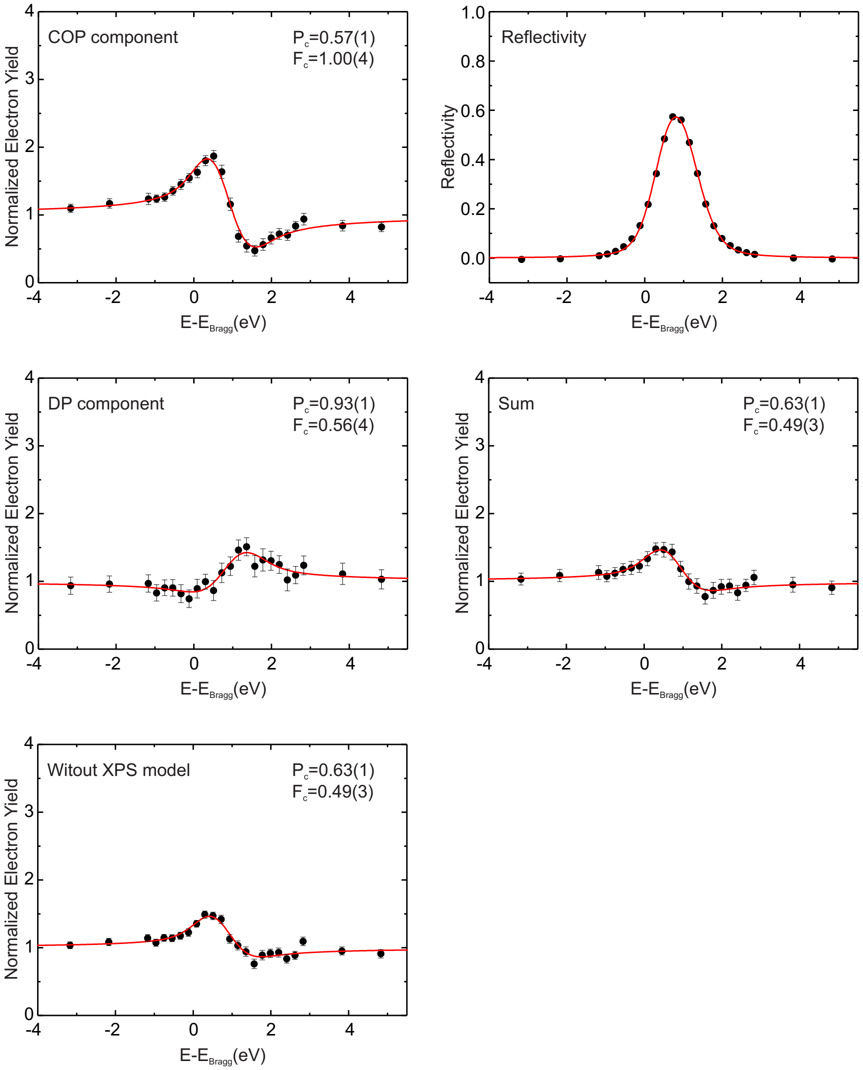

Figure 4.12: Exemplary electron yield curves from the N1s XSW fit using the XPS model depicted in Fig. 4.9. The displayed data belongs to XSW data set N1s026. The x-axis displays the photon energy relativ to the Bragg energy. The results of all N1s data sets are summarized in Table 4.6.

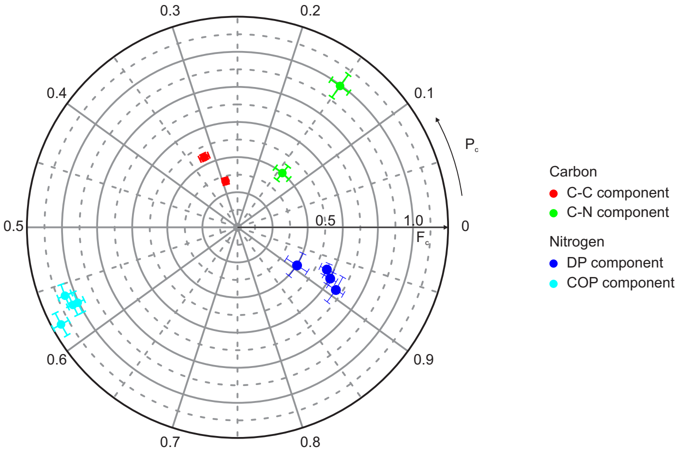

Figure 4.13: Argand diagram showing the XSW results of the PLP data. The N1s results are shown in dark blue for the DP component and in light blue for the COP component of the PLP. Indeed the DP component results are very close to the pure DP (see sec. 4.2). However the COP component shows a completely different result. It should be noted that the maximum diameter shown for F_c here equals 1.2. Unfortunately, for the C1s results (C-C component in red and C-N component in green) we have only two data points each, which show quite some scattering especially in the case of the C-N component. All values are tabulated in Table 4.5 for C1s and Table 4.6 for N1s.

Component		N1s022	N1s024	N1s026	N1s027	mean value	ads. height[Å]
COP	P_c	0.58(1)	0.56(1)	0.57(1)	0.57(1)	0.57(1)	1.19(2)
	F_c	1.14(5)	1.05(4)	1.00(4)	1.03(3)	1.05(6)	
DP	P_c	0.91(3)	0.92(1)	0.93(1)	0.91(2)	0.92(2)	1.92(4)
	F_c	0.40(7)	0.60(4)	0.56(4)	0.66(5)	0.55(11)	
Sum	P_c	0.61(2)	0.62(1)	0.63(1)	0.64(1)	0.62(1)	1.29(2)
	F_c	0.64(5)	0.52(3)	0.49(3)	0.51(3)	0.54(7)	
Without	P_c	0.60(2)	0.62(1)	0.63(1)	0.63(1)	0.62(1)	1.29(2)
XPS model	F_c	0.65(6)	0.48(3)	0.49(3)	0.52(3)	0.53(8)	

Table 4.6: Results for the N1s data of the PLP from the XSW analysis using the XPS model shown in Fig. 4.9. The two components show clearly different results, pointing out that another species coexists with the already known DP molecules in this phase. The data is visualized in the Argand diagram in Fig. 4.13.

stay very close to the previous results of 0.84 ± 0.04 for the F_c and 0.97 ± 0.01 for the P_c. However, the new COP component (bright blue) shows a mean F_c of 1.05 ± 0.06 and a P_c of 0.57 ± 0.01. A F_c larger than one might be a problem of missing nondipolar corrections as mentioned in sec. 2.4. For the C1s we see a low F_c of the C-C component of only 0.35 ± 0.12 at a P_c of 0.31 ± 0.02. This corroborates the expectation that the signal consist of several contributions. The C-N component is very difficult to interpret, because we have only two data points and we can expect this component to show quite some scattering as in the case of the DP. Therefore, the mean F_c of 0.69 ± 0.42 and the mean P_c of 0.15 ± 0.02 have to be judged carefully. All results are tabulated in Table 4.5 and Table 4.6. Later it will turn out that the PLP is a mixed phase of DP molecules which are flat lying and COP molecules, which are upright standing phenyl nitrenes after azobenzene dissociation. Hence, a direct calculation of the adsorption height from the C1s signal is not possible, as the upright phenyl ring is crossing the Bragg plane. The detailed adsorption geometry is therefore discussed later in conjunction with the other results in sec. 4.6.

4.4 Ordered commensurate phase

4.4.1 LEED results

The PLP is not the only ordered structure formed by azobenzene on Cu(111). If the deposited amount is much higher (deposition for 600 s compared to 41 s for the PLP) and the sample is kept at 220 K during the deposition, one finds a *commensurate phase* (COP) after annealing the sample to 315 K. It should be noted that the resulting coverage of the COP after the annealing step is estimated to be similar to the PLP (see Table 4.11). The observed LEED pattern is shown in Fig. 4.14a and again the *Spotplotter* [78] software was employed to simulate the spot positions shown in Fig. 4.14b. We find a commensurate superstructure with the simple matrix

$$\begin{pmatrix} 4 & 0 \\ 0 & 4 \end{pmatrix} \tag{4.2}$$

Furthermore, blue circles in Fig. 4.14 indicate spots which are present only in the simulation. These missing spots in the LEED pattern are a clear evidence for a glide plane symmetry in the unit cell of the COP [88].

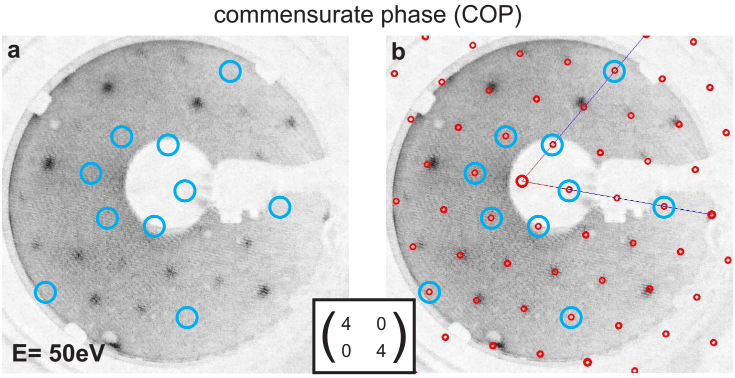

Figure 4.14: Panel (a) shows a LEED picture of the COP. In panel (b) the same picture is overlayed by a LEED simulation done with *Spotplotter* [78] leading to the commensurate superstructure matrix shown. Blue circles in both pictures indicate spots which are missing in the real picture while they are present in the simulation. This is a clear sign for a glide plane symmetry in the unit cell [88].

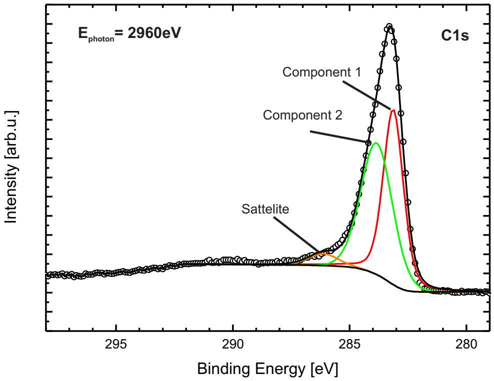

Figure 4.15: Off-Bragg XPS spectrum ($E_{\mathrm{photon}} = 2960\,\mathrm{eV}$) of C1s for the COP. The main peak is fitted with two components due to its asymmetry, one at 283.1 eV (component 1, red) and another one at 283.8 eV (component 2, green) binding energy. The fitted region is chosen such that the model can be transferred to the XSW spectra. A satellite (orange) is neccessary to fit the high binding energy tail of the peak.

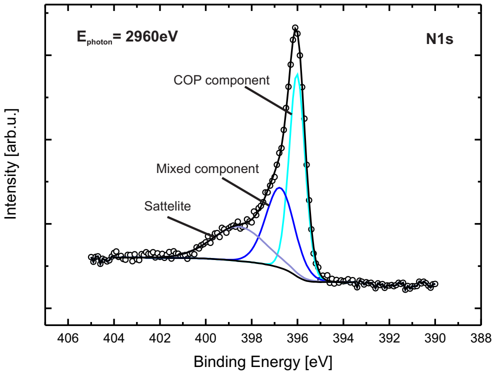

Figure 4.16: Off-Bragg XPS spectrum ($E_{\mathrm{photon}} = 2960\,\mathrm{eV}$) of N1s for the COP. Three components are clearly visible in the spectrum. The COP component at 396.0 eV, a shoulder at 396.8 eV which is attributed to a mixture of DP and COP contributions and hence named Mixed component and a Satellite feature at 398.6 eV. While the COP peak is known from the PLP as seen in Fig. 4.9 the other peaks are new.

Parameter	XSW data set acquisition		Off-Bragg XPS	
	N1s	C1s	N1s	C1s
ΔE_{photon}	8 ± 6 eV	8 ± 6 eV		
E_{photon}			2960 eV	2960 eV
# of XPS spectra	31(28)	31(28)		
repeats	1	1	30	30
pass energy	100 eV	100 eV	100 eV	100 eV
ΔE_{kin}	0.2 eV	0.2 eV	0.1 eV	0.1 eV
dwell time	0.3 s	0.2 s	0.2 s	0.2 s

Table 4.7: Acquisition parameters used for the XSW data sets and off-Bragg XPS spectra. The first data sets (N1s002, N1s006, C1s007) were acquired with the numbers given in brackets. The Bragg energy for the (111) reflection of Cu is found at $E_{\text{photon}} \approx 2977$ eV and the lattice spacing is $d_{\text{Cu}(111)} = 2.09$ Å.

4.4.2 XPS model

The C1s XPS spectrum recorded for the COP looks distinctively different to the spectra of the DP and the PLP as shown in Fig. 4.15, because the shoulder on the high binding energy side is missing. However, the main peak shows a clear asymmetry and it is therefore still neccessary to fit it with two components, but the stoichiometry of the (C-C) to (C-N) carbons in the molecule is no longer reflected by the first component (red) at 283.1 eV and the second component (green) at 283.8 eV. Compared to the PLP C1s XPS model (see Fig. 4.10), the satellite structure has to be modeled differently, because the binding energy range of the XSW spectra is unfortunately measured too short to include the binding energies up to 295 eV. The acquisition parameters for the XPS and XSW spectra can be found in table. 4.7.

The N1s of the COP which is depicted in Fig. 4.16 is different from spectra of the DP and PLP as well. It still shows a clear peak at 396.0 eV which is hence identified to be the COP component of the PLP at 396.3 eV. However, the higher binding energy side features two more components, a mixed component attributed to a mixture DP and COP contributions at 396.8 eV and a satellite at 398.6 eV.

4.4.3 XSW analysis

The XSW analysis, employing the described XPS models, leads to electron yield profiles as those exemplarily shown in Fig. 4.17 for C1s and Fig. 4.18 for N1s. All results

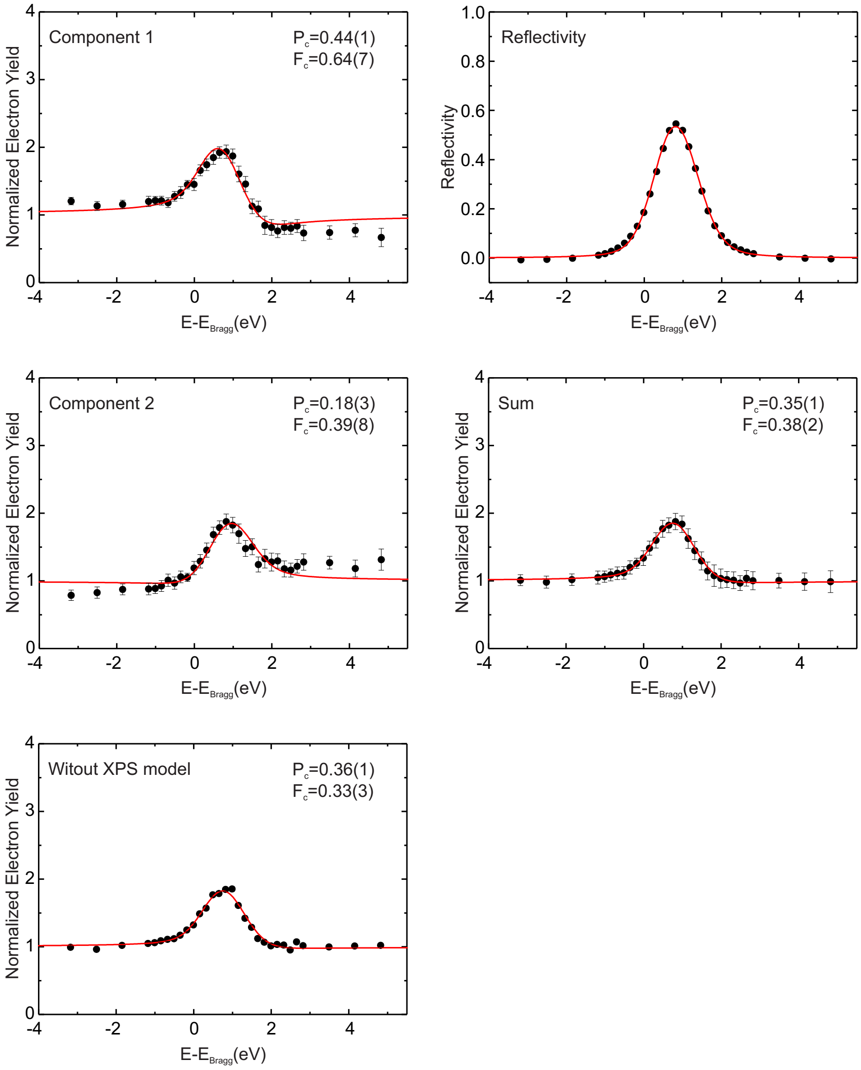

Figure 4.17: Exemplary electron yield curves from the C1s XSW fit using the XPS model depicted in Fig. 4.15. The displayed data belongs to XSW data set C1s009. The x-axis displays the photon energy relativ to the Bragg energy. The results of all C1s data sets are summarized in Table 4.9.

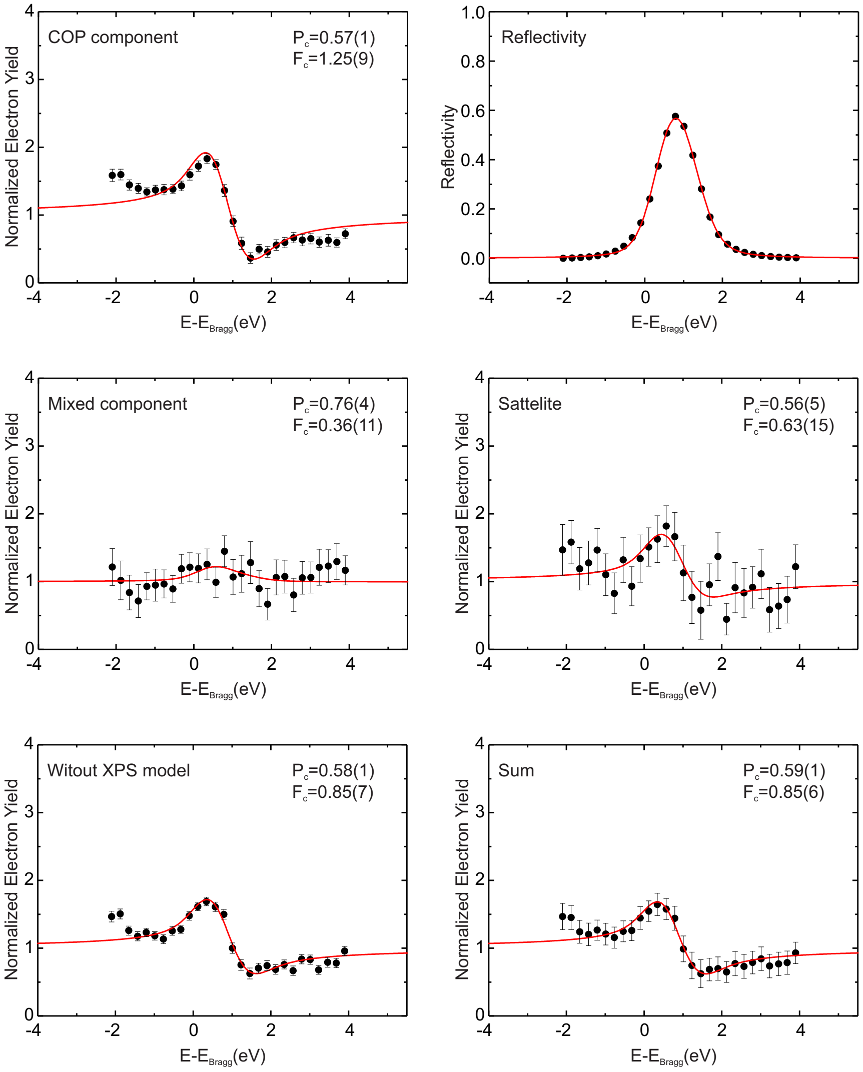

Figure 4.18: Exemplary electron yield curves from the N1s XSW fit using the XPS model depicted in Fig. 4.16. The displayed data belongs to XSW data set N1s006. The x-axis displays the photon energy relativ to the Bragg energy. The results of all N1s data sets are summarized in Table 4.8.

		Preparation 1			Preparation 2					
Component		N1s002	N1s006	N1s008	N1s010	N1s011	N1s012*	N1s014	mean value	ads. height[Å]
COP component	P_c	0.58(1)	0.57(1)	0.55(1)	0.58(1)	0.55(1)	0.55(1)*	0.55(1)	0.56(2)	1.17(4)
	F_c	1.26(10)	1.25(9)	1.17(4)	1.17(8)	1.19(5)	1.21(6)*	1.26(5)	1.21(7)	
Mixed component	P_c	0.76(3)	0.76(4)	0.79(5)	0.73(3)	0.83(6)	_0.67(2)_*	0.76(5)	0.77(4)	1.61(8)
	F_c	0.45(10)	0.36(11)	0.45(16)	0.47(9)	0.31(14)	0.52(6)*	0.25(10)	0.37(12)	
Satellite	P_c	0.58(4)	0.56(5)	0.52(5)	0.64(3)	0.62(3)	_0.78(6)_*	0.55(12)	0.59(5)	1.23(10)
	F_c	0.65(13)	0.63(15)	0.45(11)	0.59(10)	0.70(10)	0.29(14)*	0.15(9)	0.51(20)	
Sum	P_c	0.60(1)	0.59(1)	0.57(1)	0.61(1)	0.58(1)	0.61(1)*	0.57(1)	0.59(2)	1.23(4)
	F_c	0.86(6)	0.85(6)	0.72(3)	0.83(5)	0.77(3)	0.62(3)*	0.58(3)	0.77(11)	
Without XPS model	P_c	0.60(1)	0.58(1)	0.57(1)	0.61(1)	0.58(1)	0.62(1)*	0.58(1)	0.59(2)	1.23(4)
	F_c	0.87(6)	0.85(7)	0.70(4)	0.84(5)	0.75(4)	0.61(4)*	0.57(4)	0.76(12)	

Table 4.8: Results of the XSW analysis for the N1s data of the COP. All values from data sets taken on already exposed spots are marked by an asterisk. These data sets are excluded from the calculation of the mean value, as they obviously influenced by beam damage effects. Strongly deviating values are printed in italic. All data is visualized in the Argand diagram in Fig. 4.19.

		Preparation 1			Preparation 2			
Component		C1s003*	C1s007*	C1s009	C1s013	C1s015	mean value	ads. height[Å]
C-C Component	P_c	_0.56(1)_*	_0.55(1)_*	0.44(1)	0.42(1)	0.46(2)	0.44(2)	4.25(4)
	F_c	1.09(6)*	1.03(4)*	0.64(7)	0.60(4)	0.60(8)	0.61(6)	
Component 2	P_c	0.18(1)*	0.18(1)*	0.18(3)	0.21(2)	0.19(3)	0.19(3)	-
	F_c	0.62(4)*	0.68(4)*	0.39(8)	0.39(6)	0.17(4)	0.32(13)	
Sum	P_c	0.34(1)*	0.33(1)*	0.35(1)	0.35(0)	0.41(2)	0.37(3)	-
	F_c	0.29(1)*	0.32(1)*	0.38(2)	0.39(1)	0.30(3)	0.35(5)	
Without XPS model	P_c	0.32(1)*	0.33(1)*	0.36(1)	0.36(1)	0.42(2)	0.38(3)	-
	F_c	0.25(2)*	0.28(2)*	0.33(3)	0.35(2)	0.27(3)	0.31(4)	

Table 4.9: Results of the XSW analysis for the C1s data of the COP. All values from data sets taken on already exposed spots are marked by an asterisk. These data sets are excluded from the calculation of the mean values, as they obviously influenced by beam damage effects. Strongly deviating values are printed in italic. The results are visualized in the Argand diagram in Fig. 4.19. The adsorption heights are not calculated, because later we will see that the species forming the COP is an upright standing phenyl nitrene where the phenyl ring is crossing the Bragg planes and hence the P_c can not be translated directly into a height value, but a structure simulation is neccessary to match the P_c and F_c. As a result of this simulation the $4.25 \pm 0.04\,\text{Å}$ of the C-C component is evaluated.

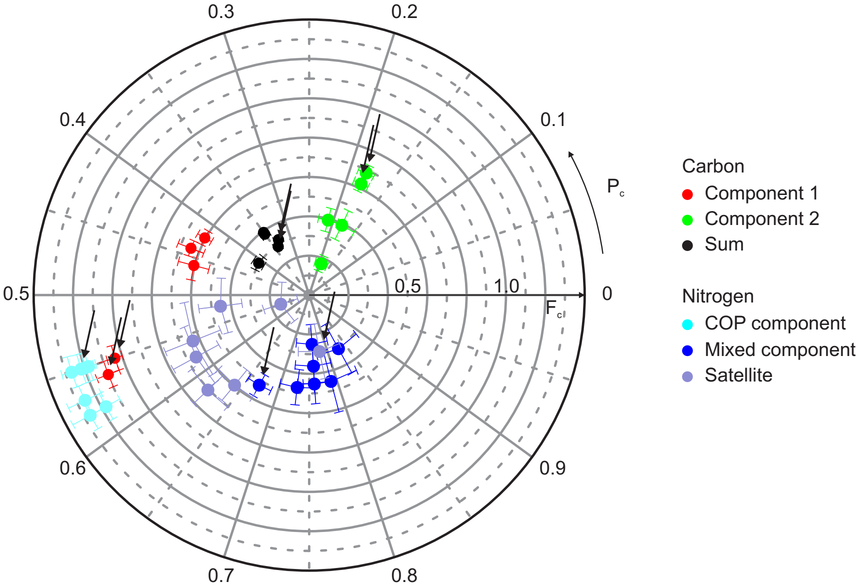

Figure 4.19: Argand diagram showing the XSW results of the COP data. N1s results are depicted in blue, C1s results in red and green according to the fitting models in figs. 4.16 and 4.15. Datapoints indicated by a black arrow are taken on already beam exposed spots and therefore deviate due to beam damage effects. All data shown here is tabulated in tables 4.8 and 4.9.

are depicted in the Argand diagram in Fig. 4.19 and the corresponding values are tabulated in Table 4.8 for N1s and Table 4.9 for C1s.

As for the PLP, we can expect beam damage on our sample. In fact, from our data for the COP we can obtain qualitative insight in which direction this influences our results. All data points marked by black arrows in the Argand diagram and asterisks in the tables are taken on an already exposed spot, where another data set has been recorded before. Except for the N1s COP component these results differ significantly from the measurements on so-far unexposed spots. Therefore, we can conclude that the N1s COP component seems to be quite stable and we know in which direction beam damage alters the results. To some extent this may already happen during the first XSW experiment on each spot, as some XPS changes within the XSW data sets can be observed.

Discarding the data on the obviously damaged spots, we turn to the results for N1s first. For the COP component we find a P_c of 0.56 ± 0.02, which is in perfect agreement with the corresponding PLP result. However, the F_c of 1.21 ± 0.07 is even higher than in the PLP, which might again be a problem of the missing non dipolar corrections. The second component at 396.8 eV of the N1s spectrum is called mixed component, because the XSW result of a P_c of 0.77 ± 0.04 and a F_c of 0.37 ± 0.12 suggests a mixture of a satellite from the main component and residual DP molecules (their binding energy would be 397.8 eV), which shift the resulting sum accordingly. The third component shows no influence of any mixture and with a P_c of 0.59 ± 0.05 and a F_c of 0.51 ± 0.20 it is simply understood as another satellite of the COP peak. This leaves us with two key results for the structure determination of the COP, namely the result of the main N1s component that indicates an adsorption height of 1.17 ± 0.04 Å, and the knowledge that residual DP molecules are still present.

For the C1s we find a F_c of 0.61 ± 0.06 and a P_c of 0.44 ± 0.02 for the C-C component and a F_c of 0.32 ± 0.13 and a P_c of 0.19 ± 0.03 for the second component. However, the physical meaning of these components is unclear, since the stoichiometry does not fit to the ratio of (C-N) to (C-C) anymore. As we could extract the coexistence of DP molecules from the N1s data, this is most probably the reason for the difficulties in the discrimination of the C1s results. The second component is not only representing the C-N of the COP, but may include contributions from the C-C and C-N of the DP. Hence, the meaningful result which we can use is the C-C component only. However, a direct calculation of the adsorption height is not possible, because later we will see that the species forming the COP is an upright standing phenyl nitrene after azobenzene dissociation, with the phenyl ring pointing towards the vacuum and hence crossing the Bragg planes. This problem was encountered for benzene/Cu(111) as well (see sec. 3.3) and again we need to do a structure simulation to interpret the XSW results. Basically, it means that the P_c and F_c of a structure model is calculated and compared to the experimental results. More details on this problem can be found in ref. [30]. Simulating an upright standing phenyl nitrene with the N adsorption height of 1.17 ± 0.04 Å, the C-C carbons yield a P_c of 0.45 and a F_c of 0.53 which is in good agreement with the experimental C-C component results of P_c of 0.44 ± 0.02 and F_c of 0.61 ± 0.03. Hence, the mean adsorption height of the C-C carbons is estimated to be 4.25 ± 0.04 Å.

4.5 Multilayer

4.5.1 XPS models

A *multilayer phase* (MLP) was prepared by the deposition of additional azobenzene on top of the COP for 600 s and again at a sample temperature of 220 K, but without any post deposition annealing step. Interestingly, the LEED pattern is the same as for the COP (see Fig. 4.14), and therefore we either face a commensurate multilayer growth, or the formation of 3D islands which leave a large area of the COP wetting layer uncovered. Unfortunately, we cannot determine the growth mode, but the XPS data suggest that the first idea of a commensurate multilayer growth is correct.

In the MLP C1s XPS spectra, as depicted in Fig. 4.20, two peaks can be distinguished. One is found at a binding energy of 285.0 eV and is dominating the spectrum and therefore identified as multilayer signal. The second feature is already known from the COP at 283.3 eV and is therefore identified as the monolayer peak.

For N1s we can observe three peaks as seen in Fig. 4.21. Again a strong signal is dominating the spectrum and therefore the peak at 400.2 eV is identified as multilayer contribution which is in agreement with the N1s azobenzene bulk binding energy of 400.3 eV [89]. The peak at 403.6 eV is attributed as a satellite to the multilayer peak. A feature at 396.4 eV which can be found in the COP at 396.1 eV and the PLP

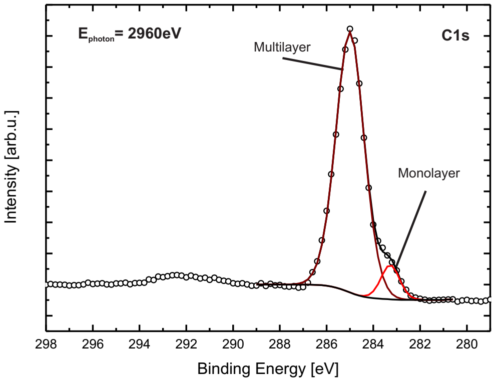

Figure 4.20: Off-Bragg XPS spectrum ($E_{\text{photon}} = 2960\,\text{eV}$) of C1s for the MLP. The spectrum is dominated by the peak at 285.0 eV (scarlet) which is therefore identified as multilayer signature while the peak at 283.3 eV (red) is already known from the COP and hence identified as monolayer peak.

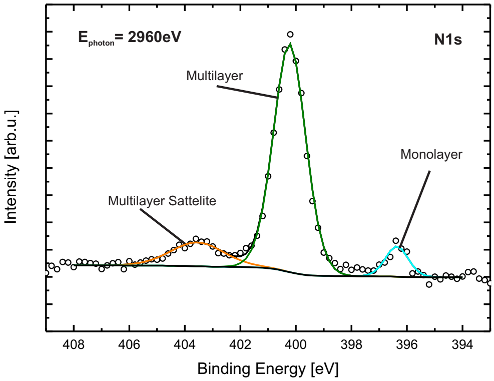

Figure 4.21: Off-Bragg XPS spectrum visualizing the XSW fitting model of N1s for the MLP. Three well separated contributions are identified. A strong multilayer peak at 400.2 eV (green), its satellite at 403.6 eV (orange) and the monolayer signature already known from the PLP and COP at 396.3 eV (blue).

at 396.3 eV is attributed as N1s monolayer signal. The intensity of this monolayer peak is much weaker for the MLP than for the COP, which is an indicator that the contact layer is indeed buried by additional molecules. The acquisition parameters for XPS and XSW spectra are shown in Table 4.10.

4.5.2 Coverage estimation

To quantify the multilayer thickness, the coverage was analysed by a comparison of the monolayer to the multilayer signal.

Parameter	XSW data set acquisition		Off-Bragg XPS	
	N1s	C1s	N1s	C1s
$\Delta E_{\mathrm{photon}}$	8 eV	8 eV		
E_{photon}			2960 eV	2960 eV
# of XPS spectra	31	31		
repeats	1	1	4	3
pass energy	100 eV	50/30 eV	100 eV	100 eV
ΔE_{kin}	0.2 eV	0.2 eV	0.2 eV	0.2 eV
dwell time	0.3 s	0.2 s	0.2 s	0.2 s

Table 4.10: Acquisition parameters used for the XSW data sets and off-Bragg XPS spectra in the MLP. For the C1s XSW spectra pass energies of 50 eV (data set C1s018) and 30 eV (data set C1s019) were used. The Bragg energy for the (111) reflection of Cu is found at $E_{\mathrm{photon}} \approx 2977$ eV and the lattice spacing is $d_{\mathrm{Cu(111)}} = 2.09$ Å.

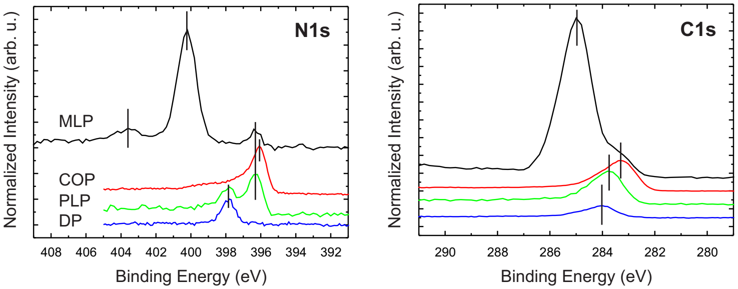

Figure 4.22: Off bragg XPS spectra of the various phases of azobenzene/Cu(111) of the (a) N1s and (b) C1s core level lines to extract the azobenzene coverage for each phase. These are the same spectra which were used for the fit model determinations, but normalized to the low binding energy background. The DP is shown in blue, the PLP in green, the COP in red, and the MLP in black. The spectra are shifted on the y-axis to allow a better comparison, peak positions are marked by black bars. The intensity values extracted for the coverage analysis are given in Table 4.11.

The XPS signals for the C1s and N1s lines depicted in Fig. 4.22 are the same off-Bragg spectra which where used for the XPS model in each chapter, taken at a photon energy of 2.960 keV. However, in Fig. 4.22 the data is normalized to the background intensity on the lower binding energy side of each spectrum to compare signal intensities. In Table 4.11 the full intensities of the normalized spectra are given, in case of the MLP the intensity of the monolayer peak is noted in brackets. It should be noted that the XPS shift which is observed for C1s between the different monolayer phases is in the same direction as the N1s shift and can be attributed to a larger surface screening due to a stronger bond of the molecule to the surface, which is reflected in the low nitrogen adsorption height for the COP molecules compared to the DP ones.

Phase	C1s Area [arb. u.]	N1s Area [arb. u.]
Multilayer (MLP)	31559 (2382)	4170 (319)
Commensurate ML (COP)	7589	1483
Point-on-line ML (PLP)	7685	1364
Disordered ML (DP)	3036	624

Table 4.11: Intensities extracted from the normalized XPS spectra shown in Fig. 4.22. The values reflect the integrated area of all corresponding peaks after subtraction of a Shirley background. However, the numbers are not corrected for damping, and therefore the multilayer value cannot directly compared to the other phases for a coverage evaluation. Within these other phases the error is expected to be smaller as the difference in damping is small. The values of the multilayer given in brackets are the intensities of the monolayer peak in the multilayer spectra.

To perform a coverage analysis one can compare these integrated photoelectron intensities of the XPS spectra. However, the direct comparison of intensities is only possible if damping is negligible. Damping is introduced, because the chance for photoelectrons to be scattered is higher the more layers they have to pass on their way to the surface. Consequently, the maximum signal is expected from a surface layer and a finite escape depth exists. Hence, already the normalization introduces an error due to the not considered damping of the substrate background which is used as a reference for the normalization. While one could expect the values for the PLP, COP and even DP to be comparable, as all coverages are in the monolayer regime, the multilayer signal can only yield a meaningful result if the damping is considered in a proper way. Thereforek, we now turn to a quantitative film thickness analysis.

The damping follows the Lambert-Beer law which depends on the inelastic mean free path of the photoelectron (λ) and the layer thickness (d), where I_0 is the undamped intensity and I is the measured intensity.

$$I = I_0 \exp\left(-\frac{d}{\lambda}\right) \tag{4.3}$$

The inelastic mean free path for organic compounds can be calculated from an empirical formula if the bulk density (ρ) in $\mathrm{kg\,m^{-3}}$ of the compound is known [21]. In that case it is calculated as

$$\lambda[\text{Å}] = 10000 \times \rho^{-1} \times \left(\frac{49}{E^2} + 0.11\sqrt{E}\right) \tag{4.4}$$

with E as kinetic energy of the photoelectrons in eV. The bulk density of azobenzene is $1230\,\frac{\mathrm{kg}}{\mathrm{m}^3}$ [90] and together with the kinetic energy of 2560 eV (N1s) and 2676 eV (C1s) used in our XPS experiments we find an inelastic mean free path of the photoelectrons of $\lambda_{N1s} = 45$ Å and $\lambda_{C1s} = 46$ Å respectively.

If we assume a layer thickness of 5.8 Å for each azobenzene layer as it is reported for the bulk unit cell [90] and take into account a grazing emission angle of 80° from the surface normal due to a slight sample tilt and the analyzer acceptance angle, we obtain an effective single layer thickness of 33.4 Å. Furthermore, we assume that the undamped intensity from each layer is equal. To estimate the overall thickness, we need two equations, as I_0 as well as d are still unknown. However, we can differentiate the intensity of the first layer (I_{first}) from the intensity of higher layers (I_{multi}) for

C1s as well as for N1s. Therefore, eq. (4.3) leads to the following expressions, with $k+1$ beeing the number of adsorbed layers:

$$I_{\text{first}} = I_0 \exp\left(-\frac{33.4 \times k}{\lambda}\right) \tag{4.5}$$

$$I_{\text{multi}} = I_0 \sum_{n=0}^{k-1} \exp\left(-\frac{33.4 \times n}{\lambda}\right) \tag{4.6}$$

If we use eq. (4.5) to replace I_0 in eq. (4.6) we find

$$I_{\text{multi}} = \frac{I_{\text{first}}}{\exp\left(-\frac{33.4\times k}{\lambda}\right)} \sum_{n=0}^{k-1} \exp\left(-\frac{33.4 \times n}{\lambda}\right) \tag{4.7}$$

Solving this equation we get a result of $k = 2.7$ for C1s and N1s, hence we can conclude that the film thickness for the multilayer preparation is about 4 layers. One should note that this estimation is very rough and strongly relies on the assumed homogeneous layer thickness. Comparing the exposure time of 41 s for the PLP, which can be expected to roughly yield a monolayer coverage, to the additional 600 s deposition on the COP to form the multilayer, a significantly reduced sticking coefficient can be expected for molecules above of the first layer.

4.5.3 XSW results

For the MLP the expectations regarding an XSW analysis differ from the other cases. One cannot expect that the layer spacing of the organic material is an integer multiple of the Bragg spacing. Therefore, the molecules occupy too many different positions within the Bragg spacing to disentangle the XSW results and in the limit towards a thick film we would therefore expect the F_c to decrease to zero.

We can indeed observe this behaviour in the MLP data for the multilayer case as seen in Table 4.12 and Table 4.13 and plotted in the Argand diagram in Fig. 4.25. Exemplary yield curves for C1s and N1s are shown in Fig. 4.23 and Fig. 4.24, respectively. The F_c for the multilayer contribution is very low in all cases indicating that we cannot determine vertical positions here. However the monolayer peaks

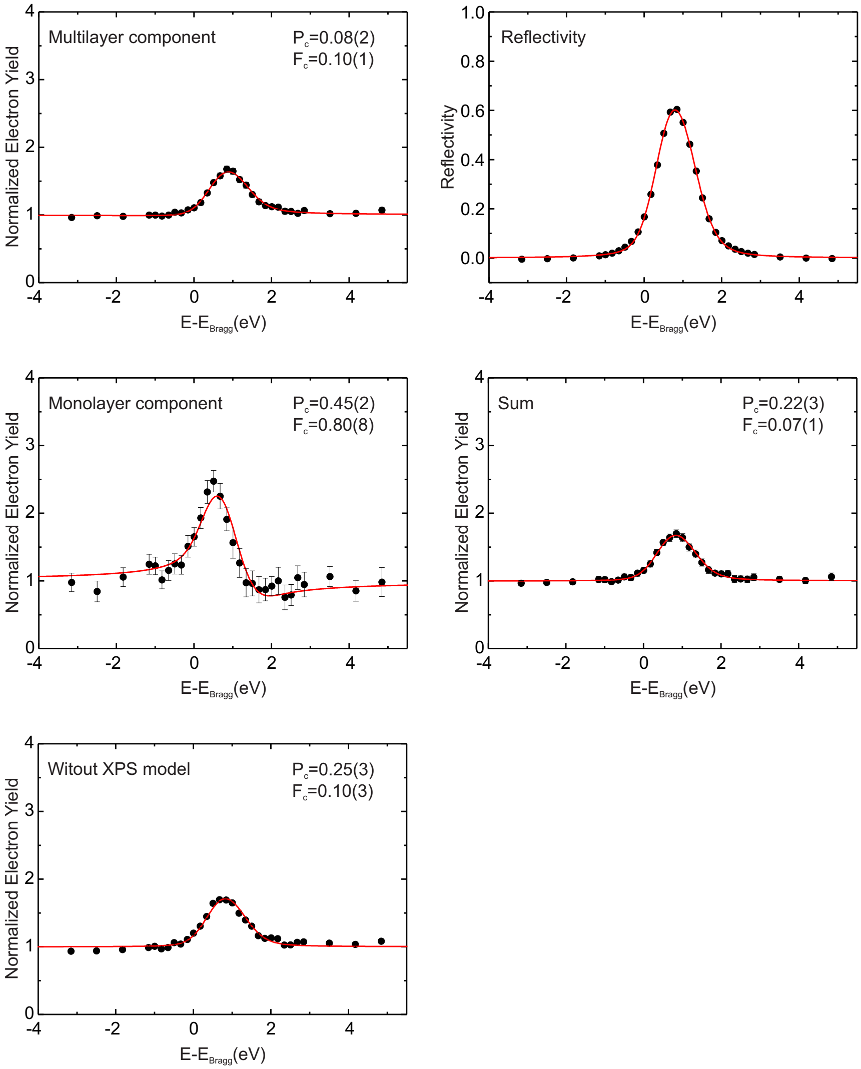

Figure 4.23: Exemplary electron yield curves from the C1s XSW fit using the XPS model depicted in Fig. 4.20. The displayed data belongs to XSW data set C1s019. The x-axis displays the photon energy relativ to the Bragg energy. The results of all C1s data sets are summarized in Table 4.13.

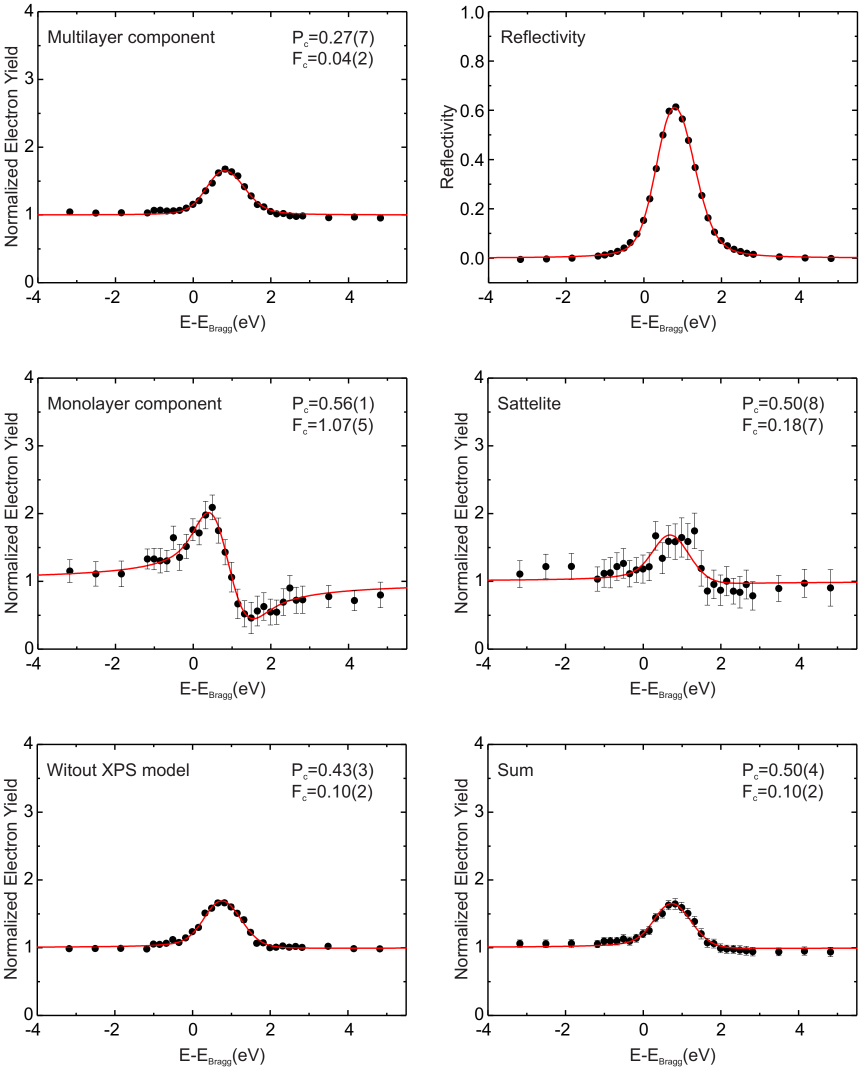

Figure 4.24: Exemplary electron yield curves from the N1s XSW fit using the XPS model depicted in Fig. 4.21. The displayed data belongs to XSW data set N1s017. The x-axis displays the photon energy relativ to the Bragg energy. The results of all N1s data sets are summarized in Table 4.12.

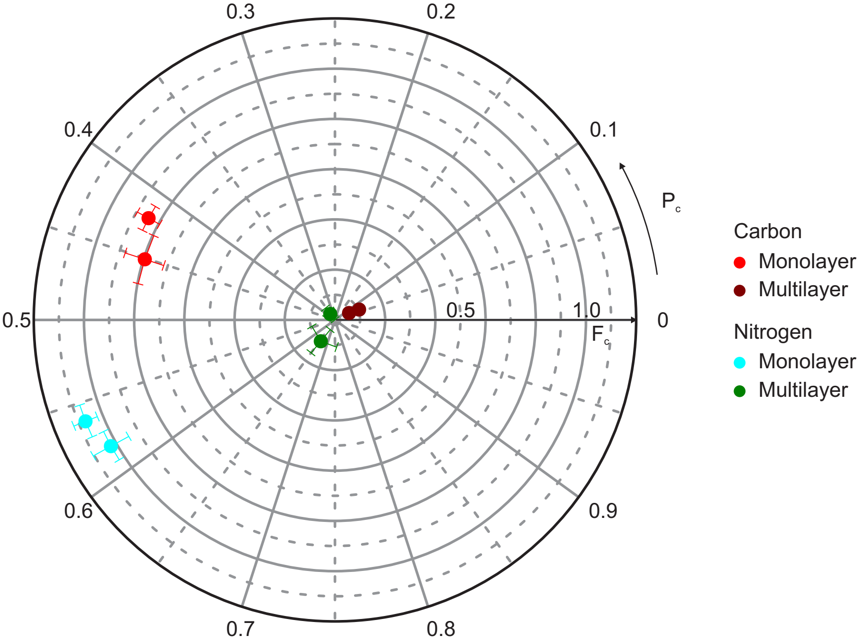

Figure 4.25: Argand diagram showing the XSW results of the MLP data. The multilayer results for N1s (green) and C1s (scarlet) are near F_c 0 as expected for vertical disorder as the multilayer spacing does not match the Bragg spacing. However, the monolayer contributions of N1s (light blue) and C1s (red) fit very well to the COP results indicating this interface layer may be unchanged. All values are tabulated in tabs. 4.12 and 4.13.

Component		N1s016	N1s017	mean value	ads. height[Å]
Multilayer	P_c	0.68(9)	0.27(7)	0.63(29)	N/A
	F_c	0.10(6)	0.04(2)	0.03(4)	
Monolayer	P_c	0.58(1)	0.56(1)	0.57(1)	1.19(2)
	F_c	1.02(8)	1.07(5)	1.04(7)	
Satellite	P_c	0.51(11)	0.50(8)	0.50(10)	N/A
	F_c	0.21(11)	0.18(7)	0.19(9)	
Sum	P_c	0.61(7)	0.50(4)	0.57(8)	N/A
	F_c	0.17(6)	0.10(2)	0.13(5)	
Without XPS model	P_c	0.56(7)	0.43(3)	0.50(7)	N/A
	F_c	0.12(4)	0.10(2)	0.10(3)	

Table 4.12: Results of the XSW analysis for the N1s data of the MLP. Due to the F_c a meaningful P_c and hence adsorption height can only be extracted for the monolayer contribution. The data is visualized in the Argand diagram in Fig. 4.25.

Component		C1s018	C1s019	mean value	ads. height[Å]
Multilayer	P_c	0.10(3)	0.08(2)	0.09(3)	N/A
	F_c	0.06(1)	0.10(1)	0.08(3)	
Monolayer	P_c	0.42(1)	0.45(2)	0.43(2)	2.98(4)
	F_c	0.85(5)	0.80(8)	0.82(7)	
Sum	P_c	0.31(2)	0.22(3)	0.27(6)	N/A
	F_c	0.08(1)	0.07(1)	0.07(1)	
Withoit XPS model	P_c	0.30(2)	0.25(3)	0.28(4)	N/A
	F_c	0.13(2)	0.10(3)	0.11(3)	

Table 4.13: Results of the XSW analysis for the C1s data of the MLP. A meaningful P_c and hence adsorption height can only be extracted for the monolayer contribution. The data is visualized in the Argand diagram in Fig. 4.25.

are clearly separated in the XPS as described above and therefore allow for a separate analysis. Here we actually find a F_c of 1.04 ± 0.07 and a P_c of 0.57 ± 0.01 for the N1s which is very similar to the findings on the COP ($F_c = 1.21 \pm 0.07$, $P_c = 0.56 \pm 0.02$). For C1s we find a F_c of 0.82 ± 0.07 and a P_c of 0.43 ± 0.02 in the monolayer which is again close to the COP findings ($F_c = 0.61 \pm 0.06$, $P_c = 0.44 \pm 0.02$).

Throughout this work the issue of non-dipolar correction parameters for the XSW analysis is mentioned. While some corrections have to be calculated, others can be determined experimentally as well. The prerequisite is a homogeneous distribution of scatterers over the Bragg-planes to reach a F_c of 0. This means we can employ the multilayer results presented above to prove that non-diplar corrections are not neccessary for the experimental geometry of 90° between incoming photon beam and analyser. However, we cannot adress any acceptance angle dependence, because only the angle integrated XPS signal was recorded in the experiments. For the fitting procedure one has to extend eq. (2.24) according to ref. [4] to include possible non-dipolar effects to

$$I = 1 + R\frac{1+Q}{1-Q} + 2\sqrt{R} \cdot F_c \frac{\sqrt{1+Q^2\tan^2\Delta}}{1-Q} \cos\left(\phi + \tan^{-1}(Q\tan\Delta) - 2\pi \cdot P_c\right) \quad (4.8)$$

with Q as forward/backward scattering asymmetry factor and Δ as phase difference between the outgoing waves exited by the electric dipole and quadrupole terms of the matrix element. For $F_c = 0$ eq. (4.8) simplifies to

$$I = 1 + R\frac{1+Q}{1-Q} \tag{4.9}$$

and we can fit Q from the experimental electron yield curves. The fit was done using *Torricelli* [36–38] for the multilayer component of C1s and N1s and the result is $Q = 0.02 \pm 0.02$. Hence, the assumption of $Q = 0$ is confirmed for the experimental setup and eq. (4.8) becomes identical to eq. (2.24), which is used to fit the XSW data throughout this work. The tiny deviation of Q from 0 can be neglected, because the the F_c of the multilayer film might not be exactly 0. Furthermore, other studies of thick disordered films at the same setup corroborate the result found here [53].

4.6 Discussion

4.6.1 Introduction

In the above sections the data of four different phases for azobenzene on Cu(111) has been presented. Now we turn to a detailed discussion of the structures of these phases and their similarities as well as differences. The section starts with the DP, where a detailed adsorption model is derived from the XSW data, and proceeds with the PLP and its differences to the DP. Furthermore, a lateral model for the unit cell is proposed based on the LEED data and the information extracted from the XSW analysis. As the unit cell changes for the COP, a new model is derived in the next step to explain these changes. Finally, the multilayer is discussed.

4.6.2 Distortion of azobenzene for the DP

To summarize the data about the DP presented in sec. 4.2 we know that the phase shows a disordered signature in the LEED pattern and we can extract the vertical heights of the nitrogen (2.02 ± 0.02 Å), the C-N carbon (2.23 ± 0.06 Å) and the C-C carbon (2.36 ± 0.02 Å), separately. We cannot extract any more information from the LEED, except that no long range order is present in the molecular layer, which points at a rather low density of molecules. This interpretation is supported by the

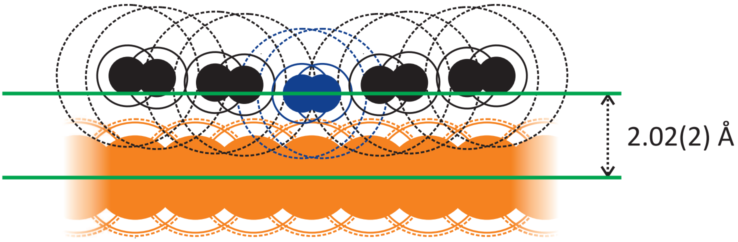

Figure 4.26: Vertical adsorption geometry of azobenzene on Cu(111) in the DP. The atomic positions are marked by filled circles, nitrogens are blue, carbons are black, copper is orange. Hydrogens are not depicted for clarity reasons. Dashed lines mark vdW radii [56], solid lines covalent radii [55]. The tilt angle of the phenyl rings is depicted in more detail in Fig. 4.27.

fact that higher coverages will lead to distinct diffraction patterns and the rough coverage estimation (see Table 4.11) confirms that we are below half the coverage of the PLP or COP. Therefore, we can conclude that the molecules on the surface are not completely isolated, but do have enough space to adsorb without any steric hindrance from their neighbours.

In Fig. 4.26 the model of azobenzene on the Cu(111) surface is depicted as concluded from the various P_c. Circles indicate the covalent (solid) [55] and vdW radii (dashed) [56]. We can see a strong overlap of all molecular vdW radii with the substrate and therefore expect an interaction for the phenyl rings as well as for the azo bridge. In the latter case, even covalent radii are in touch with the Cu, a strong hint for a chemical interaction. The adsorption height of the nitrogen of roughly 2 Å is in agreement with the LEED-IV findings for glycine on Cu(110) [91]. Such a strong molecule-surface interaction might be a reason for azobenzene to loose its photoswiching capabilities upon adsorption [10]. Furthermore, the upward bending of the phenyl rings is a signature for a repulsive interaction on the

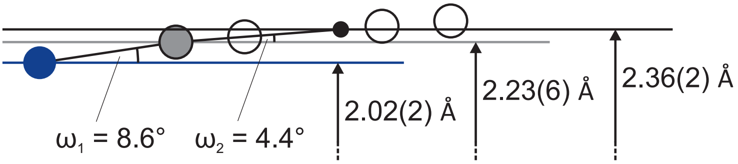

Figure 4.27: Detailed picture of the bonding angles in azobenzene adsorbed on Cu(111) in the DP. The differential XSW analysis allows to get independent vertical heights for the nitrogen (blue), the carbon which is bonding to the nitrogen (grey) and the residual carbons (open cirles). The center of mass of the residual carbons is depicted as black dot. The tilt angles are calculated assuming that bonding distances within the molecule stay constant.

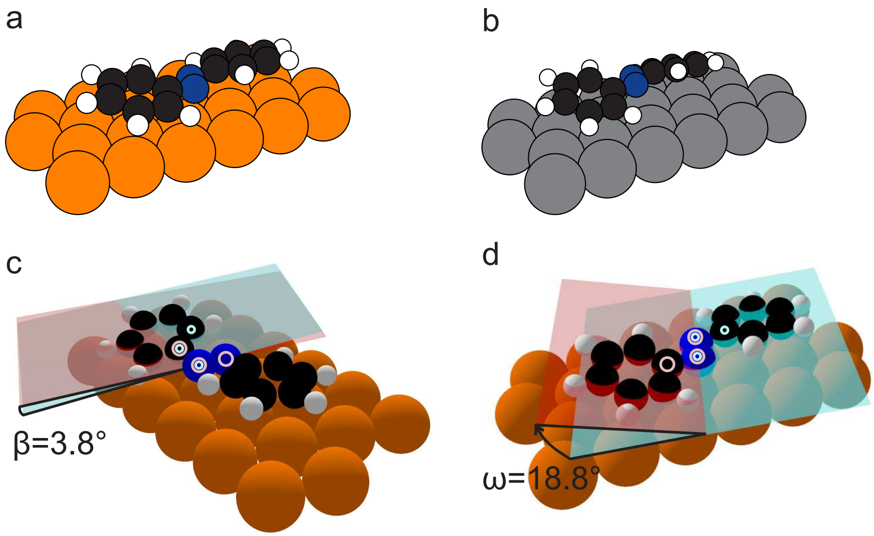

Figure 4.28: (a) Full model of the azobenzene in the adsorption geometry of the DP including the tilt of the phenyl rings around the long axis of the molecule extracted from the F_c. (b) Model for the geometry of azobenzene/Ag(111), reported from XSW measurements [59]. (c,d) Construction of the dihedral angles β (NNCC) and ω (CNNC). The angles are measured between the shown red and blue planes. Each plane is defined by three atoms, indicated with circles in the plane colour. Note that the red planes in (c) and (d) are identical, because they are defined by the same atoms. (c) is depicted in a different perspective to allow the visualization of the β angle. Cu surface atoms are shown in orange, Ag in grey, carbons in black, nitrogens in blue and hydrogens in white.

wings, as the nitrogen drags the molecule towards the surface to optimize its N-Cu bond.

Actually, the experiment allows to derive the adsorption geometry very precisely, if one assumes the bonding distances within azobenzene to be the same as in its bulk crystal structure. This assumption is justified by DFT calculations which show negligible bond length deviations [92]. The resulting geometry for one half of the molecule is depicted in Fig. 4.27 to allow a more detailed look on the adsorption angles. Starting from the nitrogen, we have a height difference of 0.21 Å to the C-N carbon, and the bonding length is 1.4 Å [93], which results in an angle of $\omega_1 \approx 8.6°$ between the N-C bond and the adsorption plane parallel to the surface. For the rest of the carbons (C-C) we know only the mean adsorption height which is 0.13 Å above the C-N carbon. Taking into account the carbon distribution and C-C bonds of 1.4 Å [93] we find a tilt angle of $\omega_2 \approx 4.4°$ between the phenyl ring and a plane parallel to the surface.

	$d_{\mathrm{Cu-N}}$ (Å)	$d_{\mathrm{Cu-CN}}$ (Å)	$d_{\mathrm{Cu-CC}}$ (Å)	ω (deg)	β (deg)
XSW Experiment	2.02(2)	2.23(6)	2.36(2)	18.8	3.8
DFT + vdW$^{\mathrm{surf}}$ [92]	2.03	2.15	2.28	11.0	3.3

Table 4.14: Comparison of the structural parameters for the DP phase deduced from the experiment presented here and DFT calculations carried out by R. J. Maurer and K. Reuter from the TU München [92] using the DFT + vdW$^{\mathrm{surf}}$ method [51, 65].

This already provides us with a very detailed understanding of the adsorption structure. However, there is the possibility of another rotation of the phenyl ring around its symmetry axis in the direction along the molecule. Such a tilt would not change the mean height of the carbon atoms as long as it is small enough, but it would affect the F_c immediately. If one simulates the structure shown in Fig. 4.26 using *Torricelli* [36–38] and assumes the nitrogen F_c to be the maximum possible value, whose divergence from one is explained by intermolecular differences, we find a corrected carbon F_c of 0.82 for this geometry. Details on the structure simulation to match experimental XSW data can be found in ref. [30]. Turning the phenyl rings by 10° reduces the simulated F_c value to 0.71 which matches quite well with the experimental value of the mean carbon F_c of 0.69 ± 0.10 and results in the final model for azobenzene/Cu(111) in the DP shown in Fig. 4.28a.

Interestingly, such a rotation points towards a non-negligible molecule-molecule interaction as it might be understood as an optimisation of π-bond overlap between neighbouring phenyl rings. However, this result depends only on the F_c and one should remember that we face several cases with too high F_c values due to missing nondipolar corrections as explained in 2.4. Therefore, the angle of 10° should be understood as a hint that we indeed see a rotation of the phenyl rings around the long axis of the molecule but it might be larger than 10° if we overestimated the experimental F_c. Furthermore, the exact angle might be very sensitive to the coverage, as the general trend of azobenzene to twist dependent on its density is indeed reported for azobenzene/Ag(111) [59]. For a comparison to our results the structure azobenzene/Ag(111), determined by XSW, is shown in Fig. 4.28b. To be able to describe the angles within the molecule in a more general fashion they are usually measured as dihedral angles. For the azobenzene geometry described above the dihedral angle (CNNC) which is called ω is 18.8° while the (NNCC) angle, called β is 3.8°. The construction of these angles is shown in Fig. 4.28c and d for β and ω, respectively.

The geometry derived here is in very good agreement with state of the art DFT calculations including vdW forces and screening effects, by using the DFT + vdW$^{\mathrm{surf}}$

method [51, 65] as can be seen from Table 4.14. The computation was done for a single *trans*-azobenzene molecule in a (6 × 4) overlayer structure on a 4-layer Cu slab [92]. It must be noted that finite temperature effects, which are found to have a crucial impact on the adsorption geometry in DFT calculations for azobenzene/Ag(111)[59], are not neccessary to archieve excellent computational results for azobenzene/Cu(111). This can rationalized by two facts. First, the temperature during the XSW experiments was only 60 K in the azobenzene/Cu(111) case, while azobenzene/Ag(111) was measured at 210 K [59] and second, the stronger and hence shorter N-metal bond in the Cu(111) case may shift the relevant molecular modes to higher energy, leaving them correspondingly less populated and hence reduce the anharmonic influences. However, it must also be noted that the experimental values from the XSW experiments assume no relaxation of the top Cu layer, while from LEED experiments on the bare Cu(111) surface a relaxation of the first layer of about −0.02 Å is reported [94]. This could introduce an additional error of the same order as the statistical error given for the XSW results and should be taken into account in the comparison whith the DFT results in Table 4.14 [92] where a relaxation of −0.03 Å for the top Cu(111) layer is indeed found and included in the calculated vertical distances.

4.6.3 Coverage dependent dissociation

With the clear picture of the DP we will now analyse the differences to the other phases. If we look at the PLP, we see two major differences to the DP. First, the PLP is ordered with clear LEED spots, and second, we see the well-separated COP peak in the XPS N1s spectrum (see Fig. 4.9), while the DP peak is still present. This raises the questions what species are formed on the surface, how do they arrange and why does this transition happen?

The last question is answered by the different preparation parameters. The coverage, which is more than doubled in the PLP than the DP (see Table 4.11), seems to be the driving force. However, with the PLP we are facing a state where we can still see coexisting molecules with a DP like fingerprint, while this is not the case in the COP. We are therefore led to conclude that the PLP is an intermediate phase in which molecules are present in the DP as well as in the COP configuration. For a full conversion into the COP it seems neccessary to deposit a multilayer amount and desorb everything but the first layer. However, we note that the coverage difference between PLP and COP is negligible if we compare the values of Table 4.11.

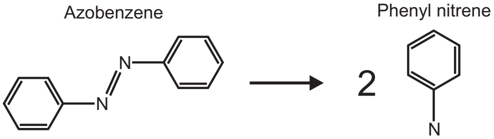

Figure 4.29: Reaktion scheme for the dissociation of azobenzene into two phenyl nitrenes.

Most probably a full COP monolayer would yield a higher intensity than the PLP monolayer, but a part of the COP molecules have been desorbed during the annealing step for the multilayer desorption.

This describes the general phase changes observed for azobenzene on Cu(111), but it does not yet explain the details of the N1s spectra observed for the COP and PLP. Naturally, we can expect the DP molecules to stay as they are characterized in sec. 4.6.2 with an overall *trans* adsorption geometry besides some small tilts. In addition, we have to consider a second species which shows a strong deviation of 1.5 eV in the N1s binding energy. This is unlikely to result from an azobenzene molecule, because a small geometrical change should not lead to such a large shift in binding energy, and a possible decoupling from the surface should actually lead to a shift towards the multilayer value and therefore to higher binding energy, whereas we observe the opposite. Thus we see a nitrogen which is interacting stronger with the surface. This is in line with the lowered adsorption height of less than 1.2 Å, which is in good agreement to the predicted height for a 3-fold coordinated nitrogen adsorbed on Cu(111) [95]. However, such a close distance between the N and Cu atoms brings up the question how the phenyl rings actually behave. Because we have already concluded from their upwards bending in the DP that they oppose a repulsive interaction at a distance of 2.36 ± 0.02 Å, it is hard to imagine that the full molecule adsorbs at low height. Instead, a major geometrical change must be expected here. Two possibilities come to mind. One could think about a change to a *cis* azobenzene adsorption shape to allow the nitrogen to get closer to the surface while the phenyl rings do not get into a repulsive regime. A second possibility to achieve this would be the dissociation of the molecule by breaking the double-bond between the nitrogens and splitting azobenzene into two phenyl nitrene molecules (C_6H_5N), which is depicted in the reaction scheme in Fig. 4.29. Such a coverage dependent dissociation process along with a (small) shift of the N1s line towards lower binding energy has already been reported for the adsorption of azobenzene on TiO_2, based on STM, LEED, XPS and ARPES experiments [12, 86]. This would allow as well a short N-Cu distance in an adsorption geometry with the phenyl ring

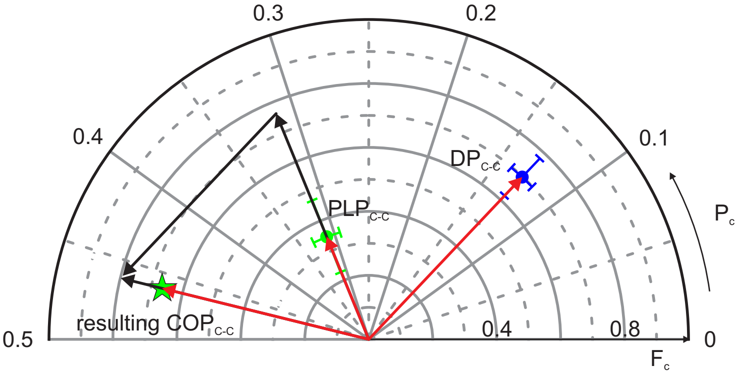

Figure 4.30: Argand diagram depicting the vector sum to subtract the DP contribution from the PLP results following eq. (4.10). The green dot represents the C1s C-C result from the PLP, the blue dot the C1s C-C result from the DP. Assuming that the PLP is a sum of the COP C-C and the DP C-C results, we can extract the COP value by subtracting the DP from the PLP (see sec. 2.4 for details). The resulting contribution is marked by the green star, representing the C1s result for the COP molecules in the PLP. The red arrows represent the vectors corresponding to the various C-C results, while the black arrows are weighted correctly for the relative abundance of COP and DP molecules in the PLP.

pointing towards the vacuum. Already the N-Cu bond in the DP azobenzene might weaken the N=N double bond and therefore allow it to break up as the coverage increases and the necessity for a closer packing arises. The latter interpretation of the two possibilities is indeed more probable, because in DFT calculations a *cis* state azobenzene is not stable on Cu(111) [92] and from the XSW experiments an upright standing phenyl ring is found as discussed below. Furthermore, the formation of a commensurate structure as it is observed by LEED favours the interpretation of dissociating molecules because such a structure can be formed more easily by the smaller phenyl nitrene, allows each nitrogen an ideal hollow adsorption site and can fulfill the glide symmetry requirements.

Before proposing a detailed structure for the PLP and the COP, we have to look at the position of the phenyl ring in these phases. Unfortunately, we only have clear data for the C-C carbons, and therefore we will limit this analysis to this easier discriminated species. Furthermore, we face the problem that we have DP and COP molecules mixed in the PLP, but unlike the N1s signal the C1s lines are not separated. However, we make use of the DP results to subtract the DP contributions from the PLP results. In Fig. 4.30 the subtraction of the DP part from the PLP results is depicted in the Argand diagram as explained earlier (see sec. 2.4). From the area of the N1s peaks we know that there is 1.2 times the amount of COP

	$d_{\mathrm{Cu-N}}$ (Å)	$d_{\mathrm{Cu-CN}}$ (Å)	$d_{\mathrm{Cu-CC}}$ (Å)
XSW Experiment - COP	1.17(4)	-	4.25(4)
XSW Experiment - PLP	1.19(2)	-	4.25(4)
DFT + vdW$^{\mathrm{surf}}$ (6 × 4) [92]	1.21	2.59	4.28
DFT + vdW$^{\mathrm{surf}}$ (4 × 4)[92]	1.18	2.58	4.27

Table 4.15: Comparison of the structural parameters from the XSW experiment presented here and DFT calculations carried out by R. J. Maurer and K. Reuter from the TU München [92] using the DFT + vdW$^{\mathrm{surf}}$ method [51, 65]. Two structures are calculated, first a (6 × 4) unit cell with two phenyl nitrenes and second, a (4 × 4) unit cell with three phenyl nitrenes, as it is proposed in sec. 4.6.4 from LEED experiments. The experimental data for $d_{\mathrm{Cu-N}}$ is calculated from the correponding P_{c}, the value for $d_{\mathrm{Cu-CC}}$ results from the comparison to a structure simulation (see text) and is therefore identical for both phases.

molecules compared to DP ones, therefore, taking this relative abundance of the species into account, we have to calculate

$$\frac{1 + 1.2 \times \vec{\mathrm{PLP}}_{\mathrm{C-C}} - \vec{\mathrm{DP}}_{\mathrm{C-C}}}{1.2} = \vec{\mathrm{COP}}_{\mathrm{C-C}} \tag{4.10}$$

to extract the COP value. From the PLP values of $F_{\mathrm{c}} = 0.35 \pm 0.12$ and $P_{\mathrm{c}} = 0.31 \pm 0.02$ and the DP values of $F_{\mathrm{c}} = 0.70 \pm 0.08$ and $P_{\mathrm{c}} = 0.13 \pm 0.01$ we find a resulting F_{c} of 0.66 and a P_{c} of 0.46 for the COP molecules in the PLP.

If we calculate the ideal values for an upright standing phenyl nitrene, starting with the COP nitrogen height value of 1.17 ± 0.04 Å as done earlier (see sec. 4.4.3), the mean C-C carbon height is 4.25 Å and we find a corresponding calculated F_{c} of 0.53 and a P_{c} of 0.45. This is in good agreement with the above values of $F_{\mathrm{c}} = 0.66$ and a $P_{\mathrm{c}} = 0.46$ extracted from the PLP experiments. Therefore, the molecular orientation of the phenyl nitrene can be expected to be upright already in the PLP and furthermore, it also agrees with the P_{c} of 0.44 ± 0.02 and F_{c} of 0.61 ± 0.03 found for the COP carbon results. In Fig. 4.31 the model for the phenyl nitrene on the Cu surface is depicted with the upright pointing phenyl ring and a three fold coordinated adsorption site.

The adsorption heights derived here are again in very good agreement with state of the art DFT calculations including vdW forces and screening effects, by using the DFT + vdW$^{\mathrm{surf}}$ method [51, 65] as can be seen from Table 4.14. The computation was done for two phenyl nitrene molecules in a (6 × 4) unit cell and for the (4 × 4) structure with 3 molecules, which is concluded from LEED below. In both cases a 4-layer Cu slab is used [92].

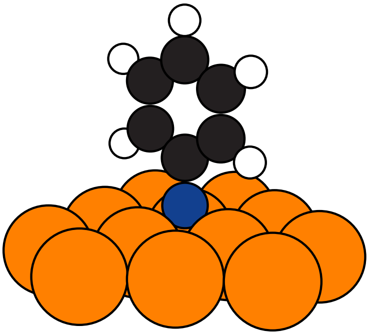

Figure 4.31: Model of the upright standing phenyl nitrene adsorbed on a 3-fold hollow site on the Cu(111) surface. Copper atoms are shown in orange, carbons in black, nitrogens in blue and hydrogens in white.

4.6.4 Ordered lateral structures

After the detailed investigation of the azobenzene adsorption we could extract two species, namely the intact azobenzene and the phenyl nitrene and their detailed adsorption geometries. Now we will use these molecules as building blocks for the lateral structure. Interestingly, the unit cell size of 81.6 Å^2 of the PLP fits very well to the space which is occupied by one *trans* azobenzene. Small deviations in the tilt angles compared to the detailed geometry of the DP would only have a minor effect on this. Therefore, the PLP looks like a condensation of azobenzene into an ordered structure driven by the additional molecules on the surface. This behaviour is reminiscent of the transition observed for phtalocyanine molecules where an ordered layer is formed above a certain coverage threshold, but already a short range order is present at lower coverages [63, 96]. In the case of azobenzene an enhanced background intensity in the LEED for the DP may be a hint for a short range order of the molecules, but only the increasing coverage forces the molecules into the ordered structure observed in the PLP. As the unit cell size fits the molecular size very well, a structure model with one azobenzene per unit cell is proposed as shown in Fig. 4.32. However, from XPS we know that there are phenyl nitrene molecules on the surface as well, which are not represented in the model. Due to the lateral dimensions of the unit cell it seems unlikely to have an additional molecule in this structure. Therefore, the phenyl nitrenes are expected to occupy space on the surface, but do not form an ordered structure yet. If it would be vice versa and the structure was formed by the phenyl nitrene while the azobenzene is disordered we would expect to find already the final commensurate phenyl nitrene structure observed in the COP. Since this is not the case, we infer that a suitable coverage and

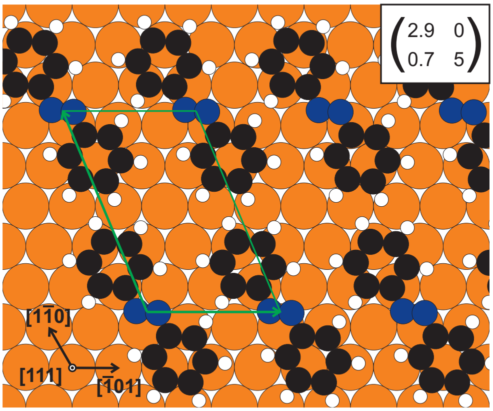

Figure 4.32: Adsorption model of the DP like molecules in the PLP as the phenyl nitrene is expected to be disordered. Green arrows indicate the superstructure unit cell according to the matrix shown at the top right corner. As the structure is not commensurate adsorption sites shown here are arbitrary. The copper surface atoms are depicted in orange, carbons in black, nitrogens in blue, and hydrogens in white.

especially annealing temperature is neccessary to form an ordered layer of phenyl nitrene.

In the COP with a commensurate unit cell with an area of 90.8 Å^2 which is therefore approximately 10 % larger than the PLP unit cell area, the COP species clearly dominates the XPS spectra. Hence, we expect the vast majority of the azobenzene molecules to be dissociated into phenyl nitrene. Together with the missing spots observed by LEED, which indicate two glide symmetry planes, the structure model proposed in Fig. 4.33 is developed. All molecules are placed as shown in Fig. 4.31 on threefold hollow sites, following the expectations for the nitrogen adsorption [95] and the measured height. The rotation of the molecule around the z-axis is chosen to fulfill the glide plane symmetry, with the symmetry planes marked by blue lines.

Remarkably the LEED structure of the COP is the same as for the MLP. Without knowledge about the growth mode of the MLP we cannot determine if the observed LEED pattern indeed stems from the multilayer or only from the interface. However, at least we know that this interface stays intact even upon adsorption of the multilayer. And if we assume a layer-by-layer growth and take into account the derived thickness of four layers, we should expect the multilayer to be ordered in the same way as the COP, because the LEED signal from the interface would be strongly damped by three molecular layers on top. Furthermore a strong diffuse background intensity would be expected in the LEED images due to the scattering on the disor-

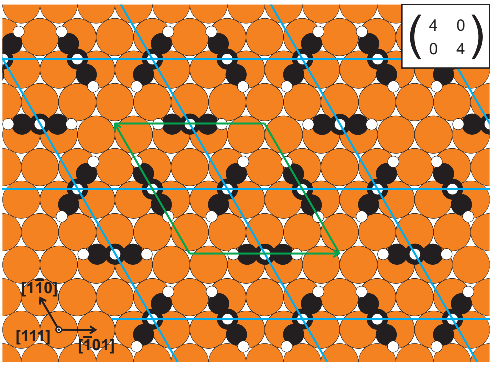

Figure 4.33: Adsorption model of the COP. The upright standing phenyl nitrene occupies 3-fold hollow sites as depicted in Fig. 4.31. The distribution and orientation of the molecules is chosen such that the super structure matrix shown in the top right corner is achieved and glide plane symmetry exists. The unit cell is marked by green arrows, the glide symmetry planes by blue lines.

dered layers, which is not observed. This forms the picture of the COP serving as a spacer group at the interface between the Cu surface and the azobenzene bulk crystal, because for higher layers one would not expect a dissociation of the molecule. In this sense, we can understand the MLP as a system of ordered molecular switches decoupled from the surface through the phenyl nitrene.

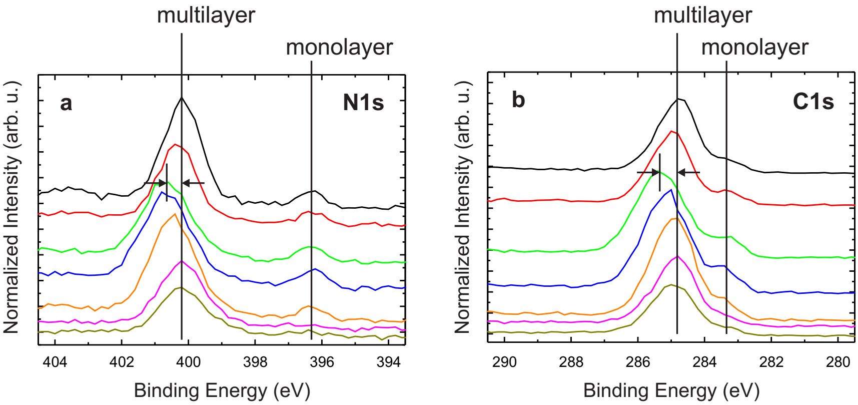

Figure 4.34: N1s(a) and C1s(b) XPS spectra from the MLP XSW measurement series. Spectra are taken at increasing photon energies from top to bottom and shifted on the y-scale for better visibility. While the first (black) and last (dark yellow) spectrum show the same position for all peaks a clear shift in binding energy of the multilayer peak is observed for the spectra in between, while the monolayer signature does not move. The intensity differences stem from the standing wave effect and the broadening of the final spectrum is expected to be a consequence of possible beam damage.

This raises the question if the multilayer azobenzene actually preserves its switching capability in this way due to the decoupling from the surface via the phenyl nitrene. Unfortunately, a final answer to this question is beyond the capabilities of the experiments conducted here, but we note an interesting behaviour from the MLP which may be a sign for possible switching. We observe a shift of the multilayer related peaks during the XSW measurement relative to the monolayer peak that is observed for the N1s ($\Delta E_\mathrm{B} = 0.4\,\mathrm{eV}$) and the C1s ($\Delta E_\mathrm{B} = 0.6\,\mathrm{eV}$) as can be seen in Fig. 4.34a and b respectively. We can exclude mistakes in the energy axis calibration or effects like charging, because the monolayer peaks in the same spectra show no shift. The idea that we face several XSW components which change in relative intensity and therefore make the envelope shift is appealing. However, in such a case one would expect to see a spectrum with similar intensities of the components and hence a much broader envelope at some point in the XSW scan. This is not observed, the width of the peak does not change significantly during the shift. Therefore, we speculate that the X-ray exposure may switch some molecules, which could result in a change of the chemical environment for the N and C atoms, hence, leading to a shift in the XPS, until the molecules relax into the original state. The monolayer is not affected, because it consists of phenyl nitrene instead of intact azobenzene. In general the switching capabilities in the multilayer can be expected as this has already been reported [97, 98]. Hence the azobenzene/Cu(111) system may be suitable to grow a switchable layer ontop of a buffer layer from the same molecular source.

4.7 Conclusion

The work presented on the azobenzene adsorption on Cu(111) could disentangle the structural properties of the adsorbed molecules in great detail. In the low coverage regime (DP) the molecules adsorb rather flat lying in *trans* confirmation with tilted phenyl rings. The adsorption height of only $2.02 \pm 0.02\,\text{Å}$ of the azobridge above the Cu surface indicates chemisorption.

The picture changes by the deposition of additional molecules, as a coverage dependent dissociation is observed which goes alongside with the formation of laterally ordered structures of the intact azobenzene molecules. As long as azobenzene stays intact, the molecular conformation seems to be the same as for the low coverage case. However, upon break up of the azobridge two phenyl nitrenes emerge from each azobenzene which adsorb with the N even closer to the Cu at $1.17 \pm 0.04\,\text{Å}$

Surface	Structure		$d_{\mathrm{M-N}} - r_{\mathrm{M}}^{\mathrm{vdW}}$	ω (deg)	β (deg)
Cu(111)	DP ($T = 60\,\mathrm{K}$)	XSW	0.62(2) Å	18.8	3.8
	(6×4) ($T = 0\,\mathrm{K}$)	vdW$^{\mathrm{surf}}$ [92]	0.63 Å	11.0	3.3
Ag(111)	(6×7) ($T = 0\,\mathrm{K}$)	vdW$^{\mathrm{surf}}$[59]	0.89 Å	4.5	-2.0
	(2×5) ($T = 0\,\mathrm{K}$)	vdW$^{\mathrm{surf}}$ [59]	1.09 Å	11.7	15.4
	(2×5) ($T = 210\,\mathrm{K}$)	vdW$^{\mathrm{surf}}$ [59]	1.26 Å	9.0	17.7
	(2×5) ($T = 210\,\mathrm{K}$)	XSW [59]	1.25(5) Å	-0.7(23)	17.7(27)

Table 4.16: Compilation of azobenzene adsorption data for Cu(111) and Ag(111)[59] from XSW experiments and DFT + vdW$^{\mathrm{surf}}$ [51, 65] calculations [92]. To allow the comparison of the adsorption height of the nitrogen $d_{\mathrm{M-N}}$ values, where M is Cu or Ag, the table shows the adsorption height after subtraction of the corresponding substrate vdW radii ($r_{\mathrm{Cu}}^{\mathrm{vdW}} = 1.4$, $r_{\mathrm{Ag}}^{\mathrm{vdW}} = 1.72$ [56]). The angles ω and β are the dihedral angles (CNNC) and (NNCC), respectively.

and the phenyl ring pointing towards the vacuum. Due to the strong molecule-surface interaction the adsorption site becomes very important and a commensurate superstructure of phenyl nitrene is observed.

If the experimental data is compared to DFT + vdW$^{\mathrm{surf}}$ [51, 65] calculations, a very good agreement is observed [92]. Together with experimental and theoretical results for the azobenzene adsorption on Ag(111)[59] the observed dissociation process can be understood as a consequence of the interplay between phenyl ring twist and the strong N-Cu bond. For ease of access a compilation of the results obtained in this work and by Mercurio *et al.* for azobenzene/Ag(111) [59] is given in Table 4.16.

Upon inspection of the Ag data two trends are obvious. First, the distortion of the molecule increases with increasing coverage ($(6 \times 7) \Rightarrow (2 \times 5)$) and second, the molecule is lifted from the surface. Although a *cis* configuration is not reached for azobenzene/Ag(111), the distortion and the lifting up of the molecule can be understood as incomplete transformation. The driving force behind the phase changes is the increasing adsorption energy per surface area which is over-compensating the energy loss of the single molecule. However, if we compare this with the situation for azobenzene/Cu(111) we find two crucial differences. First, on Cu(111) the isolated molecule adsorbs at a much lower distance to the surface, and second, it is already more bent in the low coverage regime (especially ω). Assuming that azobenzene/Cu(111) would follow the same behaviour as it was found for azobenzene/Ag(111), an increase in the coverage should lead to an enhanced distortion and subsequently to an elongation of the N-Cu bond.

In Fig. 4.35 the difference in the behaviour of azobenezene/Ag(111) and azoben-

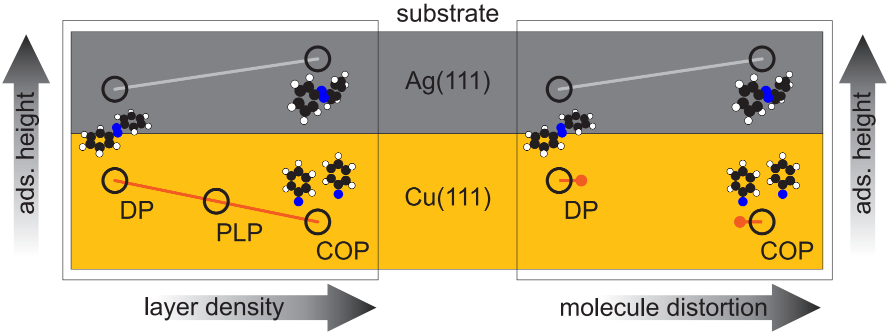

Figure 4.35: Scheme for the azobenzene adsorption height as a function of the molecule distortion and the layer density. In the grey area the behaviour of azobenzene/Ag(111) is depicted. From calculations for azobenzene/Ag(111) [59] it is known that a coverage increase leads to a tilt of the molecules, because the adsorption energy per surface area is enhanced by a denser packing. Along with the tilt (and the increasing layer density), the molecule is lifted from the surface. In the orange area the behaviour of azobenzene/Cu(111) is depicted. Due to the much stronger N-Cu bond the molecule can not lift up from the surface and hence a continuous molecule distorsion cannot be realized. An increasing density therefore leads to a dissociation at the N=N bond into phenyl nitrene following the reaction depicted in Fig. 4.29. In contrast to azobenzene/Ag(111) the continuous change in adsorption height for the increasing layer density for azobenzene/Cu(111) is realized by a change in the abundance of two species rather than in a continuous change on all molecules.

zene/Cu(111) is depicted. With an increasing layer density the molecule distortion increases for azobenzene/Ag(111), linked to the neccessary continuous increase in the adsorption height. In the azobenzene/Cu(111) case this adsorption height increase is hindered by the stiffness of the strong N-Cu bond. Hence, a continuous molecular distorsion is suppressed, because there is not enough space for the phenyl rings to twist. However, the increase in the layer density forces a reduction of the molecular footprint and therefore the azobenzene molecules dissociate. The change in the adsorption height upon an increasing layer density is therefore understood as a change in the relative abundance of intact and dissociated azobenzene from the DP where all molecules are intact through the intermediate state of coexistence in the PLP to the COP where all azobenzene is dissociated into phenyl nitrene.

A similar behaviour is reported for the adsorption of azobenzene/TiO_2, where LEED and STM experiments show an intact adsorption of azobenzene for low coverages and a dissociation upon coverage increase [12]. ARPES experiments confirmed that the species after dissociation is most probably phenyl nitrene and even show that the intact azobenzene could be dissociated due to the exposure to synchrotron radiation with a photon energy of 40 eV to 50 eV [86]. It is unclear if the irradiation directly cleaves the azobenzene or first introduces a conformational change that leads to the dissociation in a next step. If the latter would be true, it supports the reaction path for of the azobenzene/Cu(111) proposed above. This allows us to draw the general conclusion that the bond strength of the N-substrate bond is decisive for the dissociation behaviour of azobenzene. If this bond is flexible enough to allow the molecule to distort, no dissociation will take place. But if the bond is too stiff, an increase in coverage will lead to a break of the azo-bridge. Most probably the dissociation can be supported by the exposure to light as well, because a *trans* to *cis* transformation should introduce additional distortion and this may be a way to produce fully converted phenyl nitrene layers with no residual intact azobenzene molecules.

From the multilayer results we know that on top of this phenyl nitrene layer more azobenzene can be adsorbed and it looks like it follows the order of the buffer layer. One could speculate that azobenzene of the second layer can be organized in an ordered structure this way, while preserving its switching functionality due to the decoupling from the surface by the phenyl nitrene buffer layer. This last idea is already very speculative, because future experiments on the phase diagram, the growth and the switching have to be carried out.

The results presented here pave the way for a better understanding of the azobenzene/Cu interface and serve to point out the future possibilities of this system. In general they help to understand coverage dependent dissociation processes and the reason why a weak substrate coupling is a prerequisite for molecular switches to preserve their unique switching capabilities upon adsorption.

5 Geometric and electronic structure of PTCDA on low index Ag surfaces

5.1 Introduction: An attempt of a comprehensive view

The performance of organic optoelectronic devices such as solar cells and light emitting diodes is significantly influenced by the properties of interfaces between different materials in these devices [3]. Therefore a general understanding of the processes on metal-organic interfaces is crucial for the design of high performing future organic electronic devices.

A model molecule with an extended aromatic backbone and additional functional groups for the study of metal-organic interfaces, which is already very well understood in terms of structural and electronic properties, is 3,4,9,10-perylenetetracarboxylic acid dianhydride (PTCDA, see Fig. 5.1). An intense research during the last two decades revealed the properties of a wide variety of PTCDA/metal interfaces as well as PTCDA bulk and gas phase properties [6]. This enables the theoreticians to benchmark their calculations with a wealth of data and it allows experimentalists to focus on the subtle details which nevertheless contain crucial information to test present understandings and models of the behaviour of metal/organic interfaces. In this context we have chosen to investigate PTCDA on silver surfaces in the monolayer regime. Since this is an experimentalist's work, the following chapter focuses on the detailed understanding of the adsorption process by adding new experimental results where neccessary and using already available information where it is possible, with the goal to present a comprehensive view and stress the general mechanisms deduced from the PTCDA/Ag adsorption.

First we will discuss the various adsorption geometries which can be found for PTCDA/Ag. Different lateral arrangements exist depending on the substrate orientation and the preparation process of the organic layer. Most of the information about the lateral structure is already known and published from former research. However, we will correct some erroneous structure models in the literature in the context of LEED experiments on PTCDA/Ag(110) and we will complete the picture for PTCDA/Ag(100) by the determination of the adsorption site employing NIXSW.

Regarding the vertical structure, i.e. adsorption heights of PTCDA/Ag monolayers, for some time the only data available pertained to PTCDA/Ag(111) [60], but recently the geometry for PTCDA/Ag(110) was reported as well [39]. With a NIXSW study of the vertical adsorption geometry of PTCDA/Ag(100) the missing part for a comparison of the behaviour of PTCDA on low index silver surfaces will be presented. This study is done in collaboration with the group of Prof. Moritz Sokolowski (Rheinische Friedrich-Wilhelms-Universität Bonn) and especially Oliver Bauer. Some results of this collaboration have already been published [99].

The second part of this chapter focuses on the electronic properties of the interfaces. In particular, the frontier molecular orbitals of the interface systems are investigated by means of ARPES. The knowledge about the different geometric structures allows to identify the role of molecule-molecule versus molecule-substrate interactions. General rules for the energy level alignment of PTCDA/Ag are revealed and the role of the work function as the connecting property between the vertical geometry and the electronic structure is discussed. These investigations were done in collaboration with the groups of Prof. Mike Ramsey, Dr. Georg Koller and Prof. Peter Puschnig (Karl Franzens Universität Graz). Results of this collaboration have already been published [27]. The reprint of this previously published material is permitted under the Creative Commons Attribution 3.0 Unported (CC-BY) license according to the New Journal of Physics copyright statement.

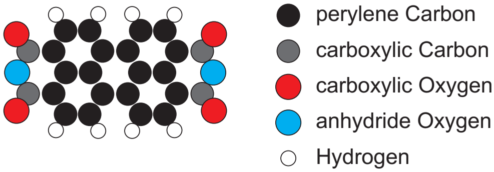

Figure 5.1: Top view of the PTCDA molecule. Carbon atoms are displayed in grey (carboxylic carbon) and black (perylene carbon), hydrogen atoms in white, and the two types of oxygen atoms in red (carboxylic oxygen) and blue (anhydride oxygen).

5.2 Lateral structures of PTCDA on Ag(111) and Ag(100)

The most intensively studied system among the PTCDA/Ag combinations is PTCDA on Ag(111) [6]. Upon adsorption at room temperature the molecules form a *herringbone* (HB) monolayer structure with two molecules per unit cell. The superstructure matrix as well as the adsorption sites and the detailed molecular orientations within the unit cell are known from STM and LEED measurements and depicted in Fig. 5.2a [54, 100, 101]. As the two molecules within the unit cell are inequivalent, the one with the long axis aligned along the $[10\bar{1}]$ direction of the Ag substrate is commonly referred to as molecule A and the other one as molecule B. Molecule B is rotated by 17° against the $[0\bar{1}1]$ direction of the Ag rows [101]. Due to the substrate symmetry of the (111) surface and the unit cell geometry one finds six differently oriented domains of the HB monolayer on a real PTCDA/Ag(111) sample. This is important for the analysis of molecular orientation dependent data, in particular to apply the orbital tomography approach presented in sec. 2.3.

The PTCDA/Ag(100) monolayer also has two molecules per unit cell. They form a commensurate T-shape arrangement and in contrast to PTCDA/Ag(111) they are equivalent regarding their molecular environment and adsorption site, because the long axis of the molecules are aligned along the [001] or [010] substrate directions respectively, which are equivalent for the (100) surface. The superstructure unit cell and the molecular orientation is known from STM and LEED experiments [102] but the adsorption site proposed in the structure model of PTCDA/Ag(100) (see Fig. 5.2b) was not yet proven experimentally. This gap is closed by our NIXSW study which allows the determination of the on-top adsorption site as discussed later in this chapter (see sec. 5.4.6).

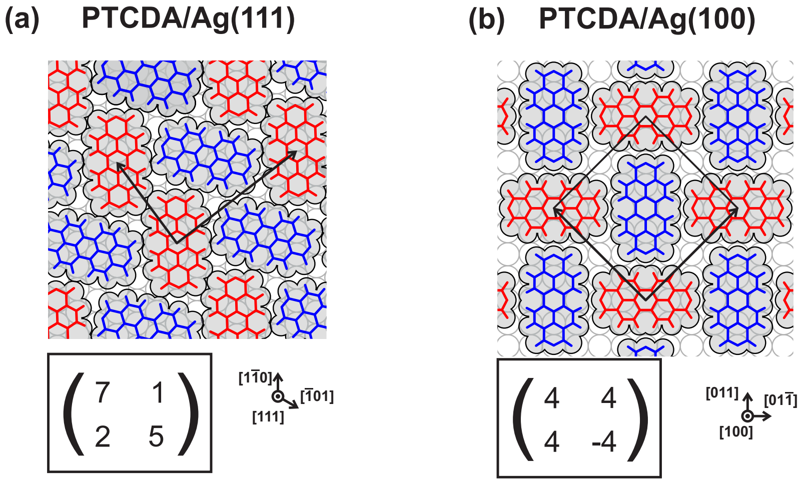

Figure 5.2: Structure models of the (a) HB monolayer of PTCDA/Ag(111) and (b) monolayer of PTCDA/Ag(100) with the corresponding superstructure matrices. Black arrows in the structure models indicate the real space unit cell. The two differently oriented molecules in the HB phase unit cells are marked as A(red) and B(blue). For the monolayer of PTCDA/Ag(100) red and blue molecules are equivalent.

5.3 Lateral structures of PTCDA/Ag(110)

In the case of PTCDA/Ag(110) two different monolayer structures can be formed depending on the preparation process. Upon adsorption on Ag(110) at room temperature, PTCDA molecules form islands by arranging in the *brickwall* (BW) structure until the surface is completely covered [54, 103, 104]. It consists of parallel oriented molecules aligned with their long axes along the [001] direction of Ag(110) (fig. 5.3a,b) and is well studied by means of LEED [54, 103], STM [54, 103–105], NIXSW [39], UPS [25, 26, 28, 106–108] and orbital tomography [8].

When depositing additional molecules on the BW monolayer, a new pattern appears in LEED, in coexistence with the BW monolayer pattern (see Fig. 5.3c). Seidel *et al.* [109] identified the correct superstructure matrix of this structure from LEED measurements, but they erroneously assigned this superstructure to a new monolayer structure. However, it was shown recently that the new LEED pattern shown in Fig. 5.3c is the signature of a HB layer formed on top of the BW monolayer, i.e. it belongs to a bilayer structure [26]. This interpretation is in agreement with earlier STM results [105]. Figures 5.3c,d show a LEED image of the HB-on-BW bilayer, together with the superstructure matrix found in ref. [109] and the corresponding structural model of the upper layer.

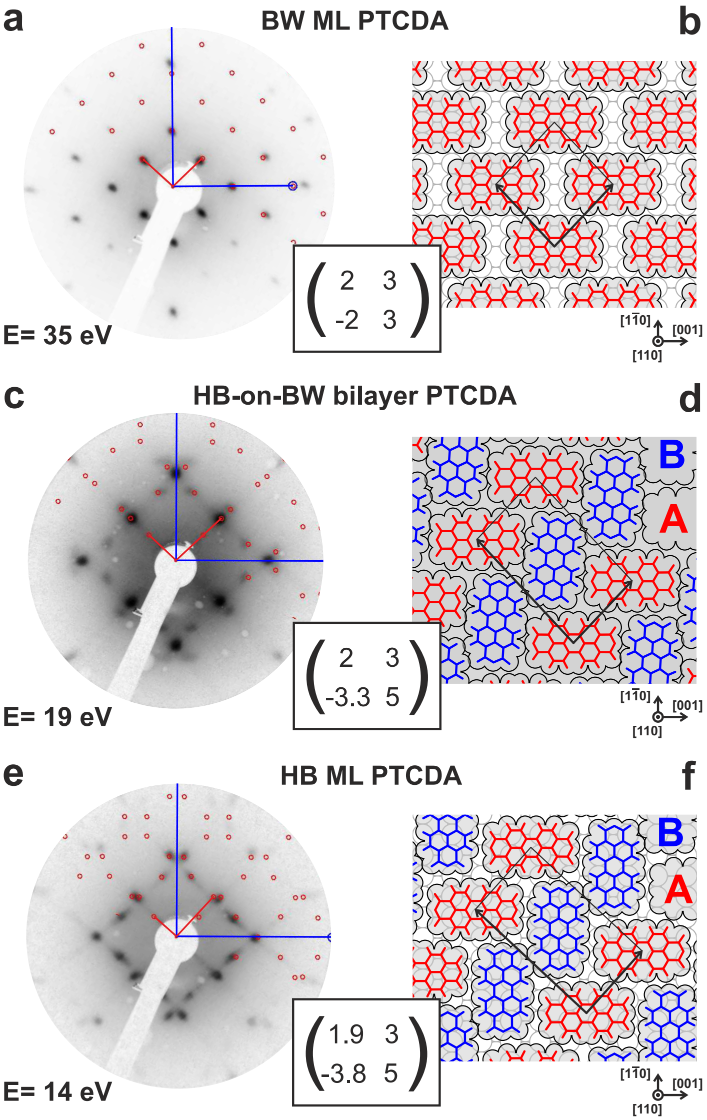
a
BW ML PTCDA
b
E= 35 eV
2 3
-2 3
[1$\bar{1}$0]
[001]
[110]
c
HB-on-BW bilayer PTCDA
d
B
A
E= 19 eV
2 3
-3.3 5
[1$\bar{1}$0]
[001]
[110]
e
HB ML PTCDA
f
B
A
E= 14 eV
1.9 3
-3.8 5
[1$\bar{1}$0]
[001]
[110]

Figure 5.3: LEED patterns and structure models of the PTCDA/Ag(110) interface with their corresponding superstructure matrices. (a-b) brickwall (BW) monolayer, (c-d) herringbone on brickwall (HB-on-BW) bilayer, (e-f) herringbone (HB) monolayer (compressed monolayer). One half of each LEED pattern is overlayed by a pattern of calculated spot positions. Blue lines in the LEED image indicate the substrate directions, red lines indicate the reciprocal space unit cell. Black arrows in the structure models indicate the real space unit cell. The two differently oriented molecules in the HB phase unit cells are marked as A(red) and B(blue). The LEED pictures were recorded with a multi channel plate LEED by K. Schönauer. The picture has already been published [27] and the reprint of this is permitted under the Creative Commons Attribution 3.0 Unported (CC-BY) license according to the New Journal of Physics copyright statement.

If the HB-on-BW bilayer or an even thicker film of PTCDA/Ag(110) is annealed to 550K, a HB monolayer is formed and excess molecules are desorbed [109]. We note here that the authors of ref. [26] have incorrectly identified the LEED image of Fig. 5.3c with the LEED image of the HB *mono*layer which is displayed in Fig. 5.3e. However, there are obvious differences between the two images: While the diffraction pattern of the bilayer has a fourfold rotational symmetry, the HB monolayer exhibits twofold symmetry only.

Since this HB monolayer is denser than the BW monolayer, it is often refered to as the ‘compressed monolayer’. The authors of ref. [109] have given an incorrect superstructure matrix for this phase, because the silver substrate directions were confounded. (Because of the fourfold symmetry of its LEED pattern (see Fig. 5.3c) the incorrect assignment of substrate crystal directions does not effect the indexing of the bilayer spots.) We note that the LEED result which is reported in ref. [106] to represent a picture of the BW phase is showing the bilayer structure instead. The correct matrix for the compressed monolayer was given by Wießner *et al.* [26]. Figures 5.3e,f display the LEED pattern, the superstructure matrix and the structure model of the HB monolayer.

STM experiments revealed that the HB monolayer consists of two molecules per unit cell, one (molecule A) oriented along the [100] direction (same orientation as the molecules in the BW phase) and the other (molecule B) along the $[1\bar{1}0]$ direction as shown in figure 5.3e,f [109]. We note here that molecules A and B are distinguishable, not only because of their different orientation with respect to the substrate, but also because of their different positions relative to their neighbours. This is a consequence of the non-orthogonality of the two superstructure unit cell vectors with $\alpha = 91.1°$.

5.4 Vertical structure of PTCDA/Ag(100)

5.4.1 Introduction

The vertical structure, i.e. the adsorption height of organic adsorbates yields an important parameter to derive the bonding strength and to investigate the bonding mechanism. For PTCDA the vertical adsorption structure was already determined for PTCDA/Au(111), PTCDA/Cu(111), PTCDA/Ag(111) and PTCDA/Ag(110) [39, 60, 61, 110]. Throughout this section we will present experimental details and

Parameter	XSW data set acquisition		Off-Bragg XPS	
	O1s	C1s	O1s	C1s
ΔE_{photon}	4.05 eV	4.05 eV		
E_{photon}			3024 eV	3024 eV
# of XPS spectra	28	28		
repeats	1	1	15	15
pass energy	100 eV	100 eV	100 eV	100 eV
ΔE_{kin}	0.2 eV	0.2 eV	0.1 eV	0.1 eV
dwell time	1.0 s	0.8 s	1.0 s	0.5 s

Table 5.1: Acquisition parameters used for the XSW data sets and off-Bragg XPS spectra. The parameters for the O1s XSW data sets are used for both Bragg-reflections measured in the experiment.

results from our NIXSW study of PTCDA/Ag(100). After a coverage analysis of the investigated samples the NIXSW results for the carbon and oxygen species will be discussed leading to a detailed adsorption picture. Furthermore, the adsorption site is determined by means of XSW. The experiments were performed in collaboration with the group of Prof. Moritz Sokolowski (Rheinische Friedrich-Wilhelms-Universität Bonn) and especially Oliver Bauer. Results of this collaboration have already been published [99].

5.4.2 Experimental details

Similar to the XSW experiments presented in the previous chapters, all measurements were done at the ESRF Grenoble synchrotron at beamline ID32 using the UHV vessel described in sec. 2.5.2. The Ag(100) single crystal was cleaned by repeated cycles of sputtering with Ar^+ ions and subsequent annealing at 1000 K. The cleanliness of the sample was validated by monitoring the C1s photoemission signal with XPS and the surface structure was checked with LEED. PTCDA was evaporated from a home-made Knudsen cell at 400 K onto the sample at room temperature. The structure of the molecular layer (see sec. 5.2) was verified by LEED. All XSW measurements were conducted at room temperature.

As the intensity of the (100) reflection is zero due to destructive interference of incoming and reflected wave for this Bragg condition, the XSW experiments were performed with the (200) reflection. The Bragg condition for the (200) reflection is expected for a photon energy of 3037 eV for normal incidence and was indeed observed for a photon energy of $E_{\text{photon}} = 3036\,\text{eV}$ in the experiment. The Bragg spacing for this reflex is $d_{200}^{\text{Bragg}} = 2.04\,\text{Å}$. In addition the (111) reflex with a Bragg spacing of $d_{111}^{\text{Bragg}} = 2.36\,\text{Å}$ and a Bragg energy of 2630 eV was used for triangulation to obtain the lateral PTCDA adsorption site (see sec. 5.4.6). The corresponding off-Bragg XPS spectra were taken at $E_{\text{photon}} = 3024\,\text{eV}$ and $E_{\text{photon}} = 2615\,\text{eV}$, respectively. The experimental parameters for the XPS and XSW data sets are given in Table 5.1.

5.4.3 Coverage estimation

The PTCDA/Ag(100) structure was prepared twice with different coverages to avoid coverage dependent errors of the height determination and to ensure that we measure in the submonolayer regime. Both preparations show the correct LEED pattern, as can be seen in Fig. 5.4b and c. However, it is ovious already from the LEED intensity that the coverage of the second deposition (black) is less. To achieve a more quantitative coverage estimation, the layers were measured by off-Bragg XPS to compare the C1s intensities of both preparations. As the intensity is not only dependent on the number of carbon atoms but also on other experimental conditions such as the photon flux and the sample position, we need to normalize the data. This is done by dividing the full spectrum by the Ag background signal. The assumptions behind this step are (1) that all experimental conditions influence the Ag background in the same way as the C1s signal and (2) that the damping of the Ag background by the molecular layer is negligible. If these assumptions are fullfilled, the ratio of C1s to the Ag background is only dependent on the concentration of carbon atoms. While damping can only be neglected if we are indeed in the submonolayer coverage regime, it can only lead to an overestimation of the coverage and therefore the qualitative result of a submonolayer coverage would still be valid independent of the error introduced here.

Technically we devide the spectrum by

$$S_{\text{norm}} = S_{\text{raw}}/B \cdot 1000 \tag{5.1}$$

where S_{norm} is the normalized spectrum, S_{raw} is the raw data and B is the mean value of the C1s spectrum in the binding energy range of 277 eV to 278 eV. The resulting spectra are depicted in Fig. 5.4 for the first (red) and second (black) deposition after background subtraction. It is immediately clear that the second preparation yields a much lower coverage. The area under the curves adds to 5028 arb. units for the

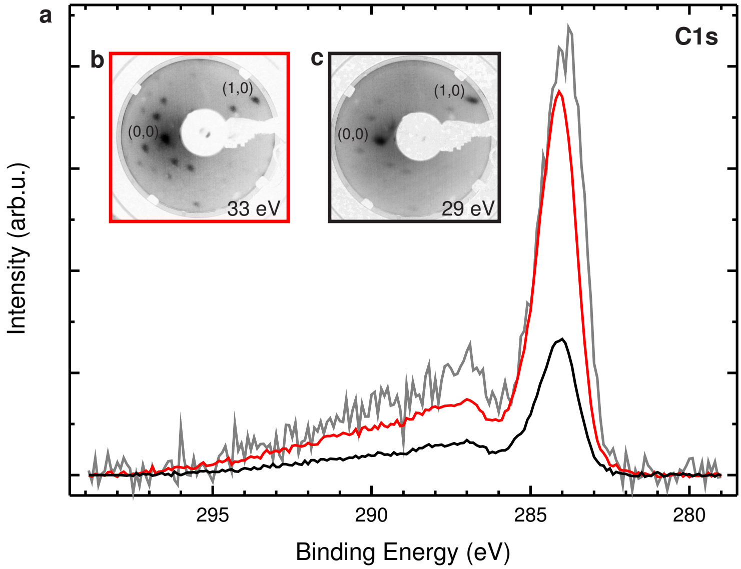

Figure 5.4: Off Bragg XPS spectra of preparation 1 (red, 0.8 ML), preparation 2 (black, 0.3 ML) and a reference spectrum (grey). The red and black spectra are recorded with $E_{\mathrm{photon}} = 3024\,\mathrm{eV}$ on PTCDA/Ag(100) submonolayer films. The grey spectrum is taken at $E_{\mathrm{photon}} = 2633\,\mathrm{eV}$ on a PTCDA/Ag(111) closed monolayer [53] and used as a reference for the absolute coverage estimation. All spectra are normalized (see text) and a Shirley background was subtracted. The spectra are not corrected for the different unit cell sizes of PTCDA/Ag(100) and PTCDA/Ag(111)

first and 1917 arb. units for the second preparation resulting in a 2.6 times higher coverage from the first deposition.

To evaluate an absolute coverage value the data is compared to a C1s spectrum of PTCDA/Ag(111) measured at the same setup [53]. For PTCDA/Ag(111) a closed monolayer can be reproducibly prepared by desorption of multilayers [54] and therefore such data can be taken as reference for a known coverage. Although an error might be introduced by the different photon energy of $E_{\mathrm{photon}} = 2633\,\mathrm{eV}$ used for the PTCDA/Ag(111) data, it is the only absolute coverage calibration available. The spectrum was treated the same way as the PTCDA/Ag(100) spectra regarding normalization and background subtraction and the resulting graph is depicted in Fig. 5.4 in grey. The area under the curve is 6698 arb. units, however one has to correct for the different carbon densities due to the different lateral structures (see sec. 5.2). Both unit cells contain two molecules but the size of the PTCDA/Ag(111) unit cell is $239\,\text{Å}^2$ [54] while the PTCDA/Ag(100) unit cell occupies $267\,\text{Å}^2$ [102]. Therefore

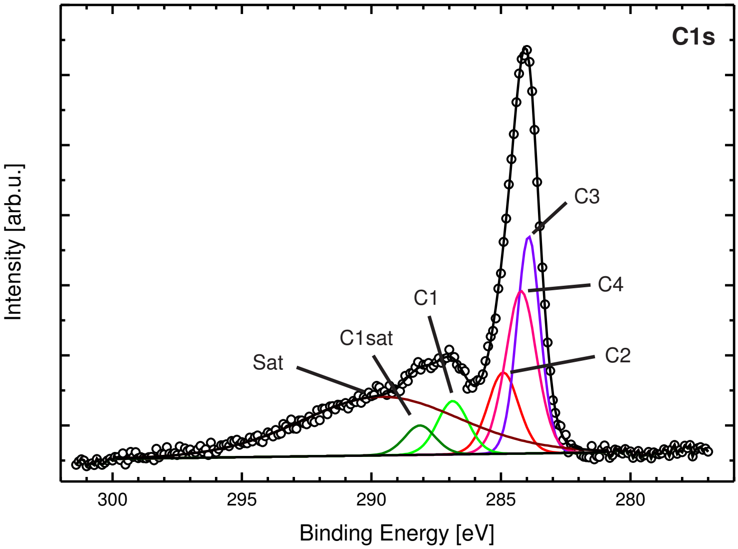

Figure 5.5: Off Bragg XPS spectrum at $E_{\text{photon}} = 3024\,\text{eV}$ of the C1s region for PTCDA/Ag(100). The spectrum is used to develop the fitting model used in the XSW analysis. Peak position, FWHM and relative area are given in tab 5.2

we would expect an integrated signal of 6698 arb. units$\times\frac{239\,\text{Å}^2}{267\,\text{Å}^2} = 5996$ arb. units for a full monolayer of PTCDA/Ag(100). The absolute coverage of preparations one and two is therefore 0.8 ML and 0.3 ML respectively. We clearly fullfill the prerequisite of a submonolayer coverage for our XSW experiment in both preparations and can now turn to the evaluation of the XSW data.

5.4.4 PTCDA/Ag(100) - C1s results

The goal of this section is to extract the adsorption height of the carbon atoms of PTCDA above the Ag(100) surface. For the simplest approach one would measure the C1s contribution and use the full intensity for the standing wave analysis as described in sec. 3.2. However, it was shown in previous work that it is possible to utilize the chemical sensitivity of the XPS to distinguish different carbon species within a molecule (see sec. 4.2) and in particular PTCDA [39] in the XSW analysis. Therefore we need to develop a dedicated fitting model for the C1s signal before we can enter the XSW analysis.

	Peak					
	C2	C3	C4	C1	C1sat	Sat
Binding energy [eV]	284.9*	283.9	284.2*	286.9	288.1	289.6
FWHM [eV]	1.4	1.1	1.4*	1.4*	1.4	7.3
relative Area [%]	10.3	20.6	20.6	6.8	3.7	38.2

Table 5.2: C1s model components for the XSW analysis. The model is derived from the off-Bragg XPS spectrum shown in Fig. 5.5. Constrained values are indicated by an asterisk. For detailed information on the model see text.

C1s XPS model To derive such a model for the XSW analysis of the carbon data we measured an off-Bragg spectrum of the C1s core level line ($E_{\mathrm{photon}} = 3024\,\mathrm{eV}$) with higher statistics than the XSW spectra. The resulting XPS spectrum is depicted in Fig. 5.5. We can clearly distinguish three different contributions in this spectrum: (1) a strong peak around $E_{\mathrm{B}} = 284\,\mathrm{eV}$, (2) a weaker double feature around $E_{\mathrm{B}} = 287\,\mathrm{eV}$ and (3) a tail towards higher binding energies. To fit the spectrum we follow the models proposed by Schöll *et al.* for PTCDA/Ag(111) multilayers [111] and Mercurio *et al.* for PTCDA/Ag(110) [39]. Therefore, we introduce three components to fit the main peak. These components represent the chemically different carbons of the perylene backbone of PTCDA, namely carbons binding to the carboxyl endgroups (C-COO, named C2), binding only to other carbons (C-C, named C3) and binding to hydrogens (C-H, named C4). Unfortunately, the resolution of our XPS spectrum is by far not good enough to distinguish these different carbon species, but nevertheless we use three components to model the main C1s feature. However, their intensity ratio is constrained such that it fits to the stoichiometric ratio of the PTCDA molecule. Specifically the intensity (I_n) constraints are $2I_{\mathrm{C2}} = I_{\mathrm{C3}} = I_{\mathrm{C4}}$. Also for the XSW analysis these three components will be fixed regarding their intensity ratio and therefore yield only one average position for all carbon atoms of the perylene core. Furthermore, the full width at half maximum (FWHM) of the components C2 and C4 is constrained to be identical. We note, that different peak assignment schemes for the deconvolution of the C2, C3 and C4 component exist [112]. However, such details do not change our results, because the impact on the sum intensity is expected to be negligible.

However, the case of the carboxylic carbon (C-O) is different. Its intensity can be clearly distinguished from the perylene core signal and therefore allows for an independent height analysis of this species later on. To model the lineshape correctly, we are still following the XPS models for the PTCDA/Ag(111) multilayer [111] and the PTCDA/Ag(110) monolayer [39] and introduce a main line (named C1) and a satellite (named C1sat) for the carboxylic carbon. For the XSW analysis these lines' intensity ratios will be fixed, as their joint intensity is used to extract the heights of the caboxylic carbons. The only constraint used here is the FWHM of C1, which is fixed to the value of C2 and C4. Finally, the higher binding energy tail is considered to consist of satellites (named Sat) which we cannot deconvolute and therefore this intensity is not taken into account for our XSW analysis. To subtract the substrate contribution, a linear background is employed for the model. A good XPS model has to reflect the stoichiometry of the PTCDA molecule. As can be seen from Table 5.2 the 1:5 intensity ratio of carboxylic to perylene carbons is indeed fullfilled, proving our model to be a valid approach.

C1s XSW analysis In the next step we apply our XPS model to the XSW data sets. All FWHM and energy positions of the fitting components are fixed to the values from the XPS model. Furthermore, the relative intensities of the components C2, C3 and C4 are fixed, because we will address only their sum which is representing the signal from the perylene core. For C1 and C1sat the ratio is also fixed and their sum represents the signal from the carboxyl groups. To extract the mean value of the carbon height over the full molecule directly, we evaluate the sum of all components including Sat as well and compare the result to the analysis without a dedicated fitting model, but only a background subtraction. As long as the envelope of our XPS model fits the spectra well, the result of the sum of all components and the analysis without XPS model should be identical.

On the first preparation we took three, on the second four C1s XSW data sets. Electron yield profiles for the data set C1s005 are shown as an example in Fig. 5.7 to provide a proof for the quality of our data. All results are summed up in the Argand diagram in Fig. 5.6 and detailed values are given in Table 5.3. Taking a closer look at these results, one finds a difference between the two preparations which can be linked to the different coverages. The F_c of the second preparation is significantly smaller than for the first preparation in all cases. This is reasonable, as the relative influence of defects in the layer gets larger as the coverage becomes smaller, if we assume that molecules stick at defects first and may therefore tilt or adsorb at a different height. However, except for a small tendency for C1+C1sat, the P_c is not preparation dependent, showing that the mean adsorption height of the carbon does not depend on the coverage and the influence of the various defect sites can be assumed to cancel each other. For the adsorption of the perylene backbone, which we cannot differentiate further, we find a mean P_c of 0.39 ± 0.01 and therefore following eq. (2.25) and using $n = 1$ and $d_{200}^{\mathrm{Bragg}} = 2.04\,\mathrm{\AA}$ the adsorption

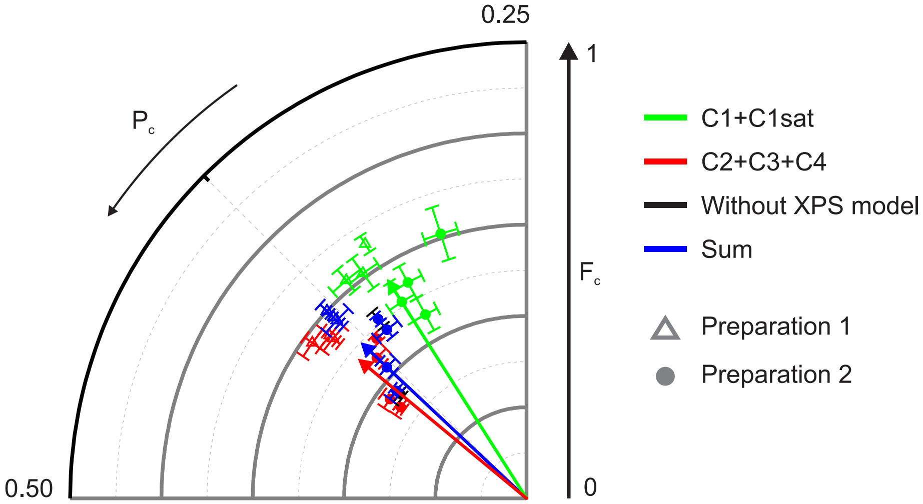

Figure 5.6: Argand diagrams visualizing the results of the XSW analysis for the C1s data. As indicated in the XPS model in Fig. 5.5 the sum for C1+C1Sat is depicted in green and the sum of C2+C3+C4 is depicted in red, the sum of all components in blue and the results without a XPS model in black. The latter is very difficult to see, because blue and black points fall on the same spot. The arrows indicate the mean values of the corresponding species. All values are shown in Table 5.3.

height is 2.84 ± 0.02 Å. The carboxyl carbons are slightly bent towards the substrate and yield a 0.11 Å lower adsorption height of 2.73 ± 0.04 Å. We will discuss the bending of the molecule together with the oxygen results later in this chapter (see sec. 5.4.8).

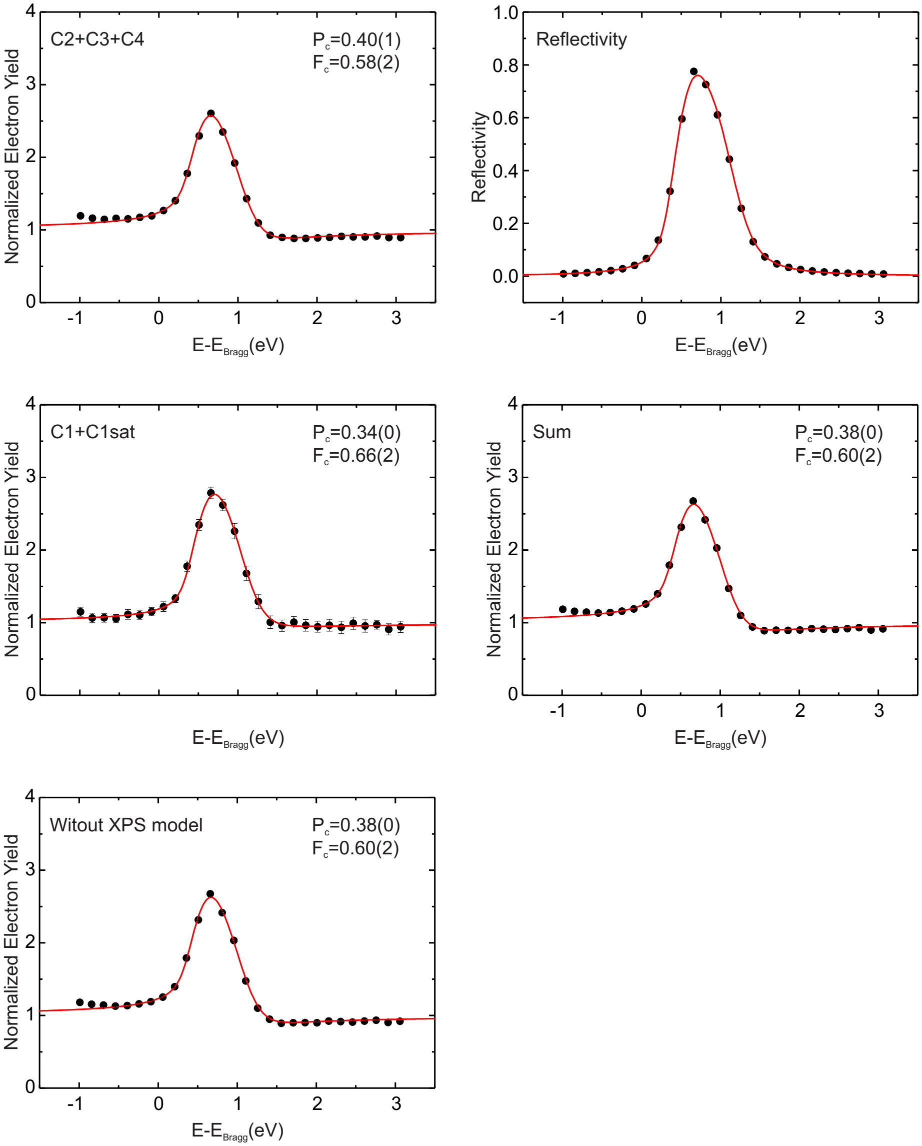

Figure 5.7: Representative electron yield curves of the C1s XSW analysis using the XPS model which is depicted in Fig. 5.5. The data belongs to data set C1s005. The results for all C1s data sets are shown in Table 5.3.

		preparation 1			preparation 2					
		C1s002	C1s005	C1s008	C1s011	C1s013	C1s015	C1s021	mean value	ads. height[Å]
C2+C3+C4	P_c	0.39(1)	0.40(1)	0.39(1)	0.37(0)	0.38(1)	0.40(1)	0.40(1)	0.39(1)	2.84(2)
	F_c	0.56(2)	0.58(2)	0.55(2)	0.48(1)	0.45(2)	0.37(2)	0.34(1)	0.48(9)	
C1+C1sat	P_c	0.36(1)	0.34(0)	0.35(1)	0.33(1)	0.30(1)	0.33(1)	0.34(1)	0.34(2)	2.73(4)
	F_c	0.62(3)	0.66(2)	0.61(4)	0.46(4)	0.61(6)	0.54(4)	0.51(5)	0.57(7)	
Sum	P_c	0.38(1)	0.38(0)	0.38(0)	0.36(0)	0.36(1)	0.38(1)	0.39(1)	0.38(1)	2.81(2)
	F_c	0.57(2)	0.60(2)	0.58(2)	0.51(1)	0.48(2)	0.42(2)	0.37(1)	0.50(9)	
Without	P_c	0.38(0)	0.38(0)	0.38(0)	0.36(0)	0.36(1)	0.38(1)	0.39(1)	0.38(1)	2.81(2)
XPS model	F_c	0.57(2)	0.60(2)	0.58(2)	0.51(2)	0.48(2)	0.42(2)	0.36(1)	0.50(9)	

Table 5.3: Results of the XSW analysis for the C1s data using the model shown in Fig. 5.5. C2+C3+C4 represents the the main carbon peak while C1+C1sat is the result for the carboxylic carbons. The Sum is the result for the sum of all components while the Region describes the result if no XPS model is employed. All results are visualized in the Argand diagram in Fig. 5.6.

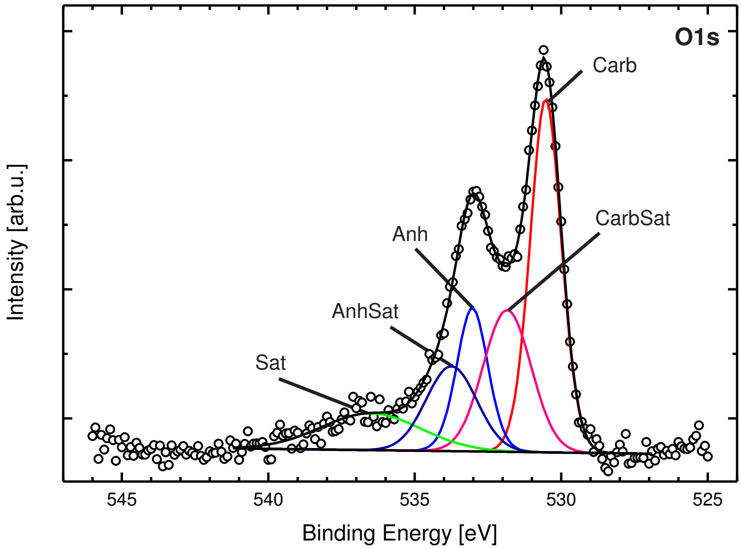

Figure 5.8: Off Bragg XPS spectrum at $E_{\mathrm{photon}} = 3024\,\mathrm{keV}$ of the O1s region for PTCDA/Ag(100). The spectrum is used to develop the fitting model used in the XSW analysis. It consist of five components: The main line of the carboxylic oxygen (Carb, red), its satellite (CarbSat, magenta), the main line of the anhydride oxygen (Anh, light blue), its satellite (AnhSat, dark blue) and a mixed satellite (Sat, green). Peak position, FWHM and relative area are given in Table 5.4

5.4.5 PTCDA/Ag(100) - O1s results

For the oxygen atoms in the PTCDA molecule we face a very similar situation as in the carbon case discussed above, because the carboxylic end group contains two species of oxygen, namely the anhydride oxygen on the central axis and the carboxylic oxygens in the corners of the molecule. This calls again for a model to separate the XPS peaks of both species to be able to determine their adsorption heights independently. Therefore, in this section we will first discuss the used fitting model and in a next step the XSW results.

O1s XPS model The XPS data set for the O1s model is measured under off-Bragg conditions at a photon energy of $E_{\mathrm{photon}} = 3024\,\mathrm{keV}$. The resulting spectrum is displayed in Fig. 5.8. It shows two clearly separated peaks and some minor intensity on the high binding energy side. The two peaks can be assigned straightforwardly to the two oxygen species of PTCDA, whereas the additional intensity at higher binding energies is considered to stem from satellite features of these main lines. To achieve a good fit one has to introduce two components, a main line and a satellite

	Peak				
	Carb	CarbSat	Anh	AnhSat	Sat
Binding energy [eV]	530.5	531.8	533.0	533.7	536.5
FWHM [eV]	1.3	1.9	1.3*	2.0	4.0
relative Area [%]	36.8	22.3	14.9	14.1	12.0

Table 5.4: O1s model components for the XSW analysis. The model is derived from the off-bragg XPS spectrum shown in fig 5.8. Constrained values are indicated by an asterisk. For detailed information on the model see text.

for each oxygen peak, as it is already known from XPS data on PTCDA/Ag(111) [60] and PTCDA/Ag(110) [39]. Therefore, we need five components in total in the model as shown in Fig. 5.8: The main line of the carboxylic oxygen (Carb, red), its satellite (CarbSat, magenta), the main line of the anhydride oxygen (Anh, light blue), its satellite (AnhSat, dark blue) and a mixed satellite (Sat, green). As the only constraint used for the fitting the FWHM of both main lines was set to be equal, because we expect each line to represent only one oxygen species, and there is no reason why one should be broader than the other. To verify the fitting model, the intensity ratio of the carboxylic components (Carb+CarbSat) and the anhydride components (Anh+AnhSat) was calculated and turns out to be 2.04. This is in good agreement with the ratio of 2 that is expected from the stoichiometry of the PTCDA molecule. All parameters of the fit are summarized in Table 5.4. In the next step the model is applied for the XSW data analysis.

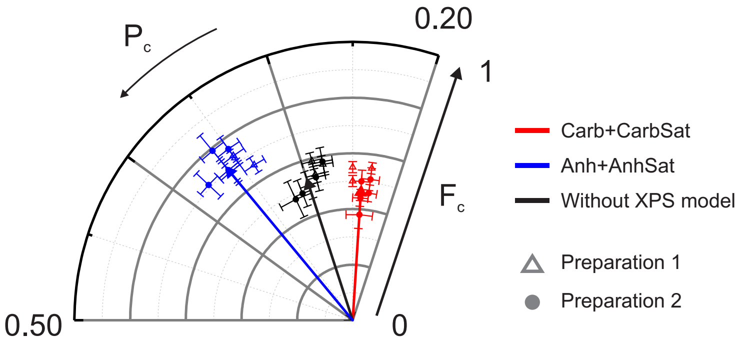

Figure 5.9: Argand diagram visualizing the results of the XSW analysis for the O1s data. The Carb+CarbSat component representing the carboxylic oxygen is displayed in red, the Anh+AnhSat representing the anhydride oxygen in blue and the result without applying any model in black. Arrows indicate the corresponding mean values. Datapoints of preparation one and two are represented by open triangles and filled circles respectively. All values are given in Table 5.5.

O1s XSW analysis The O1s model derived above is used to fit all XSW data sets. For the analysis the intensity profiles of the carboxylic and anhydride signal was evaluated, each consisting of the main peak and a satellite. For each oxygen species the ratio between main peak and satellite was kept constant during the XSW analysis. Furthermore, we evaluate the sum of all components including the satellite (Sat) and compare it to the analysis without a component model to verify the applicability of our XPS model. Exemplary electron yield curves of the data set O1s006 are shown in Fig. 5.10

From three data points on the first and five data points on the second preparation we get a mean P_c of 0.24 ± 0.01 for the carboxylic oxygen which corresponds to an adsorption height of $2.53 \pm 0.02\,\text{Å}$. The anhydride oxygen is found to yield a P_c of 0.36 ± 0.01 and therefore a $0.24\,\text{Å}$ higher adsorption height of $2.77 \pm 0.02\,\text{Å}$. The detailed values for each data set are given in Table 5.5 and the results are visulized in the Argand diagram in Fig. 5.9.

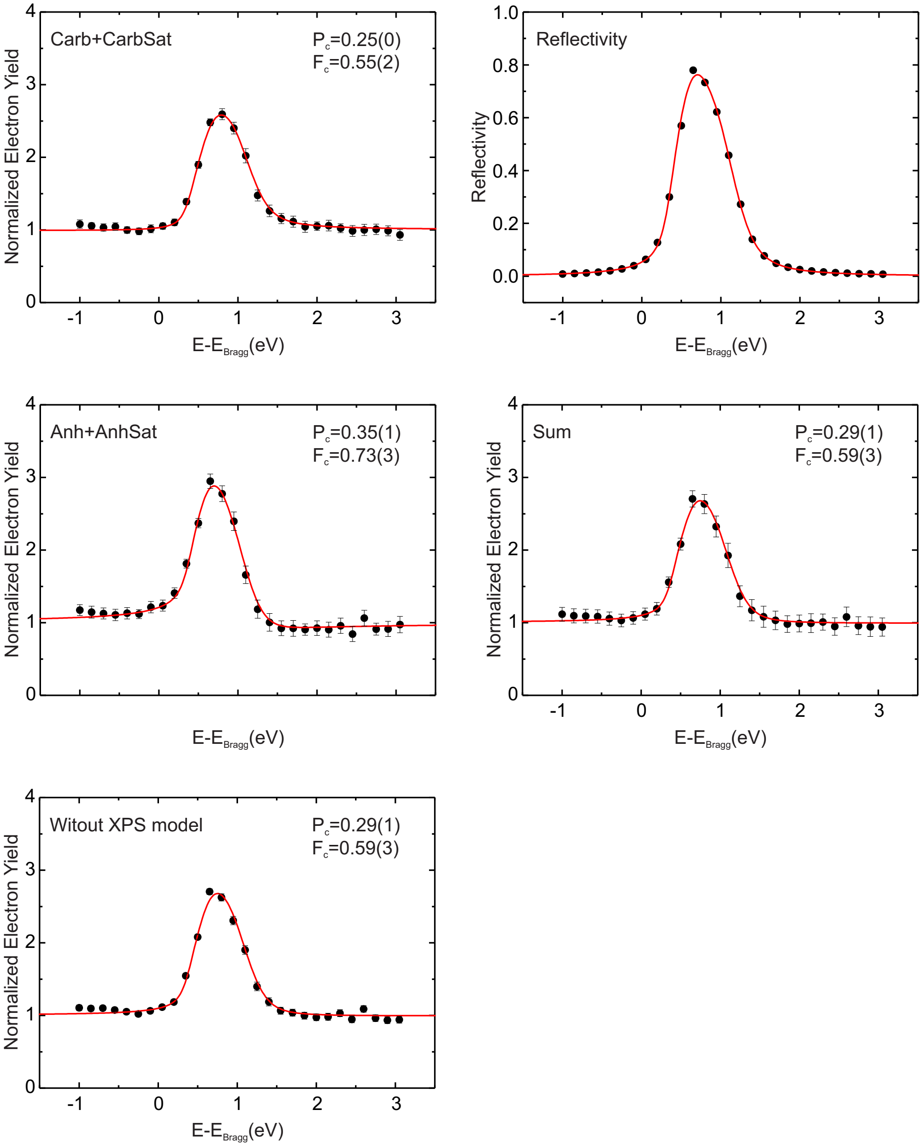

Figure 5.10: Representative electron yield curves of the O1s XSW analysis using the XPS model which is depicted in Fig. 5.8. The data belongs to data set O1s006. The results for all O1s data sets are shown in Table 5.5.

		preparation 1			preparation 2						
		O1s003	O1s006	O1s007	O1s009	O1s012	O1s013	O1s016	O1s018	mean value	ads. height[Å]
Carboxylic	P_c	0.25(0)	0.25(0)	0.23(0)	0.24(2)	0.24(1)	0.23(1)	0.23(1)	0.24(1)	0.24(1)	2.53(2)
	F_c	0.50(2)	0.55(2)	0.55(2)	0.38(5)	0.44(3)	0.51(4)	0.46(3)	0.50(4)	0.49(6)	
Anhydride	P_c	0.35(0)	0.35(1)	0.34(1)	0.38(1)	0.36(1)	0.36(1)	0.36(1)	0.35(1)	0.36(1)	2.77(2)
	F_c	0.72(3)	0.73(3)	0.66(3)	0.71(6)	0.70(5)	0.79(7)	0.69(5)	0.76(5)	0.72(5)	
Sum	P_c	0.29(0)	0.29(1)	0.27(1)	0.31(1)	0.31(1)	0.28(1)	0.30(1)	0.29(1)	0.29(1)	2.64(2)
	F_c	0.55(2)	0.59(3)	0.58(3)	0.51(6)	0.48(4)	0.61(5)	0.54(4)	0.56(5)	0.55(4)	
Without	P_c	0.29(1)	0.29(1)	0.28(1)	0.32(2)	0.31(1)	0.28(1)	0.30(1)	0.29(1)	0.30(1)	2.65(2)
XPS model	F_c	0.54(3)	0.59(3)	0.57(3)	0.48(7)	0.49(5)	0.58(5)	0.51(5)	0.53(5)	0.54(5)	

Table 5.5: Results of the XSW analysis for the O1s data using the XPS model shown in Fig. 5.8. According to the model the contribution from the carboxylic and the anhydride oxygens could be separated. The sum off all components and the result without XPS fitting model are as well tabulated. All results are visualized in the Argand diagram in Fig. 5.9.

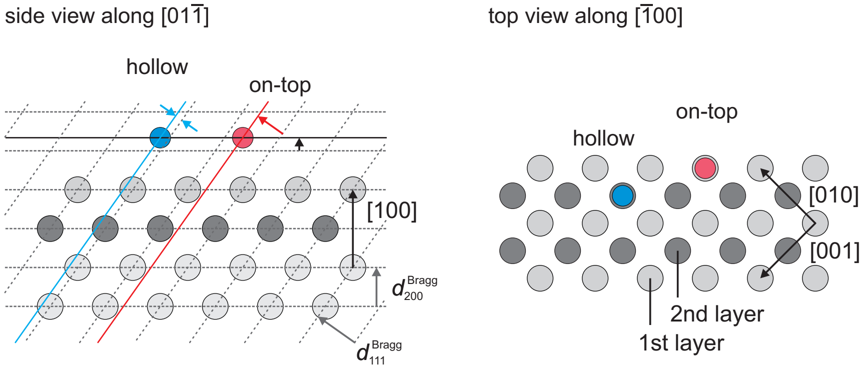

Figure 5.11: Side and top view of a (100) surface. The grey circles mark the position of substrate atoms and dashed grey lines indicate the corresponding (200) and (111) Bragg planes. A red circle represents an adsorbate on an on-top adsorption site, while the blue circle represents an adsorbate on the hollow adsorption site. As indicated by the red and blue arrows in the side view, they would yield different P_c in the XSW experiment employing the (111) Bragg reflection. Hence, the on-top and hollow adsorption sites could be unambiguously differentiated.

5.4.6 Adsorption site determination for PTCDA/Ag(100)

This section deals with the determination of the adsorption site of PTCDA on Ag(100). Stricly speaking, the adsorption site is a lateral property of PTCDA/-Ag(100), but since the determination is done by XSW, it fits much better into the present section on the vertical structure.

In general the XSW method allows three dimensional imaging and *a priori* determination of atom positions for impurities and adsorbates, if an adequate number of Bragg reflexes are accessible [4, 113, 114]. To determine an adsorption site by simple triangulation one usually needs at least three Bragg reflexes [4]. Each measurement determines the adsorbate distance from a Bragg plane, hence one measurement confines the position to a plane, a second to a line a the third to a point, if the corresponding Bragg planes are not parallel. It should be noted that for the determination of high symmetry adsorption sites, even two Bragg reflexes can be sufficient. This is illustrated in Fig. 5.11 for the example of a (100) surface. If it is known that the adsorbate is either in an on-top (red) or hollow position (blue) an XSW experiment using the (111) Bragg reflection can distinguish these unambiguously, because they yield different P_c indicated by the red and blue arrows.

To determine the adsorption site of PTCDA/Ag(100) we perform an XSW experiment as it is described in sec. 2.4, but we use Bragg planes belonging to a different

		preparation 2					
		O1s023	O1s030	O1s032	O1s033	mean value	distance [Å]
Carboxylic	P_c	0.63(1)	0.65(2)	0.68(2)	0.65(2)	0.65(2)	1.53(5)
	F_c	0.37(3)	0.32(3)	0.37(6)	0.34(3)	0.35(4)	
Anhydride	P_c	0.62(2)	0.65(1)	0.65(2)	0.64(1)	0.64(2)	1.51(5)
	F_c	0.75(7)	0.59(4)	0.62(7)	0.65(5)	0.65(7)	
Sum	P_c	0.59(2)	0.61(2)	0.64(2)	0.62(2)	0.62(2)	1.46(5)
	F_c	0.57(4)	0.48(4)	0.51(6)	0.46(5)	0.51(5)	
Without	P_c	0.60(2)	0.61(2)	0.65(3)	0.63(2)	0.62(2)	1.46(5)
XPS model	F_c	0.54(6)	0.48(5)	0.57(9)	0.49(7)	0.52(7)	

Table 5.6: Results of the XSW analysis for the (111) reflection used for the triangulation to derive the adsorption site as described in the text and shown in Fig. 5.12. The XPS model used here is the same as the one for the (200) reflection data shown in Fig. 5.8. The results match the expected P_c values of 0.62 and 0.68 for the carboxylic and anhydride oxygen for an on-top adsorption site very well while one would expect a P_c of 0.12 and 0.18 for the hollow site.

high symmetry direction, namely we employ the (111) planes to generate the standing wave field. From LEED experiments it is known that the structure shows a glide plane symmetry, therefore the O atoms must fulfill the prerequisite of a high symmetry adsorption site [102]. Hence, according to the construction in Fig. 5.11, the two Bragg reflexes, i.e. (200) and (111), are sufficient for our adsorption site determination. Nevertheless, we will do the calculation with three planes later, employing the fact that the (111) and $(1\bar{1}1)$ are equivalent in respect to the (100) surface. It should be noted that the two PTCDA molecules in the PTCDA/Ag(100) superstructure unit cell are equivalent in respect to the substrate (see Fig. 5.2) and all oxygens of the same species within one molecule yield the same adsorption position. Therefore, the mean position of the species, which is measured in the experiment, indeed corresponds directly to the real adsorption distance.

For the experiment the crystal had to be rotated and the photon energy changed to $E_{\text{photon}} = 2630\,\text{eV}$ to fulfill the (111) Bragg condition. The experiment was performed directly after the measurements described above on the second preparation of PTCDA/Ag(100). From the XPS point of view the cross-sections have changed slightly due to the photon energy adjustment of about 400 eV. However, the model developed for the oxygen analysis earlier (see sec. 5.4.5) still fits the spectra very well and is therefore employed unchanged. The results are summarized in Table 5.6.

To calculate the position vector of the carboxylic oxygen $\vec{c} = (x, y, z)$ we use the coordinate system of the bulk Ag unit cell and without loss of generality choose a Ag surface atom centre as origin. In this way the origin is placed on the Bragg planes, i.e. an atom at the origin shows a P_c of 0 and we can use eq. (2.25) to directly calculate the distance to each of the three non-parallel planes, which are needed to define $\vec{c}$. The planes are represented by the number of points $\vec{r}$ which fulfill the equation $\vec{r} = \vec{r_0} + a \cdot \vec{u} + b \cdot \vec{v}$, if $\vec{u}$ and $\vec{v}$ are not collinear. The first plane stems from the height measurement on the (200) reflex of sec. 5.4.5, it is therefore parallel to the (100) Ag surface and $\vec{r_0}$ is constructed from the distance $d_{[200]} = 2.53 \pm 0.02\,\text{Å}$ to the origin. This leads to the first equation:

$$d_{[200]} \begin{pmatrix} 1 \\ 0 \\ 0 \end{pmatrix} + a_{[200]} \begin{pmatrix} 0 \\ 1 \\ 0 \end{pmatrix} + b_{[200]} \begin{pmatrix} 0 \\ 0 \\ 1 \end{pmatrix} = \begin{pmatrix} x \\ y \\ z \end{pmatrix}. \tag{5.2}$$

The second plane is parallel to the (111) crystal planes, and $\vec{r_0}$ is constructed from the determined distance of $d_{[111]} = 1.53 \pm 0.05\,\text{Å}$ resulting in the second equation:

$$\frac{1}{\sqrt{3}} d_{[111]} \begin{pmatrix} 1 \\ 1 \\ 1 \end{pmatrix} + a_{[111]} \begin{pmatrix} 0 \\ 1 \\ -1 \end{pmatrix} + b_{[111]} \begin{pmatrix} -1 \\ 1 \\ 0 \end{pmatrix} = \begin{pmatrix} x \\ y \\ z \end{pmatrix}. \tag{5.3}$$

To get a third plane we employ the crystal symmetry and use the fact that the (111) and $(1\bar{1}1)$ planes are equivalent in respect to the (100) surface and therefore $d_{[111]} = d_{[1\bar{1}1]} = 1.53 \pm 0.05\,\text{Å}$ must be valid. Hence, the equation for the third plane, parallel to the $(1\bar{1}1)$ crystal planes can be written as

$$\frac{1}{\sqrt{3}} d_{[111]} \begin{pmatrix} 1 \\ -1 \\ 1 \end{pmatrix} + a_{[1\bar{1}1]} \begin{pmatrix} 0 \\ 1 \\ 1 \end{pmatrix} + b_{[1\bar{1}1]} \begin{pmatrix} -1 \\ -1 \\ 0 \end{pmatrix} = \begin{pmatrix} x \\ y \\ z \end{pmatrix}. \tag{5.4}$$

Solving this system of equations (for details see appendix A) results in the carboxylic oxygen position

$$\vec{c} = \begin{pmatrix} d_{[200]} \\ 0 \\ \sqrt{3} d_{[111]} - d_{[200]} \end{pmatrix} = \begin{pmatrix} 2.53 \pm 0.02\,\text{Å} \\ 0 \\ 0.12 \pm 0.11\,\text{Å} \end{pmatrix}. \tag{5.5}$$

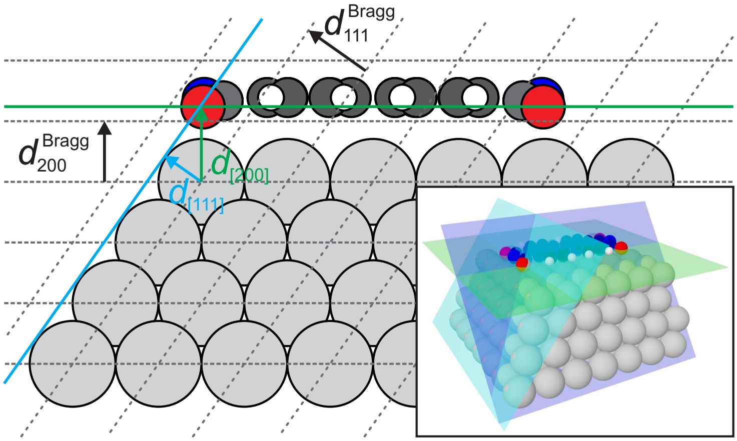

Figure 5.12: Sideview of a PTCDA molecule adsorbed on-top on a Ag(100) surface. The picture is overlayed by the Bragg-planes in the [200] and [111] direction drawn as dashed lines. A green line indicates the plane parallel to the (200) Bragg planes with the adsorption height $d_{[200]}$ of the carboxylic oxygen (red) and a blue line marks the plane parallel to the (111) Bragg planes with the corresponding distance $d_{[111]}$. Hence, their crossing point references to the adsorption site of the carboxylic oxygen. An inset shows a 3D model of the adsorption geometry and the planes used to calculate the carboxylic carbon position.

This means we find the carboxylic oxygen in a distance of $x = d_{[200]} = 2.53 \pm 0.02$ Å from the (100) surface, which is not surprising, because this is the adsorption height of the carboxylic oxygen, which is directly determined in the XSW experiemnt of sec. 5.4.5. In this terms the y and z values determine the lateral adsorption site. Both values are very close to, or in the case of y even exactly zero, therefore the adsorption site of the carboxylic oxygen is on-top. For the adsorption on the four-fold hollow site either $y = 0$ and $z = 0.5 \times a_{\mathrm{Ag}} = 2.04$ Å ($a_{\mathrm{Ag}} = 4.08$ Å is the Ag lattice constant) or vice versa would be expected. This can be rationalized by looking on the top view in Fig. 5.11. The four-fold hollw adsorption site is right above a second layer substrate atom. With the origin on a first layer substrate atom this position is described by half a unit cell vector either in the [010] or [001] direction, which are identical to the y and z coordinates.

In Fig. 5.12 the construction of the three planes is visualized in the inset and the result is sketched in a two dimensional way, leaving out the third plane for reasons of clarity. The dashed lines indicate the Bragg planes for the (111) and (200) reflection and the green and blue lines mark the experimental results, i.e. the planes with corresponding distances from the Bragg planes. Hence the position of the carboxylic oxygen is the crossing point of the green and blue lines. This point is very close to an on-top adsorption site, as can be seen by comparison to the drawn PTCDA molecule which is indeed placed in the ideal on-top position.

The ideal result for the on-top position would mean that $y = z = 0 = \sqrt{3}d_{[111]} - d_{[200]} \Rightarrow d_{[111]} = 1.46\,\text{Å}$. Inverting eq. (2.25) we therefore expect a P_c of 0.62 for the carboxylic and, from an analouge analysis, 0.68 for the anhydride oxygen in the case of an on-top adsorption. For the four-fold hollow site we expect a P_c of 0.12 and 0.18 respectively. This rules out a four-fold hollow adsorption site. Other sites which do not show a four-fold symmetry are excluded already by the glide plane symmetry which is observed in LEED experiments [102] .

We can therefore clearly draw the conclusion that the oxygen adsorption site is on-top as the measured values match the expectations very well. This means the centre of the PTCDA molecule is in an on-top position as drawn in Fig. 5.2. However, we can see some small discrepancies in our results. The expected small difference of 0.06 in the P_c between the carboxylic and the anhydride oxygen is not visible in the experiment (see Table 5.6). Furthermore, the P_c of the sum and the result without XPS model are lower than both single oxygen species. One would expect the sum and the result without XPS model to agree with the vector sum of the single oxygen species in the argand diagram and hence to be found in between these two P_c values. To explain these slight inconsistencies, we note that our data quality is worse than for the measurements on the (200) reflection, because the sample has a higher age and the beam intensity and therefore count rate was significantly lower for the (111) reflection data. Furthermore, we could not keep track of already illuminated sample positions during the sample rotation and the beamline re-adjustment on the new energy. Hence, we cannot exclude that we have collected data from surface areas already damaged by the X-rays. However, as the hollow site would yield dramatically different P_c there is no doubt about the conclusion that the oxygen is occupying the on-top adsorption site.

5.4.7 PTCDA/Ag(100) - Substrate results

As a reference for the P_c and F_c of PTCDA we measured XSW data for the substrate. We chose the Ag3d signal as well as the AgMVV Auger peak. Unlike the cases of oxygen and carbon, a fitting model is not necessary, because there are no overlapping contributions in the Ag signals. Therefore, only the background was subtracted and the full intensity of the XPS spectra evaluated. The results are shown in Table 5.7.

Signal	Name	preparation	Bragg reflection [hkl]	F_c	P_c
Ag3d	Ag3d001	1	200	0.90(1)	0.99(0)
Ag3d	Ag3d004	1	200	0.90(1)	1.00(0)
Ag3d	Ag3d010	2	200	0.90(1)	0.99(0)
Ag3d	Ag3d014	2	200	0.89(1)	0.99(0)
AgMVV	AgMVV022	2	200	0.85(1)	1.00(0)
Ag3d	Ag3d031	2	111	0.86(1)	0.97(0)

Table 5.7: Results of the XSW analysis for the substrate from the Ag3d and the AgMVV Auger lines. No XPS model was applied, only the background was subtracted.

The data fulfills the expectation to find the Ag atoms positioned at the Bragg planes ($P_c \approx 1$) but the F_c deviates from the expected value of 1.00. It is an indicator that either the crystalline quality is not as good as for the crystals used for other XSW investigations [39, 60] or a surface buckling is present without a shift of the mean Ag adsorption height. The latter is supported by the absence of a difference between the Ag3d and the AgMVV signal for the P_c, while the F_c for the AgMVV signal is indeed lower by about 0.05. This conclusion is based on the higher surface sensitivity of the AgMVV signal due to the lower kinetic energy and therefore escape depth of the photoelectrons. Therefore, one expects to see a stronger influence of a surface relaxation or buckling on this signal's P_c and F_c respectively. However, the P_c shows no difference, which means that surface relaxations seem to be negligible in our case, but a buckling might be present. Of course, this is only a weak argument, because we do not have a sufficient number of data sets from the AgMVV signal to draw a stronger conclusion.

5.4.8 Discussion

With the results of our XSW studies we have revealed the vertical adsorption geometry of PTCDA/Ag(100) in considerable detail. We find the PTCDA perylene core at a distance of 2.84 ± 0.02 Å above the Ag Bragg plane. The carboxylic end groups, however, bend down towards the Ag substrate with the carboxylic oxygens acquiring the lowest height at 2.53 ± 0.02 Å, i.e. 0.31 Å lower than the carbon backbone. At intermediate distance we find the carboxylic carbons and the anhydride oxygens at 2.73 ± 0.04 Å and 2.77 ± 0.02 Å, respectively. The adsorption geometry is visualized in the central part of Fig. 5.13. Besides this detailed vertical structure we also determined the adsorption site of the carboxylic oxygens to be on-top of the Ag atoms.

Before we compare the adsorption geometry found here for PTCDA/Ag(100) to the other PTCDA/Ag systems, we will shortly discuss the observed F_c. This said, we will first look for a preparation dependence in our data. Two PTCDA/Ag(100) monolayers were prepared, and carbon as well as oxygen spectra were recorded on each preparation. Overall, we measured the results of three carbon and three oxygen data points for the first preparation and four carbon and five oxygen data points for the second (see Tables 5.3 and 5.5). The P_c is very similar over all data sets of the same species and shows no preparation dependence. However, for the F_c of all components (with the exception of the anhydride oxygen) we can identify a trend towards lower values for the second preparation. Whereas it is not clear why the anhydride oxygen signal does not follow this trend (this might just be a matter of insufficient statistics in terms of data sets), the overall result can be rationalized taking into account the coverage. The higher the coverage is, the less influence molecules on defect sites, island boundaries or step edges have, because their relative abundance compared to molecules within the well-ordered PTCDA islands decreases. This argument is based on the assumption that defect sites and step edges are occupied first and therefore the number of molecules adsorbed in such places saturates already at low coverages [6]. Additional molecules form and attach to ordered islands and thus improve the coherence of the majority of scatterers. Furthermore, a higher coverage results in a larger area covered by condensed islands, leaving less space for a surface gas phase [115]. Assuming a constant gas phase density at a given temperature, this is an additional effect to reduce the relative number of incoherent contributions to the XSW signal. The P_c is not necessarily affected by the coverage, because the height distribution may get broader without changing its centre point. Summarizing, we do see a preparation dependence, but this is limited to the F_c and does not alter the resulting adsorption heights.

The F_c shows another interesting behaviour: The mean values of the F_c are highest for the anhydride oxygen (0.72 ± 0.05), followed by the carboxylic carbon (0.57 ± 0.07). The carboxylic oxygen and the perylene core show very similar F_c (0.49 ± 0.06 and 0.48 ± 0.09). This is puzzeling, because one would expect a different order from the lateral structure model as it is shown in Fig. 5.2b. The anhydride oxygen is indeed expected to show the highest F_c, because there are only two per molecule and they are located on a symmetry axis rendering their height less influenced by possible molecule rotations around this axis. The perylene core, on the other hand, consists of 20 carbon atoms and is expected to bend and hence to show the smallest F_c. The carboxylic carbons and oxygens exhibit the same symmetry and should therefore show a similar F_c, intermediate between the perylene core and the anhydride

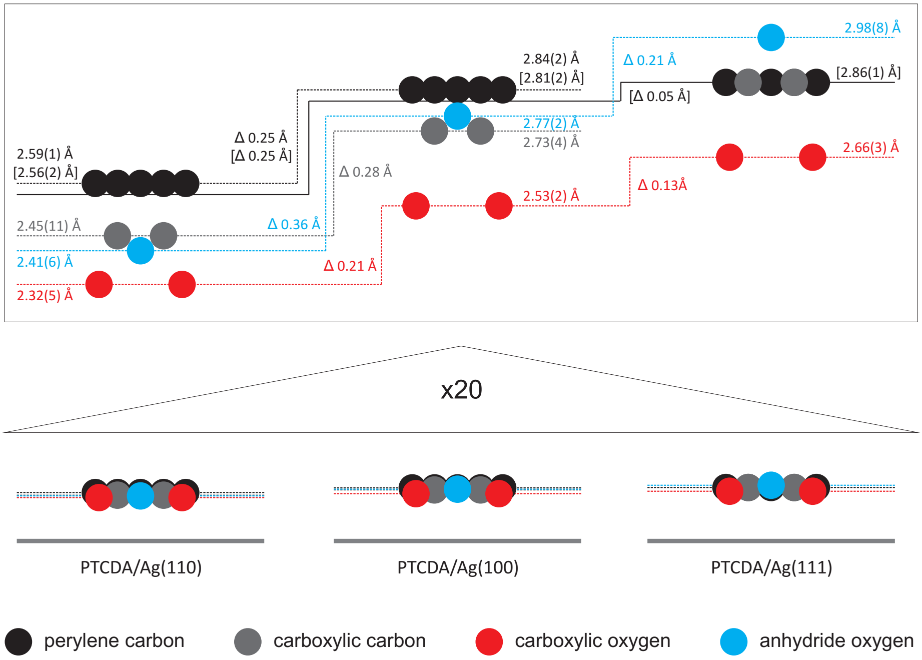
2.98(8) Å
Δ 0.21 Å
2.84(2) Å
[2.81(2) Å]
[2.86(1) Å]
[Δ 0.05 Å]
Δ 0.25 Å
[Δ 0.25 Å]
2.77(2) Å
2.73(4) Å
2.59(1) Å
[2.56(2) Å]
Δ 0.28 Å
2.66(3) Å
Δ 0.13Å
2.53(2) Å
2.45(11) Å
Δ 0.36 Å
2.41(6) Å
Δ 0.21 Å
2.32(5) Å
x20
PTCDA/Ag(110)
PTCDA/Ag(100)
PTCDA/Ag(111)
perylene carbon
carboxylic carbon
carboxylic oxygen
anhydride oxygen

Figure 5.13: Side view along the long axis of PTCDA for the vertical adsorption geometry of PTCDA on Ag(110) [39], Ag(100) and Ag(111) [60]. The bottom part of the figure shows the adsorption height from the Ag Bragg plane (indicated by the grey bar) and the molecular distortion in scale. To depict the differences between the three systems in detail, the z-axis distances (along the surface normal) are enhanced by a factor of 20 in the upper part of the figure. The numbers in brackets, given for the perylene core, refer to the mean value of all carbon atoms, i.e. to the sum value of the perylene and carboxylic carbon atoms. This allows the comparison to PTCDA/-Ag(111), where the carboxylic carbon contribution was not differentiated from the perylene carbon signal. H atoms are not shown.

oxygens. However, this is not what is observed. Althought one might expect that the carboxylic oxygens are even stabilized by their O-Ag bonds as they are closest to the surface, their F_c is as low as that of the perylene core, in spite of the fact that differences in the carboxylic oxygens at first glance seem to be very unlikely. The effect of the surprising low F_c of the carboxylic oxygen compared to the other atom species in PTCDA is not limited to PTCDA/Ag(100). One can make the same qualitative observation for PTCDA/Ag(111) [60] and PTCDA/Ag(110) [39]. We will not discuss this interesting observation further in this work, but possible explanations are that this effect stems from molecular vibration modes or that the height of the carboxylic oxygens is especially prone to defect influences due to their local interaction with surface atoms.

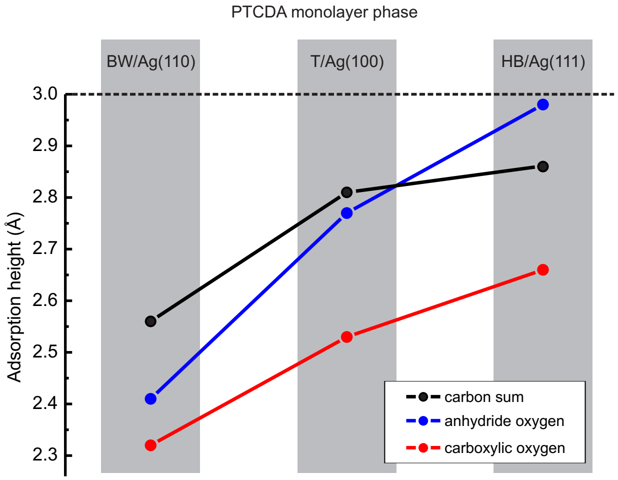

Figure 5.14: Changes of the bond length for the oxygen and carbon species of PTCDA for the different low index Ag surfaces. Values for PTCDA/Ag(110) and PTCDA/Ag(111) are taken from refs. [39, 60]. For a visualization of the detailed geometries see Fig. 5.13.

Coming back to the vertical adsorption geometry, we find PTCDA/Ag(100) in between the other two systems, namely HB PTCDA/Ag(111) [60] and BW PTCDA/Ag(110) [39] as it is shown in Fig. 5.13. While the perylene core still resides at basically the same height for PTCDA/Ag(100) (average carbon height 2.81 ± 0.02 Å) and PTCDA/Ag(111) (average carbon height 2.86 ± 0.01 Å), the oxygens are more strongly bent towards the surface, thus enhancing the difference between the carboxylic oxygen and the perylene core from 0.2 Å in the PTCDA/Ag(111) case to 0.3 Å for PTCDA/Ag(100). Furthermore, in the latter case the anhydride oxygen is now found below the perylene core. However, compared to PTCDA/Ag(110) the perylene core is by 0.25 Å and the carboxylic oxygens by 0.21 Å higher for PTCDA/Ag(100). The overall bending of the molecule is also different, as the anhydride oxygen is only 0.09 Å higher than the carboxylic oxygen for PTCDA/Ag(110), while the difference between the oxygens is 0.24 Å in the PTCDA/Ag(100) case. For an easier comparison all adsorption height values are plotted in a diagram in Fig. 5.14.

First, we note that there is an equalization of the oxygen species on the PTCDA/Ag adsorption geometry from PTCDA/Ag(111) over PTCDA/Ag(100) towards PTCDA/Ag(110). While the carboxylic oxygens are always closest to the Ag surface, the anhydride oxygens bend more and more down, thus getting very close to the carboxylic oxygens. This transformation of the adsorption geometry from a saddle like picture (PTCDA/Ag(111)) to a M-shape (PTCDA/Ag(110)) might be related to a stabilization of the corresponding LUMO, i.e. its shift to higher binding energy (see sec. 5.6 for a detailed discussion). The same trend could be observed for hetero-molecular systems and in particular non commensurate superstructures [116]. Hence, it is opposing the argument of a site specific O-Ag influence as responsible mechanism for the changes in the anhydride oxygen.

Second, from the decreasing adsorption height we can expect that the molecule-substrate interaction is stronger the more open the surface structure of the Ag and consequently the smaller its work function is (for calculated work function values see Table 5.10), but it is difficult to understand if the O-Ag interaction or rather the perylene core is the driving force for the molecule approaching the surface.

While one idea is that a strengthening of the O-Ag bond allows the perylene core to be dragged deeper into the repulsive part of the surface potential [99], this would mean that a weakening of the O-Ag bonds should lead to a significant lifting of the molecule. However, a distinct study tuning these O-Ag bonds by potassium doping on PTCDA/Ag(110) showed only a minor effect on the perylene core adsorption height [117]. Furthermore, hetero-molecular structures show that substrate mediated molecule-molecule interactions can indeed decisively change the carbon backbone adsorption height due to a charge rearrangement of the surface spill-out and its uptake by the molecule via the perylene core interaction channel, while the O-Ag bonds stay rather unchanged [64, 116]. In that case the lateral arrangement of the molecules seems to be more substantial for the final adsorption height than the local O-Ag bonds.

Following this picture, the molecule-surface interaction channel, which is decisively influencing the adsorption height, is the interaction of the π-system of the perylene core with the charge spill out above the surface. This explains that the work function is a crucial surface parameter, because it is a measure for the electron density above the surface. Hence, the idea of a molecule which is *floating* on the surface electron spill out can explain the general trend that the adsorption height is larger the higher the work function is. However, we can expect that the molecule itself will modify the spill out due to the push-back effect and possible hybridization of molecular and metal states upon adsorption. The difference in the molecular buckling which is observed for PTCDA on the three Ag surfaces is an indication that the molecule is not just *floating* on the unmodified electron cloud but chemical interaction takes place. This may have a crucial influence on the adsorption height, rendering the

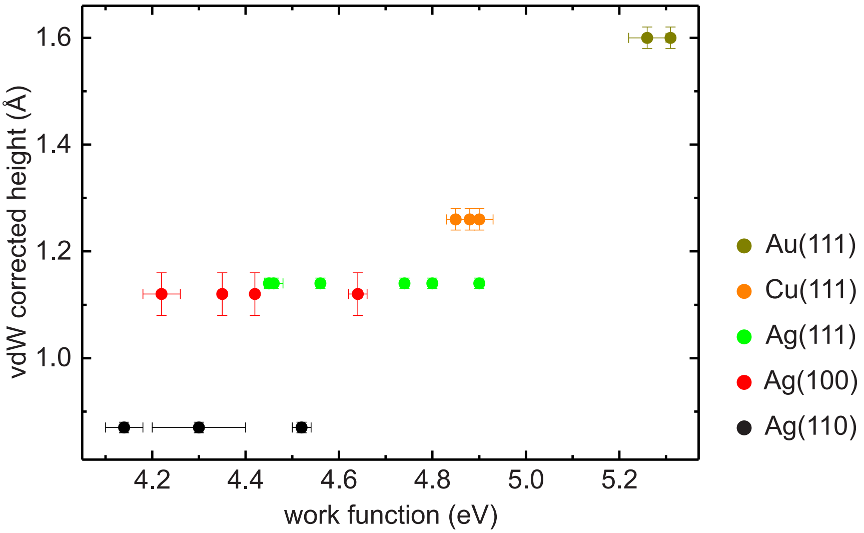

Figure 5.15: Adsorption height depending on the substrate work function. The adsorption heights for PTCDA/Au(111) [61], PTCDA/Cu(111) [110], PTCDA/Ag(111) [60], PTCDA/Ag(100) (this work) and PTCDA/Ag(110) [39] are corrected by a subtraction of the corresponding substrate vdW radius ($r_{\mathrm{Au}}^{\mathrm{vdW}} = 1.66\,\text{Å}$, $r_{\mathrm{Cu}}^{\mathrm{vdW}} = 1.40\,\text{Å}$, $r_{\mathrm{Ag}}^{\mathrm{vdW}} = 1.72\,\text{Å}$) [56] and plotted against experimental work function values for the bare Au(111) [118, 119], Cu(111) [120–122], Ag(111) [106, 122–126], Ag(100) [124, 125, 127, 128], and Ag(110) [124, 127, 129] surface.

simple picture drawn above incomplete.

Comparing the situation on different metals, it was shown that PTCDA adsorption heights on the closed packed surfaces Ag(111) [60], Cu(111) [110] and Au(111) [61], if they are corrected by the corresponding substrate vdW radius [56], show indeed a linear trend towards larger adsorption heights for larger substrate work functions [60] (see also Fig. 5.15). If one assumes that the vdW radius of the metal is, at least to some extend, also a measure of the electron spill out, one would expect a constant for the corrected adsorption height. However, the reduced adsorption distance is smallest for Ag(111) and largest for Au(111) with Cu(111) in between, indicating that a chemical reaction is indeed taking place, i.e. the simple picure of the molecule *floating* on the charge spill out is incomplete. Note, that a NIXSW study on the so far missing HB PTCDA/Ag(110) would be very interesting to compare to the results to BW PTCDA/Ag(110) to quantify the influence of the lateral molecular arrangement on the balance of the molecule-substrate interaction.

The above discussion mainly focuses on the extent of the electron spill out as a decisive adsorption height parameter. This can be understood as a focus on the repulsive part of the surface potential in form of the Pauli repulsion. However, it is clear that the final adsorption height will be defined by the interplay of the Pauli repulsion with an attractive potential. Therefore, one should consider the dependence of this attractive part on the work function to draw a more complete picture of the adsorption process. If we imagine an organic-metal interface with a certain work function Φ and a molecule with an electron affinity level E_A and consider vacuum level alignment, the work required to move an electron from the metal into the LUMO is $\Phi - E_\mathrm{A}$. When the molecule approaches the surface, E_A gets larger, following the attractive image charge potential (although the state is still empty). As soon as E_A crosses the Fermi level E_F with the molecule at the distance r_t from the surface, the molecule gets charged and continues to move towards the surface until at r_0 an equilibrium between image charge potential and Pauli repulsion is reached. The situation is sketched for two different workfunctions in Fig. 5.16. From this picture we can understand that the work function not only influences r_0 via the larger electron spill out, but in addition through the attractive image charge potential. Because both shifts move the equilibrium adsorption distance further away from the surface, the higher the work function is, this explains the behaviour observed for PTCDA/Ag and also the discussed trend from PTCDA/Ag(111) over PTCDA/Cu(111) to PTCDA/Au(111) towards larger corrected adsorption heights.

At the same time the energy position of the LUMO, i.e. its final binding energy, will depend on the distance between $r_\mathrm{t} - r_0$. Naturally, this means that a smaller r_0 and a larger r_t will lead to a higher binding energy. Both parameters are controlled by the work function, because a larger work function means a larger electron spill out and hence an earlier onset of the Pauli repulsion, and at the same time a larger work function means a shorter distance from the surface to the Fermi-level crossing point r_t, because E_A always follows the same image charge potential. Therefore, the binding energy of the LUMO and the final adsorption height are linked through the work function. However, the picture is more complicated because the adsorption distance itself will have an impact on the final work function of the metal-organic interface.

At this point it is clear that we need to investigate the electronic properties of the PTCDA/Ag systems to put forward an explanation about the correlation of molecule-surface interaction, LUMO binding energy, molecule-molecule interaction, metal properties and the adsorption height. Therefore the following sections will focus on different aspects of the electronic structure of the various PTCDA/Ag interfaces.

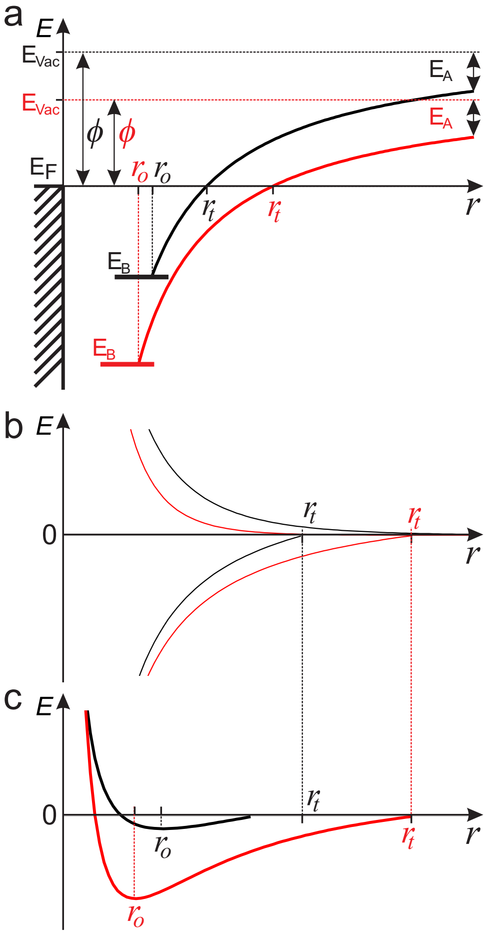

Figure 5.16: Schematic view of LUMO binding energy alignment, molecular adsorption height and π-metal bonding strength (not to scale). (a) The LUMO level of the molecule follows the one-electron image potential in front of the surface. This is shown for a high-work function metal (black) and a low work function metal (red). (b) Once the LUMO reaches the Fermi level, charge is transferred into the molecule, and an attractive potential energy results. The repulsive potential energy is also shown, with the high-work function metal having the larger spill-out. (c) The sum of attractive and repulsive energies shows stronger bonding and shorter adsorption height for the low-work function metal, which also has the larger LUMO binding energy (panel a).

5.5 A/B split for PTCDA/Ag(110)

5.5.1 Introduction

A fundamental issue in the field of organic-metal interfaces is the influence of molecule-substrate and molecule-molecule interactions on the electronic (and structural) properties of the interface, and their relative importance [62, 130–132]. In particular, molecule-molecule interactions are difficult to study quantitatively, because their influence tends to be small. Moreover, in most systems multiple adsorption sites and multiple intermolecular environments coexist, making it difficult to disentangle their influence on the electronic structure of the interface.

In this chapter we employ the orbital tomography technique described in sec. 2.3 to disentangle the environment-specific electronic structure, i.e. orbital energy level splittings between different molecules in complex structures. Up to now this information was only available from cryogenic scanning tunneling microscopy/spectroscopy (STM/STS) [101, 130–134]. We demonstrate the capability of orbital tomography using the environment-specific electronic structure of the model system PTCDA/-Ag(110) as an example. This provides an excellent test system as, depending on preparation, either BW or HB monolayers can be formed as discussed in sec. 5.3.

The tomographic analysis of the ARPES data reveals an energy level offset between [001] and [$1\bar{1}0$] oriented molecules for both emissions from the highest occupied molecular orbital (HOMO) and LUMO, the latter being filled through charge transfer from the metal substrate [106]. In order to reveal the origin of the observed level splittings, DFT calculations were performed by Prof. Peter Puschnig (Karl-Franzens Universität Graz) for freestanding PTCDA layers. The computed HOMO and LUMO splittings are found in excellent agreement with the values derived from ARPES experiments and are explained by constant energy level offsets arising from the distinct electro-static environments of the two inequivalent molecules present in the HB structure.

The results presented in this chapter were developed in collaboration with the groups of Prof. Michael G. Ramsey, Dr. Georg Koller and Prof. Peter Puschnig (Karl Franzens Universität Graz) and have already been published [27]. The reprint of the previously published material is permitted under the Creative Commons Attribution 3.0 Unported (CC-BY) license according to the New Journal of Physics copyright statement.

5.5.2 Results

The ARPES experiments were performed at the BESSY synchrotron using the toroidal analyzer chamber described in sec. 2.5.1 on BW and HB PTCDA/Ag(110) structures as they are described in sec. 5.3.

In Figs. 5.17a-b two experimental CBE maps (left half of the polar diagrams) of the BW monolayer are shown together with the calculated electron distributions (right half of the polar diagrams). These CBE maps at 1.96 eV and 0.76 eV binding energy (E_{B}) reveal the PE angular patterns of the HOMO (a) and LUMO (b) of a single PTCDA molecule and hence match the results of previous studies [8, 25, 106].

CBE maps acquired under the same conditions from the HB monolayer reveal more complex patterns (Fig. 5.17c for the HOMO and Fig. 5.17d for the LUMO). Nonetheless, on simple inspection of these CBE maps, one finds that both HOMO and LUMO maps of the HB monolayer consist of a superposition of two identical patterns that are rotated by 90° with respect to each other [26]. This agrees with the arrangement of molecules in the unit cell of the HB monolayer: The unit cell contains two types of molecules (A and B) that are oriented perpendicular to each other (Fig. 5.3f) [109]. Clearly, molecules of each type give rise to independent but identical anisotropic photoelectron distributions, and the analyzer detects the summed PE intensity. It is also clearly apparent in the data that the intensity contributions of the two orientations at a given energy are not equal. This is because both the HOMO and LUMO PE intensities $I_i(E_{\mathrm{B}})$ emerging from molecules A and B have different energy dependencies, where $i = A, B$.

To access the energy-dependent photoelectron contributions of the corresponding molecular orbitals separately for the A and B molecules of the HB monolayer, we employ in a first step the k-space deconvolution method proposed in [8] as described in chapter 2.3. Note, however, that as a result of the fitting described so far we cannot distinguish between [001] oriented molecules in the HB monolayer (A molecules) and molecules in the BW monolayer which may still be present. Therefore we have labelled the corresponding components in figure 5.18a A+BW.

It can be seen in figure 5.18a that the A+BW peaks have a higher integrated signal than the corresponding B peaks. This indicates the existence of the BW monolayer as a minority phase on the surface. To extract the relative amount of this minority phase, we employ two facts. Firstly, the PDOS of B molecules in figure 5.18a can only arise from the HB monolayer. Secondly, the ratio of A and B molecules

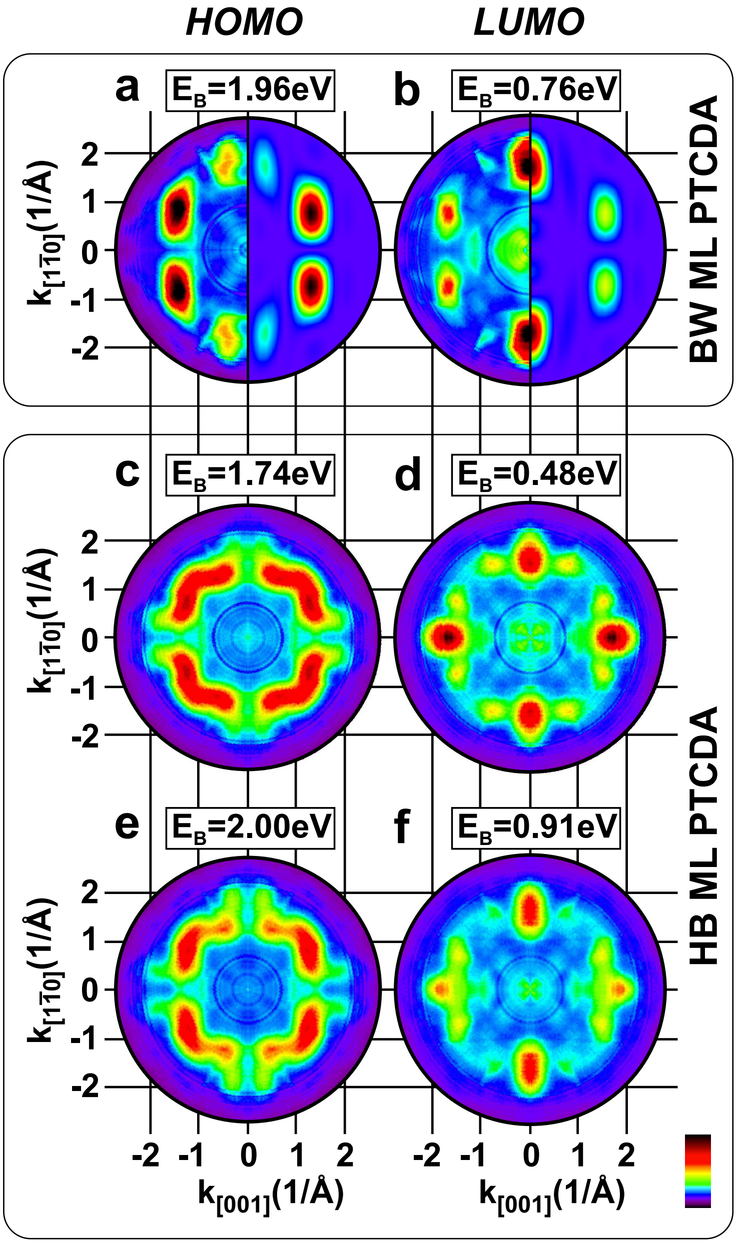

Figure 5.17: (a-b) CBE maps of the HOMO (a) and LUMO (b) of the BW monolayer of PTCDA/Ag(110). The right half of each map shows theoretical calculations of the electron distribution in k-space calculated for a gas phase molecule. (c-f) CBE maps of the HOMO(c,e) and LUMO(d,f) of the HB monolayer of PTCDA/Ag(110) at different binding energies. Maps in (c-f) are generated from data recorded over an azimuthal angle range of 180° and symmetrized.

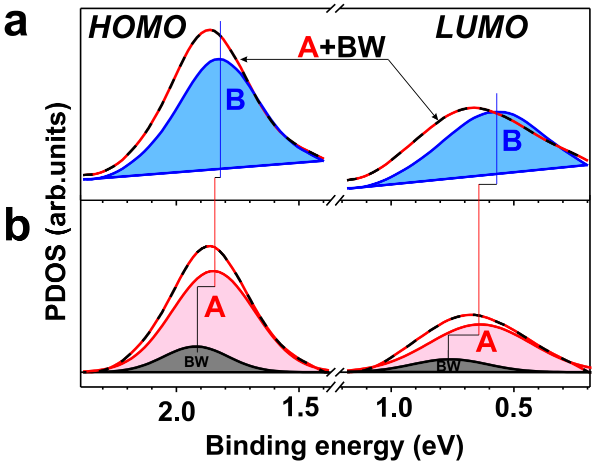

Figure 5.18: (a) Results for the projected density of states of the HOMO and LUMO extracted from orbital tomography (see text) of the HB monolayer of PTCDA/Ag(110). Two contributions can be identified: The intensity from the B molecules (B, blue) and the joint intensity from the HB A and a minority of BW molecules (A+BW, dashed red/black). (b) Results of the fitting of the joint A+BW contribution (dashed red/black) from panel a. The BW intensity is shown in black, the HB A molecule intensity in red. A linear background is subtracted for the fitting.

in the HB monolayer is known (1:1). Hence we obtain a minority contribution of less than 20% for the BW monolayer on the surface (from the analysis of the HOMO peaks). Since we know the binding energies of the LUMO (0.75 eV) and HOMO (1.93 eV) in the BW monolayer from our measurements on the pure BW monolayer as well as from previous experiments [8], we are finally able to separate the A+BW peaks in figure 5.18a into the contributions of BW molecules and A molecules in the HB monolayer, by fitting the A+BW signal by two Gaussian peaks after the subtraction of a linear background. The results are shown in Fig. 5.18b. All resulting peak positions and full widths at half maximum (FWHM) are summarized in Table 5.8.

	$\mathrm{BW}_{\mathrm{HOMO}}$	$\mathrm{A}_{\mathrm{HOMO}}$	$\mathrm{B}_{\mathrm{HOMO}}$	$\mathrm{BW}_{\mathrm{LUMO}}$	$\mathrm{A}_{\mathrm{LUMO}}$	$\mathrm{B}_{\mathrm{LUMO}}$
E_{B}(eV)	1.93*	1.85	1.83	0.75*	0.64	0.59
FWHM(eV)	0.31	0.39	0.39	0.36	0.49	0.45

Table 5.8: Binding energies (E_{B}) and full widths at half maximum (FWHM) of the resulting peaks (figure 5.18) from the orbital tomography and fit procedure (see text) for the molecules in the HB monolayer and the minority BW species. Values marked with an asterisk are fixed in the second step of the fitting procedure and taken from an experiment with pure BW PTCDA/Ag(110).

5.5.3 Discussion

From the data in Table 5.8, the following trends can be recognized: (1) HOMO and LUMO levels of molecules in the HB monolayer have significantly smaller binding energies (by at least 80 meV for the HOMO, 110 meV for the LUMO) relative to molecules in the BW monolayer. (2) HOMO and LUMO peaks of molecules in the HB monolayer have a larger FWHM than their counterparts in the BW monolayer. (3) Both in the BW monolayer and in the HB monolayer the LUMO peak is broader than the HOMO peak. This is found for A and B molecules, and similar to the situation found for PTCDA/Ag(111) [9, 101, 135]. (4) Finally, within the HB monolayer HOMO and LUMO peaks of molecule A have larger binding energies E_B compared to molecule B, by 20 meV (HOMO) and 50 meV (LUMO).

We now compare the orbital energies of BW and A molecules. Although both molecules are oriented parallel to the [001] direction of Ag, they have different HOMO and LUMO binding energies. The difference amounts to 80 meV for the HOMO and 110 meV for the LUMO. The fact that the BW structure is commensurate and all its molecules are therefore in identical adsorption sites, while the HB monolayer structure is incommensurate, explains that both HOMO and LUMO peaks of the BW phase are sharper (smaller FWHM) than their counterparts in the HB monolayer phase. Another effect which may contribute to the broadening of the peaks in the HB monolayer is the dispersion which will be discussed later.

However, it is *a priori* not clear whether the difference in peak energies of the HB monolayer can also be explained solely on the basis of the loss of commensurability. Another, possibly even more important reason for this shift may be the difference in intermolecular interactions in the two phases, because the local environment around an A molecule in the HB monolayer differs from that of a molecule in the BW monolayer. This explanation would be in agreement with the results of Kilian *et al.* [62], who have compared the LUMO position of single PTCDA molecules adsorbed on Ag(111) and PTCDA molecules in the disordered low temperature phase on Ag(111) and reported a strong influence of the local molecular environment on the LUMO level, even if the situation regarding the orientation was comparable.

To check whether the binding energy differences between HOMO and LUMO of A and B molecules can indeed be traced back to differences in the respective molecular environments, P. Puschnig *et al.* have carried out a DFT calculation for a freestand-

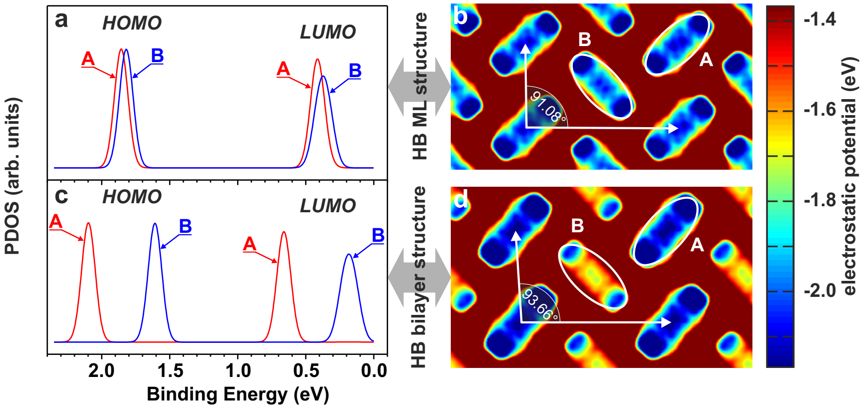

Figure 5.19: Results of the calculation of the freestanding PTCDA HB monolayer (figure 5.3f) and the freestanding upper layer of the HB-on-BW bilayer (figure 5.3d). (a,c) Calculated HOMO and LUMO positions of the two inequivalent molecules A(red) and B(blue) with a gaussian broadening of 50 meV of the HB monolayer (panel a) and the upper layer of the HB-on-BW bilayer (panel c). The binding energy of the HB monolayer B-HOMO is aligned with the experiment. (b,d) Electrostatic potential maps in the plane 1 Å above the calculated layer of the HB monolayer (panel b) and the upper layer of the HB-on-BW bilayer (panel d). The regions which were taken into account to calculate an average potential value for molecules A and B are indicated by white ellipses. The unit cell vectors are represented by white arrows. The DFT calculations were carried out by D. Lüftner and Prof. P. Puschnig at the Karl-Franzens-Universität Graz, Austria.

ing PTCDA layer in the HB monolayer structure. The results of this calculation are displayed in Fig. 5.19a,b. In Fig. 5.19a we indeed see that A and B molecules have different HOMO and LUMO binding energies. In the case of the HOMO the calculated split amounts to 36 meV, while for the LUMO a split of 41 meV is predicted. Both the sizes of the splittings and their signs (A-HOMO and A-LUMO have larger binding energies than their B counterparts) are in agreement with our experimental findings from orbital tomography. Since the substrate is not considered in the calculation, and hence there is no difference in orientation of A and B molecules relative to an external reference direction, and since the effect of the adsorption site in the experiment is expected to be averaged out by the fact that the layer is incommensurate, this agreement between theory and experiment strongly suggests that differences in the molecular environment contribute decisively to the observed binding energy shifts between A and B molecules in the HB monolayer, as well as between the HB and BW monolayer.

Since, as discussed in chapter 5.3, the HB-on-BW bilayer structure of figure 5.3d was in the literature mistaken for a second possible single monolayer structure, we also calculated this HB structure as a freestanding monolayer. The result is shown in figure 5.19c and d. One finds a very large offset of the energy levels for molecules A and B (485 meV for the HOMO). We do not observe such a large offset in our deconvoluted data. This confirms that our sample indeed consisted of the HB monolayer and not of the HB-on-BW bilayer, which has a very similar LEED pattern (Figs. 5.3c,e).

We note that in the calculation the LUMO of the B molecule is substantially broader than the other three orbitals. This can be traced back to a larger in-plane intermolecular dispersion (due to a larger orbital overlap between neighbouring molecules), which yields a band width of 80 meV (compared to 30 meV for the A-LUMO and less than 30 meV for the HOMO of A and B molecules). However, for the freestanding layer one can effectively speak of separate emissions from molecules A and B as the LUMO bands do not cross and effectively there is no hybridization of the orbitals of A and B. In experiment the LUMO of the B molecule is not significantly broadened with respect to the LUMO of the A molecule. This may be a consequence of the limited analyzer resolution. Moreover, we do not observe any signs for dispersion in our experimental data, i.e. the k-patterns of A and B molecules do not change for different energy slices. This again may be a consequence of limited analyser resolution.

Finally we want to address the question how the molecular environment influences the orbital binding energies. Figs. 5.19b,d show maps of the local electrostatic potentials of the freestanding layers, with submolecular resolution. The sign of the potential is chosen such that it gives the potential energy of a negative test charge relative to the vacuum level. A potential of $-1.0\,\mathrm{V}$ means that the work required to remove an electron from this place to infinity is 1 eV. For both layers the potential distribution for A and B molecules is not identical. On average, A molecules have a more negative potential than B molecules ($-1.945\,\mathrm{V}$ vs. $-1.891\,\mathrm{V}$) in case of the HB monolayer. This means that on average it costs 54 meV more energy to remove electrons from A molecules than from B molecules. In other words, the apparent binding energy of equivalent electrons is larger by 54 meV in A molecules than in B molecules. For the HB bilayer structure this discrepancy between A molecules ($-2.091\,\mathrm{V}$) and B molecules ($-1.630\,\mathrm{V}$) is even larger and results in a difference of 461 meV. The fact that the binding energy shifts of the electronic levels are of similar sizes as the potential differences shows that these potential differences are the dominant origin of the observed binding energy offsets between molecules A and B. We note, however, that the HOMO and LUMO levels shift by different amounts when comparing A and B molecules. This is a consequence of the different spatial distributions of the two orbitals; the potential energy map in figure 5.19b is therefore sampled differently for the two orbitals.

Of course, one expects the metal surface to screen the electrostatic fields of the freestanding layer. A DFT calculation of the HB monolayer on the Ag(110) substrate would therefore be desirable. Unfortunately, a direct calculation of the incommensurate HB monolayer on Ag(110) is not possible due to the prohibitively large unit cell, containing at least six PTCDA molecules. The only realistic possibility in the framework of a full DFT calculation to gauge the influence of the metal on the energy offsets between molecules within a HB layer is the calculation of the HB monolayer on the Ag(111) surface, because this structure is commensurate. Such a calculation has been carried out by Rohlfing *et al.* [135]. P. Puschnig *et al.* have repeated this calculation and obtain essentially identical results. There is, however, a problem with this calculation: While the calculation for the freestanding layer in the geometry of the HB monolayer on Ag(111) yields an energy offset between A and B molecules that is in essential agreement with experimental results, i.e. the binding energies of HOMO and LUMO of B molecules are larger than the corresponding binding energies of A molecules, the screening by the metal leads to a reversal of the order of A and B orbitals: Now the HOMO of the A molecule has a larger binding energy than that of the B molecule [135] (We note here that the designation of molecules as A and B on the two surfaces Ag(111) and Ag(110) is arbitrary, and for Ag(111) we follow the convention of Rohlfing *et al.* [135]). While this confirms the influence of the metal, it also shows that DFT is currently unable to predict this influence correctly. Rohlfing *et al.* observe as much and conclude that energy offsets within molecular layers are extremely subtle and may well constitute the limit of the reliability of the calculations, because they may depend on the specifications of the DFT calculation (code, pseudopotential, basis set, and exchange correlation functional) and may be subject to many-body effects beyond the present theory [135]. Improved theoretical methodology may clarify the the situation in the future.

Nevertheless, to estimate the influence of the screening in the present case of HB layers on Ag(110) semi-quantitatively, we employed an electrostatic model based on the electrostatic potentials calculated for the freestanding layer (Fig. 4b), in which the presence of the metal is taken into account by a simple image potential due to the metallic substrate with a spatial distribution corresponding to the orbital. Since the HB monolayer structure on Ag(110) is incommensurate and one hence does not expect a site-specific screening to show up in the experimental spectra, with the consequence that the effect of screening on the measured orbital energies of A and

B molecules is expected to be uniform (except for directional effects), this approximation may not be too bad. Assuming an effective image plane position of 0.5 Å above the topmost Ag-layer, a rough estimate taken from comparison with Al from Table I of Garcia-Lastra *et al.* [136], the image fields lead to a reduction of the level offsets by roughly 30%. This slightly worsens the agreement of the predicted with the measured energy offsets, but nevertheless suggests the major cause of the energy offsets to be of intermolecular electrostatic origin.

5.6 Energy level alignment of LUMO and HOMO in PTCDA/Ag

5.6.1 Introdction

The above section 5.5 stresses the importance of the understanding of energy level alignment for metal-organic interfaces. This section will continue to derive a detailed understanding of the alignment processes, focusing on the frontier molecular orbitals, i.e. LUMO and HOMO, discussing mainly the molecule-substrate interaction. This continues the comparison of the various PTCDA/Ag interfaces which was started in sec. 5.4 in the context of differences in their vertical adsorption height. To draw a complete picture of the interface, geometric and electronic properties have to be discussed together and we will see that, as already mentioned in sec. 5.4, the work function indeed plays a crucial role to merge both aspects in to one picture, but one has to be careful which work function to consider. The adsorption of organic molecules in general modifies the work function of the clean metal and we show here that different molecular states may follow different work functions for their energy level alignment. In particular the PTCDA HOMO follows the work function of the clean metal, while the LUMO follows the combined work function of the interface for the investigated PTCDA/Ag systems.

While experimental data on the electronic structure is already available for HB PTCDA/Ag(111) [9], BW PTCDA/Ag(110) [8] and HB PTCDA/Ag(110) (see sec. 5.5), the data set needs to be completed for PTCDA/Ag(100). Hence, in the first part of this section the missing data on the electronic structure of PTCDA/Ag(100) is presented. It turns out that the work function is a crucial parameter to understand the energy level alignment of the molecular orbitals, but unfortunately the experimental

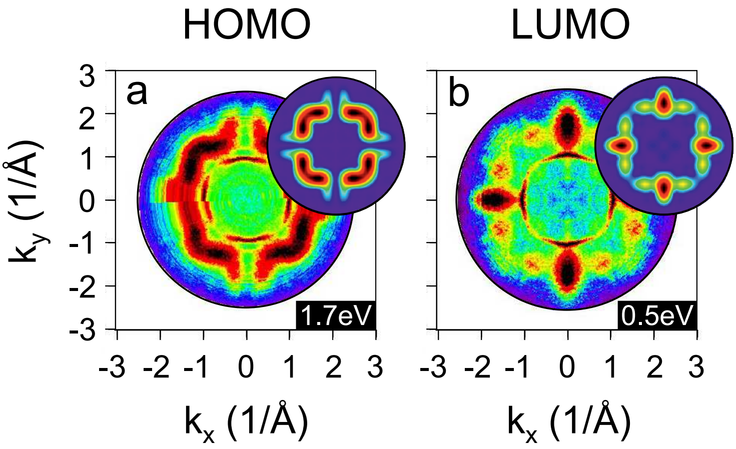

Figure 5.20: CBE maps of the HOMO (a) and the LUMO (b) of PTCDA/Ag(100) with the corresponding calculated CBE maps used for the tomography approach as inset. Fitting the complete 3D data cube leads to the density of states shown in Fig. 5.21b.

results for the work function of the various low index Ag surfaces are not conclusive for our discussion, because a large discrepancy between the various results reported in literature is observed (compare Fig. 5.15). Therefore, we will employ calculated work function values in our discussion. These are provided by the group of Prof. Peter Puschnig (Karl Franzens Universität Graz). Unfortunately, this restricts the discussion to the commensurate HB PTCDA/Ag(111), PTCDA/Ag(100) and BW PTCDA/Ag(110) interfaces and excludes the HB PTCDA/Ag(110) system from our discussion, because work function data could not be calculated for the latter system (due to its non commensurability).

5.6.2 Experimental results

All experimental data on the electronic structure discussed in this section stem from beam times at the BESSY II synchrotron in Berlin, using the setup described in sec. 2.5.1 and the orbital-tomograhy approach described in sec. 2.3 and already employed in sec. 5.5. While the data on PTCDA/Ag(111) [9] and BW PTCDA/Ag(110) [8] is already known, new data on PTCDA/Ag(100) is presented. The Ag(100) single crystal was cleaned by repeated cycles of sputtering with Ar^+ ions and subsequent annealing. The surface structure was checked with LEED. PTCDA was evaporated from a home-made Knudsen cell at 400 K onto the sample at room temperature. The structure of the molecular layer (see sec. 5.2) was verified by LEED. All measure-

	averaged HOMO (eV)	averaged LUMO (eV)	LUMO-HOMO gap (eV)
BW PTCDA/Ag(110)	1.93	0.75	1.18
PTCDA/Ag(100)	1.70	0.47	1.23
HB PTCDA/Ag(111)	1.58	0.22	1.37

Table 5.9: Binding energies of electronic levels for different ordered monolayer phases of PTCDA. These should be compared to the following literature values: BW/Ag(110): HOMO 1.8 eV, LUMO 0.6 eV [106]; HB/Ag(111): HOMO 1.6 eV, LUMO 0.3 eV [106]; Bulk values: HOMO 2.52 eV, LUMO −1.26 eV [137–139].

ments were conducted at room temperature. Hence, our experimental conditions match the cases for HB PTCDA/Ag(111) [9] and BW PTCDA/Ag(110) [8] and results are directly comparable.

Fig. 5.20 shows experimental CBE maps of the resulting datacubes with a presentation of the corresponding calculated CBE maps used for the orbital tomography analysis. The observed shape of the intensities is very similar to the case of HB PTCDA/Ag(110) (see Fig. 5.17), because in both layers we find two molecules per unit cell, rotated by 90° to each other (compare lateral structures in Fig. 5.2b and Fig. 5.3f). However, in contrast to the A-B energy split discussed for the case of HB PTCDA/Ag(110) in sec. 5.5, both molecules in the PTCDA/Ag(100) unit cell are equivalent, which is confirmed by the result of the orbital tomography shown in Fig. 5.21b, where the red and blue curves show their peaks at the same binding energy position. Furthermore Fig. 5.21 shows the trend of the LUMO and HOMO binding energies to increase in the order of HB PTCDA/Ag(111), PTCDA/-Ag(100) and BW PTCDA/Ag(110), hence following the order of decreasing carbon backbone adsorption height (see sec. 5.4). To allow a quantitative analysis, the molecule averaged HOMO and LUMO binding energy positions are given in Table 5.9.

5.6.3 Discussion

To discuss the results in terms of energy level alignment, we need to take into account the work function of the different systems. Because experimental data for work function measurements seem to be unreliable due to their large scattering (see Fig. 5.15), calculated work function values are considered, which can be expected to yield reasonably accurate values [64, 140]. The calculation was carried out in the group of Prof. Peter Puschnig (Karl Franzens Universität Graz) and the resulting numbers are presented in Table 5.10. The calculation was carried out on a Ag

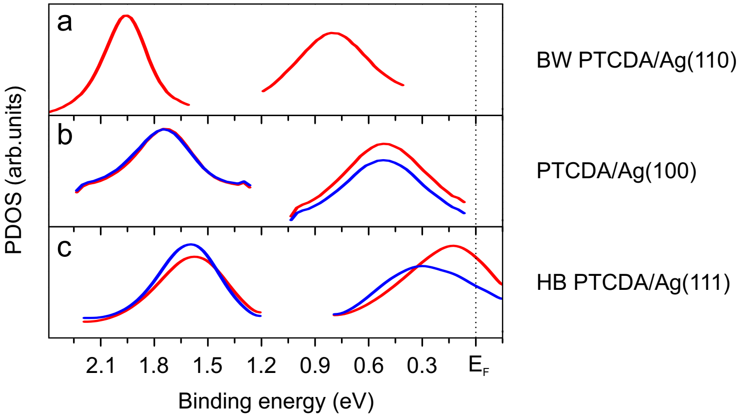

Figure 5.21: PDOS extracted by the tomography approach (see sec. 2.5.1 for details) for BW PTCDA/Ag(110) [8] (a), PTCDAAg(100) (b), and HB PTCDA/Ag(111) [9] (c). Two inequivalent molecules in the unit cell lead to different results depicted in red (blue) for molecules A(B) as it is seen here for HB PTCDA/Ag(111) [9] and discussed in detail in sec. 5.5. For PTCDA/Ag(100) the peak positions of the blue and red lines coincide, confirming that the molecules of different orientation in the unit cell are equivalent.

slab with PTCDA adsorbed on top in the corresponding lateral configuration (see Figs. 5.2 and 5.3b) and adsorption height (see Fig. 5.13). The work function Φ is the resulting work function of the PTCDA/Ag system, while Φ_0 is is the work function ofbare Ag determined at the bottom of the Ag slab.

Inspecting the values of Φ_0 we find the highest work function for HB PTCDA/-Ag(111), next is PTCDA/Ag(100), and lowest the value for BW PTCDA/Ag(110), in agreement with the tendency observed in experiment (see Fig. 5.15). The impact of the PTCDA adsorption, indicated by the difference $\Phi - \Phi_0$ interestingly follows the same trend, increasing the overall spread of the work function from 0.35 eV in case of the bare metals to 0.47 eV for the PTCDA/Ag interfaces.

To construct the expected energy level alignment on the example of HB PTCDA/-

DFT	BW PTCDA/Ag(110)	PTCDA/Ag(100)	HB PTCDA/Ag(111)
Φ	4.23 eV	4.49 eV	4.70 eV
Φ_0	4.05 eV	4.23 eV	4.40 eV
$\Phi - \Phi_0$	0.18 eV	0.26 eV	0.30 eV

Table 5.10: Work functions and electrostatic potentials from DFT, calculated by the group of Prof. Peter Puschnig (Karl Franzens Universität Graz). Φ: work function of PTCDA/Ag(hkl); Φ_0: work function of Ag(hkl), determined at the bottom side of the PTCDA/Ag slab;

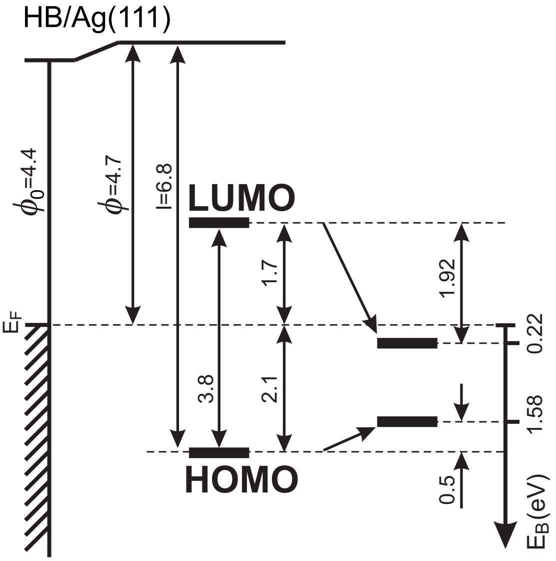

Figure 5.22: Energy level alignment of HOMO and LUMO for HB/Ag(111), constructed from the theoretical work function data of Table 5.10, the bulk ionisation energy of PTCDA [137, 141] and its bulk energy gap [139, 142] (left), compared with the true alignment (right). The latter determined from the experimental data [9] shown in Fig. 5.21c and Table 5.9.

Ag(111) from these work function values, we take into account the bulk ionisation potential of PTCDA, which is $I = 6.8\,\text{eV}$ [137, 141] and its bulk energy gap of 3.8 eV [139, 142] and end up with the construction shown in the left part of Fig. 5.22. Compared to our experimental results, drawn on the right side of Fig. 5.22, this construction fails to predict the correct binding energies in respect to the Fermi level E_F. While the HOMO is found only 0.5 eV above the constructed value, the LUMO is found 1.92 eV lower. Hence, a symmetrical movement of both energy levels towards E_F, as it could be expected by screening effects, cannot explain the significantly larger shift of the LUMO. Therefore, we can see that both orbitals are affected in a different way, and we can expect them to play substantially different roles in the adsorption process.

First we will discuss the situation for the HOMO. According to Table 5.9 the HOMO binding energy increases from HB PTCDA/Ag(111) over PTCDA/Ag(100) to BW PTCDA/Ag(110), while the work function is decreasing in this order. If we calculate the ionisation energy of the HOMO (I_HOMO), taking into account the work function values for the metal substrate, the shift in binding energy is always canceled out and we find the value of $I_\text{HOMO} \approx 5.96\,\text{eV}$ for all three low index Ag surfaces with a spread

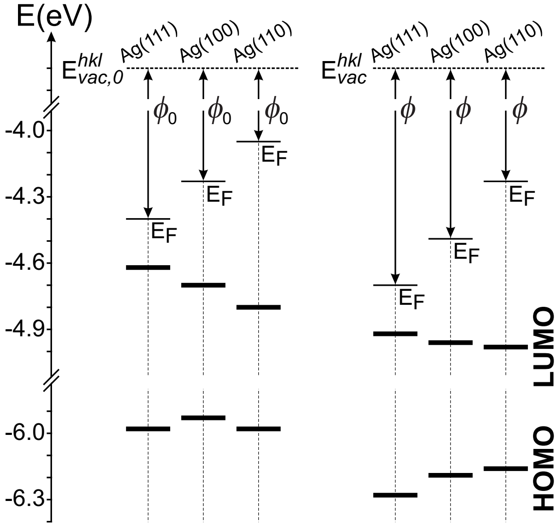

Figure 5.23: Measured HOMO and LUMO binding energies E_B, relative to the Fermi level E_F, of PTCDA monolayers on Ag(111), Ag(100) and Ag(110). (a) Vacuum levels of the bare surfaces $E_{\text{vac},0}^{hkl}$ are aligned. Φ_0^{hkl} are the calculated work functions of the correspondin Ag(hkl) surfaces. (b) Vacuum levels of the covered surfaces E_{vac}^{hkl} are aligned. Φ^{hkl} are the calculated work functions of the corresponding monolayer PTCDA/Ag(hkl) surfaces.

of only 50 meV, while the spread in HOMO binding energies is 350 meV. This means that the HOMO is vacuum level aligned for all three PTCDA/Ag systems with the work function of the metal surface, as it is drawn in the left part of Fig. 5.23, and a general ionisation potential, calculated from the metal work function and the HOMO binding energy, exists for all PTCDA/Ag systems.

We excluded the HB PTCDA/Ag(110) from this picture, because work function calculations for the HB PTCDA/Ag(110) interface are not possible due to the missing commensurability of the superstructure unit cell. However, if the above statement is correct, only the work function of the bare metal has to be considered, which is of course independent of the superstructure. Hence, the HOMO binding energy should be identical for BW PTCDA/Ag(110) and HB PTCDA/Ag(110). Upon inspection of Table 5.8 we find a mean value of 1.84 eV for the HOMO binding energy of HB PTCDA/Ag(110) while BW PTCDA/Ag(110) is reported to yield 1.93 eV [8]. Although this HOMO binding energies are not identical, the observed difference of 90 meV is still much smaller than the mentioned spread of HOMO binding energies of 350 meV. Hence, this finding does not invalidate our finding, but may serve as an indicator for the expected variation of the ionisation potential. Furthermore, one

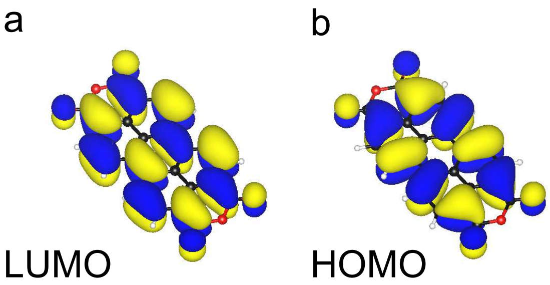

Figure 5.24: PTCDA ball-and-stick models with wavefunction isosurfaces of the LUMO (a) and HOMO (b) orbital, calculated for a free molecule in the gas phase by D. Lüftner (Karl Franzens Universität Graz) and visualized using the *VESTA 3* Software [143].

should note that it is of the same order as the spread of reported binding energy values in literature, e.g. compare the reported BW PTCDA/Ag(110) HOMO binding energy of 1.8 eV [106] to the 1.93 eV [8] used in this analysis. Despite this uncertainties, it is very surprising that one parameter, namely the bare metal workfunction Φ_0, determines the final binding energy of the HOMO to this extent for this collection of interfaces with different lateral arrangements, molecular and surface densities, adsorption heights and intramolecular bending.

Inspecting Fig. 5.23 we find that the LUMO does not follow the alignment of the HOMO. However, if we take into account the work functions of the PTCDA/Ag system instead of the values for the bare metal, we find the situation depicted on the right side of Fig. 5.23. The sum of LUMO binding energy plus the the work function of the PTCDA/Ag system results in an ionisation potential of $I_{\mathrm{LUMO}} \approx 4.95\,\mathrm{eV}$. Hence, we find the same surprising situation for the LUMO as for the HOMO if the work function of the interface (Φ) is considered instead of the bare metal (Φ_0). Again, the variation of I_{LUMO} with 60 meV is much smaller than the spread of 530 meV for the LUMO binding energies. Surprisingly, the single value I_{LUMO} determines the LUMO binding energy position accurately for the PTCDA adsorption on all Ag surfaces, although even the LUMO occupation is different between these systems.

Considering the results obtained for the vertical adsorption height for PTCDA on Ag substrates in sec. 5.4.8 and the role of the work function in the determination of the equilibrium height, the analysis here clarifies the interplay between the adsorption height, the work function of the PTCDA/Ag system and the LUMO binding energy. A change in one of these parameters would immediatly affect the other two, hence the adsorption distance must follow from the neccessary binding energy and work function value which are fixed due to their relation to I_{LUMO}.

While the finding of constant ionisation potentials of HOMO and LUMO for PTCDA on all low index Ag surfaces is very surprising on its own, the difference in the two orbitals is astonishing as well. Due to their reference to different work functions, namely the bare metal work function for the HOMO and the PTCDA/Ag work function for the LUMO, it becomes clear that both orbitals are involved in different ways in the adsorption and bonding process. One may consider the HOMO to be part of an weakly interacting physisorbed system aligned with the metal workfunction. At the same time the LUMO is obviously more involved and even becomes (partially) occupied in the adsorption process. Hence, its reference to the final PTCDA/Ag work function seems reasonable. In terms of interplay between work function, binding energy and molecular adsorption height, the LUMO orbital seems the proper canditate for manipulation to tune these parameters. However, the striking question that is brought up by this arrangement becomes clear by looking at the real space wave functions of both orbitals in Fig. 5.24. The density of states of the metal sp-band is broad and the spatial overlap of HOMO and LUMO is very large. How can such a situation lead to the observed, completely different behaviour of both orbitals?

Although a surprising rule for the prediction of the HOMO and LUMO energy level alignment for PTCDA/Ag interfaces is presented, which needs to be adapted to other molecule-metal systems in a next step to prove its general applicability, the most interesting part which future research should adress is to answer the question what is the reason behind the different alignment processes revealed here.

5.7 Native order of stronger bound molecular Orbitals

5.7.1 Introduction

The knowledge of the energy level alignment of molecular orbitals at metal-organic interfaces is crucial for the understanding and the improvement of organic opto-electronic devices. This alignment has two aspects. First, the primal ordering of molecular levels in gas phase molecules and, second, the modification of the energy level sequence by either shifting or even changes of the primal energy level ordering. The primal order is so far only accessible by theory. This is critical, since in calculations the ordering is influenced by many-body effects such as self screening of the electrons, such that DFT often gets this ordering wrong [144]. Therefore, an experimental determination of the primal molecular energy level odering would be highly desirable.

How can this be achieved? Standard angle integrating photoemission experiments only reveal ernergy level positions of orbitals, without the possibility to identify them. The identification is possible via the angular distribution of the photoelectrons, but of course this cannot be measured in gas phase, due to the intrinsic averaging over all emission angles. One may try to measure on inert substrates, but we have chosen another way to have the advantage that molecules are embedded in ordered structures, and hence the angular distribution can be accessed. Of course, the question arises whether the measured energy level ordering corresponds to the gas phase. Therefore, a systematic study of the influence of interfaces on the energy level ordering is necessary. If it turned out that the influence of the interface was small, we could use ARPES as introduced in sec. 2.3 and in particular orbital tomography [7–9] for a study of the primal gas phase energy level ordering.

In this section we present a systematic study of the energy level ordering of PTCDA on Ag. We have chosen Ag, because the low position of the d-band in comparison to Au and Cu [145] allows a large number of orbitals to be studied without interference from the d-states. In order to investigate the possible influence of the interface, we vary both the surface orientation and the molecular packing systematically. In this way the influence of molecule-substrate as well as molecule-molecule interactions can be studied. For the present purpose, PTCDA is an ideal molecule, because it forms

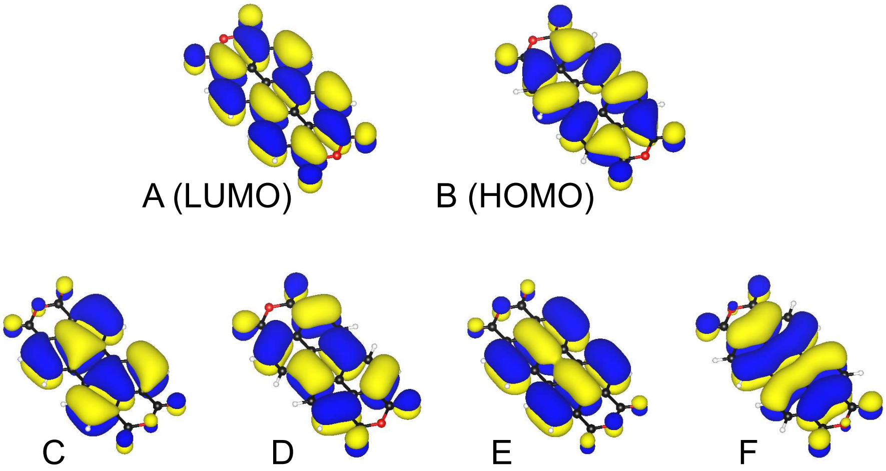

Figure 5.25: PTCDA ball-and-stick models with wavefunction isosurfaces of the LUMO, HOMO and the four in energy following π-orbitals (C-F), calculated for a free molecule in the gas phase by D. Lüftner (Karl Franzens Universität Graz) and visualized using the *VESTA 3* Software [143].

highly ordered phases on all three low index Ag surfaces, ranging from commensurate to incommensurate and covering different packing motifs as shown in chaps. 5.2 and 5.3. Moreover, in previous work [8] as well as sec. 5.5 it was already demonstrated that PTCDA/Ag(110) is suitable for orbital tomography. In particular, we study 4 different monolayers on three substrate orientations: PTCDA/Ag(111) [6, 60, 101], PTCDA/Ag(100)[99, 102] and the two monolayer phases of PTCDA/Ag(110) [8, 25–27, 39, 54, 99, 103, 104, 106, 109].

5.7.2 Results

The ARPES experiments were performed at the BESSY synchrotron using the toroidal analyzer chamber described in sec. 2.5.1 and the orbital tomography approach was applied as described in sec. 2.3. To obtain the theoretical CBE maps used for the fit, the calculated CBE map of a single gas phase PTCDA molecule was summed up according to the orientations of the molecules in the unit cells (see secs. 5.2 and 5.3) and the presence of multiple superstructure domains on the sample.

Following gas phase calculations [8], the molecular orbitals are named alphabetically with ascending binding energy starting from LUMO and HOMO as A and B, respectively. The corresponding wave functions are shown in Fig. 5.25.

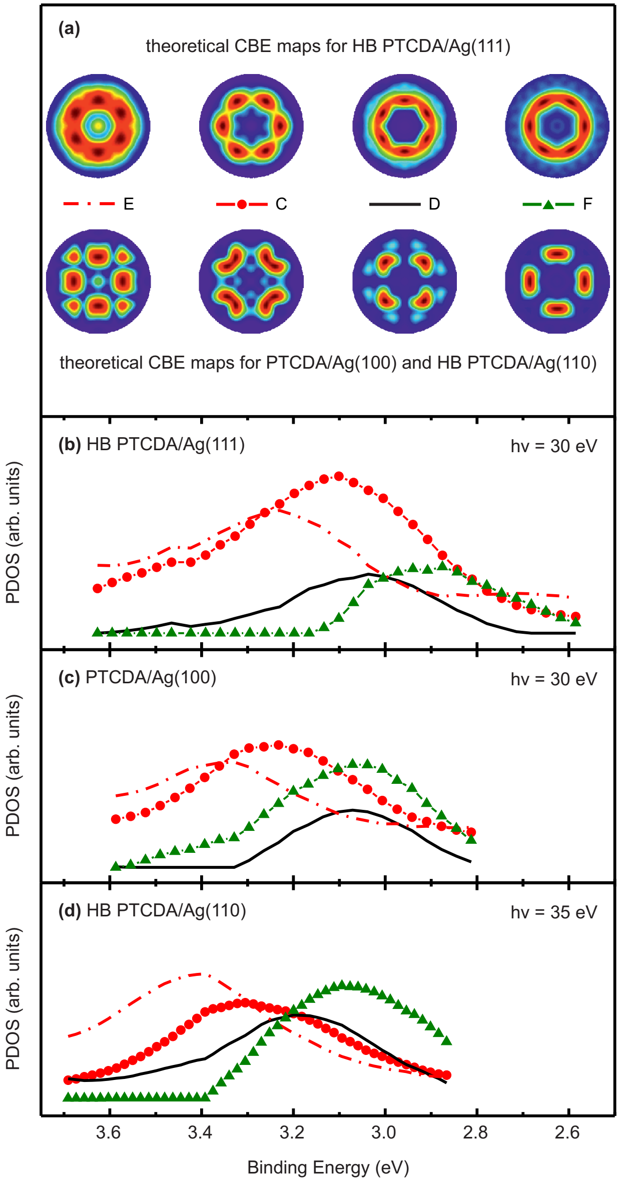

Figure 5.26: Orbital tomography results for the various PTCDA/Ag systems. In each case four orbitals could be deconvoluted. The theoretical CBE maps used for the identification of each orbital are shown in panel (a). The maps differ between the investigated systems due to the differences in the surface symmetry and the molecule orientation in the unit cells. For the corresponding lateral structures see sec. 5.2 and 5.3.

	Binding Energy (eV)			
	E	C	D	F
HB PTCDA/Ag(111)	3.24	3.11	2.98	2.88
PTCDA/Ag(100)	3.36	3.23	3.07	3.05
HB PTCDA/Ag(110)	3.41	3.29	3.18	3.08
BW PTCDA/Ag(110)[8]	3.53	3.38	3.30	3.25

Table 5.11: Binding energy positions of the orbitals in the fitting results (see Fig. 5.26) in eV. Values for BW PTCDA/Ag(110) are taken from ref. [8]

The resulting PDOS are shown in Fig. 5.26 and the corresponding peak positions are visualized in Fig. 5.27 and summarized in Table 5.11. Several observations can be made, but most prominent is the finding that the order of the orbitals is the same for all investigated systems, namely the order is E-C-D-F for descending binding energy. Furthermore, this agrees with the orbital order which was reported for PTCDA/Ag(110) in the BW arrangement [8]. Numbers from ref. [8] are included in Table 5.11 and will be included in the discussion of the data. Inspecting the results more carefully, it is found that the relative energy offsets between the peaks are very similar for all surfaces, but slight deviations are visible. The overall energy difference between the first peak (from orbital E) and the last peak (from orbital F) differs therefore between all investigated systems and this difference ranges from 360 meV in case of PTCDA/Ag(111) to 280 meV in case of BW PTCDA/Ag(110). The absolute binding energy of all orbitals increases from PTCDA/Ag(111) over PTCDA/Ag(100) to PTCDA/Ag(110) by more than 270 meV, which is of the same order as the shift of the HOMO and LUMO, discussed in sec. 5.6.

Looking at the relative intensities of the peaks in Fig. 5.26, one finds differences between the systems which are especially obvious when comparing the HB PTCDA/-Ag(110) to the PTCDA/Ag(111) results. We attribute these intensity differences on the one hand to the difference in the photon energy, as we used 30 eV to measure PTCDA/Ag(111) (and PTCDA/Ag(100)) but 35 eV to measure PTCDA/Ag(110) and, on the other hand, to the uncertainty of the fitting procedure, which is actually most challenging for PTCDA/Ag(111), because the differences in the electron k-space distributions of the orbitals are smallest in this case, due to the many rotational superstructure domains. Therefore the following discussion is constrained to the energy positions of the orbitals.

The observation that the difference between peaks E and F is not equal among the investigated systems can be linked to the presence of inequivalent molecules in the unit cell of the corresponding superstructures. PTCDA in the HB phases on Ag(111)

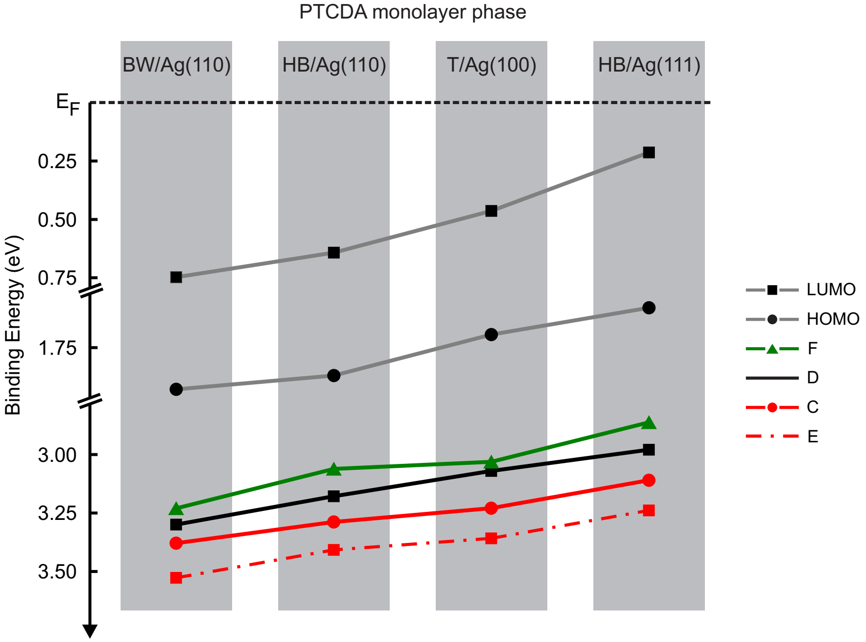

Figure 5.27: Binding ernergies of the orbitals C-F for PTCDA on different surfaces and in different lateral arrangements. Visualization of the results presented in Table 5.11. Values for BW PTCDA/Ag(110) are taken from ref. [8]. For an easier comparison the values for the HOMO and LUMO, taken from Table 5.21 and Table 5.8 are plotted as well.

and Ag(110) show the largest differences of 360 meV and 330 meV, respectively. As one should expect a difference in binding energy between molecule A and B, which is not resolved here but known from investgations of the HOMO and LUMO as discussed in sec. 5.5 [9, 27, 62], this may lead to a slightly broader distribution of the orbitals compared to PTCDA/Ag(100) with an E-F peak to peak distance of 310 meV. This is in agreement with the results for BW PTCDA/Ag(110), which has only one molecule per unit cell and shows an even smaller E-F peak to peak distance of 280 meV.

The absolute energy shift of all orbitals is much larger than the differences of the orbital distribution discussed above. From HB PTCDA/Ag(111) to BW PTCDA/-Ag(110) we see energy shifts in the range of 270 meV (orbital C) to 370 meV (orbital F). The absolute shift follows the trend of the higher orbitals, namely HOMO and LUMO which also shift to higher binding energy from HB PTCDA/Ag(111) to BW PTCDA/Ag(110) as shown in Fig. 5.27. This absolute shift can be understood as a result of the molecule-substrate interactions and is linked to the corresponding work function, which is discussed in detail in sec. 5.6 and therefore need not be addressed here. However, besides the absolute shift we see as well a differential shift. The orbitals with the lower binding energy are affected more (F, 370 meV; D, 320 meV) than the orbitals with higher binding energy (C, 270 meV; E, 290 meV). Interestingly this follows the observation that the LUMO is shifted more than the HOMO due to their different alignment procedure (see sec. 5.6). Hence, this differential shift can be interpreted as the different degree to which the orbitals are affected by molecule-substrate interactions.

Nevertheless the orbital order E-C-D-F is preserved in all systems, contradicting the orbital ordering of PTCDA which is reported from gas phase calculations, where the order F-E-D-C is prevalent [8, 144]. This leads to two possible explanations: Either these calculations predict a wrong order or the order is changed upon adsorption in an identical manner for all Ag surfaces. Here, it must be mentioned that the LUMO shift upon adsorption (compare Fig. 5.22) might be responsible for pushing the orbitals C and E to higher binding energy, because they belong to the same band [8]. While this would explain the energy order of C and E in a general manner for all Ag surfaces, the resulting order would be expected to be E-C-F-D from theory which leaves the question open, why D and F are interchanged. To answer this question we have to discuss the possible mechanisms which may lead to a reordering of the orbitals. One can expect that a reordering would be driven by the molecule-substrate interaction, the molecule-molecule interaction or a combination of both.

5.7.3 Discussion

First we look at the molecule-molecule interaction. It is known that the resulting molecule-molecule interaction is strongly dependent on the lateral adsorption geometry of the molecule [27]. This is especially interesting in the case of the HB and BW phase of PTCDA/Ag(110), where two different lateral structures can be directly compared on the same surface. If the molecule-molecule interaction was decisive for the order of the molecular orbitals investigated here, a difference should be observed comparing especially this two systems. This is not the case, and therefore we conclude that a possible orbital reordering upon adsorption cannot be explained by molecule-molecule interactions.

Turning to the molecule-substrate interaction we have shown in sec. 5.4 that the vertical adsorption height is a good parameter to deduce the strenght of this interaction. For the PTCDA adsorption on Ag, all surfaces were investigated by means of normal incidence X-ray standing wave measurements, showing that the adsorption height decreases from PTCDA/Ag(111) [60] over PTCDA/Ag(100) to BW PTCDA/Ag(110) [39] as discussed in sec. 5.4.8. A crucial influence of the molecule-substrate interaction on the orbital ordering should therefore reflect the different interaction strengths as differences in the orbital order of the investigated systems. This is not the case, and therefore the orbital ordering seems to be rather independent of the molecule-substrate interaction. This leaves only the opportunity that changes in the molecule-substrate interaction are always countered by the molecule-molecule interaction and vice versa, but such a cancellation of changes seems to be very unlikely for the extent of the data presented here.

The fact that all three surfaces show the same energy level ordering suggests that in spite of charge transfer and hybridization, the general character of the wave functions, which determines the energy order (nodal planes) is a robust property of the molecule and survives interaction with the surface or a very general influence of silver determines the orbital ordering. Note in particular that the speculation in ref. [8] which ascribes the different energy level ordering on BW PTCDA/Ag(110) compared to theory to the specific adsorption site and therefore the specific orbital overlap with silver atoms, is disproven by the results of this chapter.

Interpreting the results on a more general level, the stability of the orbital ordering shows that adsorbed molecules can be used to study gas phase energy level ordering. In our example the molecule-molecule and the molecule-substrate interactions lead to shifts but no interchange of the orbital order although the four orbitals studied here are very closely spread in energy. We suggest that this robustness of the energy level ordering also applies to other examples of not too strongly interacting molecules. However, future experiments on ordered molecules on other surfaces, especially insulators are highly desirable to confirm the results and rule out any Ag specific influence. In ref. [8] a range of methods was used to calculate the orbital order, including various DFT functionals (PBE, HSE), selfinteraction correction and the GW approximation. Most of them show the same energy level order, but this order deviates strongly from the one found in our experiments. Therefore, parallel to new experiments theoretical approximations should also be inspected to indentify possible mistakes.

5.8 Summary

This chapter about the adsorption of PTCDA on various Ag surfaces presents a comprehensive overview over several aspects which define the adsorption behaviour. Employing LEED, XSW and the orbital tomography technique, results on the lateral and vertical geometry of the PTCDA molecules in the condensed monolayer structures are revealed, and the electronic properties of the layers are investigated. The multitude of already available results in the literature regarding the various PTCDA/Ag systems is used, and existing gaps in the data base are filled by the presented experiments to draw a complete picture of these model systems. Especially in the case of PTCDA/Ag(100) data was missing regarding its vertical adsorption heights and electronic structure, but also lateral adsorption site, which is presented in the respective sections of this chapter. This collection of results from various perspectives allows to unravel some general adsorption mechanisms on the example of PTCDA/Ag, which are expected to be valid for a broader range of metal-organic interfaces.

First, the different roles of LUMO and HOMO in terms of their involvement in the bonding process are revealed. While the energy level alignment of the HOMO is driven by the bare metal workfunction, which is justifying the expectation of a rather passive role in the bonding, the situation for the LUMO is different. So far, this is not surprising, because the (partial) occupation of the LUMO is already a strong hint that this orbital plays a key role in the bonding. However, the astonishing point is that the general mechanism behind the energy level alignment of the LUMO is very similar to the HOMO with a difference in the reference point. Namely, where the work function of the bare metal surface determines the HOMO binding energy of the interface, the work function of the final metal-organic interface determines the energy level alignment of the LUMO.

Second, a link between the electronic and the geometric structure is established. The larger the adsorption height of the adsorbate is, the lower is the final binding energy of the LUMO. Again, the linking quantity is the work function, because it is a measure for the charge spill-out above the surface. This spill-out and the degree of its uptake by the molecule define the adsorption height on one hand and the final LUMO binding energy on the other hand.

Third, while the molecule-substrate interaction via the LUMO filling and the work function plays the decisive role in the energy and adsorption height alignment, it is shown that molecule-molecule interactions and the resulting lateral order of the adsorbate layer alter the precise outcome of the erngy level alignment. They are responsible for the 'fine-structure' of the energy level alignment, which can lead to an orbital energy shift between molecules within the same adsorbate layer.

6 TPA:Fe/Cu(100) - A metal organic network

6.1 Introduction

The development of future nanotechnology devices is strongly dependent on the level of miniaturization that can be archieved. While current integrated circuits are manufactured by lithography in a top down approach, the development of devices on an even smaller scale asks for design on the molecular and atomic scale. A promising way to achieve this is to make use of the self assembly processes on surfaces to produce small-scale structures by the bottom up approach [13]. Therefore this field of research has attracted great interest in the past decade and several kinds of systems, for example self assembled monolayers and metal-organic coordination networks are worked on in parallel, to achieve a controlled structure growth [14].

In this chapter we focus on the formation of metal coordinated molecular networks. Our example is terephtalic acid (TPA, see Fig. 6.1a) coordinated by Fe atoms on a Cu(100) surface. As the lateral structures formed for the various stoichiometric molecule metal ratios are already well investigated by means of STM and XPS [15, 16], we will focus on the so-called cloverleaf phase that is shown in Fig. 6.1c. In this picture one Fe atom is present per four TPA molecules. It forms a nanometer sized two dimensional grid which exhibits a well-ordered arrangement of magnetically active centers on the surface [17]. To get a fundamental understanding of the interplay between the coordinative metal-molecule and the chemical molecule-substrate bond, the vertical adsorption height is a useful indicator. Furthermore, additional O_2 can be selectively adsorbed on the Fe centers, allowing to tune their magnetic properties [17]. Again the fundamental understanding of this process would benefit from the knowledge of precise vertical structures.

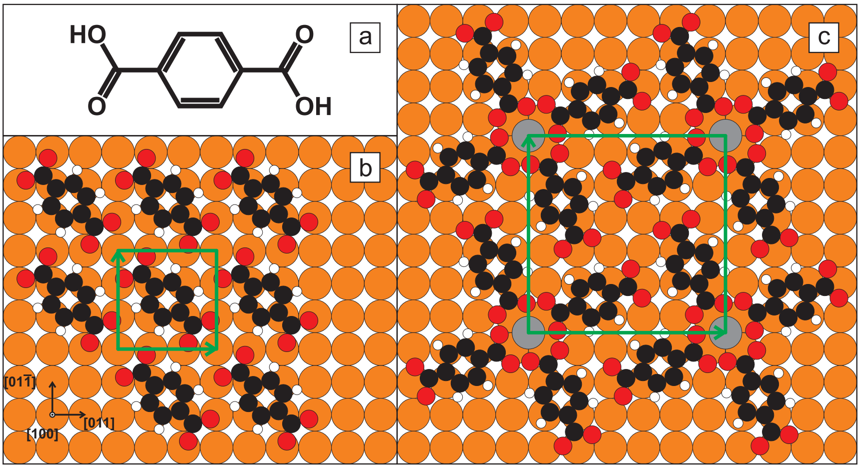

Figure 6.1: Panel (a) shows the structure formula for TPA. Furthermore two unit cells for different TPA phases are depicted. In panel (b) the pure TPA/Cu(100) structure is presented after complete deprotonation of the molecule as reported in ref. [146]. In panel (c) the so called clover leaf phase is shown which can be formed by Fe deposition onto the pure TPA/Cu(100) phase. Around each Fe center four molecules are coordinated [15]. Carbon is shown in black, oxygen in red, hydrogen in white, copper in orange and iron in grey. Green lines indicate the corresponding 3×3 and 6×6 unit cells, respectively.

To achieve this, XSW measurements on the TPA:Fe/Cu(100) sample were conducted before and after O_2 deposition. Previous XSW investigations on the pure molecular phase of TPA/Cu(100) (see Fig. 6.1b for the lateral structure) done by Mercurio [36] allow to trace the influence of the Fe presence on the molecules.

6.2 Experimental

The experiments were performed at the ESRF Grenoble light source at beamline ID 32 in the UHV vessel described in sec. 2.5.2 with molecule and metal evaporators mounted on the preparation chamber. The Cu(100) crystal was cleaned by repeated Ar^+ ion sputtering and subsequent annealing cycles. Because Cu forms a fcc crystal, the (100) reflection is extinct, and the (200) reflection is used for the XSW measurement. This results in a Bragg plane distance of 1.81 Å. The parameters for the XPS and XSW data acquisition are given in Table 6.1.

The TPA was evaporated from a homemade Knudsen cell at 165 °C onto the sample at room temperature. Subsequent annealing at 130 °C was applied to fully depro-

Parameter	XSW data sets			Off-Bragg XPS			
	O1s	C1s	Fe2p	O1s	C1s	Fe2p	O1s after O_2 dose
$\Delta E_{\mathrm{photon}}$ (eV)	4-8	4-8	4-8				
E_{photon} (eV)				3420	3420	3420	3420
XPS spectra	28-30	28-30	16-30				
repeats	1	1	1/3	7	9	4	3
pass energy (eV)	100	100	100	100	100	100	100
ΔE_{kin} (eV)	0.2	0.2	0.4/0.6	0.2	0.2	0.4	0.2
dwell time (s)	0.4	0.4	1.5/1	0.4	0.4	1.5	0.5

Table 6.1: Acquisition parameters used for the XSW data sets and off-Bragg XPS spectra. The number of XPS data sets and the photon energy range for an XSW scan were varied to speed up the measurement process. Fig. 6.10 shows the yield curves for two datasets with different parameters. To cover the large $\Delta E_{\mathrm{photon}}$ values the photon energy step is chosen larger in the beginning and the end of the yield curve than in its centre. In the Fe2p XSW case two numbers separated by a slash are given for several parameters. The left number corresponds to the data sets 006, 013, 031, 041, 042, and 043, the right number to all other data sets.

tonate the TPA and form the ordered TPA/Cu(100) phase shown in Fig. 6.1b. The successfull preparation of the TPA monolayer phase was confirmed by LEED measurements (see Fig.6.2a) which show the characteristic 3 × 3 structure of fully deprotonated TPA/Cu(100) [146].

To achieve the formation of a metal-organic network Fe was deposited on top of the TPA/Cu(100) film at room temperature from an electron beam evaporator and subsequent annealing of the sample at 200 °C was applied. The successfull preparation

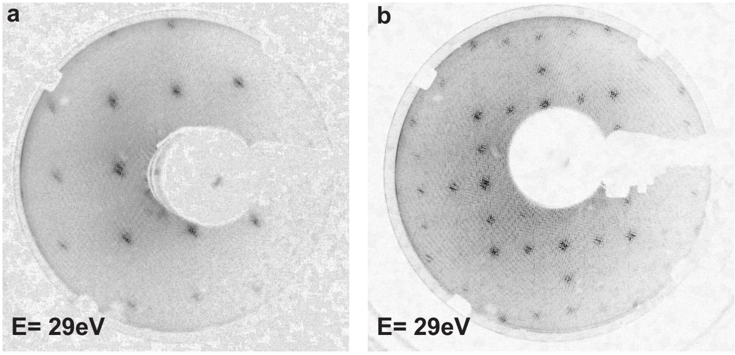

Figure 6.2: LEED pictures of (a) the 3 × 3 structure which corresponds to the fully deprotonated TPA/Cu(100) system [146] and (b) the 6×6 structure which indicates the formation of the cloverleaf phase after Fe deposition [15]. The corresponding structure models are shown in Fig. 6.1b and c respectively.

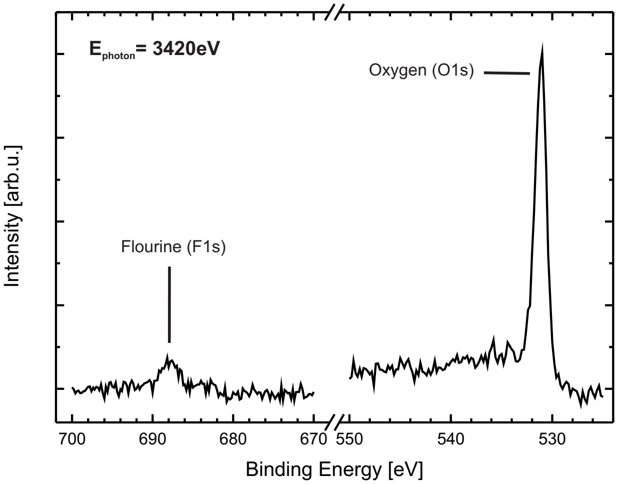

Figure 6.3: Off-Bragg XPS spectrum showing the presence of F1s and relating the peak height to the intensity of the O1s peak. The F1s energy of 688 eV raises the expectation that it is present in a F_c compound [147]

of the well-known cloverleaf phase (see Fig. 6.1c) of the TPA:Fe/Cu(100) system [15] was again confirmed by the characteristic LEED pattern, which shows a 6 × 6 superstructure as depicted in Fig. 6.2b.

Unfortunately, the observation of the 6 × 6 LEED pattern for the cloverleaf phase does not allow to deduce information about possibly coexisting domains of pure TPA/Cu(100), since all 3 × 3 superstructure spots coincide with spots of the 6 × 6 pattern. Therefore, the possible presence of molecules not coordinated in a metal organic network has to be kept in mind for the data analysis.

The second unfortunate detail about the experiments is the presence of flourine within the UHV chamber during the experiments. While the source of the flourine contamination remained unclear, it was visible in the mass spectra of the residual gas and in XPS spectra taken from our sample. In Fig. 6.3 the F1s peak is shown in comparison to the oxygen signal of subsequent XPS spectra. From the binding energy of 688 eV one could expect the flourine to appear as a CF compound [147]. The possible influence of flourine will be addressed in the discussion of the data especially in sec. 6.4 and sec. 6.5.

6.3 O1s results

This section discusses the data analysis for the oxygen species. While in the pure TPA/Cu(100) phase all oxygens are identical and therefore only one peak is observed in the O1s spectrum, which is located at a binding energy of 531.4 eV [146] (531.2 Å [36]), for the prepared TPA:Fe/Cu(100) network this peak is expected to split into a component for the coordinated oxygen at 531.6 eV and a component for the uncoordinated oxygen at 531.0 eV [16].

Therefore, we follow Tait *et al.* [16] and assign two components to our O1s peak with an energy separation of 0.6 eV, while the background signal is modeled by a Shirley background as depicted in Fig. 6.4. This leaves us with component 1(red) at 531.1 eV and component 2 (green) at 531.7 eV.

Both peaks indeed show an independent behaviour in the XSW profile and therefore lead to distinctively different results, as can be seen in Table 6.2 and its visualization as an Argand diagram in Fig. 6.5. Exemplary yield curves are shown in Fig. 6.6. Component 1 (red) shows a mean P_c of 0.11 ± 0.02 and hence an adsorption height of 2.01 ± 0.04 Å. Component 2 yields a mean P_c of 0.95 ± 0.03 which calculates to an adsorption height of 1.72 ± 0.05 Å. Following the peak assignment of Tait *et al.* [16] component 1 represents the uncoordinated and component 2 the coordinated oxygen. Therefore the adsorption heights must be interpreted as a lowering of the

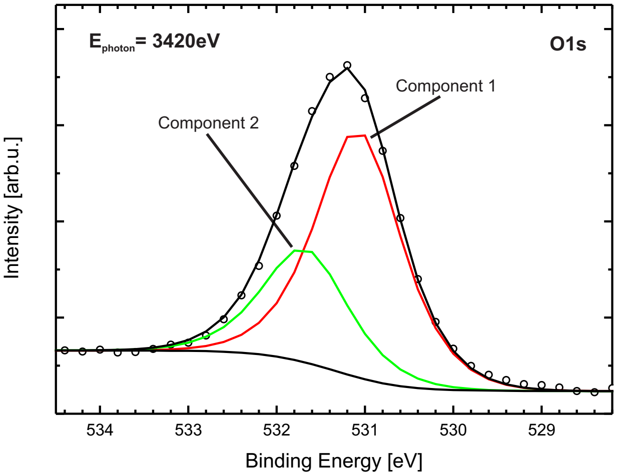

Figure 6.4: Off-Bragg XPS spectrum of the O1s region for TPA:Fe/Cu(100). The spectrum is fitted with two components centred at 531.1 eV (component 1, red) and 531.7 eV (component 2, green)

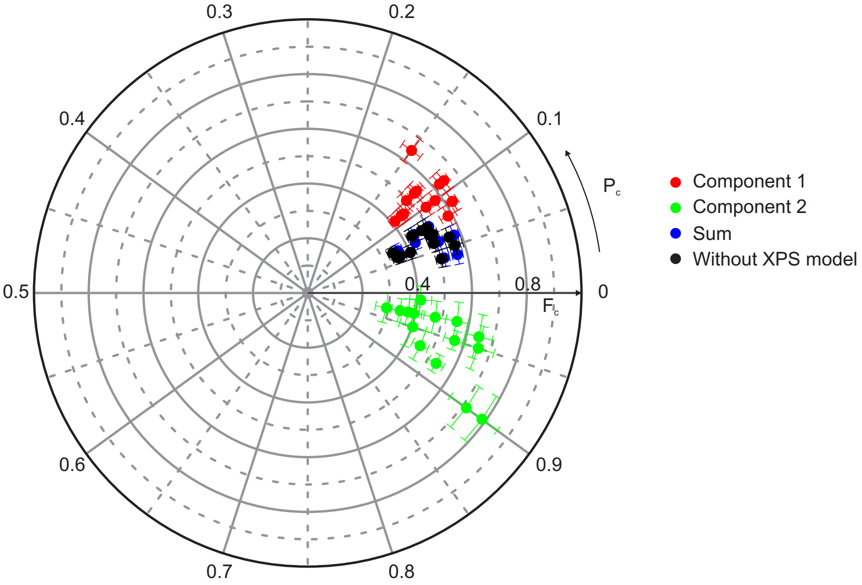

Figure 6.5: Argand diagram displaying O1s results. In accordance with Fig. 6.4 the red dots represent the result for component 1 with a mean P_c of 0.11 ± 0.02 and the green dots for component 2 with a mean P_c of 0.95 ± 0.03. Blue and black dots represent the results for the sum and the result without XPS model, respectively. All results are tabulated in Table 6.2.

coordinated oxygen compared to the uncoordinated. Hence, the Fe would push the oxygen towards the surface. However, this is very surprising, because one would expect a weakening of the O-Cu bond due to the Fe coordination and hence a larger adsorption height for the coordinated species.

While it is evident that we can resolve two different oxygen species in our experiment and they yield the quoted adsorption heights, the interpretation as coordinated and uncoordinated oxygen might be erroneous. Comparing the adsorption heights to the findings for the pure TPA/Cu(100) shows a remarkable coincidence: The adsorption height of 1.70 ± 0.02 Å for the oxygen in that case [36] is exactly where we find component 2 (1.72 ± 0.05 Å). Taking into account that we cannot exclude the co-existence of TPA/Cu(100) by LEED as described in sec. 6.2, another interpretation seems possible: Component 2 can be understood as result from pure TPA/Cu(100) domains and only component 1 shows a signal from the TPA:Fe/Cu(100) but we cannot resolve any intramolecular differences.

In this interpretation, still some open questions remain. First, it should be pointed out that the XPS binding energy of the TPA/Cu(100) peak (531.2 Å [36]) in contrast to the agreement in adsorption heights is rather identified with component 1 (531.1 eV) than component 2 (531.7 eV). Second, this would mean that the Fe influenced species is actually at lower binding energy than the TPA/Cu(100), while in the data of Tait *et al.* [16] the O1s peak evolving by Fe deposition clearly appears on the higher binding energy side. Maybe our data suffers from the influence of the flourine, which may lead to an energy shift for some species. However, there is no time dependence in the oxygen data and compared to the carbon and iron results, to be discussed now, everything appears to be very stable, which might be due to rather strong metal-oxygen bonds.

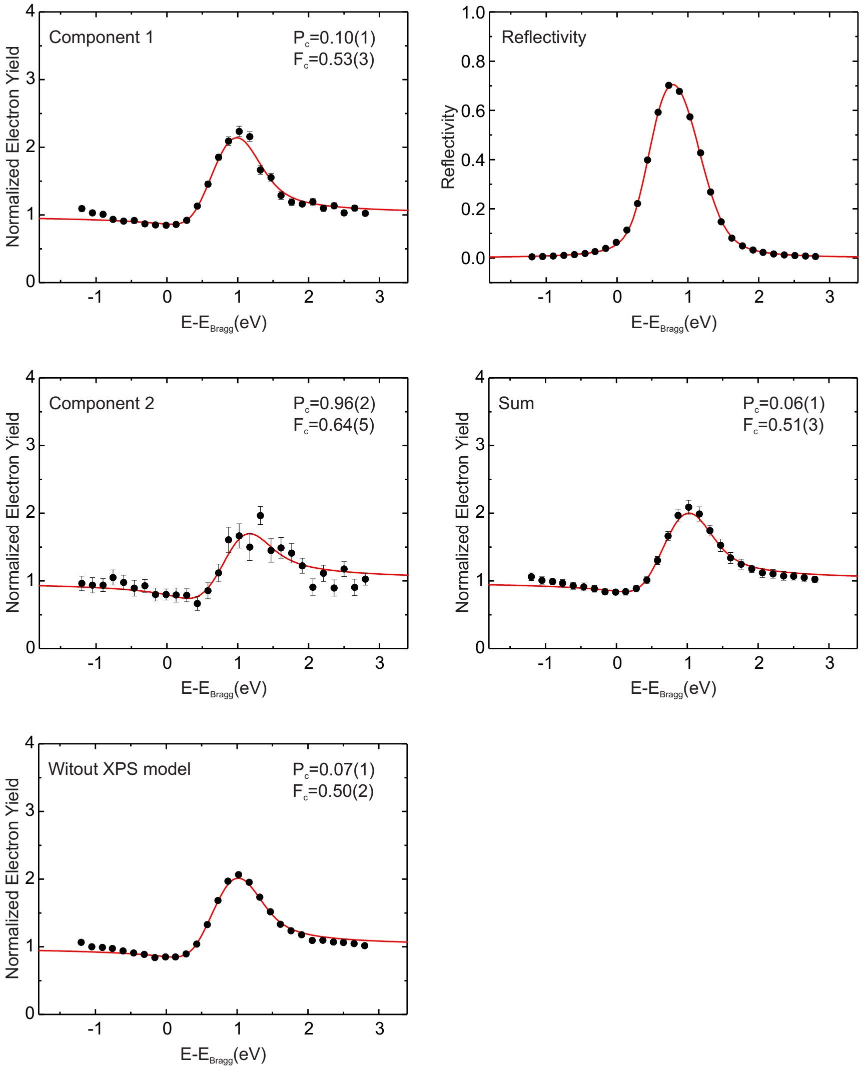

Figure 6.6: Exemplary electron yield curves from the O1s XSW fit using the XPS model depicted in Fig. 6.4. The displayed data belongs to XSW data set 019. The x-axis displays the photon energy relativ to the Bragg energy. The results of all O1s data sets are summarized in Table 6.2.

Prep.	Data set	Component 1			Component 2			Sum			Without XPS model		
		F_c	P_c	d_c[Å]	F_c	P_c	d_c[Å]	F_c	P_c	d_c[Å]	F_c	P_c	d_c[Å]
1	003	0.45(3)	0.11(1)		0.29(4)	0.97(3)		0.36(2)	0.07(1)		0.34(2)	0.07(1)	
	007	0.41(2)	0.11(1)		0.37(4)	0.97(2)		0.36(2)	0.06(1)		0.35(2)	0.06(1)	
	010	0.44(3)	0.11(1)		0.34(3)	0.97(2)		0.36(2)	0.06(1)		0.36(2)	0.06(1)	
	014	0.53(3)	0.12(1)		0.39(3)	0.97(2)		0.44(2)	0.08(1)		0.43(2)	0.08(1)	
	017	0.44(3)	0.11(1)		0.41(4)	0.99(2)		0.40(2)	0.06(1)		0.40(2)	0.06(1)	
	019	0.53(3)	0.10(1)		0.64(5)	0.96(2)		0.51(3)	0.06(1)		0.50(2)	0.07(1)	
2	032	0.49(3)	0.12(1)		0.53(3)	0.92(1)		0.43(1)	0.07(1)		0.43(1)	0.08(1)	
	035	0.54(3)	0.12(1)		0.55(4)	0.97(2)		0.50(2)	0.06(1)		0.49(2)	0.06(1)	
	040	0.57(2)	0.10(1)		0.47(4)	0.97(2)		0.49(2)	0.07(1)		0.49(2)	0.07(1)	
4	045	0.64(2)	0.11(1)		0.78(7)	0.90(2)		0.57(2)	0.06(1)		0.55(2)	0.06(1)	
	048	0.62(2)	0.09(1)		0.71(7)	0.90(2)		0.56(1)	0.05(0)		0.56(2)	0.05(1)	
6	068	0.58(3)	0.08(1)		0.65(6)	0.95(2)		0.56(2)	0.04(1)		0.56(3)	0.05(1)	
	070	0.62(2)	0.09(1)		0.45(3)	0.93(2)		0.51(2)	0.04(1)		0.50(2)	0.04(1)	
7	076	0.62(2)	0.11(1)		0.40(5)	0.95(3)		0.50(1)	0.08(1)		0.49(2)	0.08(1)	
8	081	0.64(5)	0.15(1)		0.56(4)	0.95(1)		0.49(2)	0.07(1)		0.47(2)	0.08(1)	
mean value		0.49(14)	0.11(2)	2.01(4)	0.54(8)	0.95(3)	1.72(5)	0.47(7)	0.06(1)	1.92(2)	0.46(7)	0.06(1)	1.92(2)

Table 6.2: O1s results for the TPA+Fe network from the XSW analysis using the XPS model depicted in Fig. 6.4. The results are plotted in the argand diagram in Fig. 6.5.

6.4 Fe results

Now we turn to the evaluation of the Fe results. The Fe2p photoemission signal was chosen to evaluate the adsorption height. For Fe the Fe2p$_{1/2}$ and Fe2p$_{3/2}$ peaks are reported at a binding energy of 719.9 eV and 706.8 eV[148], respectively. Hence, the split between the two amounts to 13 eV. Together with the known intensity ratio of 1:2 between these lines, the two component XPS model depicted in Fig. 6.7 is developed. We find the Fe2p$_{3/2}$ line at 709.7 eV (red) and hence the Fe2p$_{1/2}$ line (green) at 722.7 eV, corresponding to a shift of 3 eV to the above values. In contrast to organic adsorbates, where shake-up events usually lead to the formation of distinct satellite features, shake-up events in metallic or conductive systems, like Fe/Cu(100), introduce an asymmetric peak shape due to the quasi continuous distribution of unfilled one-electron levels [149]. For the fit of the XPS data this is usually taken into account by the so called Doniach-Sunjic peak shape [150]. However, this peak shape features a relatively high intensity in the far end of the tail of the peak, leading to problems in the peak area quantification for restricted binding energy regions. Furthermore, the peak shape is best suited if a non monochromatized X-ray source is used. Both facts are problematic in our case, but fortunately the software *CasaXPS* [35] allows to create a synthetic asymmetric lineshape by introducing an exponential decay on the high binding energy side. The resulting peak shape $Y(x)$ is a multiple

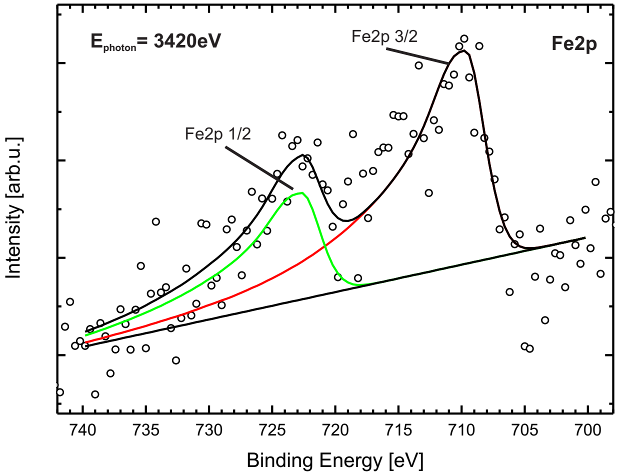

Figure 6.7: Off-Bragg XPS spectrum of the Fe2p region for TPA:Fe/Cu(100). The spectrum is fitted with two components for the Fe2p$_{3/2}$ (red) and Fe2p$_{1/2}$ peak (green), respectively. The assymetric peak shape is taken into account by the convolution with an exponential tail on the high binding energy side of each peak (see text).

of a Lorentzian (30%) and Gaussian (70%) named $GL(x)$, which is then modified by the exponential term $T(x)$ according to eq. (6.1)

$$Y(x) = GL(x) + (1 - GL(x)) \times T(x) \begin{cases} T(x) = \exp\left(-k\frac{x-E}{F}\right) & x \leq E \\ T(x) = 0 & x > E \end{cases} \tag{6.1}$$

where E is the peak position and F the width of $GL(x)$. Both E and F are both fitting parameters. The asymmetry parameter k is carefully adjusted to yield a reasonable peak shape. For this adjustment it is expected that the binding energy region between the peaks is most difficult to fit, while the low binding energy side of the Fe2p$_{3/2}$ component can be used to adjust the $GL(x)$ and the high binding energy tail of the Fe2p$_{1/2}$ component to find the proper asymmetric tail. However, the exact shape of the tail remains uncertain due to the relativly low signal-to-noise ratio and especially the intensity between the peaks seems to be underestimated. Nevertheless, the quality of the model is well suited to allow for the XSW analysis, because we are only interested in the summed up area of the peaks and do not need to differentiate their contributions, because they originate from the same chemical species. Adding a third component to the model will of course improve the fit, but in the XSW analysis such a model is beyond our data resolution. The low signal-to-noise ratio stems from the low coverage of only one Fe atom per unit cell, which calculates to a surface density of $4 \times 10^{-5}\,\mathrm{nm}^{-2}$ and furthermore from the large photon energy of 3420 eV leading to a low cross-section for the XPS.

A rather surprising result is found, as can be seen from the Argand diagram in Fig. 6.8 and the tabulated values in Table 6.3. As the intensity of the individual components is not independent in this case, only the sum is considered for the analysis. The results scatter over a large section of the argand diagram, yielding a P_c difference of more than 0.3. This can neither be explained by the poor signal-to-noise ratio of the XPS data nor by a real distribution of adsorption heights. In Fig. 6.10 exemplary yield curves of two different data sets are depicted.

Investigating the P_c dependence on parameters such as X-ray exposure time and preparation does not lead to any clear tendency, but if it is plotted against the time which has passed between the preparation and the end of the XSW measurement, i.e. the sample age, a clear correlation is found as shown in Fig. 6.9. Within the first ten hours after the preparation the P_c seems to rise while it is stable and maybe slightly reduced again for older samples. Unfortunately, even the fastest measurements are

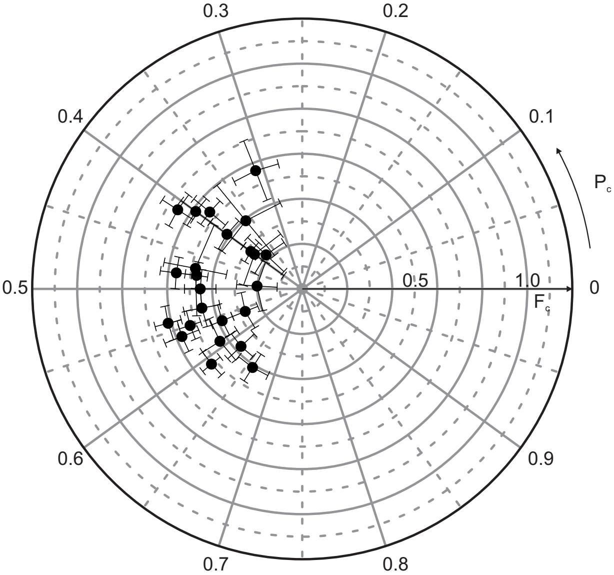

Figure 6.8: Argand diagram displaying the XSW results for Fe as deduced from the Fe2p signal using the XPS model shown in Fig. 6.7. Due to the intrinsic intensity dependenc of both components, only the sum result is depicted. The corresponding numbers together with the resulting adsorption heights are given in Table 6.3. The huge scattering of the data can be explained by a time dependence (see text) and a clear trend of the P_c against the sample age is observed as shown in Fig. 6.9.

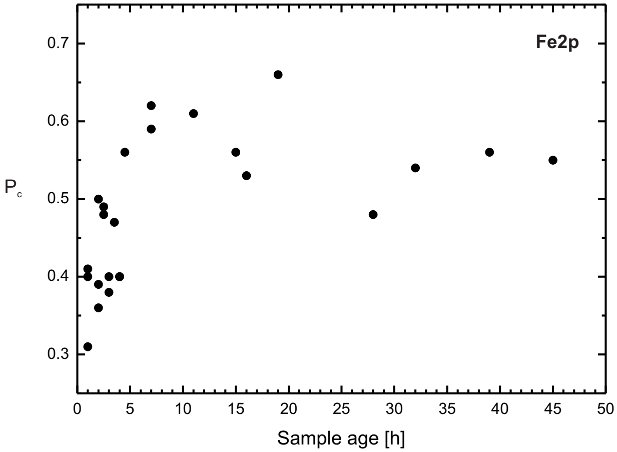

Figure 6.9: P_c results of the Fe2p measurements as given in Table 6.3 and depicted in the argand diagram in Fig. 6.8, plotted against the sample age which is calculated as the time between sample preparation and end of the corresponding measurement. A clear dependence on the sample age is indeed observed.

already located on a slope, preventing us from deducing an initial P_c unambiguously. It is clear that a mean value of all the Fe results has no meaning. The results of Fig. 6.9 indicate that a precise Fe position cannot be determined. However, on the basis of the experiment we can deduce an upper limit of the Fe position, corresponding to a P_c of 0.30 ± 0.05. Why the Fe height changes dramatically over time is not clear from the data, but the presence of flourine in the residual gas and its adsorption which was reported above (see sec. 6.2) might be involved in this process.

A faster measurement of the Fe signal would be desirable also in future experiments to investigate the dependencies of this effect and the initial position of the Fe, but this was beyond the possibilities of the used experimental setup. Furthermore, it raises the question how the results for the other species are influenced. While no time dependence was observed for oxygen, the next chapter will indeed show a similar behaviour for the carboxylic carbon.

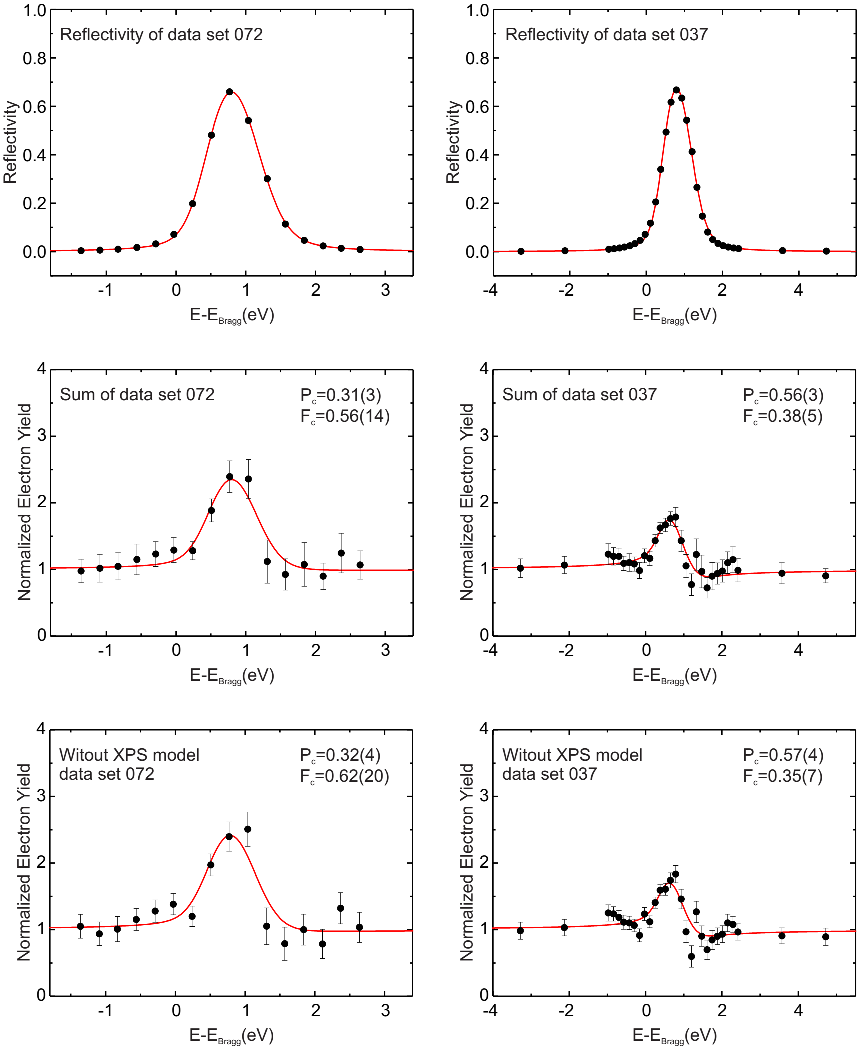

Figure 6.10: Exemplary electron yield curves from the Fe2p XSW fit using the XPS model depicted in Fig. 6.7. The displayed data belongs to XSW data set 072 (left column) and 037 (right column). The x-axis displays the photon energy relativ to the Bragg energy. The results of all Fe2p data sets are summarized in Table 6.3.

Prep.	Data set	Sum			Without XPS model		
		F_c	P_c	d_c[Å]	F_c	P_c	d_c[Å]
1	006	0.45(8)	0.53(3)	2.77(5)	0.44(10)	0.54(4)	2.78(7)
	013	0.56(7)	0.48(2)	2.68(4)	0.57(9)	0.46(3)	2.64(5)
	015	0.61(6)	0.54(2)	2.78(4)	0.58(7)	0.54(2)	2.78(4)
	018	0.57(8)	0.56(2)	2.82(4)	0.58(8)	0.53(3)	2.77(5)
	023	0.52(5)	0.55(2)	2.8(4)	0.56(7)	0.56(2)	2.82(4)
2	031	0.58(8)	0.40(2)	2.53(4)	0.53(13)	0.37(3)	2.48(5)
	036	0.52(5)	0.61(2)	2.91(4)	0.58(6)	0.61(2)	2.91(4)
	037	0.38(5)	0.56(3)	2.82(5)	0.35(7)	0.57(4)	2.84(7)
	039	0.41(7)	0.66(3)	3.00(5)	0.41(9)	0.67(3)	3.02(5)
3	041	0.20(9)	0.49(9)	2.69(16)	0.19(12)	0.56(12)	2.82(22)
	042	0.27(6)	0.56(5)	2.82(9)	0.21(8)	0.53(8)	2.77(14)
	043	0.43(9)	0.59(4)	2.87(7)	0.35(11)	0.60(6)	2.89(11)
6	063	0.41(9)	0.40(3)	2.53(5)	0.41(12)	0.42(4)	2.57(7)
	064	0.39(20)	0.36(7)	2.46(13)	0.29(26)	0.32(11)	2.39(20)
	065	0.22(11)	0.38(7)	2.49(13)	0.22(14)	0.35(8)	2.44(14)
	066	0.48(14)	0.47(7)	2.66(13)	0.33(16)	0.46(9)	2.64(16)
	067	0.26(16)	0.40(9)	2.53(16)	0.32(21)	0.30(8)	2.35(14)
	071	0.37(8)	0.62(3)	2.93(5)	0.31(11)	0.62(6)	2.93(11)
7	072	0.56(14)	0.31(3)	**2.37(5)**	0.62(20)	0.32(4)	2.39(7)
	073	0.53(9)	0.39(2)	2.51(4)	0.60(15)	0.38(3)	2.49(5)
	074	0.28(4)	0.40(3)	2.53(5)	0.33(8)	0.43(4)	2.58(7)
8	077	0.65(8)	0.41(2)	2.55(4)	0.65(10)	0.44(2)	2.60(4)
	078	0.45(7)	0.50(3)	2.71(5)	0.52(10)	0.48(3)	2.68(5)
	079	0.47(5)	0.48(2)	2.68(4)	0.56(6)	0.46(2)	2.64(4)

Table 6.3: Fe2p results for the TPA:Fe/Cu(100) network from the XSW analysis using the XPS model shown in Fig. 6.7. The results are visualized in the argand diagram in Fig. 6.8. The lowest height measured during the experiment, which is taken for the structure model in sec. 6.7 is highlighted in bold.

6.5 C1s results

To analyse the information from the carbon signal the situation is naturally more complicated, because one has to account for several species and their satellites in the XPS spectrum. A detailed analysis of the C1s spectrum of the deprotonated TPA/Cu(100) is given by Stepanow *et al.* [146] and the relative energy positions are used for the XSW analysis by Mercurio [36] as well. However, we do not find this model to be able to describe the XPS data correctly in our case, and therefore propose a different model which is shown in Fig. 6.11. The spectrum clearly shows a main peak at the low binding energy side which is labeled 'Ring component 1' (red, 284.6 eV), as it is attributed to the aromatic ring of TPA. A well separated feature named 'Carboxylic' (dark blue, 288.0 eV) arises from the carboxylic carbons. In addition a small side peak is found close to the Ring component 1 which we therefore name 'Ring component 2' (green, 285.4 eV). A broad satellite basically lying underneath the Carboxylic peak at 287.7 eV (orange) and a small satellite in the high binding energy tail at 292.3 eV (light blue) are completing the spectrum.

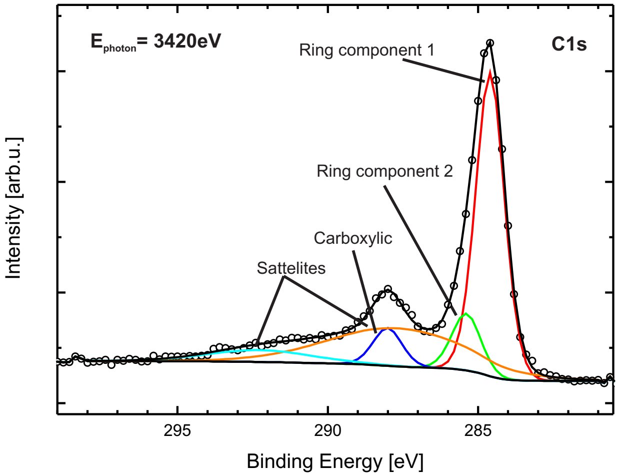

Figure 6.11: Off-Bragg XPS spectrum of the C1s region for TPA:Fe/Cu(100). The spectrum is fitted with five components. The main component at 284.6 eV represents the intensity of the aromatic ring (Ring component 1, red) while the component at 288.0 eV (Carboxylic, dark blue) is attributed to the carboxylic side groups. Next to Ring component 1 at 285.4 eV a second component is identified, called Ring component 2 (green). Its origin is not clear (see text), however its XSW behaviour is clearly different as seen in the argand diagram in Fig. 6.12. Two satellites at 287.7 eV (orange) and 292.3 eV (light blue) complete the model.

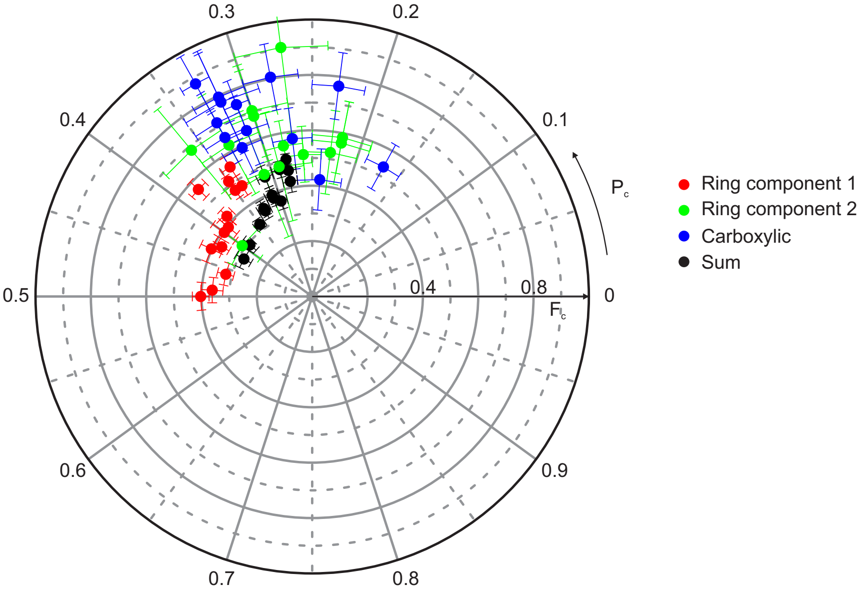

Figure 6.12: Argand diagram displaying C1s results from the XSW analysis employing the XPS model shown in Fig. 6.11. The color code follows the XPS model as well and we see the results for Ring component 1 in red, Ring component 2 in green, Carboxylic in dark blue, and the sum in black. Unfortunately a large scattering is observed. All values are given in Table 6.4.

While the main features (Ring component 1 and Carboxylic) are in good agreement with the previous models, two differences are observed. First, we find the Ring component 2 much closer to the Ring component 1, because they are only separated by 0.8 eV, while this is 1.6 eV in the model of Stepanow *et al.* [146] and Mercurio [36]. This leads to a clearly reduced intensity in the binding enery range between Ring component 1 and the Carboxylic peak in our case. Second, the presence of the broad satellite underneath the Carboxylic peak, which was not reported before. The origin of these differences is not clear, but possible parameters leading to the observed changes might be the presence of Fe, the different 2D superstructure, an influence of the flourine or the coexistence of coordinated and uncoordinated molecules.

Looking at the XSW results which are given in Table 6.4 and depicted in the Argand diagram in Fig. 6.12, we see indeed a qualitative difference: The XSW result of Ring component 2 is independent of the Ring component 1, hence it cannot be interpreted as satellite peak of the latter, which one would expect from the results on the pure TPA/Cu(100) [36] and the XPS model by Stepanow *et al.* [146]. Exemplary yield

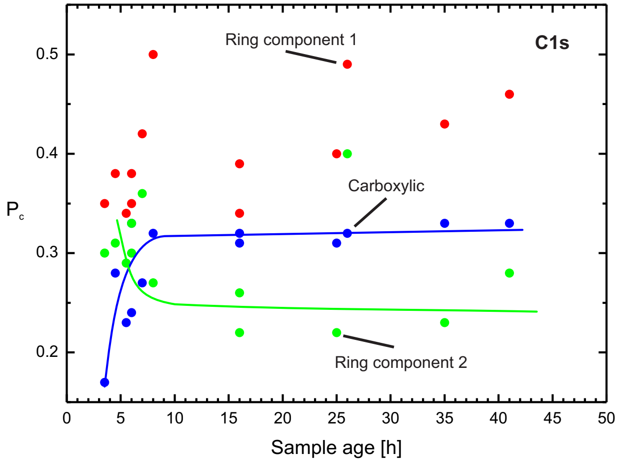

Figure 6.13: P_c results of the C1s measurements as depicted in the argand diagram in Fig. 6.12 and given in Table 6.4 plotted against the time between sample preparation and end of the corresponding measurement, namely sample age in hours. Only the Carboxylic (blue) shows the same trend as it was observed for Fe before (see Fig. 6.9) while the scattering in P_c for the Ring component 1 does not yield such clear behaviour and Ring component 2 (green) seems to follow an opposite trend. The corresponding lines are only guides to the eye.

curves are shown in Fig. 6.15. This finding suggests the idea of coexisting phases, interpreting Ring component 2 as representative of a minority species. However, its P_c does not coincide with result for the pure TPA/Cu(100) [36]. Therefore it might have to be interpreted as part of the flourine contamination. The F1s binding energy of 688 eV (see Fig. 6.3) points towards a CF compound [147] and hence this can explain the appearence of Ring component 2 in the spectrum, representing the flourine bound carbon.

Furthermore, we observe again a large scattering of the results similar to what was found for Fe (see sec. 6.4). Therefore, we have analyzed the time dependence of the carbon experiments. This is plotted in Fig. 6.13. The result is not as clear as it was for Fe, because three different dependencies are revealed. While the carboxylic peak (blue) indeed follows the Fe behaviour, Ring component 1 (red) does not show a clear dependence on the sample age and Ring component 2 (green) an inverted trend with a decreasing P_c. Hence, if we assume the time dependence to stem from flourine adsorption, we can draw the following conclusions: First, the position of the aromatic ring seems to be stable against the flourine contamination, second the change in Ring component 2 can be attributed to a rising contribution of carbon from a CF compound to this signal, and third the carboxylic carbon suffers a strong influence

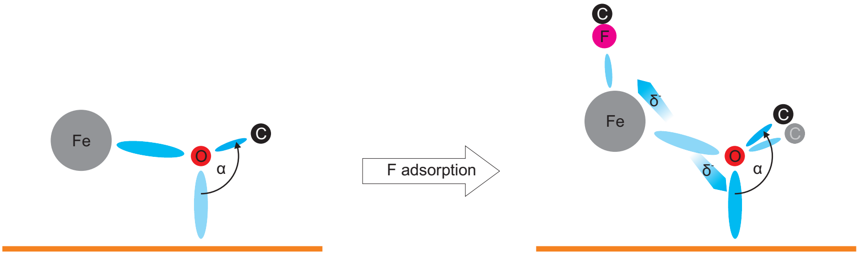

Figure 6.14: Explanatory sketch for the change in the carboxylic carbon adsorption height upen flourine adsorption. The equilibrium adsorption geometry shown on the left is disturbed by the flourine adsorption. The additional ligand on the Fe atom weakens the Fe-O bond as the charge density is rearranged, leading to a stronger Cu-O bond and therefore changing the equilibrium geometry by increasing the bond angle (α) to the carboxylic carbon. As a result the carboxylic carbon is lifted. The Cu surface is represented by the orange line.

from the flourine, while the connected oxygens do not.

The latter might be explained by a charge rearrangement if the O-Fe bond is weakened (due to flourine adsorption at the Fe) and the O-Cu bond is strengthened. The idea is sketched in Fig. 6.14. Before F adsorption the system is in an equlibrium geometry, but the additional ligand on the Fe atom weakens the Fe-O bond, indicated by a charge transfer into the O-Cu bond, changing the equlilibrium geometry by increasing the bonding angle α, hence resulting in a larger adsorption height of the carboxylic carbon.

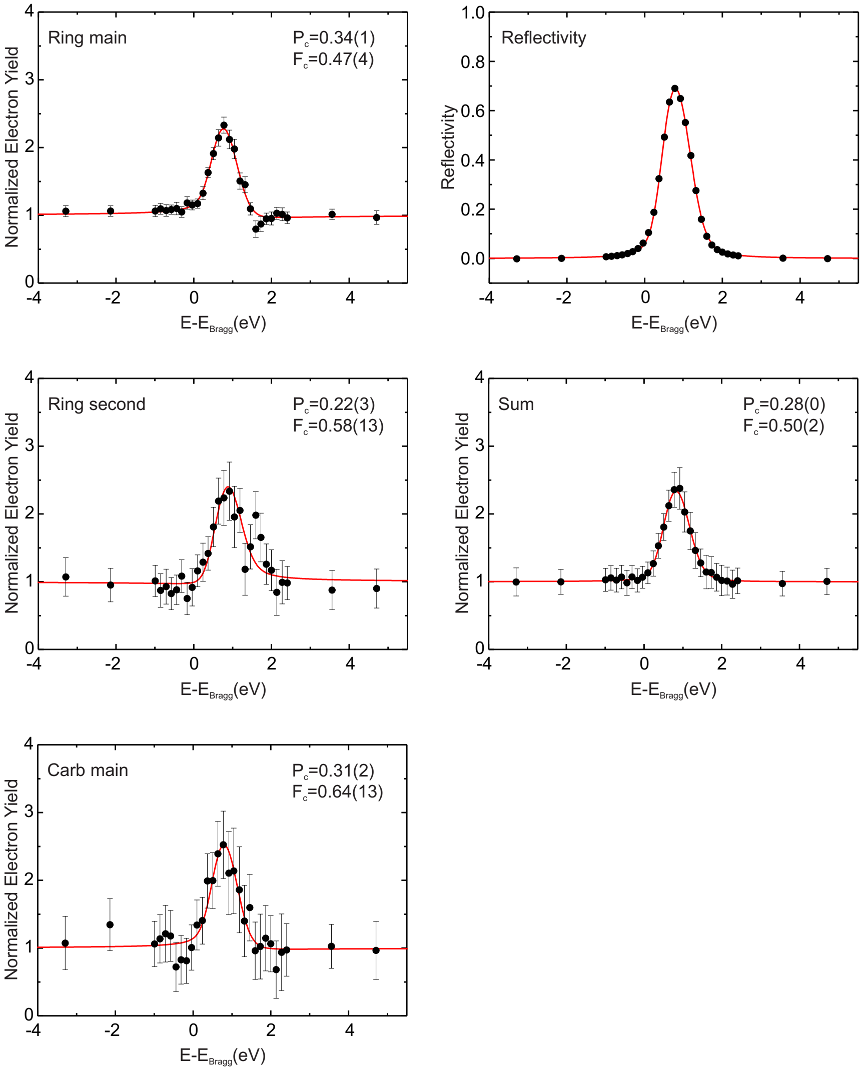

Figure 6.15: Exemplary electron yield curves from the C1s XSW fit using the XPS model depicted in Fig. 6.11. The displayed data belongs to XSW data set 038. The x-axis displays the photon energy relativ to the Bragg energy. The results of all Fe2p data sets are summarized in Table 6.4.

Prep.	Data set	Ring component 1			Ring component 2			Carboxylic			Sum		
		F_c	P_c	d_c[Å]	F_c	P_c	d_c[Å]	F_c	P_c	d_c[Å]	F_c	P_c	d_c[Å]
1	002	0.40(3)	0.50(2)	2.71(4)	0.90(31)	0.27(3)	2.30(5)	0.77(20)	0.32(3)	2.39(5)	0.29(3)	0.39(1)	2.51(2)
	008	0.39(4)	0.39(1)	2.51(2)	0.51(10)	0.26(2)	2.28(4)	0.79(17)	0.32(2)	2.39(4)	0.38(3)	0.31(1)	2.37(2)
	011	0.39(5)	0.40(2)	2.53(4)	0.56(15)	0.22(3)	2.21(5)	0.74(9)	0.31(1)	2.37(2)	0.36(3)	0.30(1)	2.35(2)
	012	0.36(4)	0.49(2)	2.69(4)	0.31(8)	0.40(4)	2.53(7)	0.59(10)	0.32(2)	2.39(4)	0.28(3)	0.42(2)	2.57(4)
	016	0.40(4)	0.43(2)	2.58(4)	0.52(15)	0.23(3)	2.22(5)	0.71(12)	0.33(2)	2.40(4)	0.36(3)	0.33(1)	2.40(2)
	020	0.32(3)	0.46(2)	2.64(4)	0.55(9)	0.28(2)	2.31(4)	0.87(11)	0.33(1)	2.40(2)	0.32(2)	0.35(1)	2.44(2)
2	033	0.42(3)	0.38(1)	2.49(2)	0.68(17)	0.30(2)	2.35(4)	0.65(10)	0.33(2)	2.40(4)	0.39(3)	0.31(1)	2.37(2)
	034	0.37(3)	0.42(1)	2.57(2)	0.68(19)	0.36(3)	2.46(5)	0.57(11)	0.27(2)	2.30(4)	0.35(3)	0.33(1)	2.40(2)
	038	0.47(4)	0.34(1)	2.42(2)	0.58(13)	0.22(3)	2.21(5)	0.64(13)	0.31(2)	2.37(4)	0.50(2)	0.28(0)	2.31(0)
	047	0.51(2)	0.35(0)	2.44(0)	0.70(17)	0.30(3)	2.35(5)	0.53(9)	0.17(2)	2.11(4)	0.46(3)	0.28(1)	2.31(2)
	050	0.47(3)	0.35(1)	2.44(2)	0.62(20)	0.33(3)	2.40(5)	0.42(11)	0.24(3)	2.24(5)	0.47(3)	0.29(1)	2.33(2)
6	069	0.55(4)	0.34(1)	2.42(2)	0.48(20)	0.29(4)	2.33(7)	0.76(12)	0.23(2)	2.22(4)	0.42(4)	0.28(1)	2.31(2)
7	075	0.56(4)	0.38(1)	2.49(2)	0.47(24)	0.31(5)	2.37(9)	0.80(12)	0.28(2)	2.31(4)	0.46(4)	0.31(1)	2.37(2)

Table 6.4: C1s results for the TPA:Fe/Cu(100) network from the XSW analysis using the XPS model shown in Fig. 6.11. All values are visualized in the argand diagram in Fig. 6.12. Due to the large scatter of the results mean values are not calculated. The scattering reminds of the Fe results (see Table 6.3 and Fig. 6.8) but in this case only the carboxylic shows a clear timedependence.

6.6 Oxygen dosing on TPA:Fe/Cu(100)

An important aspect of the well ordered arrangement of single Fe atoms on Cu, which is achieved in the TPA:Fe/Cu(100) system, are its magnetic properties. Gambardella *et al.* [17] reported the follwing interesting findings: Due to the coordination to the TPA molecules the Fe atoms reveal a high-spin configuration, despite their bond to the surface. Furthermore, X-ray magnetic circular dichroism experiments reveal an in plane magnetic anisotropy in the system. Interestingly, the Fe centers in this network serve as selective adsorption sites for O_2, which is observed in STM experiments. This opens an opportunity to tune the magnetic properties, because the site-selective oxygen adsorption leads to a reorientation of the easy magnetization axis. DFT calculations predict an increase of the Fe-Cu adsorption height from 2.71 Å in the TPA:Fe/Cu(100) cloverleaf phase to 3.32 Å after O_2 is adsorbed on top of the Fe atom. To understand the adsorption of oxygen on the Fe atoms and to verify the DFT calculations, O_2 was dosed onto the sample directly after the preparation of the TPA:Fe/Cu(100) layer and investigated by XSW.

For the C1s as well as the Fe2p spectra no changes could be resolved and therefore the same XPS models as shown in Fig. 6.11 and Fig. 6.7, respectively, are used for the

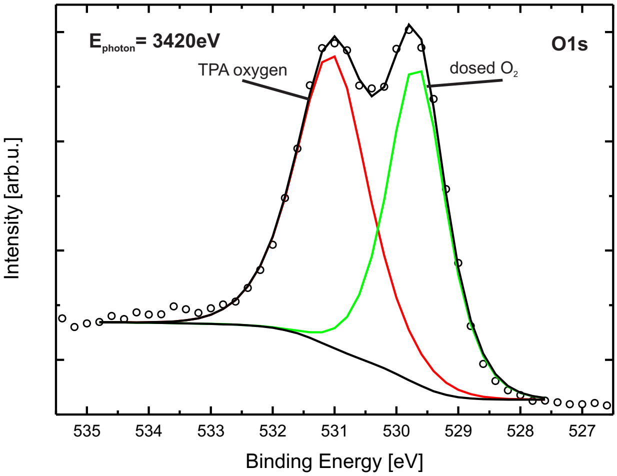

Figure 6.16: Off-Bragg XPS spectrum of the O1s region for TPA:Fe/Cu(100) after O_2 adsorption. Although one would expect two components to represent the molecular oxygen as it has been modeled for the O1s spectrum before (see Fig. 6.4) in this case it was not possible. Therefore the TPA oxygen at 531.0 eV (red) represents the sum of all molecular oxygen contributions. The new dosed O_2 component at 529.7 eV (green) stems from the adsorbed O_2.

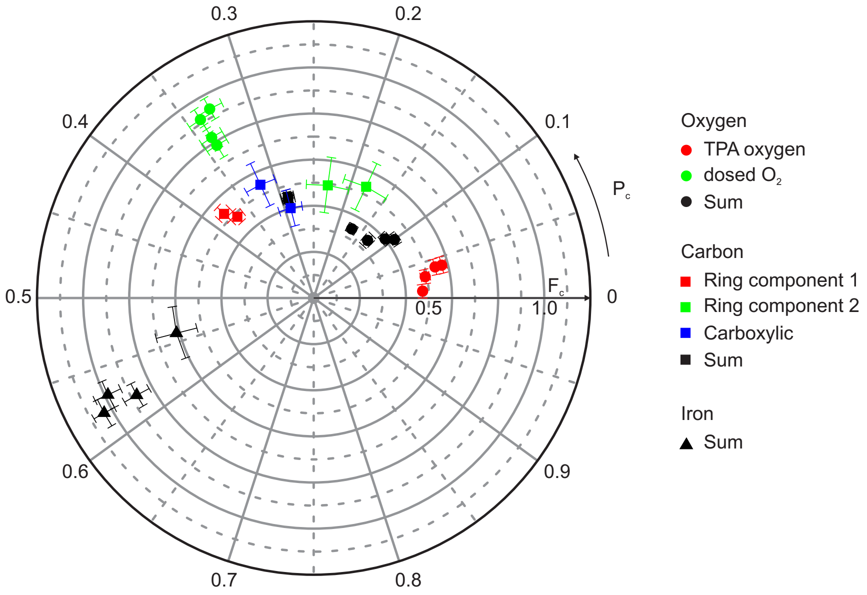

Figure 6.17: Argand diagram displaying XSW results after O_2 dosage. For the C1s (squares) and Fe2p (black triangles) results the same XPS models as before have been used as shown in Fig. 6.11 and Fig. 6.7. For the oxygen (circles) the new XPS model shown in Fig. 6.16 was employed. While for C1s all components, namels Ring component 1 (red square), Ring component 2 (green square), Carboxylic (blue square) and the sum (black square) stay the same, for O1s the new dosed O_2 species (green circles) appears at a P_c of 0.34 ± 0.01 and hence the O1s sum (black circles) is changed as well. The TPA oxygen (red circles) however, shows no major change. All results are given in Table 6.5.

XSW analysis. For oxygen a new model as shown in Fig. 6.16 is neccessary, of course. The new component representing the adsorbed O_2 appears at a binding energy of 529.7 eV (green) and therefore 1.3 eV below the molecular oxygen at 531.0 eV (red). Note that different species of the TPA oxygen cannot be resolved any more in this case, and therefore the molecular results of this section should always be compared to the sum result for O1s before oxygen dosing. Exemplary yield curves for O1s are shown in Fig. 6.19

From the XSW results in the Argand diagram in Fig. 6.17 which are tabulated in Table 6.5 we can see that the carbon results (squares) are rather similar as before, while for the oxygen (circles) the new species appears at a distinct new P_c of 0.34 ± 0.01. As one expects it to be on top of the Fe atoms [17], the corresponding adsorption height would be 6.04 ± 0.02 Å.

The Fe results are most interesting, because the DFT calculations [17] expect the

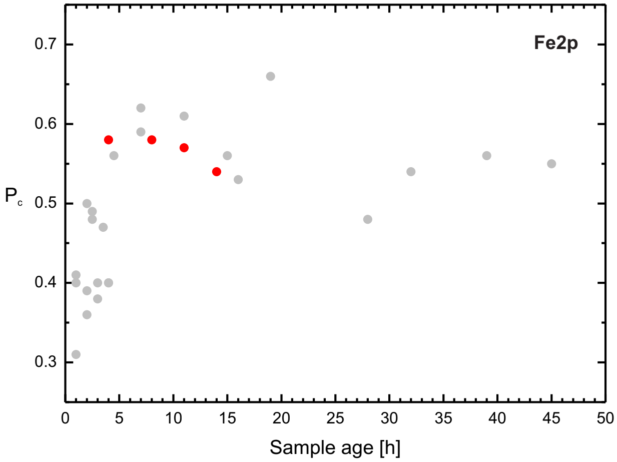

Figure 6.18: P_c results of the Fe2p measurements after O_2 adsorption (red dots) plotted against the time between sample preparation and end of the corresponding measurement, namely the sample age in hours. The values for the time dependence of Fe2p without O_2 dosing (grey dots) as depicted in Fig. 6.9 are plotted to ease comparison. So far no difference can be observed between both datasets, but it may be due to the small amount of data available after O_2 adsorption.

Fe to clearly lift up from the surface upon O_2 adsorption. Furthermore the time dependent behaviour of Fe which was observed before might be suppressed, if flourine adsorption on the metal centers was the reason for the shift and the O_2 adsorption can passivate the Fe. Unfortunately, both questions cannot be finally answered. From the Argand diagram in Fig. 6.17 it can be seen that the scattering for the Fe results (triangles) is reduced. However, the dataset is much smaller, and if plotted against the sample age and compared to the former Fe results as shown in Fig. 6.18 no difference can be observed for Fe before and after O_2 adsorption. However, the measurements are all done on relatively old samples such that it is impossible to decide whether this adsorption height is maybe stable and would be found in faster measurements as well. If so, it would be an indicator that, first, the O_2 indeed lifts the Fe, second, the flourine had the same effect as the O_2, and third, that O_2 adsorption is passivating the layer against the F adsorption.

C Data set	Ring component 1			Ring component 2			Carboxylic			Sum		
	F_c	P_c	d_c[Å]	F_c	P_c	d_c[Å]	F_c	P_c	d_c[Å]	F_c	P_c	d_c[Å]
053	0.48(3)	0.37(1)		0.49(12)	0.23(3)		0.40(8)	0.29(2)		0.44(3)	0.29(1)	
058	0.53(4)	0.38(1)		0.53(11)	0.18(3)		0.54(10)	0.32(2)		0.45(3)	0.29(1)	
mean	0.50(4)	0.38(1)	2.49(2)	0.50(12)	0.20(4)	2.17(7)	0.47(10)	0.31(2)	2.37(4)	0.45(3)	0.29(1)	2.33(2)

O Data set	TPA oxygen			dosed O_2			Sum		
	F_c	P_c	d[Å]	F_c	P_c	d[Å]	F_c	P_c	d[Å]
052	0.47(1)	0.01(1)		0.93(5)	0.33(1)		0.34(2)	0.17(1)	
057	0.49(2)	0.03(1)		0.82(6)	0.34(1)		0.34(3)	0.13(1)	
060	0.54(1)	0.04(1)		0.91(5)	0.34(1)		0.40(2)	0.11(1)	
061	0.57(2)	0.04(1)		0.78(6)	0.34(1)		0.43(2)	0.10(1)	
mean	0.52(5)	0.03(1)	1.86(2)	0.86(7)	0.34(1)	6.04(2)	0.37(5)	0.13(3)	2.04(5)

Fe Data set	Sum		
	F_c	P_c	d[Å]
051	1.03(5)	0.58(1)	
056	0.87(6)	0.58(1)	
059	0.98(6)	0.57(1)	
062	0.61(9)	0.54(3)	
mean	0.87(19)	0.57(2)	2.84(4)

Table 6.5: Results of the XSW analysis for the TPA:Fe/Cu(100) network after additional O_2 dosage. While for Fe and C the XPS models of the former sections could be used (see Fig. 6.7 and Fig. 6.11) for oxygen the model shown in Fig. 6.16 was employed. All values are visualized in the argand diagram in Fig. 6.17.

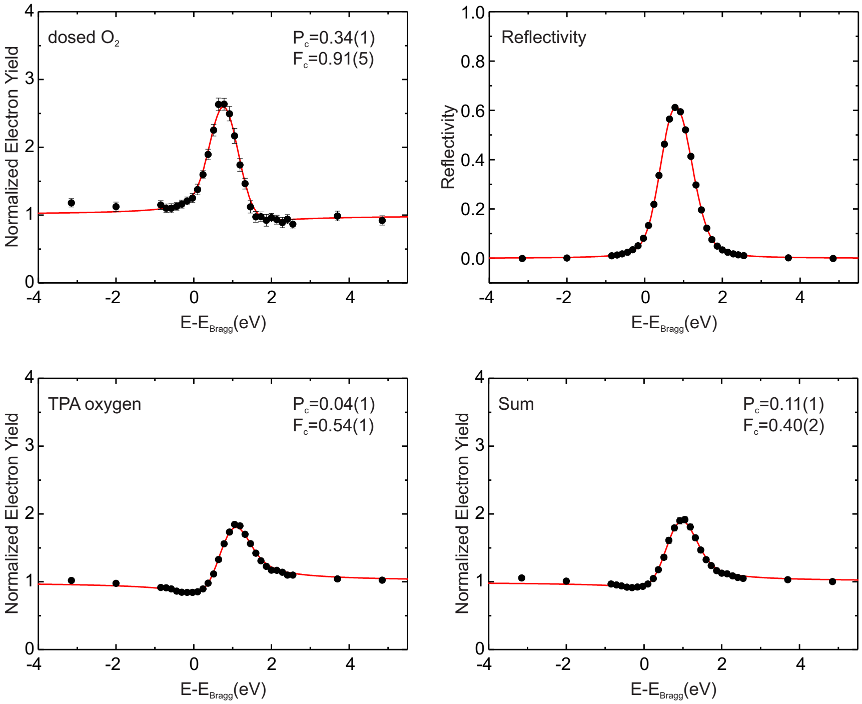

Figure 6.19: Exemplary electron yield curves from the O1s XSW fit using the XPS model depicted in Fig. 6.16. The displayed data belongs to XSW data set 060. The x-axis displays the photon energy relativ to the Bragg energy. The results of all O1s data sets are summarized in Table 6.5.

6.7 Conclusions

The results presented throughout the chapter allow an insight into the vertical structure of the metal-organic network formed by TPA and Fe on the Cu(100) surface. Unfortunately, the results remain inconclusive in several respects, because the experimental conditions were not optimal, namely the UHV system was suffering from a flourine contamination, which lead to an adsorption on our sample. Most probably this flourine adsorption is also the reason for observed time dependent changes in the vertical structure of the sample.

Nevertheless, the obtained preliminary adsorption heights can be compared to previous results on the pure deprotonated TPA/Cu(100) as it is done in Fig. 6.20. Panel a represents the results for TPA/Cu(100) with the downward bending oxygens as anchoring atoms to the surface [36]. In panel b the information gained in this work for the cloverleaf phase of TPA:Fe/Cu(100) is summarized. The Fe re-

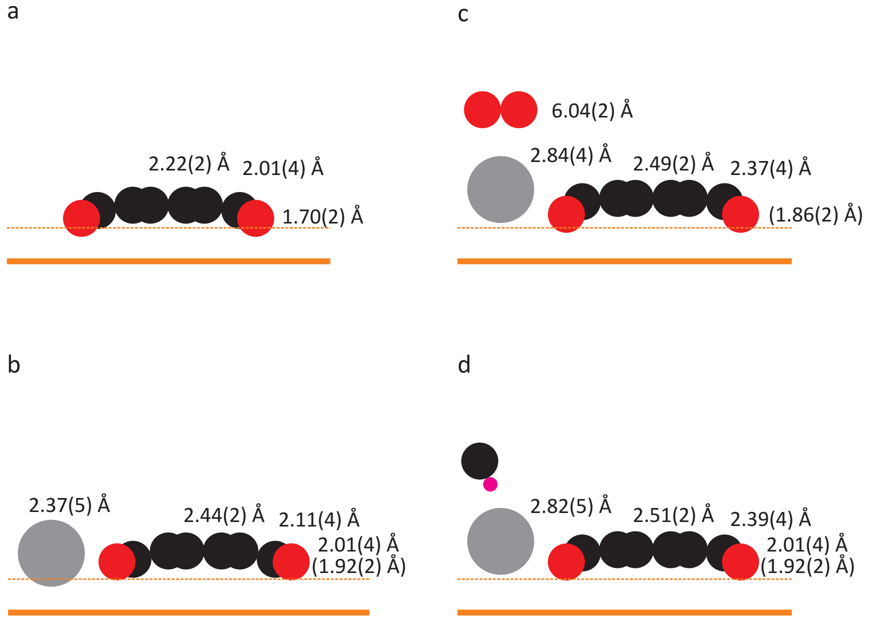

Figure 6.20: Adsorption models for the (a) pure TPA/Cu(100)[36], (b) TPA:Fe/Cu(100) in the cloverleaf phase, (c) TPA:Fe/Cu(100) cloverleaf phase after O_2 adsorption, and (d) the TPA:Fe/Cu(100) cloverleaf phase with a high sample age and expected flourine adsorption. The Cu surface plane is indicated by a straight orange line, while the dashed orange line indicates the covalent Cu radius [55]. Fe is depicted in grey, C in black, O in red, and F in purple. All atoms are scaled according to their covalent radii [55]. Numbers in brackets represent the sum values for TPA oxygen, including possible signal from uncoordinated molecules.

sides at 2.37 ± 0.05 Å, if we take the lowest adsorption height measured. It may even be slightly lower for the initial layer. Compared to TPA/Cu(100) the aromatic ring is lifted by about 0.2 Å while the oxygens even lift 0.3 Å. Hence, the overall bending of the molecule is reduced by 0.1 Å from 0.52 Å (TPA/Cu(100)) to 0.43 Å (TPA:Fe/Cu(100)). Interestingly, the carboxylic carbon is only lifted by 0.1 Å, if data for for a relative fresh sample is considered.

The picture is significantly different, if data taken at higher sample age is considered. The situation is depicted in Fig. 6.20d. The Fe is lifted by about 0.45 Å to 2.82 ± 0.05 Å and the carboxylic carbon by 0.28 Å to 2.39 ± 0.04 Å, while the aromatic ring may also lift, but less than than 0.1 Å. The oxygen stays unchanged. The observed changes are attributed to the adsorption of flourine. Panel c of Fig. 6.20 shows the picture after the additional O_2 dosage on a freshly prepared TPA:Fe/Cu(100) cloverleaf phase, which is very similar to the flourine influenced

	Fe/Cu(100) (single atom)	TPA:Fe/ Cu(100)	O_2+TPA:Fe/ Cu(100)	Δ TPA coordination	Δ O_2 adsorption
DFT [17]	2.32 Å	2.71 Å	3.32 Å	0.39 Å	0.61 Å
XSW		2.37 ± 0.05 Å	2.84 ± 0.04 Å		0.47 Å

Table 6.6: Comparison of experimental findings and DFT calculations [17] for the Fe adsorption height.

adsorption geometry. Assuming that the measured Fe height is valid also for fresh samples (a passivating effect of the O_2 would suggest this), one finds the Fe to be lifted upwards by 0.47 Å compared to the fresh cloverleaf phase (see Fig. 6.20b). The oxygens are slightly moved towards the surface by about 0.06 Å, the aromatic ring is rather unchanged, but the carboxylic carbons move up by 0.25 Å. Above the Fe we find the adsorbed O_2 at 6.04 ± 0.02 Å.

The qualitative trend of the Fe atom being lifted from the surface by the adsorption of an additional ligand, and therefore the Fe-Cu interaction beeing weakened, is in agreement with the expectations from DFT calculations [17]. However, these calculations expect an Fe height of 2.32 Å for single Fe atoms on Cu, 2.71 Å for Fe in the cloverleaf phase and 3.32 Å after additional O_2 adsorption, hence largely overestimating the absolute adsorption height, but predicting a relative shift reasonably close to the experiment (see Table. 6.6).

Upon inspection of Fig. 6.20c and Fig. 6.20d all heights are very similar. The largest difference is visible for the oxygens with 0.06 Å, if the sum values of the TPA oxygen contribution are compared. The insufficient resolution which prevents to distinguish different TPA oxygen species in the case of additionally adsorbed O_2 does not allow to compare the oxygens for coordinated molecules only. The difference in the sum height of the TPA oxygens might be introduced by the relative abundance of the oxygen species. Hence, we conclude that the impact of flourine and O_2 adsorption onto the TPA:Fe/Cu(100) in terms of the vertical structure is very similar, if not identical. This finding supports the assumption that F indeed adsorbs at the Fe atoms and that the additional O_2 adsorption can passivate the layer against F influence.

In general the adsorption of an additional ligand at the Fe weakens its other coordinated bonds, namely the Fe-O bond with the TPA oxygen. Besides the lift of the Fe we can therefore expect a change in the electron density between Fe and O. Hence, charge may be taken from the Fe-O bond, enhancing the O-Cu bond and therefore leads to a movement in the bond angle of the O-C bond. The situation is depicted in Fig. 6.14 and explains the time dependence of the carboxylic carbon due to the F adsorption.

It should be noted that the oxygens were stable against any aging effects which influence the carbon and Fe positions. Together with the fact that the superstructure observed by LEED was stable, this highlights the important role of the anchoring oxygen groups in the superstructure formation.

To refine the preliminary results presented here, the experiments should be repeated, concentrating on the reduction of measurement time. However, this is difficult to achieve, since the Fe density and hence its signal-to-noise ratio is very small. For a future experiment one should clarify if the time dependent effect observed here stems from the flourine. If that is not the case, measurements must be sped up significantly and only very few datapoints per sample preparation would be possible. However, the systematic study of the time dependence in this layer is definetely an interesting aspect to be investigated in detail.

7 Summary

In this work a study on the adsorption properties of organic molecules on low index coinage metal surfaces is presented. The systems studied are submonolayer to monolayer coverages of benzene on Ag(111) and Cu(111), azobenzene/Cu(111), Fe:TPA/Cu(100), and PTCDA on the low index Ag surfaces. To investigate the geometric interface properties and in particular the adsorption height of the molecules, NIXSW is employed. Electronic properties of the PTCDA/Ag systems are studied by ARPES using the relatively new orbital tomography approach.

An aromatic building block In chap. 3 the benzene molecule is studied. It is the smalles aromatic molecule possible and can therefore be considered as building block for larger molecules. Hence, from the behaviour of benzene one can expect to learn about general aspects for the adsorption of organic molecules. The benzene/Ag(111) interface reveals the expected flat adsorption geometry [43, 46–48] and we find an adsorption height of $3.04 \pm 0.02\,\text{Å}$ in our XSW study. Due to the expected weak interacion between benzene and Ag this can be understood as a reference height for mainly vdW interacting systems on Ag. To investigate the situation after the substitution of the Ag(111) crystal by Cu(111), XSW experiments are conducted on benzene/Cu(111). Indeed, the expected change in the molecule-substrate interaction has a large impact on the interface structure. Although the benzene was expected to adsorb flat on Cu(11), too [71], the XSW analysis reveals a coexistence of a flat and an upright species. LEED experiments prove the formation of a commensurate overlayer by the upright standing benzene. This is a clear indication of enhanced molecule-substrate interaction. The flat lying benzene resides at an unsual high adsorption distance of $3.55 \pm 0.02\,\text{Å}$. Because this adsorption distance is much larger than the reference of the weakly interacting benzene/Ag(111), it is expected to become only feasible through molecule-molecule interactions with the upright species.

Intermolecular interactions To investigate changes in the interplay of adsorbate-adsorbate and adsorbate-substrate interactions, TPA was studied on Cu(100). The TPA molecule consists of a phenyl ring in the center and two carboxyl groups attached in para orientation. While the vertical structure of the pure TPA/Cu(100) is already known [36], the focus is on changes upon the coadsorption of Fe. The Fe atoms act as coordination centers and a well known metal-organic network is formed [15, 16]. The vertical structure of the cloverleaf network phase, including the adsorption heights of the TPA molecule and the Fe atoms are revealed. The phenyl ring is found at an adsorption height of 2.44 ± 0.02 Å, compared to pure TPA/Cu(100) the molecule is therefore lifted by about 0.2 Å due to the Fe coordination, with a slightly larger impact on the oxygens. The reason is the weakening of the molecule-substrate by the additional bonding possibility to the Fe atom. A time dependent increase in the Fe height is observed, preventing an accurate determination of its initial adsorption height, but 2.37 ± 0.05 Å could be extracted as an upper limit. The movement of the Fe is attributed to a slow adsorption of flourine on the Fe atoms, due to a contamination of the setup. However, the adsorption of molecular oxygen onto the TPA:Fe/Cu(100) layer seems to have the same effect as the flourine adsorption, i.e. it is lifting the Fe to 2.84 ± 0.04 Å and passivates it against the flourine.

Another example for the influence of intermolecular interactions is studied quantitatively in sec. 5.5 on the example of PTCDA/Ag(110). Using the relatively new orbital tomography approach (see sec. 2.3) it is possible to separately access information of differently oriented molecules in the unit cell by ARUPS. This allows to measure the difference in the energy level alignment within a monolayer of PTCDA/-Ag(110) between the two inequivalent molecules in the superstructure. A split of the LUMO and HOMO level in the order of 50 meV is resolved. By a comparison to the calculation of a free standing layer of PTCDA molecules in the correct superstructure arrangement the observed split is clearly indentified as a result of the molecule-molecule interaction.

A comprehensive view on energy level alignment The PTCDA/Ag(110) experiments are embedded in chap. 5, where a comprehensive view on the adsorption of PTCDA on low index Ag surfaces is presented. Because of the extended data base of the geometric and electronic properties of PTCDA/Ag this system is the perfect candidate to understand its adsorption behaviour in a general way. So far missing data on the adsorption height and the LUMO and HOMO binding energies is presented in secs. 5.4 and 5.6 as a result from NIXSW and orbital tomography experiments, respectively. Furthermore, triangulation of XSW data allowed to determine the adsorption site for PTCDA/Ag(100), the carboxylic oxygens and thus the molecule center adsorb in on-top position. Former results from literature, in particular the adsorption heights of PTCDA/Ag(111) [60] and PTCDA/Ag(110) [39], and the new findings are merged into one adsorption picture. A crucial role of the work function is revealed: On one hand the adsorption heights of PTCDA/Ag(111), PTCDA/Ag(100) and PTCDA/Ag(110) follow the the trend of the work function (the trend is the same for the bare metal and the final interface work function) and on the other hand the binding energy of HOMO and LUMO is connected to the work function as well. However, the details of the dependency are a surprising finding. The energy level alignment of the HOMO is determined by the work function of the bare metal substrate, this means that the sum of the HOMO binding energy and the metal work function, i.e. a kind of ionisation potential, is nearly constant for all PTCDA/Ag surfaces. This is underlining the passive role of the HOMO orbital in the adsorption process. Even more surprising, the LUMO follows the same behaviour if the work function of the resulting PTCDA/Ag interface is considered instead of the bare substrate, this means one ionisation potential is valid for the various PTCDA/Ag monolayers despite their differences in adsorption height, degree of hybridization and lateral superstructure. The finding of general properties for the PTCDA/Ag interfaces is continued in sec. 5.7 by a study of the orbital ordering of stronger bound molecular orbitals, following the HOMO towards higher binding energy. The order of the next four orbitals, which are closely spaced in energy, is found the same for all PTCDA/Ag systems investigated. However, the order disagrees with the calculations for a free PTCDA molecule in the gas phase, raising the question if we can measure the primal orbital ordering with the orbital tomography approach (and the calculations ar not correct) or if a general property of Ag determines this order.

Density driven dissociation Molecules which are promising candidates for future organic electronic devices are a prominent subject for experiments. Only the understanding of fundamental principles in complex processes allows to develop target oriented properties of interfaces due to the multitude of available molecule-substrate combinations. Therefore the adsorption behaviour of the archetypal molecular switch azobenzene on the Cu(111) surface was studied in detail in chap. 4. In the submonolayer to monolayer regime two most interesting findings are revealed:

First, the detailed vertical adsorption geometry of the molecule is derived from

XSW experiments. The azo-bridge resides at $2.02 \pm 0.02\,\text{Å}$, which is indicating a strong chemisorptive interaction through this functional linker group. Furthermore, the detailed geometry of the attached benzene rings is extracted. Serving as a benchmark tool for the challenge to include dispersive interactions in DFT, it should be noted that our result is found in perfect agreement with state of the art DFT calculations [92].

The second result is a phase change in the azobenzene layer which is identified as a coverage driven dissociation. The phase change can be traced by LEED, because the lateral structure appears disordered at low coverages, where the azobenzene molecule is still intact, and laterally ordered structures are found upon a coverage increase. At the same time the signature of the N1s undergoes a prominent change in XPS. We could identify, that the formation of ordered structures is accompanied by a dissociation of azobenzene molecules into phenyl nitrene, similar to the azobenzene/TiO_2 behaviour [12], hence leading to a clear change in the XPS. The phenyl nitrene species is characterized by NIXSW and shows an adsorption height of $1.17 \pm 0.04\,\text{Å}$ for the nitrogen and an upright pointing phenyl ring. The dissociation into phenyl nitrene might be a reason why the switching probability of azobenzene is quenched: The molecule can not undergo the neccessary conformational change without breaking apart.

Outlook Altogether the work presented here provides interesting data on several metal-organic interfaces and promotes the understanding and disentangling of various contributions in the complicated adsorption process. In many cases unexpected results are found, which stresses the importance of our research and shows that the systematic understanding of metal-organic interfaces is still rather rudimentary. Hence, further research on a fundamental level is an essential step to ultimately achieve the goal to enable target oriented engineering of novel organic devices and their properties.

A Appendix

Calculation for the adsorption site of PTCDA/Ag(100)

In sec. 5.4.6 the adsorption position $\vec{c} = (x, y, z)$ of the carboxylic oxygen in PTCDA/Ag(100) is calculated by the intersection of three planes. Here the calculation is given in detail. First we repeat the equations for the planes:

$$d_{[200]} \begin{pmatrix} 1 \\ 0 \\ 0 \end{pmatrix} + a_{[200]} \begin{pmatrix} 0 \\ 1 \\ 0 \end{pmatrix} + b_{[200]} \begin{pmatrix} 0 \\ 0 \\ 1 \end{pmatrix} = \begin{pmatrix} x \\ y \\ z \end{pmatrix} \tag{A.1}$$

$$\frac{1}{\sqrt{3}} d_{[111]} \begin{pmatrix} 1 \\ 1 \\ 1 \end{pmatrix} + a_{[111]} \begin{pmatrix} 0 \\ 1 \\ -1 \end{pmatrix} + b_{[111]} \begin{pmatrix} -1 \\ 1 \\ 0 \end{pmatrix} = \begin{pmatrix} x \\ y \\ z \end{pmatrix} \tag{A.2}$$

$$\frac{1}{\sqrt{3}} d_{[111]} \begin{pmatrix} 1 \\ -1 \\ 1 \end{pmatrix} + a_{[1\bar{1}1]} \begin{pmatrix} 0 \\ 1 \\ 1 \end{pmatrix} + b_{[1\bar{1}1]} \begin{pmatrix} -1 \\ -1 \\ 0 \end{pmatrix} = \begin{pmatrix} x \\ y \\ z \end{pmatrix} \tag{A.3}$$

This leads to a system of nine equations:

$$d_{[200]} = x \tag{A.4}$$

$$a_{[200]} = y \tag{A.5}$$

$$b_{[200]} = z \tag{A.6}$$

$$\frac{1}{\sqrt{3}} d_{[111]} - b_{[111]} = x \tag{A.7}$$

$$\frac{1}{\sqrt{3}} d_{[111]} + a_{[111]} + b_{[111]} = y \tag{A.8}$$

$$\frac{1}{\sqrt{3}} d_{[111]} - a_{[111]} = z \tag{A.9}$$

$$\frac{1}{\sqrt{3}} d_{[111]} - b_{[1\bar{1}1]} = x \tag{A.10}$$

$$-\frac{1}{\sqrt{3}} d_{[111]} + a_{[1\bar{1}1]} - b_{[1\bar{1}1]} = y \tag{A.11}$$

$$\frac{1}{\sqrt{3}} d_{[111]} + a_{[1\bar{1}1]} = z \tag{A.12}$$

From (A.7) = (A.10) we find

$$\frac{1}{\sqrt{3}} d_{[111]} - b_{[111]} = \frac{1}{\sqrt{3}} d_{[111]} - b_{[1\bar{1}1]} \Rightarrow b_{[111]} = b_{[1\bar{1}1]}. \tag{A.13}$$

From (A.9) = (A.12) we find

$$\frac{1}{\sqrt{3}} d_{[111]} - a_{[111]} = \frac{1}{\sqrt{3}} d_{[111]} + a_{[1\bar{1}1]} \Rightarrow a_{[111]} = -a_{[1\bar{1}1]}. \tag{A.14}$$

From (A.8) + (A.11) we find

$$\frac{1}{\sqrt{3}} d_{[111]} + a_{[111]} + b_{[111]} - \frac{1}{\sqrt{3}} d_{[111]} + a_{[1\bar{1}1]} - b_{[1\bar{1}1]} = 2y \tag{A.15}$$

and using (A.13) and (A.14) it becomes

$$\frac{1}{\sqrt{3}} d_{[111]} + a_{[111]} + b_{[111]} - \frac{1}{\sqrt{3}} d_{[111]} - a_{[111]} - b_{[111]} = 2y \Rightarrow \underline{\mathbf{y} = \mathbf{0}}. \tag{A.16}$$

From (A.8) + (A.9) we get

$$\frac{1}{\sqrt{3}}d_{[111]} + a_{[111]} + b_{[111]} + \frac{1}{\sqrt{3}}d_{[111]} - a_{[111]} = y + z \Rightarrow \frac{2}{\sqrt{3}}d_{[111]} + b_{[111]} = z \quad \text{(A.17)}$$

and rewriting (A.7) using (A.4) we find

$$\frac{1}{\sqrt{3}}d_{[111]} - b_{[111]} = d_{[200]} \Rightarrow b_{[111]} = \frac{1}{\sqrt{3}}d_{[111]} - d_{[200]} \quad \text{(A.18)}$$

together (A.17) and (A.18) give

$$\frac{2}{\sqrt{3}}d_{[111]} + b_{[111]} + \frac{1}{\sqrt{3}}d_{[111]} - d_{[200]} = \underline{\boldsymbol{\sqrt{3}}\mathbf{d}_{[\mathbf{111}]} - \mathbf{d}_{[\mathbf{200}]} = \mathbf{z}}. \quad \text{(A.19)}$$

Hence, the resulting vector is

$$\vec{c} = \begin{pmatrix} d_{[200]} \\ 0 \\ \sqrt{3}d_{[111]} - d_{[200]} \end{pmatrix}. \quad \text{(A.20)}$$

List of Figures

2.1 (a) Experimental datacube $I(k_x, k_y, E_\mathrm{B})$ as schematic false colour plot. For the orbital tomography slices of constant binding energy are extracted and the resulting $I(k_x, k_y)$ CBE map is fitted by theoretical CBE maps of contributing orbitals. (b) Fourier transform of the molecular orbital with the hemispherical cut to extract the calculated CBE map which is shown in panel c. The figure is done by D. Lüftner, KFU Graz. (c) Calculated CBE map for the LUMO of PTCDA. The calculations were done by D. Lüftner and P. Puschnig, KFU Graz. 9

2.2 Two Argand diagrams are shown to visualize the use of P_c and F_c as Fourier components. In these polar plots P_c acts as the angle parameter and F_c is the radius. This intrinsically fulfills the requirement $0 \equiv 1$ for P_c. In panel a the vector sum of the red and the blue lead to the green result, assuming that the population of red and blue is equal. In panel b the red and blue results differ by a P_c of 0.5 and therefore their mean value (green) has a F_c of 0, rendering its P_c meaningless despite the well defined results for red and blue. 14

2.3 Sketch of the experimental UHV chamber system at ID 32 at the ESRF Grenoble. It consists of two main parts: First the analysis chamber (top part of the figure) equipped with an electron analyzer (Phoibos 225, SPECS), a coolable sample stage which allows for precise sample positioning, a reflectivity screen to record the intensity of the reflected beam, the beamline connection, the mesh I0 to measure incoming beam intensity and the benzene doser. Second the preparation chamber (bottom part of the figure) equipped with a sample storage, evaporators, a load lock, the transfer system, a LEED, a sputter gun and a QMS 17

3.1 Sketch of the benzene molecule (C_6H_6) with the carbons depicted in black and the hydrogens in white. All carbons are equivalent with a C-C distance of 1.4 Å and consequently 120° bond angles. 20

3.2 Off-Bragg XPS spectra at $E_{\text{photon}} = 2620\,\text{eV}$ of the C1s signal for Bz/Ag(111) to visualize beam induced changes. The spectra show a time dependent change of the peak-position, starting at 284.3 eV (black) changing to 284.2 eV (red) and further to 284.1 eV (green). The overall shift is 200 meV. Besides the centre position also the width is changed. The difference is more prominent on the low binding energy side. The reason for this change is the X-ray exposure time given in the top right corner for all spectra. All spectra were normalized to the mean value of the Ag background in the interval [280 eV,281 eV] which is indicated by a grey box. 23

3.3 On individual XPS spectra of a XSW measurement of preparation 2 the enhanced beam damage during the XSW measurement is depicted. The XSW data set consists of 22 consecutive XPS spectra of which eight are shown in this figure starting with the first (01) at the top left and ending with the last (22) at the bottom right. All spectra show the raw data (open circles), the background (black line) two components (dashed grey lines) and the resulting envelope (red line). From spectrum 11 on the consistence of raw data and envelope clearly gets worse due to a shift of the C1s peak. The components cannot follow the shift as they are constrained in position, width and relative intensity. The effect is similar to the beam damage observed from XPS as shown in Fig. 3.2. 24

3.4 Off-Bragg XPS spectra at $E_{\text{photon}} = 2620\,\text{eV}$ of the C1s signal used for the coverage estimation for preparation 2 (black), 3 (red) and 4 (blue) together with a C1s reference spectrum of a PTCDA/Ag(111) monolayer [53] (grey) measured at $E_{\text{photon}} = 2633\,\text{eV}$. While the benzene specra can be directly compared the PTCDA spectrum is not corrected for the different carbon density on the surface. In Table 3.2 the intensities are tabulated together with the corrected PTCDA intensity as reference. All spectra were normalized to the mean value of the Ag background in the interval [276 eV,278 eV] which is indicated by a grey box. 25

3.5 Example for an electron yield (a) and a reflectivity fit (b) for benzene/-Ag(111). The displayed data belongs to XSW data set 085 and the x-axis displays the photon energy relativ to the Bragg energy of $E_{\mathrm{Bragg}} = 2636.2\,\mathrm{eV}$. 28

3.6 Argand diagram visualizing the results for benzene/Ag(111) for preparations 2 (black), 3 (red) and 4 (blue) (see Table 3.3). The data spread is very low and no preparation dependence is observed. 28

3.7 Vertical adsorption geometry of benzene/Ag(111). The filled circles represent the carbon (black) and silver (grey) positions. The solid cirles represent the covalent ($r^{\mathrm{cov}}_{\mathrm{Ag}} = 1.45\,\text{Å}$, $r^{\mathrm{cov}}_{\mathrm{C}} = 0.73\,\text{Å}$)[55] and the dashed lines the vdW bonding radii ($r^{\mathrm{vdW}}_{\mathrm{Ag}} = 1.72\,\text{Å}, r^{\mathrm{vdW}}_{\mathrm{C}} = 1.77\,\text{Å}$) [56]. The small overlap of the vdW radii of silver and carbon of 0.45 Å suggests that benzene is only physisorbed on Ag(111). 29

3.8 Off-Bragg XPS spectra at $E_{photon} = 2960\,\mathrm{eV}$ of the C1s signal for Bz/Cu(111) to observe possible exposure time related changes. In contrast to benzene/Ag(111) (see Fig. 3.2) the spectra show no time dependent behaviour within the measured time of 35 min. The exposure times are given at the top right corner. 35

3.9 Exemplary reflectivity curve of preparation 4. The experimental data shows a clear tilt of the baseline which is a consequence of a normalization error due to an unstable beam. Therefore the results from this preparation are discarded. 36

3.10 The graph shows normalized off-Bragg XPS spectra ($E_{\mathrm{photon}} = 2960\,\mathrm{eV}$) of the C1s signal for Bz/Cu(111) from preparations 1 (black), 2 (red) and 3 (green), to compare their coverages. Clearly preparation 1 yields the highest coverage while 2 has a lower one than 3 as preparation 3 is done by dosing more material onto preparation 2. The quantitative estimation leads to the numbers given in Table 3.5. The normalization of all spectra was done in the low binding energy range indicated by the grey box. 37

3.11 Representative XPS spectra from the XSW data set 058 (Preparation 1). Each color represents the C1s XPS spectrum at a different photon energy during the XSW measurement. Two independent XSW components are clearly present (marked by arrows). Therefore the shoulder on the carbon peak cannot (only) be explained by satellites. The behaviour is not restricted to preparation 1 but observed in all XSW spectra for benzene/Cu(111) and makes a dedicated XPS model (see Fig. 3.12) mandatory for a meaningful XSW analysis. 38

3.12 Sum of 3 off-Bragg XPS spectra, taken at $E_{\text{photon}} = 2960\,\text{eV}$ of the C1s region for benzene/Cu(111) to derive a model for the XSW analysis. A two component model was chosen as the quality of the single XSW spectra asks for a simple model, although a third component could increase the fitting quality on the high binding energy side. Furthermore, the position of the tilted component (green) was extracted from single XPS spectra of the XSW data sets where the peak is more pronounced in comparison to the flat component (red) (see Fig. 3.11). The shown spectrum is a sum of 3 normalized XPS spectra to get better statistics. They were taken at different positions on the sample during preparation 1. 38

3.13 Argand diagram displaying the results of the XSW analysis for benzene/-Cu(111). The datapoints of the flat component (red) are found at very high F_{c} (note that the scale goes up to 1.2) while the tilted component (green) is found at rather low F_{c}. The P_{c} is identical for both components. Hence the sum (black) is at the same P_{c} with the F_{c} in between the components and it is in good agreement with the result for the full intensity after background subtraction (blue). 39

3.14 Yield curves of XSW data set C1s064 ater employing the XPS model shwon in ig. 3.12 for the XSW fitting. The corresponding reflectivity curve is shown as well. The results of all XSW data sets are given in Table 3.6. 40

3.15 To visualize possible preparation dependent effects of the results from Table 3.6 the data points are plotted into four Argand diagrams. We see that preparation 1 (red) and 2 (black) are in agreement in all cases and no preparation dependence is found. 43

3.16 In panel (a) the commensurate LEED pattern of benzene/Cu(111) is shown together with an overlayed simulation performed by *Spotplotter* [78]. In the simulation, small red circles mark the superstructure, the big red circle the (00), and blue circles the substrate spots. Thin lines indicate the substrate (blue) and the superstructure (red) reciprocal unit cell vectors. The observed mismatch between LEED picture and simulation, especially present in the left part of the picture, is a technical artifact and originates from the distortion of the LEED image. The resulting real space unit cell is indicated in the picture in panel (b) by a green rectangle and its matrix is shown in the top left corner. Such a small unit cell can only exist if the benzene molecules are tilted. The tilt angle of 70° is extracted from the XSW analysis of component two. Flat benzene molecules would not fit in the unit cell and therefore they are expected to form disordered arrangements which are therefore not recognized in the LEED image. 44

3.17 Side view of the benzene adsorption geometry for the $70 \pm 20°$ tilted (a) and the flat (b) adsorbing species. The adsorption heights of $4.64 \pm 0.15\,\text{Å}$ and $3.55 \pm 0.02\,\text{Å}$, and the tilt angles are the result of the XSW data evaluation (numbers are given in Table 3.6). The Cu surface layer is depicted in orange, carbon atoms are drawn in black and Hydrogen as open circles. Spheres mark the corresponding covalent ($r_{\text{Cu}}^{\text{cov}} = 1.32\,\text{Å}$, $r_{\text{C}}^{\text{cov}} = 0.73\,\text{Å}$, $r_{\text{H}}^{\text{cov}} = 0.31\,\text{Å}$) [55] and dashed circles the vdW radii ($r_{\text{Cu}}^{\text{vdW}} = 1.4\,\text{Å}$, $r_{\text{C}}^{\text{vdW}} = 1.77\,\text{Å}$) [56]. The vdW radii of the H atoms ($r_{\text{H}}^{\text{vdW}} = 1.00\,\text{Å}$)[56] are not displayed for simplicity. Shadowed molecular outlines in the background display the possible deviation due to the error of the angle of 20° for the tilted and 10° for the flat species. 45

3.18 (a) Schematic picture of a dendritic mixture of flat (red area) and tilted (green area) molecules. The black arrow marks the position of the sideview depicted in panel (b), where the flat (red) and tilted (green) molecules are sketched. 47

4.1 *trans* (left) and *cis* (right) configuration of azobenzene. In the gas phase the molecule can be switched from its *trans* to the *cis* state by UV light and vice versa by blue light. 49

4.2 LEED picture of the DP of azobenzene on Cu(111). No spots are visible but a hexagonal shaped background intensity is identified to be characteristic for this phase. 51

4.3 Off-Bragg XPS spectrum ($E_{\text{photon}} = 2960\,\text{eV}$) for the N1s emission of the DP. The XSW fitting model contains only the DP component shown in blue located at 397.8 eV. A shirley background is subtracted shown in black, to account for the Cu background intensity. 52

4.4 Off-Bragg XPS spectrum ($E_{\text{photon}} = 2960\,\text{eV}$) for the C1s emission of the DP. In contrast to N1s (see Fig. 4.3) the XSW fitting model contains several components. The C-C component (red) at 284.0 eV represents the carbons which only bind to other carbons while the C-N component (green) at 284.9 eV represents the carbons bonded to nitrogen. In the high binding energy tail two satellites (orange and pink) are identified. A shirley background (black) is subtracted to account for the background intensity. 52

4.5 Results of the XSW analysis for the submonolayer azobenzene on Cu(111) depicted in an Argand diagram. The results for nitrogen from the N1s spectra are shown in blue, the results for carbon are shown in black, red and green. The red (C-C component) and green (C-N component) data points refer to the corresponding components of the XPS model shown in Fig. 4.4, the black datapoints represent the sum of both components. All values are tabulated in Table 4.2 for C1s and Table 4.3 for N1s. 53

4.6 Exemplary electron yield curves from the C1s XSW fit using the XPS model depicted in Fig. 4.4. The displayed data belongs to XSW data set C1s047. The x-axis displays the photon energy relativ to the Bragg energy. The results of all C1s data sets are summarized in Table 4.2. 54

4.7 Exemplary electron yield curves from the N1s XSW fit using the XPS model depicted in Fig. 4.3. The displayed data belongs to XSW data set N1s046. The x-axis displays the photon energy relativ to the Bragg energy of. The results of all N1s data sets are summarized in Table 4.3. 56

4.8 Panel (a) shows a LEED picture of the PLP taken at an energy of 30 eV. It shows a clear hexagonal structure of spots. In panel (b) the same picture is shown with a simulated LEED pattern on top corresponding to the given point-on-line coincident superstructure matrix. Due to this matrix the phase is named *point-on-line phase* (PLP). The LEED simulation is done with *Spotplotter* [78]. 58

4.9 Off-Bragg XPS spectrum ($E_{\text{photon}} = 2960\,\text{eV}$) of the N1s region for the PLP. Two peaks are visible each fitted with one component. The DP component at 397.8 eV (dark blue) is already known from the DP (see Fig. 4.3) but at 396.3 eV a new feature appeared (light blue), which is named COP component. This new peak will later be identified as a signature of the dissociated phenyl nitrene species. 59

4.10 Off-Bragg XPS spectrum ($E_{\text{photon}} = 2960\,\text{eV}$) visualizing the XSW fitting model for C1s for the PLP. In general the spectrum looks like the one of the DP in Fig. 4.4 but peaks are slightly shifted. The C-C component (red) is now at 283.7 eV and the C-N component (green) at 284.7 eV. However a distinct new feature as it appeared in the N1s spectrum (see Fig. 4.9) is not visible. 59

4.11 Exemplary electron yield curves from the C1s XSW fit using the XPS model depicted in Fig. 4.10. The displayed data belongs to XSW data set C1s025. The x-axis displays the photon energy relativ to the Bragg energy. The results of all C1s data sets are summarized in Table 4.5. 61

4.12 Exemplary electron yield curves from the N1s XSW fit using the XPS model depicted in Fig. 4.9. The displayed data belongs to XSW data set N1s026. The x-axis displays the photon energy relativ to the Bragg energy. The results of all N1s data sets are summarized in Table 4.6. 62

4.13 Argand diagram showing the XSW results of the PLP data. The N1s results are shown in dark blue for the DP component and in light blue for the COP component of the PLP. Indeed the DP component results are very close to the pure DP (see sec. 4.2). However the COP component shows a completely different result. It should be noted that the maximum diameter shown for F_c here equals 1.2. Unfortunately, for the C1s results (C-C component in red and C-N component in green) we have only two data points each, which show quite some scattering especially in the case of the C-N component. All values are tabulated in Table 4.5 for C1s and Table 4.6 for N1s. 63

4.14 Panel (a) shows a LEED picture of the COP. In panel (b) the same picture is overlayed by a LEED simulation done with *Spotplotter* [78] leading to the commensurate superstructure matrix shown. Blue circles in both pictures indicate spots which are missing in the real picture while they are present in the simulation. This is a clear sign for a glide plane symmetry in the unit cell [88]. 65

4.15 Off-Bragg XPS spectrum ($E_{\mathrm{photon}} = 2960\,\mathrm{eV}$) of C1s for the COP. The main peak is fitted with two components due to its asymmetry, one at 283.1 eV (component 1, red) and another one at 283.8 eV (component 2, green) binding energy. The fitted region is chosen such that the model can be transferred to the XSW spectra. A satellite (orange) is neccessary to fit the high binding energy tail of the peak. 66

4.16 Off-Bragg XPS spectrum ($E_{\mathrm{photon}} = 2960\,\mathrm{eV}$) of N1s for the COP. Three components are clearly visible in the spectrum. The COP component at 396.0 eV, a shoulder at 396.8 eV which is attributed to a mixture of DP and COP contributions and hence named Mixed component and a Satellite feature at 398.6 eV. While the COP peak is known from the PLP as seen in Fig. 4.9 the other peaks are new. . 66

4.17 Exemplary electron yield curves from the C1s XSW fit using the XPS model depicted in Fig. 4.15. The displayed data belongs to XSW data set C1s009. The x-axis displays the photon energy relativ to the Bragg energy. The results of all C1s data sets are summarized in Table 4.9. 68

4.18 Exemplary electron yield curves from the N1s XSW fit using the XPS model depicted in Fig. 4.16. The displayed data belongs to XSW data set N1s006. The x-axis displays the photon energy relativ to the Bragg energy. The results of all N1s data sets are summarized in Table 4.8. 69

4.19 Argand diagram showing the XSW results of the COP data. N1s results are depicted in blue, C1s results in red and green according to the fitting models in figs. 4.16 and 4.15. Datapoints indicated by a black arrow are taken on already beam exposed spots and therefore deviate due to beam damage effects. All data shown here is tabulated in tables 4.8 and 4.9. 72

4.20 Off-Bragg XPS spectrum ($E_{\mathrm{photon}} = 2960\,\mathrm{eV}$) of C1s for the MLP. The spectrum is dominated by the peak at 285.0 eV (scarlet) which is therefore identified as multilayer signature while the peak at 283.3 eV (red) is already known from the COP and hence identified as monolayer peak. 74

4.21 Off-Bragg XPS spectrum visualizing the XSW fitting model of N1s for the MLP. Three well separated contributions are identified. A strong multilayer peak at 400.2 eV (green), its satellite at 403.6 eV (orange) and the monolayer signature already known from the PLP and COP at 396.3 eV (blue). 75

4.22 Off bragg XPS spectra of the various phases of azobenzene/Cu(111) of the (a) N1s and (b) C1s core level lines to extract the azobenzene coverage for each phase. These are the same spectra which were used for the fit model determinations, but normalized to the low binding energy background. The DP is shown in blue, the PLP in green, the COP in red, and the MLP in black. The spectra are shifted on the y-axis to allow a better comparison, peak positions are marked by black bars. The intensity values extracted for the coverage analysis are given in Table 4.11. 76

4.23 Exemplary electron yield curves from the C1s XSW fit using the XPS model depicted in Fig. 4.20. The displayed data belongs to XSW data set C1s019. The x-axis displays the photon energy relativ to the Bragg energy. The results of all C1s data sets are summarized in Table 4.13. 79

4.24 Exemplary electron yield curves from the N1s XSW fit using the XPS model depicted in Fig. 4.21. The displayed data belongs to XSW data set N1s017. The x-axis displays the photon energy relativ to the Bragg energy. The results of all N1s data sets are summarized in Table 4.12. 80

4.25 Argand diagram showing the XSW results of the MLP data. The multilayer results for N1s (green) and C1s (scarlet) are near F_{c} 0 as expected for vertical disorder as the multilayer spacing does not match the Bragg spacing. However, the monolayer contributions of N1s (light blue) and C1s (red) fit very well to the COP results indicating this interface layer may be unchanged. All values are tabulated in tabs. 4.12 and 4.13. 81

4.26 Vertical adsorption geometry of azobenzene on Cu(111) in the DP. The atomic positions are marked by filled circles, nitrogens are blue, carbons are black, copper is orange. Hydrogens are not depicted for clarity reasons. Dashed lines mark vdW radii [56], solid lines covalent radii [55]. The tilt angle of the phenyl rings is depicted in more detail in Fig. 4.27. 84

4.27 Detailed picture of the bonding angles in azobenzene adsorbed on Cu(111) in the DP. The differential XSW analysis allows to get independent vertical heights for the nitrogen (blue), the carbon which is bonding to the nitrogen (grey) and the residual carbons (open cirles). The center of mass of the residual carbons is depicted as black dot. The tilt angles are calculated assuming that bonding distances within the molecule stay constant. 84

4.28 (a) Full model of the azobenzene in the adsorption geometry of the DP including the tilt of the phenyl rings around the long axis of the molecule extracted from the F_c. (b) Model for the geometry of azobenzene/Ag(111), reported from XSW measurements [59]. (c,d) Construction of the dihedral angles β (NNCC) and ω (CNNC). The angles are measured between the shown red and blue planes. Each plane is defined by three atoms, indicated with circles in the plane colour. Note that the red planes in (c) and (d) are identical, because they are defined by the same atoms. (c) is depicted in a different perspective to allow the visualization of the β angle. Cu surface atoms are shown in orange, Ag in grey, carbons in black, nitrogens in blue and hydrogens in white. 85

4.29 Reaktion scheme for the dissociation of azobenzene into two phenyl nitrenes. 88

4.30 Argand diagram depicting the vector sum to subtract the DP contribution from the PLP results following eq. (4.10). The green dot represents the C1s C-C result from the PLP, the blue dot the C1s C-C result from the DP. Assuming that the PLP is a sum of the COP C-C and the DP C-C results, we can extract the COP value by subtracting the DP from the PLP (see sec. 2.4 for details). The resulting contribution is marked by the green star, representing the C1s result for the COP molecules in the PLP. The red arrows represent the vectors corresponding to the various C-C results, while the black arrows are weighted correctly for the relative abundance of COP and DP molecules in the PLP. 89

4.31 Model of the upright standing phenyl nitrene adsorbed on a 3-fold hollow site on the Cu(111) surface. Copper atoms are shown in orange, carbons in black, nitrogens in blue and hydrogens in white. . . 91

4.32 Adsorption model of the DP like molecules in the PLP as the phenyl nitrene is expected to be disordered. Green arrows indicate the superstructure unit cell according to the matrix shown at the top right corner. As the structure is not commensurate adsorption sites shown here are arbitrary. The copper surface atoms are depicted in orange, carbons in black, nitrogens in blue, and hydrogens in white. 92

4.33 Adsorption model of the COP. The upright standing phenyl nitrene occupies 3-fold hollow sites as depicted in Fig. 4.31. The distribution and orientation of the molecules is chosen such that the super structure matrix shown in the top right corner is achieved and glide plane symmetry exists. The unit cell is marked by green arrows, the glide symmetry planes by blue lines. 93

4.34 N1s(a) and C1s(b) XPS spectra from the MLP XSW measurement series. Spectra are taken at increasing photon energies from top to bottom and shifted on the y-scale for better visibility. While the first (black) and last (dark yellow) spectrum show the same position for all peaks a clear shift in binding energy of the multilayer peak is observed for the spectra in between, while the monolayer signature does not move. The intensity differences stem from the standing wave effect and the broadening of the final spectrum is expected to be a consequence of possible beam damage. 93

4.35 Scheme for the azobenzene adsorption height as a function of the molecule distortion and the layer density. In the grey area the behaviour of azobenzene/Ag(111) is depicted. From calculations for azobenzene/Ag(111) [59] it is known that a coverage increase leads to a tilt of the molecules, because the adsorption energy per surface area is enhanced by a denser packing. Along with the tilt (and the increasing layer density), the molecule is lifted from the surface. In the orange area the behaviour of azobenzene/Cu(111) is depicted. Due to the much stronger N-Cu bond the molecule can not lift up from the surface and hence a continuous molecule distorsion cannot be realized. An increasing density therefore leads to a dissociation at the N=N bond into phenyl nitrene following the reaction depicted in Fig. 4.29. In contrast to azobenzene/Ag(111) the continuous change in adsorption height for the increasing layer density for azobenzene/Cu(111) is realized by a change in the abundance of two species rather than in a continuous change on all molecules. 96

5.1 Top view of the PTCDA molecule. Carbon atoms are displayed in grey (carboxylic carbon) and black (perylene carbon), hydrogen atoms in white, and the two types of oxygen atoms in red (carboxylic oxygen) and blue (anhydride oxygen). 101

5.2 Structure models of the (a) HB monolayer of PTCDA/Ag(111) and (b) monolayer of PTCDA/Ag(100) with the corresponding superstructure matrices. Black arrows in the structure models indicate the real space unit cell. The two differently oriented molecules in the HB phase unit cells are marked as A(red) and B(blue). For the monolayer of PTCDA/Ag(100) red and blue molecules are equivalent. 102

5.3 LEED patterns and structure models of the PTCDA/Ag(110) interface with their corresponding superstructure matrices. (a-b) brickwall (BW) monolayer, (c-d) herringbone on brickwall (HB-on-BW) bilayer, (e-f) herringbone (HB) monolayer (compressed monolayer). One half of each LEED pattern is overlayed by a pattern of calculated spot positions. Blue lines in the LEED image indicate the substrate directions, red lines indicate the reciprocal space unit cell. Black arrows in the structure models indicate the real space unit cell. The two differently oriented molecules in the HB phase unit cells are marked as A(red) and B(blue). The LEED pictures were recorded with a multi channel plate LEED by K. Schönauer. The picture has already been published [27] and the reprint of this is permitted under the Creative Commons Attribution 3.0 Unported (CC-BY) license according to the New Journal of Physics copyright statement. 103

5.4 Off Bragg XPS spectra of preparation 1 (red, 0.8 ML), preparation 2 (black, 0.3 ML) and a reference spectrum (grey). The red and black spectra are recorded with $E_{\text{photon}} = 3024\,\text{eV}$ on PTCDA/Ag(100) submonolayer films. The grey spectrum is taken at $E_{\text{photon}} = 2633\,\text{eV}$ on a PTCDA/Ag(111) closed monolayer [53] and used as a reference for the absolute coverage estimation. All spectra are normalized (see text) and a Shirley background was subtracted. The spectra are not corrected for the different unit cell sizes of PTCDA/Ag(100) and PTCDA/Ag(111) 107

5.5 Off Bragg XPS spectrum at $E_{\text{photon}} = 3024\,\text{eV}$ of the C1s region for PTCDA/Ag(100). The spectrum is used to develop the fitting model used in the XSW analysis. Peak position, FWHM and relative area are given in tab 5.2 108

5.6 Argand diagrams visualizing the results of the XSW analysis for the C1s data. As indicated in the XPS model in Fig. 5.5 the sum for C1+C1Sat is depicted in green and the sum of C2+C3+C4 is depicted in red, the sum of all components in blue and the results without a XPS model in black. The latter is very difficult to see, because blue and black points fall on the same spot. The arrows indicate the mean values of the corresponding species. All values are shown in Table 5.3. 111

5.7 Representative electron yield curves of the C1s XSW analysis using the XPS model which is depicted in Fig. 5.5. The data belongs to data set C1s005. The results for all C1s data sets are shown in Table 5.3.112

5.8 Off Bragg XPS spectrum at $E_{\mathrm{photon}} = 3024\,\mathrm{keV}$ of the O1s region for PTCDA/Ag(100). The spectrum is used to develop the fitting model used in the XSW analysis. It consist of five components: The main line of the carboxylic oxygen (Carb, red), its satellite (CarbSat, magenta), the main line of the anhydride oxygen (Anh, light blue), its satellite (AnhSat, dark blue) and a mixed satellite (Sat, green). Peak position, FWHM and relative area are given in Table 5.4 114

5.9 Argand diagram visualizing the results of the XSW analysis for the O1s data. The Carb+CarbSat component representing the carboxylic oxygen is displayed in red, the Anh+AnhSat representing the anhydride oxygen in blue and the result without applying any model in black. Arrows indicate the corresponding mean values. Datapoints of preparation one and two are represented by open triangles and filled circles respectively. All values are given in Table 5.5. 115

5.10 Representative electron yield curves of the O1s XSW analysis using the XPS model which is depicted in Fig. 5.8. The data belongs to data set O1s006. The results for all O1s data sets are shown in Table 5.5. . 117

5.11 Side and top view of a (100) surface. The grey circles mark the position of substrate atoms and dashed grey lines indicate the corresponding (200) and (111) Bragg planes. A red circle represents an adsorbate on an on-top adsorption site, while the blue circle represents an adsorbate on the hollow adsorption site. As indicated by the red and blue arrows in the side view, they would yield different P_c in the XSW experiment employing the (111) Bragg reflection. Hence, the on-top and hollow adsorption sites could be unambiguously differentiated. 119

5.12 Sideview of a PTCDA molecule adsorbed on-top on a Ag(100) surface. The picture is overlayed by the Bragg-planes in the [200] and [111] direction drawn as dashed lines. A green line indicates the plane parallel to the (200) Bragg planes with the adsorption height $d_{[200]}$ of the carboxylic oxygen (red) and a blue line marks the plane parallel to the (111) Bragg planes with the corresponding distance $d_{[111]}$. Hence, their crossing point references to the adsorption site of the carboxylic oxygen. An inset shows a 3D model of the adsorption geometry and the planes used to calculate the carboxylic carbon position. 122

5.13 Side view along the long axis of PTCDA for the vertical adsorption geometry of PTCDA on Ag(110) [39], Ag(100) and Ag(111) [60]. The bottom part of the figure shows the adsorption height from the Ag Bragg plane (indicated by the grey bar) and the molecular distortion in scale. To depict the differences between the three systems in detail, the z-axis distances (along the surface normal) are enhanced by a factor of 20 in the upper part of the figure. The numbers in brackets, given for the perylene core, refer to the mean value of all carbon atoms, i.e. to the sum value of the perylene and carboxylic carbon atoms. This allows the comparison to PTCDA/Ag(111), where the carboxylic carbon contribution was not differentiated from the perylene carbon signal. H atoms are not shown. 126

5.14 Changes of the bond length for the oxygen and carbon species of PTCDA for the different low index Ag surfaces. Values for PTCDA/-Ag(110) and PTCDA/Ag(111) are taken from refs. [39, 60]. For a visualization of the detailed geometries see Fig. 5.13. 127

5.15 Adsorption height depending on the substrate work function. The adsorption heights for PTCDA/Au(111) [61], PTCDA/Cu(111) [110], PTCDA/Ag(111) [60], PTCDA/Ag(100) (this work) and PTCDA/-Ag(110) [39] are corrected by a subtraction of the corresponding substrate vdW radius ($r_{\mathrm{Au}}^{\mathrm{vdW}} = 1.66\,\text{Å}$, $r_{\mathrm{Cu}}^{\mathrm{vdW}} = 1.40\,\text{Å}$, $r_{\mathrm{Ag}}^{\mathrm{vdW}} = 1.72\,\text{Å}$) [56] and plotted against experimental work function values for the bare Au(111) [118, 119], Cu(111) [120–122], Ag(111) [106, 122–126], Ag(100) [124, 125, 127, 128], and Ag(110) [124, 127, 129] surface. . . 129

5.16 Schematic view of LUMO binding energy alignment, molecular adsorption height and π-metal bonding strength (not to scale). (a) The LUMO level of the molecule follows the one-electron image potential in front of the surface. This is shown for a high-work function metal (black) and a low work function metal (red). (b) Once the LUMO reaches the Fermi level, charge is transferred into the molecule, and an attractive potential energy results. The repulsive potential energy is also shown, with the high-work function metal having the larger spill-out. (c) The sum of attractive and repulsive energies shows stronger bonding and shorter adsorption height for the low-work function metal, which also has the larger LUMO binding energy (panel a). 131

5.17 (a-b) CBE maps of the HOMO (a) and LUMO (b) of the BW monolayer of PTCDA/Ag(110). The right half of each map shows theoretical calculations of the electron distribution in k-space calculated for a gas phase molecule. (c-f) CBE maps of the HOMO(c,e) and LUMO(d,f) of the HB monolayer of PTCDA/Ag(110) at different binding energies. Maps in (c-f) are generated from data recorded over an azimuthal angle range of 180° and symmetrized. 134

5.18 (a) Results for the projected density of states of the HOMO and LUMO extracted from orbital tomography (see text) of the HB monolayer of PTCDA/Ag(110). Two contributions can be identified: The intensity from the B molecules (B, blue) and the joint intensity from the HB A and a minority of BW molecules (A+BW, dashed red/black). (b) Results of the fitting of the joint A+BW contribution (dashed red/black) from panel a. The BW intensity is shown in black, the HB A molecule intensity in red. A linear background is subtracted for the fitting. 135

5.19 Results of the calculation of the freestanding PTCDA HB monolayer (figure 5.3f) and the freestanding upper layer of the HB-on-BW bilayer (figure 5.3d). (a,c) Calculated HOMO and LUMO positions of the two inequivalent molecules A(red) and B(blue) with a gaussian broadening of 50 meV of the HB monolayer (panel a) and the upper layer of the HB-on-BW bilayer (panel c). The binding energy of the HB monolayer B-HOMO is aligned with the experiment. (b,d) Electrostatic potential maps in the plane 1 Å above the calculated layer of the HB monolayer (panel b) and the upper layer of the HB-on-BW bilayer (panel d). The regions which were taken into account to calculate an average potential value for molecules A and B are indicated by white ellipses. The unit cell vectors are represented by white arrows. The DFT calculations were carried out by D. Lüftner and Prof. P. Puschnig at the Karl-Franzens-Universität Graz, Austria. 137

5.20 CBE maps of the HOMO (a) and the LUMO (b) of PTCDA/Ag(100) with the corresponding calculated CBE maps used for the tomography approach as inset. Fitting the complete 3D data cube leads to the density of states shown in Fig. 5.21b. 141

5.21 PDOS extracted by the tomography approach (see sec. 2.5.1 for details) for BW PTCDA/Ag(110) [8] (a), PTCDAAg(100) (b), and HB PTCDA/Ag(111) [9] (c). Two inequivalent molecules in the unit cell lead to different results depicted in red (blue) for molecules A(B) as it is seen here for HB PTCDA/Ag(111) [9] and discussed in detail in sec. 5.5. For PTCDA/Ag(100) the peak positions of the blue and red lines coincide, confirming that the molecules of different orientation in the unit cell are equivalent. 143

5.22 Energy level alignment of HOMO and LUMO for HB/Ag(111), constructed from the theoretical work function data of Table 5.10, the bulk ionisation energy of PTCDA [137, 141] and its bulk energy gap [139, 142] (left), compared with the true alignment (right). The latter determined from the experimental data [9] shown in Fig. 5.21c and Table 5.9. 144

5.23 Measured HOMO and LUMO binding energies E_B, relative to the Fermi level E_F, of PTCDA monolayers on Ag(111), Ag(100) and Ag(110). (a) Vacuum levels of the bare surfaces $E^{hkl}_{\mathrm{vac},0}$ are aligned. Φ^{hkl}_0 are the calculated work functions of the correspondin Ag(hkl) surfaces. (b) Vacuum levels of the covered surfaces E^{hkl}_vac are aligned. Φ^{hkl} are the calculated work functions of the corresponding monolayer PTCDA/Ag(hkl) surfaces. 145

5.24 PTCDA ball-and-stick models with wavefunction isosurfaces of the LUMO (a) and HOMO (b) orbital, calculated for a free molecule in the gas phase by D. Lüftner (Karl Franzens Universität Graz) and visualized using the *VESTA 3* Software [143]. 146

5.25 PTCDA ball-and-stick models with wavefunction isosurfaces of the LUMO, HOMO and the four in energy following π-orbitals (C-F), calculated for a free molecule in the gas phase by D. Lüftner (Karl Franzens Universität Graz) and visualized using the *VESTA 3* Software [143]. 149

5.26 Orbital tomography results for the various PTCDA/Ag systems. In each case four orbitals could be deconvoluted. The theoretical CBE maps used for the identification of each orbital are shown in panel (a). The maps differ between the investigated systems due to the differences in the surface symmetry and the molecule orientation in the unit cells. For the corresponding lateral structures see sec. 5.2 and 5.3. 150

5.27 Binding ernergies of the orbitals C-F for PTCDA on different surfaces and in different lateral arrangements. Visualization of the results presented in Table 5.11. Values for BW PTCDA/Ag(110) are taken from ref. [8]. For an easier comparison the values for the HOMO and LUMO, taken from Table 5.21 and Table 5.8 are plotted as well. . . . 152

6.1 Panel (a) shows the structure formula for TPA. Furthermore two unit cells for different TPA phases are depicted. In panel (b) the pure TPA/Cu(100) structure is presented after complete deprotonation of the molecule as reported in ref. [146]. In panel (c) the so called clover leaf phase is shown which can be formed by Fe deposition onto the pure TPA/Cu(100) phase. Around each Fe center four molecules are coordinated [15]. Carbon is shown in black, oxygen in red, hydrogen in white, copper in orange and iron in grey. Green lines indicate the corresponding 3 × 3 and 6 × 6 unit cells, respectively. 158

6.2 LEED pictures of (a) the 3×3 structure which corresponds to the fully deprotonated TPA/Cu(100) system [146] and (b) the 6 × 6 structure which indicates the formation of the cloverleaf phase after Fe deposition [15]. The corresponding structure models are shown in Fig. 6.1b and c respectively. 159

6.3 Off-Bragg XPS spectrum showing the presence of F1s and relating the peak height to the intensity of the O1s peak. The F1s energy of 688 eV raises the expectation that it is present in a F_c compound [147] 160

6.4 Off-Bragg XPS spectrum of the O1s region for TPA:Fe/Cu(100). The spectrum is fitted with two components centred at 531.1 eV (component 1, red) and 531.7 eV (component 2, green) 161

6.5 Argand diagram displaying O1s results. In accordance with Fig. 6.4 the red dots represent the result for component 1 with a mean P_c of 0.11 ± 0.02 and the green dots for component 2 with a mean P_c of 0.95 ± 0.03. Blue and black dots represent the results for the sum and the result without XPS model, respectively. All results are tabulated in Table 6.2. 162

6.6 Exemplary electron yield curves from the O1s XSW fit using the XPS model depicted in Fig. 6.4. The displayed data belongs to XSW data set 019. The x-axis displays the photon energy relativ to the Bragg energy. The results of all O1s data sets are summarized in Table 6.2. 164

6.7 Off-Bragg XPS spectrum of the Fe2p region for TPA:Fe/Cu(100). The spectrum is fitted with two components for the Fe2p$_{3/2}$ (red) and Fe2p$_{1/2}$ peak (green), respectively. The assymetric peak shape is taken into account by the convolution with an exponential tail on the high binding energy side of each peak (see text). 166

6.8 Argand diagram displaying the XSW results for Fe as deduced from the Fe2p signal using the XPS model shown in Fig. 6.7. Due to the intrinsic intensity dependenc of both components, only the sum result is depicted. The corresponding numbers together with the resulting adsorption heights are given in Table 6.3. The huge scattering of the data can be explained by a time dependence (see text) and a clear trend of the P_c against the sample age is observed as shown in Fig. 6.9.168

6.9 P_c results of the Fe2p measurements as given in Table 6.3 and depicted in the argand diagram in Fig. 6.8, plotted against the sample age which is calculated as the time between sample preparation and end of the corresponding measurement. A clear dependence on the sample age is indeed observed. 168

6.10 Exemplary electron yield curves from the Fe2p XSW fit using the XPS model depicted in Fig. 6.7. The displayed data belongs to XSW data set 072 (left column) and 037 (right column). The x-axis displays the photon energy relativ to the Bragg energy. The results of all Fe2p data sets are summarized in Table 6.3. 170

6.11 Off-Bragg XPS spectrum of the C1s region for TPA:Fe/Cu(100). The spectrum is fitted with five components. The main component at 284.6 eV represents the intensity of the aromatic ring (Ring component 1, red) while the component at 288.0 eV (Carboxylic, dark blue) is attributed to the carboxylic side groups. Next to Ring component 1 at 285.4 eV a second component is identified, called Ring component 2 (green). Its origin is not clear (see text), however its XSW behaviour is clearly different as seen in the argand diagram in Fig. 6.12. Two satellites at 287.7 eV (orange) and 292.3 eV (light blue) complete the model. 172

6.12 Argand diagram displaying C1s results from the XSW analysis employing the XPS model shown in Fig. 6.11. The color code follows the XPS model as well and we see the results for Ring component 1 in red, Ring component 2 in green, Carboxylic in dark blue, and the sum in black. Unfortunately a large scattering is observed. All values are given in Table 6.4. 173

6.13 P_c results of the C1s measurements as depicted in the argand diagram in Fig. 6.12 and given in Table 6.4 plotted against the time between sample preparation and end of the corresponding measurement, namely sample age in hours. Only the Carboxylic (blue) shows the same trend as it was observed for Fe before (see Fig. 6.9) while the scattering in P_c for the Ring component 1 does not yield such clear behaviour and Ring component 2 (green) seems to follow an opposite trend. The corresponding lines are only guides to the eye. 174

6.14 Explanatory sketch for the change in the carboxylic carbon adsorption height upen flourine adsorption. The equilibrium adsorption geometry shown on the left is disturbed by the flourine adsorption. The additional ligand on the Fe atom weakens the Fe-O bond as the charge density is rearranged, leading to a stronger Cu-O bond and therefore changing the equilibrium geometry by increasing the bond angle (α) to the carboxylic carbon. As a result the carboxylic carbon is lifted. The Cu surface is represented by the orange line. 175

6.15 Exemplary electron yield curves from the C1s XSW fit using the XPS model depicted in Fig. 6.11. The displayed data belongs to XSW data set 038. The x-axis displays the photon energy relativ to the Bragg energy. The results of all Fe2p data sets are summarized in Table 6.4. 176

6.16 Off-Bragg XPS spectrum of the O1s region for TPA:Fe/Cu(100) after O_2 adsorption. Although one would expect two components to represent the molecular oxygen as it has been modeled for the O1s spectrum before (see Fig. 6.4) in this case it was not possible. Therefore the TPA oxygen at 531.0 eV (red) represents the sum of all molecular oxygen contributions. The new dosed O_2 component at 529.7 eV (green) stems from the adsorbed O_2. 178

6.17 Argand diagram displaying XSW results after O_2 dosage. For the C1s (squares) and Fe2p (black triangles) results the same XPS models as before have been used as shown in Fig. 6.11 and Fig. 6.7. For the oxygen (circles) the new XPS model shown in Fig. 6.16 was employed. While for C1s all components, namels Ring component 1 (red square), Ring component 2 (green square), Carboxylic (blue square) and the sum (black square) stay the same, for O1s the new dosed O_2 species (green circles) appears at a P_c of 0.34 ± 0.01 and hence the O1s sum (black circles) is changed as well. The TPA oxygen (red circles) however, shows no major change. All results are given in Table 6.5. 179

6.18 P_c results of the Fe2p measurements after O_2 adsorption (red dots) plotted against the time between sample preparation and end of the corresponding measurement, namely the sample age in hours. The values for the time dependence of Fe2p without O_2 dosing (grey dots) as depicted in Fig. 6.9 are plotted to ease comparison. So far no difference can be observed between both datasets, but it may be due to the small amount of data available after O_2 adsorption. 180

6.19 Exemplary electron yield curves from the O1s XSW fit using the XPS model depicted in Fig. 6.16. The displayed data belongs to XSW data set 060. The x-axis displays the photon energy relativ to the Bragg energy. The results of all O1s data sets are summarized in Table 6.5. 182

6.20 Adsorption models for the (a) pure TPA/Cu(100)[36], (b) TPA:Fe/Cu(100) in the cloverleaf phase, (c) TPA:Fe/Cu(100) cloverleaf phase after O_2 adsorption, and (d) the TPA:Fe/Cu(100) cloverleaf phase with a high sample age and expected flourine adsorption. The Cu surface plane is indicated by a straight orange line, while the dashed orange line indicates the covalent Cu radius [55]. Fe is depicted in grey, C in black, O in red, and F in purple. All atoms are scaled according to their covalent radii [55]. Numbers in brackets represent the sum values for TPA oxygen, including possible signal from uncoordinated molecules. 183

List of Tables

3.1 Acquisition parameters used for the XSW data sets and off-Bragg XPS spectra. 21

3.2 Coverage estimation results of benzene/Ag(111) compared to the reference of a monolayer of PTCDA/Ag(111)[53]. The values are taken from the XPS spectra shown in Fig. 3.4 and the PTCDA intensity was corrected by the different surface density to serve as a reference. . 26

3.3 Results of the XSW analysis for benzene/Ag(111). The adsorption height is calculated following eq. (2.25) with the Ag(111) lattice distance of $d_{\mathrm{Ag(111)}} = 2.36\,\text{Å}$ and $n = 1$. No preparation dependence can be observed. The results are visualized in the Argand diagram in Fig. 3.6. Errors are calculated following sec. 2.5.2 27

3.4 Acquisition parameters used for the XSW data sets and off-Bragg XPS spectra in the benzene/Cu(111) experiments. 34

3.5 Results of the relative coverage estimation for benzene/Cu(111) based on the intensities of the normalized off-Bragg XPS spectra shown in Fig. 3.10. Preparation 1 is found to yield the highest coverage with twice as much material as preparation 3. The deposition onto preparation 2 which lead to preparation 3 approximately doubled the amount of benzene adsorbed on the surface. 36

3.6 Results of the XSW analysis for benzene/Cu(111). The components show the same P_c and only differ in their F_c but this does not neccessarily indicate indentical adsorption heights. The tilted component represents molecules which are crossing the bragg planes and therefore the calculation of the height from the P_c gets more complicated (see sec. 2.4). Flat and tilted component refers to the components of the fitting model as it is shown in Fig. 3.12 while the sum describes the analysis of their summed up intensities and without XPS model is the outcome of an XSW analysis without components and only background subtraction. The good agreement between sum and region indicates that a meaningful XPS model was used. 42

4.1 Acquisition parameters used for the XSW data sets and off-Bragg XPS spectra for the DP. The Bragg energy for the (111) reflection of Cu is found at $E_\mathrm{photon} \approx 2977\,\mathrm{eV}$ and the lattice spacing is $d_\mathrm{Cu(111)} = 2.09\,\text{Å}$. 51

4.2 Results of the XSW analysis for the C1s data from two preparations of the DP. The XSW analysis is based on the model shown in Fig. 4.4 and distinguishes two carbon components, namely only carbon binding carbons (C-C component) and nitrogen bonding carbons (C-N component). These results are visualized in the Argand diagram in Fig. 4.5. Furthermore the results for the sum of all components (including satellites) and the fit without XPS model are given. The adsorption height d_c is calculated according to eq. (2.25) with $n = 1$ and $d_\mathrm{Cu(111)} = 2.09\,\text{Å}$. 55

4.3 Results of the XSW analysis for N1s from two preparations of the DP. The results are visualized in the Argand diagram in Fig. 4.5 and were extracted by an XSW evaluation using the one component model shown in Fig. 4.3. 56

4.4 Acquisition parameters used for the XSW data sets and off-Bragg XPS spectra for the PLP. The Bragg energy for the (111) reflection of Cu is found at $E_\mathrm{photon} \approx 2977\,\mathrm{eV}$ and the lattice spacing is $d_\mathrm{Cu(111)} = 2.09\,\text{Å}$. 60

4.5 Results of the XSW analysis for the C1s data of the PLP. Unfortunately we have only two data points available, rendering the mean value prone to a large error bar in the F_c. The results are obtained by using the C1s model from Fig. 4.10 for the XSW analysis and are depicted in the Argand diagram in Fig. 4.13. Adsorption heights cannot be calculated, because the signal is a mixture of DP molecules (flat) and COP molecules, which later turns out to be upright standing phenyl nitrene after azobenzene dissociation. Hence, the phenyl ring is crossing the Bragg plane, complicating the interpretation of the data as explained in sec. 2.4. 60

4.6 Results for the N1s data of the PLP from the XSW analysis using the XPS model shown in Fig. 4.9. The two components show clearly different results, pointing out that another species coexists with the already known DP molecules in this phase. The data is visualized in the Argand diagram in Fig. 4.13. 63

4.7 Acquisition parameters used for the XSW data sets and off-Bragg XPS spectra. The first data sets (N1s002, N1s006, C1s007) were acquired with the numbers given in brackets. The Bragg energy for the (111) reflection of Cu is found at $E_{\mathrm{photon}} \approx 2977\,\mathrm{eV}$ and the lattice spacing is $d_{\mathrm{Cu(111)}} = 2.09\,\mathrm{Å}$. 67

4.8 Results of the XSW analysis for the N1s data of the COP. All values from data sets taken on already exposed spots are marked by an asterisk. These data sets are excluded from the calculation of the mean value, as they obviously influenced by beam damage effects. Strongly deviating values are printed in italic. All data is visualized in the Argand diagram in Fig. 4.19. 70

4.9 Results of the XSW analysis for the C1s data of the COP. All values from data sets taken on already exposed spots are marked by an asterisk. These data sets are excluded from the calculation of the mean values, as they obviously influenced by beam damage effects. Strongly deviating values are printed in italic. The results are visualized in the Argand diagram in Fig. 4.19. The adsorption heights are not calculated, because later we will see that the species forming the COP is an upright standing phenyl nitrene where the phenyl ring is crossing the Bragg planes and hence the P_c can not be translated directly into a height value, but a structure simulation is neccessary to match the P_c and F_c. As a result of this simulation the $4.25 \pm 0.04\,\text{Å}$ of the C-C component is evaluated. 71

4.10 Acquisition parameters used for the XSW data sets and off-Bragg XPS spectra in the MLP. For the C1s XSW spectra pass energies of 50 eV (data set C1s018) and 30 eV (data set C1s019) were used. The Bragg energy for the (111) reflection of Cu is found at $E_\mathrm{photon} \approx 2977\,\mathrm{eV}$ and the lattice spacing is $d_{\mathrm{Cu}(111)} = 2.09\,\text{Å}$. 75

4.11 Intensities extracted from the normalized XPS spectra shown in Fig. 4.22. The values reflect the integrated area of all corresponding peaks after subtraction of a Shirley background. However, the numbers are not corrected for damping, and therefore the multilayer value cannot directly compared to the other phases for a coverage evaluation. Within these other phases the error is expected to be smaller as the difference in damping is small. The values of the multilayer given in brackets are the intensities of the monolayer peak in the multilayer spectra. 76

4.12 Results of the XSW analysis for the N1s data of the MLP. Due to the F_c a meaningful P_c and hence adsorption height can only be extracted for the monolayer contribution. The data is visualized in the Argand diagram in Fig. 4.25. 81

4.13 Results of the XSW analysis for the C1s data of the MLP. A meaningful P_c and hence adsorption height can only be extracted for the monolayer contribution. The data is visualized in the Argand diagram in Fig. 4.25. 82

4.14 Comparison of the structural parameters for the DP phase deduced from the experiment presented here and DFT calculations carried out by R. J. Maurer and K. Reuter from the TU München [92] using the DFT + vdW^{surf} method [51, 65]. 86

4.15 Comparison of the structural parameters from the XSW experiment presented here and DFT calculations carried out by R. J. Maurer and K. Reuter from the TU München [92] using the DFT + vdW^{surf} method [51, 65]. Two structures are calculated, first a (6×4) unit cell with two phenyl nitrenes and second, a (4×4) unit cell with three phenyl nitrenes, as it is proposed in sec. 4.6.4 from LEED experiments. The experimental data for $d_{\text{Cu-N}}$ is calculated from the correponding P_c, the value for $d_{\text{Cu-CC}}$ results from the comparison to a structure simulation (see text) and is therefore identical for both phases. 90

4.16 Compilation of azobenzene adsorption data for Cu(111) and Ag(111)[59] from XSW experiments and DFT + vdW^{surf} [51, 65] calculations [92]. To allow the comparison of the adsorption height of the nitrogen $d_{\text{M-N}}$ values, where M is Cu or Ag, the table shows the adsorption height after subtraction of the corresponding substrate vdW radii ($r_{\text{Cu}}^{\text{vdW}} = 1.4$, $r_{\text{Ag}}^{\text{vdW}} = 1.72$ [56]). The angles ω and β are the dihedral angles (CNNC) and (NNCC), respectively. 95

5.1 Acquisition parameters used for the XSW data sets and off-Bragg XPS spectra. The parameters for the O1s XSW data sets are used for both Bragg-reflections measured in the experiment. 105

5.2 C1s model components for the XSW analysis. The model is derived from the off-Bragg XPS spectrum shown in Fig. 5.5. Constrained values are indicated by an asterisk. For detailed information on the model see text. 109

5.3 Results of the XSW analysis for the C1s data using the model shown in Fig. 5.5. C2+C3+C4 represents the the main carbon peak while C1+C1sat is the result for the carboxylic carbons. The Sum is the result for the sum of all components while the Region describes the result if no XPS model is employed. All results are visualized in the Argand diagram in Fig. 5.6. 113

5.4 O1s model components for the XSW analysis. The model is derived from the off-bragg XPS spectrum shown in fig 5.8. Constrained values are indicated by an asterisk. For detailed information on the model see text. 115

5.5 Results of the XSW analysis for the O1s data using the XPS model shown in Fig. 5.8. According to the model the contribution from the carboxylic and the anhydride oxygens could be separated. The sum off all components and the result without XPS fitting model are as well tabulated. All results are visualized in the Argand diagram in Fig. 5.9. 118

5.6 Results of the XSW analysis for the (111) reflection used for the triangulation to derive the adsorption site as described in the text and shown in Fig. 5.12. The XPS model used here is the same as the one for the (200) reflection data shown in Fig. 5.8. The results match the expected P_c values of 0.62 and 0.68 for the carboxylic and anhydride oxygen for an on-top adsorption site very well while one would expect a P_c of 0.12 and 0.18 for the hollow site. 120

5.7 Results of the XSW analysis for the substrate from the Ag3d and the AgMVV Auger lines. No XPS model was applied, only the background was subtracted. 124

5.8 Binding energies (E_B) and full widths at half maximum (FWHM) of the resulting peaks (figure 5.18) from the orbital tomography and fit procedure (see text) for the molecules in the HB monolayer and the minority BW species. Values marked with an asterisk are fixed in the second step of the fitting procedure and taken from an experiment with pure BW PTCDA/Ag(110). 135

5.9 Binding energies of electronic levels for different ordered monolayer phases of PTCDA. These should be compared to the following literature values: BW/Ag(110): HOMO 1.8 eV, LUMO 0.6 eV [106]; HB/Ag(111): HOMO 1.6 eV, LUMO 0.3 eV [106]; Bulk values: HOMO 2.52 eV, LUMO −1.26 eV [137–139]. 142

5.10 Work functions and electrostatic potentials from DFT, calculated by the group of Prof. Peter Puschnig (Karl Franzens Universität Graz). Φ: work function of PTCDA/Ag(hkl); Φ_0: work function of Ag(hkl), determined at the bottom side of the PTCDA/Ag slab; 143

5.11 Binding energy positions of the orbitals in the fitting results (see Fig. 5.26) in eV. Values for BW PTCDA/Ag(110) are taken from ref. [8] 151

6.1 Acquisition parameters used for the XSW data sets and off-Bragg XPS spectra. The number of XPS data sets and the photon energy range for an XSW scan were varied to speed up the measurement process. Fig. 6.10 shows the yield curves for two datasets with different parameters. To cover the large ΔE_{photon} values the photon energy step is chosen larger in the beginning and the end of the yield curve than in its centre. In the Fe2p XSW case two numbers separated by a slash are given for several parameters. The left number corresponds to the data sets 006, 013, 031, 041, 042, and 043, the right number to all other data sets. 159

6.2 O1s results for the TPA+Fe network from the XSW analysis using the XPS model depicted in Fig. 6.4. The results are plotted in the argand diagram in Fig. 6.5. 165

6.3 Fe2p results for the TPA:Fe/Cu(100) network from the XSW analysis using the XPS model shown in Fig. 6.7. The results are visualized in the argand diagram in Fig. 6.8. The lowest height measured during the experiment, which is taken for the structure model in sec. 6.7 is highlighted in bold. 171

6.4 C1s results for the TPA:Fe/Cu(100) network from the XSW analysis using the XPS model shown in Fig. 6.11. All values are visualized in the argand diagram in Fig. 6.12. Due to the large scatter of the results mean values are not calculated. The scattering reminds of the Fe results (see Table 6.3 and Fig. 6.8) but in this case only the carboxylic shows a clear timedependence. 177

6.5 Results of the XSW analysis for the TPA:Fe/Cu(100) network after additional O_2 dosage. While for Fe and C the XPS models of the former sections could be used (see Fig. 6.7 and Fig. 6.11) for oxygen the model shown in Fig. 6.16 was employed. All values are visualized in the argand diagram in Fig. 6.17. 181

6.6 Comparison of experimental findings and DFT calculations [17] for the Fe adsorption height. 184

Bibliography

[1] D. Ferrucci, Introduction to 'This is Watson', *IBM Journal of Research and Development* **56**, 1:1 (2012).

[2] S. Kim, H.-J. Kwon, S. Lee, H. Shim, Y. Chun, W. Choi, J. Kwack, D. Han, M. Song, S. Kim, S. Mohammadi, I. Kee and S. Y. Lee, Low-Power Flexible Organic Light-Emitting Diode Display Device, *Advanced Materials* **23**, 3511 (2011).

[3] G. Witte and C. Wöll, Growth of aromatic molecules on solid substrates for applications in organic electronics, *Journal of Materials Research* **19**, 1889 (2004).

[4] D. P. Woodruff, Surface structure determination using x-ray standing waves, *Reports on Progress in Physics* **68**, 743 (2005).

[5] B. W. Batterman and H. Cole, Dynamical Diffraction of X Rays by Perfect Crystals, *Rev. Mod. Phys.* **36**, 681 (1964).

[6] F. Tautz, Structure and bonding of large aromatic molecules on noble metal surfaces: The example of PTCDA, *Progress in Surface Science* **82**, 479 (2007).

[7] P. Puschnig, S. Berkebile, A. J. Fleming, G. Koller, K. Emtsev, T. Seyller, J. D. Riley, C. Ambrosch-Draxl, F. P. Netzer and M. G. Ramsey, Reconstruction of Molecular Orbital Densities from Photoemission Data, *Science* **326**, 702 (2009).

[8] P. Puschnig, E.-M. Reinisch, T. Ules, G. Koller, S. Soubatch, M. Ostler, L. Romaner, F. S. Tautz, C. Ambrosch-Draxl and M. G. Ramsey, Orbital tomography: Deconvoluting photoemission spectra of organic molecules, *Phys. Rev. B* **84**, 235427 (2011).

[9] B. Stadtmüller, M. Willenbockel, E. M. Reinisch, T. Ules, F. C. Bocquet, S. Soubatch, P. Puschnig, G. Koller, M. G. Ramsey, F. S. Tautz and C. Kumpf, Orbital tomography for highly symmetric adsorbate systems, *EPL (Europhysics Letters)* **100**, 26008 (2012).

[10] B. K. Pathem, S. A. Claridge, Y. B. Zheng and P. S. Weiss, Molecular Switches and Motors on Surfaces, *Annual Review of Physical Chemistry* **64**, 605 (2013).

[11] P. Tegeder, Optically and thermally induced molecular switching processes at metal surfaces, *Journal of Physics: Condensed Matter* **24**, 394001 (2012).

[12] S.-C. Li and U. Diebold, Reactivity of TiO2 Rutile and Anatase Surfaces toward Nitroaromatics, *Journal of the American Chemical Society* **132**, 64 (2010).

[13] V. Balzani, A. Credi and M. Venturi, The Bottom-Up Approach to Molecular-Level Devices and Machines, *Chemistry - A European Journal* **8**, 5524 (2002).

[14] F. Klappenberger, Two-dimensional functional molecular nanoarchitectures - Complementary investigations with scanning tunneling microscopy and X-ray spectroscopy, *Progress in Surface Science* **89**, 1 (2014).

[15] M. A. Lingenfelder, H. Spillmann, A. Dmitriev, S. Stepanow, N. Lin, J. V. Barth and K. Kern, Towards Surface-Supported Supramolecular Architectures: Tailored Coordination Assembly of 1,4-Benzenedicarboxylate and Fe on Cu(100), *Chemistry - A European Journal* **10**, 1913 (2004).

[16] S. L. Tait, Y. Wang, G. Costantini, N. Lin, A. Baraldi, F. Esch, L. Petaccia, S. Lizzit and K. Kern, Metal-Organic Coordination Interactions in Fe-Terephthalic Acid Networks on Cu(100), *Journal of the American Chemical Society* **130**, 2108 (2008).

[17] P. Gambardella, S. Stepanow, A. Dmitriev, J. Honolka, F. M. F. de Groot, M. Lingenfelder, S. S. Gupta, D. D. Sarma, P. Bencok, S. Stanescu, S. Clair, S. Pons, N. Lin, A. P. Seitsonen, H. Brune, J. V. Barth and K. Kern,

Supramolecular control of the magnetic anisotropy in two-dimensional high-spin Fe arrays at a metal interface, *Nat Mater* **8**, 189 (2009).

[18] A. Einstein, Über einen die Erzeugung und Verwandlung des Lichtes betreffenden heuristischen Gesichtspunkt, *Annalen der Physik* **322**, 132 (1905).

[19] H. Hertz, Ueber einen Einfluss des ultravioletten Lichtes auf die electrische Entladung, *Annalen der Physik* **267**, 983 (1887).

[20] W. Hallwachs, Ueber den Einfluss des Lichtes auf electrostatisch geladene Körper, *Annalen der Physik* **269**, 301 (1888).

[21] M. P. Seah and W. A. Dench, Quantitative electron spectroscopy of surfaces: A standard data base for electron inelastic mean free paths in solids, *Surface and Interface Analysis* **1**, 2 (1979).

[22] C. Fadley, X-ray photoelectron spectroscopy: Progress and perspectives, *Journal of Electron Spectroscopy and Related Phenomena* **178-179**, 2 (2010).

[23] S. Hüfner, *Photoelectron Spectroscopy, Principles and Applications*, Third Edition, Springer (2003).

[24] P. J. Feibelman and D. E. Eastman, Photoemission spectroscopy — Correspondence between quantum theory and experimental phenomenology, *Phys. Rev. B* **10**, 4932 (1974).

[25] J. Ziroff, F. Forster, A. Schöll, P. Puschnig and F. Reinert, Hybridization of Organic Molecular Orbitals with Substrate States at Interfaces: PTCDA on Silver, *Phys. Rev. Lett.* **104**, 233004 (2010).

[26] M. Wießner, D. Hauschild, A. Schöll, F. Reinert, V. Feyer, K. Winkler and B. Krömker, Electronic and geometric structure of the PTCDA/Ag(110) interface probed by angle-resolved photoemission, *Phys. Rev. B* **86**, 045417 (2012).

[27] M Willenbockel, B Stadtmüller, K Schönauer, F. C. Bocquet, D Lüftner, E. M. Reinisch, T Ules, G Koller, C Kumpf, S Soubatch, P Puschnig, M. G. Ramsey and F. S. Tautz, Energy offsets within a molecular monolayer: the

influence of the molecular environment, *New Journal of Physics* **15**, 033017 (2013).

[28] D. Lüftner, T. Ules, E. M. Reinisch, G. Koller, S. Soubatch, F. S. Tautz, M. G. Ramsey and P. Puschnig, Imaging the wave functions of adsorbed molecules, *Proceedings of the National Academy of Sciences* **111**, 605 (2014).

[29] J. Zegenhagen, Surface structure determination with X-ray standing waves, *Surface Science Reports* **18**, 202 (1993).

[30] G. Mercurio, R. J. Maurer, S. Hagen, F. Leyssner, J. Meyer, P. Tegeder, S. Soubatch, K. Reuter and F. S. Tautz, X-ray standing wave simulations based on Fourier vector analysis as a method to retrieve complex molecular adsorption geometries, *Frontiers in Physics* **2**, 13 (2014).

[31] I. A. Vartanyants and J. Zegenhagen, Photoelectric scattering from an X-ray interference field, *Solid State Communications* **113**, 299 (1999).

[32] J. Lee, C. Fisher, D. Woodruff, M. Roper, R. Jones and B. Cowie, Non-dipole effects in photoelectron-monitored X-ray standing wave experiments: characterisation and calibration, *Surface Science* **494**, 166 (2001).

[33] C. Wiemann, M. Patt, I. P. Krug, N. B. Weber, M. Escher, M. Merkel and C. M. Schneider, A New Nanospectroscopy Tool with Synchrotron Radiation: NanoESCA@Elettra, *e-Journal of Surface Science and Nanotechnology* **9**, 395 (2011).

[34] L. Broekman, A. Tadich, E. Huwald, J. Riley, R. Leckey, T. Seyller, K. Emtsev and L. Ley, First results from a second generation toroidal electron spectrometer, *Journal of Electron Spectroscopy and Related Phenomena* **144-147**, 1001 (2005).

[35] N. Fairley, *CasaXPS*.

[36] G. Mercurio, Study of Molecule-Metal Interfaces by Means of the Normal Incidence X-ray Standing Wave Technique, PhD thesis, Schriften des Forschungszentrums Jülich, Reihe Schlüsseltechnologien Vol. 49 (Dissertation,

RWTH Aachen University, 2012), available at http://www.fz-juelich.de/zb/juwel., (2012).

[37] G. Mercurio, S. Soubatch and F. S. Tautz, *in preparation.*

[38] Torricelli is an XSW data analysis and simulation program written by G. Mercurio; copies can be obtained from s.tautz@fz-juelich.de.

[39] G. Mercurio, O. Bauer, M. Willenbockel, N. Fairley, W. Reckien, C. H. Schmitz, B. Fiedler, S. Soubatch, T. Bredow, M. Sokolowski and F. S. Tautz, Adsorption height determination of nonequivalent C and O species of PTCDA on Ag(110) using x-ray standing waves, *Phys. Rev. B* **87**, 045421 (2013).

[40] G. Heimel, S. Duhm, I. Salzmann, A. Gerlach, A. Strozecka, J. Niederhausen, C. Bürker, T. Hosokai, I. Fernandez-Torrente, G. Schulze, S. Winkler, A. Wilke, R. Schlesinger, J. Frisch, B. Bröker, A. Vollmer, B. Detlefs, J. Pflaum, S. Kera, K. J. Franke, N. Ueno, J. I. Pascual, F. Schreiber and N. Koch, Charged and metallic molecular monolayers through surface-induced aromatic stabilization, *Nat Chem* **5**, 187 (2013).

[41] H.-P. Steinrück, W. Huber, T. Pache and D. Menzel, The adsorption of benzene mono- and multilayers on Ni(111) studied by TPD and LEED, *Surface Science* **218**, 293 (1989).

[42] K. H. Frank, P. Yannoulis, R. Dudde and E. E. Koch, Unoccupied molecular orbitals of aromatic hydrocarbons adsorbed on Ag(111), *The Journal of Chemical Physics* **89**, 7569 (1988).

[43] P. Avouris and J. E. Demuth, Electronic excitations of benzene, pyridine, and pyrazine adsorbed on Ag(111), *The Journal of Chemical Physics* **75**, 4783 (1981).

[44] X.-L Zhou, M. Castro and J. White, Interactions of UV photons and low energy electrons with chemisorbed benzene on Ag(111), *Surface Science* **238**, 215 (1990).

[45] T. J. Rockey, M. Yang and H.-L. Dai, Adsorption Energies, Inter-adsorbate Interactions, and the Two Binding Sites within Monolayer Benzene on Ag(111), *The Journal of Physical Chemistry B* **110**, 19973 (2006).

[46] P. Yannoulis, R. Dudde, K. Frank and E. Koch, Orientation of aromatic hydrocarbons on metal surfaces as determined by nexafs, *Surface Science* **189-190**, 519 (1987).

[47] R. Dudde, K. H. Frank and E. E. Koch, The electronic structure of benzene adsorbed on Ag(111) studied by angle resolved photoemission, *Surface Science* **225**, 267 (1990).

[48] V. M. Hallmark and A. Campion, Selection rules for surface Raman spectroscopy: Experimental results, *The Journal of Chemical Physics* **84**, 2933 (1986).

[49] K. Gaffney, C. Wong, S. Liu, A. Miller, J. McNeill and C. Harris, Femtosecond electron dynamics at the benzene/Ag(111) interface, *Chemical Physics* **251**, 99 (2000).

[50] L. Firment and G. Somorjai, Low energy electron diffraction studies of the surfaces of molecular crystals (ice, ammonia, naphthalene, benzene), *Surface Science* **84**, 275 (1979).

[51] V. G. Ruiz, W. Liu, E. Zojer, M. Scheffler and A. Tkatchenko, Density-Functional Theory with Screened van der Waals Interactions for the Modeling of Hybrid Inorganic-Organic Systems, *Phys. Rev. Lett.* **108**, 146103 (2012).

[52] T. S. Chwee and M. B. Sullivan, Adsorption studies of C_6H_6 on Cu (111), Ag (111), and Au (111) within dispersion corrected density functional theory, *The Journal of Chemical Physics* **137**, 134703, 134703 (2012).

[53] B. Stadtmüller, *private communication.*

[54] K Glöckler, C Seidel, A Soukopp, M Sokolowski, E Umbach, M Böhringer, R Berndt and W.-D Schneider, Highly ordered structures and submolecular scanning tunnelling microscopy contrast of PTCDA and DM-PBDCI monolayers on Ag(111) and Ag(110), *Surface Science* **405**, 1 (1998).

[55] B. Cordero, V. Gomez, A. E. Platero-Prats, M. Reves, J. Echeverria, E. Cremades, F. Barragan and S. Alvarez, Covalent radii revisited, *Dalton Trans.* 2832 (2008).

[56] A. Bondi, van der Waals Volumes and Radii, *The Journal of Physical Chemistry* **68**, 441 (1964).

[57] C. Wagner, N. Fournier, V. G. Ruiz, C Li, K Müllen, M. Rohlfing, A. Tkatchenko, R. Temirov and F. S. Tautz, *in preparation.*

[58] S. Duhm, C. Bürker, J. Niederhausen, I. Salzmann, T. Hosokai, J. Duvernay, S. Kera, F. Schreiber, N. Koch, N. Ueno and A. Gerlach, Pentacene on Ag(111): Correlation of Bonding Distance with Intermolecular Interaction and Order, *ACS Applied Materials & Interfaces* **5**, 9377 (2013).

[59] G. Mercurio, R. J. Maurer, W. Liu, S. Hagen, F. Leyssner, P. Tegeder, J. Meyer, A. Tkatchenko, S. Soubatch, K. Reuter and F. S. Tautz, Quantification of finite-temperature effects on adsorption geometries of π-conjugated molecules: Azobenzene/Ag(111), *Phys. Rev. B* **88**, 035421 (2013).

[60] A. Hauschild, R. Temirov, S. Soubatch, O. Bauer, A. Schöll, B. C. C. Cowie, T.-L. Lee, F. S. Tautz and M. Sokolowski, Normal-incidence x-ray standing-wave determination of the adsorption geometry of PTCDA on Ag(111): Comparison of the ordered room-temperature and disordered low-temperature phases, *Phys. Rev. B* **81**, 125432 (2010).

[61] S. K. M. Henze, O. Bauer, T.-L. Lee, M. Sokolowski and F. S. Tautz, Vertical bonding distances of PTCDA on Au(111) and Ag(111): Relation to the bonding type, *Surface Science* **601**, 1566 (2007).

[62] L. Kilian, A. Hauschild, R. Temirov, S. Soubatch, A. Schöll, A. Bendounan, F. Reinert, T.-L. Lee, F. S. Tautz, M. Sokolowski and E. Umbach, Role of Intermolecular Interactions on the Electronic and Geometric Structure of a Large π-Conjugated Molecule Adsorbed on a Metal Surface, *Phys. Rev. Lett.* **100**, 136103 (2008).

[63] I. Kröger, B. Stadtmüller, C. Stadler, J. Ziroff, M. Kochler, A. Stahl, F. Pollinger, T.-L. Lee, J. Zegenhagen, F. Reinert and C. Kumpf, Submonolayer growth of copper-phthalocyanine on Ag(111), *New Journal of Physics* **12**, 083038 (2010).

[64] B. Stadtmüller, D. Lüftner, M. Willenbockel, E. M. Reinisch, T. Sueyoshi, G. Koller, S. Soubatch, M. G. Ramsey, P. Puschnig, F. S. Tautz and C. Kumpf, Unexpected interplay of bonding height and energy level alignment at heteromolecular hybrid interfaces, *Nat Commun* **5**, 3685 (2014).

[65] A. Tkatchenko and M. Scheffler, Accurate Molecular Van Der Waals Interactions from Ground-State Electron Density and Free-Atom Reference Data, *Phys. Rev. Lett.* **102**, 073005 (2009).

[66] A. D. Becke and E. R. Johnson, A density-functional model of the dispersion interaction, *The Journal of Chemical Physics* **123**, 154101 (2005).

[67] S. J. Stranick, M. M. Kamna and P. S. Weiss, Atomic-Scale Dynamics of a Two-Dimensional Gas-Solid Interface, *Science* **266**, 99 (1994).

[68] S. J. Stranick, M. M. Kamna and P. S. Weiss, Interactions and dynamics of benzene on Cu111 at low temperature, *Surface Science* **338**, 41 (1995).

[69] P. S. Weiss, M. M. Kamna, T. M. Graham and S. J. Stranick, Imaging Benzene Molecules and Phenyl Radicals on Cu111, *Langmuir* **14**, 1284 (1998).

[70] S. Lukas, S. Vollmer, G. Witte and C. Wöll, Adsorption of acenes on flat and vicinal Cu(111) surfaces: Step induced formation of lateral order, *Journal of Chemical Physics* **114**, 10123 (2001).

[71] M. Xi, M. X. Yang, S. K. Jo, B. E. Bent and P. Stevens, Benzene adsorption on Cu(111): Formation of a stable bilayer, *Journal of Chemical Physics* **101**, 9122 (1994).

[72] D. Velic, A. Hotzel, M. Wolf and G. Ertl, Electronic states of the C_6H_6/Cu111 system: Energetics, femtosecond dynamics, and adsorption morphology, *Journal of Chemical Physics* **109**, 9155 (1998).

[73] D. B. Dougherty, P. Maksymovych, J. Lee and J. T. Yates, Local Spectroscopy of Image-Potential-Derived States: From Single Molecules to Monolayers of Benzene on Cu(111), *Phys. Rev. Lett.* **97**, 236806 (2006).

[74] K. H. Frank, R. Dudde and E. E. Koch, Electron affinity levels of benzene and azabenzenes on Cu(111) and Au(110) revealed by inverse photoemission, *Chemical Physics Letters* **132**, 83 (1986).

[75] T. Munakata, T. Sakashita, M. Tsukakoshi and J. Nakamura, Fine structure of the two-photon photoemission from benzene adsorbed on Cu(111), *Chemical Physics Letters* **271**, 377 (1997).

[76] T. Yamada, M. Shibuta, Y. Ami, Y. Takano, A. Nonaka, K. Miyakubo and T. Munakata, Novel Growth of Naphthalene Overlayer on Cu(111) Studied by STM, LEED, and 2PPE, *The Journal of Physical Chemistry C* **114**, 13334 (2010).

[77] Z. R. Robinson, P. Tyagi, T. R. Mowll, C. A. Ventrice and J. B. Hannon, Argon-assisted growth of epitaxial graphene on Cu(111), *Phys. Rev. B* **86**, 235413 (2012).

[78] P. Bayersdorfer, SPA-LEED-Studie zur Adsorption von metallfreien Phthalocyaninen auf Ag(111) Bereich kleiner Bedeckungen, MA thesis, Universität Würzburg, (2008).

[79] E. Mitscherlich, Ueber die Zusammensetzung des Nitrobenzids und Sulfobenzids, *Annalen der Physik* **107**, 625 (1834).

[80] C. Bronner, B. Priewisch, K. Rück-Braun and P. Tegeder, Photoisomerization of an Azobenzene on the Bi(111) Surface, *The Journal of Physical Chemistry C* **117**, 27031 (2013).

[81] M. Wolf and P. Tegeder, Reversible molecular switching at a metal surface: A case study of tetra-tert-butyl-azobenzene on Au(111), *Surface Science* **603**, 1506 (2009).

[82] M. J. Comstock, N. Levy, A. Kirakosian, J. Cho, F. Lauterwasser, J. H. Harvey, D. A. Strubbe, J. M. J. Fréchet, D. Trauner, S. G. Louie and M. F. Crommie, Reversible Photomechanical Switching of Individual Engineered Molecules at a Metallic Surface, *Phys. Rev. Lett.* **99**, 038301 (2007).

[83] B.-Y. Choi, S.-J. Kahng, S. Kim, H. Kim, H. W. Kim, Y. J. Song, J. Ihm and Y. Kuk, Conformational Molecular Switch of the Azobenzene Molecule: A Scanning Tunneling Microscopy Study, *Phys. Rev. Lett.* **96**, 156106 (2006).

[84] M. Alemani, M. V. Peters, S. Hecht, K.-H. Rieder, F. Moresco and L. Grill, Electric Field-Induced Isomerization of Azobenzene by STM, *Journal of the American Chemical Society* **128**, 14446 (2006).

[85] M. Alemani, S. Selvanathan, F. Ample, M. V. Peters, K.-H. Rieder, F. Moresco, C. Joachim, S. Hecht and L. Grill, Adsorption and Switching Properties of Azobenzene Derivatives on Different Noble Metal Surfaces: Au(111), Cu(111), and Au(100), *The Journal of Physical Chemistry C* **112**, 10509 (2008).

[86] S.-C. Li, Y. Losovyj, V. K. Paliwal and U. Diebold, Photoemission Study of Azobenzene and Aniline Adsorbed on TiO2 Anatase (101) and Rutile (110) Surfaces, *The Journal of Physical Chemistry C* **115**, 10173 (2011).

[87] S. C. B. Mannsfeld, K. Leo and T. Fritz, Line-on-Line Coincidence: A New Type of Epitaxy Found in Organic-Organic Heterolayers, *Phys. Rev. Lett.* **94**, 056104 (2005).

[88] M. A. Van Hove, W. H. Weinberg and C.-M. Chan, *Low-Energy Electron-Diffraction, Experiment, Theory and Surface Structure Determination*, ed. by G. Ertl and R. Gomer, Springer Verlag (1986).

[89] B. J. Lindberg and J. Hedman, Molecular Spectroscopy by Means of ESCA, *Chemica Scripta* **7**, 155 (1975).

[90] C. J. Brown, A refinement of the crystal structure of azobenzene, *Acta Crystallographica* **21**, 146 (1966).

[91] Z. V. Zheleva, T. Eralp and G. Held, Complete Experimental Structure Determination of the p(3x2)pg Phase of Glycine on Cu110, *The Journal of Physical Chemistry C* **116**, 618 (2012).

[92] R. J. Maurer and K. Reuter, *private communication.*

[93] J. M. Robertson, 47. Crystal structure and configuration of the isomeric azobenzenes, *J. Chem. Soc.* 232 (1939).

[94] S. A. Lindgren, L. Walldén, J. Rundgren and P. Westrin, Low-energy electron diffraction from Cu(111): Subthreshold effect and energy-dependent inner potential; surface relaxation and metric distances between spectra, *Phys. Rev. B* **29**, 576 (1984).

[95] A. Soon, L. Wong, M. Lee, M. Todorova, B. Delley and C. Stampfl, Nitrogen adsorption and thin surface nitrides on Cu(111) from first-principles, *Surface Science* **601**, 4775 (2007).

[96] C. Stadler, S. Hansen, I. Kröger, C. Kumpf and E. Umbach, Tuning intermolecular interaction in long-range-ordered submonolayer organic films, *Nat Phys* **5**, 153 (2009).

[97] J. Iwicki, E. Ludwig, M. Kallane, J. Buck, F. Kohler, R. Herges, L. Kipp and K. Rossnagel, Photoswitching of azobenzene multilayers on a layered semiconductor, *Applied Physics Letters* **97**, 063112, 063112 (2010).

[98] C. Bronner and P. Tegeder, Photo-induced and thermal reactions in thin films of an azobenzene derivative on Bi(111), *New Journal of Physics* **16**, 053004 (2014).

[99] O. Bauer, G. Mercurio, M. Willenbockel, W. Reckien, C. Heinrich Schmitz, B. Fiedler, S. Soubatch, T. Bredow, F. S. Tautz and M. Sokolowski, Role of functional groups in surface bonding of planar π-conjugated molecules, *Phys. Rev. B* **86**, 235431 (2012).

[100] L. Kilian, E. Umbach and M. Sokolowski, Molecular beam epitaxy of organic films investigated by high resolution low energy electron diffraction (SPA-

LEED): 3,4,9,10-perylenetetracarboxylicacid-dianhydride (PTCDA) on Ag(111), *Surface Science* **573**, 359 (2004).

[101] A. Kraft, R. Temirov, S. K. M. Henze, S. Soubatch, M. Rohlfing and F. S. Tautz, Lateral adsorption geometry and site-specific electronic structure of a large organic chemisorbate on a metal surface, *Phys. Rev. B* **74**, 041402 (2006).

[102] J. Ikonomov, O. Bauer and M. Sokolowski, Highly ordered thin films of perylene-3,4,9,10-tetracarboxylic acid dianhydride (PTCDA) on Ag(100), *Surface Science* **602**, 2061 (2008).

[103] C. Seidel, C. Awater, X. D. Liu, R. Ellerbrake and H. Fuchs, A combined STM, LEED and molecular modelling study of PTCDA grown on Ag(110), *Surface Science* **371**, 123 (1997).

[104] M. Böhringer, W.-D. Schneider, K. Glöckler, E. Umbach and R. Berndt, Adsorption site determination of PTCDA on Ag(110) by manipulation of adatoms, *Surface Science* **419**, L95 (1998).

[105] D. Braun, A. Schirmeisen and H. Fuchs, Molecular growth and sub-molecular resolution of a thin multilayer of PTCDA on Ag(110) observed by scanning tunneling microscopy, *Surface Science* **575**, 3 (2005).

[106] Y. Zou, L. Kilian, A. Schöll, T. Schmidt, R. Fink and E. Umbach, Chemical bonding of PTCDA on Ag surfaces and the formation of interface states, *Surface Science* **600**, 1240 (2006).

[107] M. Wießner, J. Ziroff, F. Forster, M. Arita, K. Shimada, P. Puschnig, A. Schöll and F. Reinert, Substrate-mediated band-dispersion of adsorbate molecular states, *Nat Commun* **4**, 1514 (2013).

[108] M. Wießner, D. Hauschild, C. Sauer, V. Feyer, A. Schöll and F. Reinert, Complete determination of molecular orbitals by measurement of phase symmetry and electron density, *Nat Commun* **5**, 4156 (2014).

[109] C. Seidel, J. Poppensieker and H. Fuchs, Real-time monitoring of phase transitions of vacuum deposited organic films by molecular beam deposition LEED, *Surface Science* **408**, 223 (1998).

[110] A. Gerlach, S. Sellner, F. Schreiber, N. Koch and J. Zegenhagen, Substrate-dependent bonding distances of PTCDA: A comparative x-ray standing-wave study on Cu(111) and Ag(111), *Phys. Rev. B* **75**, 045401 (2007).

[111] A. Schöll, Y. Zou, M. Jung, T. Schmidt, R. Fink and E. Umbach, Line shapes and satellites in high-resolution x-ray photoelectron spectra of large pi-conjugated organic molecules, *The Journal of Chemical Physics* **121**, 10260 (2004).

[112] D. R. T. Zahn, G. N. Gavrila and G. Salvan, Electronic and Vibrational Spectroscopies Applied to Organic/Inorganic Interfaces, *Chemical Reviews* **107**, 1161 (2007).

[113] L. Cheng, P. Fenter, M. J. Bedzyk and N. C. Sturchio, Fourier-Expansion Solution of Atom Distributions in a Crystal Using X-Ray Standing Waves, *Phys. Rev. Lett.* **90**, 255503 (2003).

[114] J. A. van Bokhoven, T.-L. Lee, M. Drakopoulos, C. Lamberti, S. Thiesz and J. Zegenhagen, Determining the aluminium occupancy on the active T-sites in zeolites using X-ray standing waves, *Nat Mater* **7**, 551 (2008).

[115] J. Ikonomov, P. Bach, R. Merkel and M. Sokolowski, Surface diffusion constants of large organic molecules determined from their residence times under a scanning tunneling microscope tip, *Phys. Rev. B* **81**, 161412 (2010).

[116] B. Stadtmüller, S. Schröder, F. m. c. C. Bocquet, C. Henneke, C. Kleimann, S. Soubatch, M. Willenbockel, B. Detlefs, J. Zegenhagen, T.-L. Lee, F. S. Tautz and C. Kumpf, Adsorption height alignment at heteromolecular hybrid interfaces, *Phys. Rev. B* **89**, 161407 (2014).

[117] G. Mercurio, O. Bauer, M. Willenbockel, B. Fiedler, T. Sueyoshi, C. Weiss, R. Temirov, S. Soubatch, M. Sokolowski and F. S. Tautz, Tuning and probing

interfacial bonding channels for a functionalized organic molecule by surface modification, *Phys. Rev. B* **87**, 121409 (2013).

[118] G. V. Hansson and S. A. Flodström, Photoemission study of the bulk and surface electronic structure of single crystals of gold, *Phys. Rev. B* **18**, 1572 (1978).

[119] H. C. Potter and J. M. Blakely, LEED, Auger spectroscopy, and contact potential studies of copper - gold alloy single crystal surfaces, *Journal of Vacuum Science and Technology* **12**, 635 (1975).

[120] P. O. Gartland and B. J. Slagsvold, Transitions conserving parallel momentum in photoemission from the (111) face of copper, *Phys. Rev. B* **12**, 4047 (1975).

[121] K. Giesen, F. Hage, F. J. Himpsel, H. J. Riess and W. Steinmann, Hydrogenic image-potential states: A critical examination, *Phys. Rev. B* **33**, 5241 (1986).

[122] S. Duhm, A. Gerlach, I. Salzmann, B. Bröker, R. Johnson, F. Schreiber and N. Koch, PTCDA on Au(111), Ag(111) and Cu(111): Correlation of interface charge transfer to bonding distance, *Organic Electronics* **9**, 111 (2008).

[123] A. W. Dweydari and C. H. B. Mee, Oxygen adsorption on the (111) face of silver, *physica status solidi (a)* **17**, 247 (1973).

[124] M Chelvayohan and C. H. B. Mee, Work function measurements on (110), (100) and (111) surfaces of silver, *Journal of Physics C: Solid State Physics* **15**, 2305 (1982).

[125] K. Giesen, F. Hage, F. J. Himpsel, H. J. Riess, W. Steinmann and N. V. Smith, Effective mass of image-potential states, *Phys. Rev. B* **35**, 975 (1987).

[126] W. Hansen, M. Bertolo and K. Jacobi, Physisorption of CO on Ag(111): investigation of the monolayer and the multilayer through HREELS, ARUPS, and TDS, *Surface Science* **253**, 1 (1991).

[127] A. W. Dweydari and C. H. B. Mee, Work function measurements on (100) and (110) surfaces of silver, *physica status solidi (a)* **27**, 223 (1975).

[128] B. Reihl and J. Nicholls, Image-potential surface states on Ag(100): A reinvestigation, English, *Zeitschrift für Physik B Condensed Matter* **67**, 221 (1987).

[129] M Canepa, P Cantini, L Mattera, S Terreni and F Valdenazzi, Electronic States of the Ag(110)-O(n×1) Phases Studied by Photoemission and Metastable Deexcitation Spectroscopies, *Physica Scripta* **1992**, 226 (1992).

[130] J. Kröger, H. Jensen, R. Berndt, R. Rurali and N. Lorente, Molecular orbital shift of perylenetetracarboxylic-dianhydride on gold, *Chemical Physics Letters* **438**, 249 (2007).

[131] K. J. Franke, G. Schulze, N. Henningsen, I. Fernández-Torrente, J. I. Pascual, S. Zarwell, K. Rück-Braun, M. Cobian and N. Lorente, Reducing the Molecule-Substrate Coupling in C_{60}-Based Nanostructures by Molecular Interactions, *Phys. Rev. Lett.* **100**, 036807 (2008).

[132] S. Soubatch, C. Weiss, R. Temirov and F. S. Tautz, Site-Specific Polarization Screening in Organic Thin Films, *Phys. Rev. Lett.* **102**, 177405 (2009).

[133] G. Schull and R. Berndt, Orientationally Ordered (7×7) Superstructure of C_{60} on Au(111), *Phys. Rev. Lett.* **99**, 226105 (2007).

[134] K. J. F. I. Fernandez-Torrente and J. I. Pascual, Spectroscopy of C60 single molecules: the role of screening on energy level alignment, *J. Phys.: Condens. Matter.* **20**, 184001 (2008).

[135] M. Rohlfing, R. Temirov and F. S. Tautz, Adsorption structure and scanning tunneling data of a prototype organic-inorganic interface: PTCDA on Ag(111), *Phys. Rev. B* **76**, 115421 (2007).

[136] J. M. Garcia-Lastra, C. Rostgaard, A. Rubio and K. S. Thygesen, Polarization-induced renormalization of molecular levels at metallic and semiconducting surfaces, *Phys. Rev. B* **80**, 245427 (2009).

[137] R. Schlaf, B. A. Parkinson, P. A. Lee, K. W. Nebesny and N. R. Armstrong, HOMO/LUMO Alignment at PTCDA/ZnPc and PTCDA/ClInPc Heterointerfaces Determined by Combined UPS and XPS Measurements, *The Journal of Physical Chemistry B* **103**, 2984 (1999).

[138] T. Kampen, Electronic structure of organic interfaces - a case study on perylene derivatives, English, *Applied Physics A* **82**, 457 (2006).

[139] S Krause, M. B. Casu, A Schöll and E Umbach, Determination of transport levels of organic semiconductors by UPS and IPS, *New Journal of Physics* **10**, 085001 (2008).

[140] L Romaner, D Nabok, P Puschnig, E Zojer and C Ambrosch-Draxl, Theoretical study of PTCDA adsorbed on the coinage metal surfaces, Ag(111), Au(111) and Cu(111), *New Journal of Physics* **11**, 053010 (2009).

[141] I. G. Hill, A. Rajagopal, A. Kahn and Y. Hu, Molecular level alignment at organic semiconductor-metal interfaces, *Applied Physics Letters* **73**, 662 (1998).

[142] I. Hill, A. Kahn, Z. Soos, R. Pascal and Jr, Charge-separation energy in films of π-conjugated organic molecules, *Chemical Physics Letters* **327**, 181 (2000).

[143] K. Momma and F. Izumi, *VESTA3* for three-dimensional visualization of crystal, volumetric and morphology data, *Journal of Applied Crystallography* **44**, 1272 (2011).

[144] N. Dori, M. Menon, L. Kilian, M. Sokolowski, L. Kronik and E. Umbach, Valence electronic structure of gas-phase 3,4,9,10-perylene tetracarboxylic acid dianhydride: Experiment and theory, *Phys. Rev. B* **73**, 195208 (2006).

[145] T. Sham, A. Bzowski, M. Kuhn and C. Tyson, Observations on the d-band width of Au-Ag and Au-Cu alloys, *Solid State Communications* **80**, 29 (1991).

[146] S. Stepanow, T. Strunskus, M. Lingenfelder, A. Dmitriev, H. Spillmann, N. Lin, J. V. Barth, C. Wöll and K. Kern, Deprotonation-Driven Phase Transformations in Terephthalic Acid Self-Assembly on Cu(100), *The Journal of Physical Chemistry B* **108**, 19392 (2004).

[147] G. Beamson and D. Briggs, *High Resolution XPS of Organic Polymers: The Scienta ESCA300 Database*, 1st, Wiley (1992).

[148] J. C. Fuggle and N. Mårtensson, Core-level binding energies in metals, *Journal of Electron Spectroscopy and Related Phenomena* **21**, 275 (1980).

[149] D. Briggs and J. T. Grant, eds., *Surface Analysis by Auger and X-ray Photoelectron Spectroscopy*, IMPublications (2003).

[150] S Doniach and M Sunjic, Many-electron singularity in X-ray photoemission and X-ray line spectra from metals, *Journal of Physics C: Solid State Physics* **3**, 285 (1970).

Publications

1. B. Stadtmüller, S. Schröder, F. C. Bocquet, C. Hennecke, C. Kleimann, S. Soubatch, M. Willenbockel, B. Detlefs, J. Zegenhagen, T.-L. Lee, F. S. Tautz and C. Kumpf, *Adsorption height alignment at heteromolecular hybrid interfaces*, *Phys. Rev.* B **89**, 161407(R) (2014).
2. B. Stadtmüller, D. Lüftner, M. Willenbockel, E. M. Reinisch, T. Sueyoshi, G. Koller, S. Soubatch, M. G. Ramsey, P. Puschnig, F. S. Tautz and C. Kumpf, *More than the sum of its parts: Bonding, adsorption height and orbital energy alignment at heteromolecular hybrid interfaces*, *Nature Commun.* **5**, 3685 (2014).
3. T. Sueyoshi, M. Willenbockel, M. Naboka, A. Nefedov, S. Soubatch, C. Wöll and F. S. Tautz, *Spontaneous Change in Molecular Orientation at Order-Disorder Transition of Tetracene on Ag(111)*, *J. Phys. Chem. C* **117**, 9212 (2013).
4. G. Mercurio, O. Bauer, M. Willenbockel, B. Fiedler, T. Sueyoshi, C. Weiss, R. Temirov, S. Soubatch, M. Sokolowski and F. S. Tautz, *Tuning and probing interfacial bonding channels for a functionalized organic molecule by surface modification*, *Phys. Rev.* B **87**, 121409(R) (2013).
5. M. Willenbockel, B. Stadtmüller, K. Schönauer, F. C. Bocquet, D. Lüftner, E. M. Reinisch, T. Ules, G. Koller, C. Kumpf, S. Soubatch, P. Puschnig, M. G. Ramsey and F. S. Tautz, *Energy offsets within a molecular monolayer: the influence of the molecular environment*, *New J. Phys.* **15**, 033017 (2013).
6. G. Mercurio, O. Bauer, M. Willenbockel, N. Fairley, W. Reckien, C. H. Schmitz, B. Fiedler, S. Soubatch, T. Bredow, M. Sokolowski and F. S. Tautz, *Adsorption height determination of nonequivalent C and O species of PTCDA on Ag(110) using x-ray standing waves*, *Phys. Rev.* B **87**, 045421 (2013).
7. O. Bauer, G. Mercurio, M. Willenbockel, W. Reckien, C. H. Schmitz, B. Fiedler, S. Soubatch, T. Bredow, F. S. Tautz and M. Sokolowski, *Role of*

functional groups in surface bonding of planar π-conjugated molecules, *Phys. Rev.* B **86**, 235431 (2012).

8. B. Stadtmüller, M. Willenbockel, E. M. Reinisch, T. Ules, F. C. Bocquet, S. Soubatch, P. Puschnig, G. Koller, M. G. Ramsey, F. S. Tautz and C. Kumpf, *Orbital tomography for highly symmetric adsorbate systems*, *EPL* **100**, 26008 (2012).

Curriculum Vitae

Martin Willenbockel
born on March 10th, 1985 in Soltau, Germany.

2010–2014: PhD student at the RWTH Aachen University in the group of Prof. Tautz at the Peter Grünberg Institut 3, Forschungszentrum Jülich

2010: Diploma degree in Physics. Diploma thesis "STM-Untersuchungen an ultradünnen Co-Filmen auf der sauberen und modifizierten Ru(0001)-Einkristalloberfläche" in the group of Prof. Jakob at the Philipps Universität Marburg

2005–2010: Student in Physics at the Philipps Universität Marburg

2004–2005: Military Service

2004: Abitur at the KGS Schneverdingen

Band / Volume 86
Development and Characterization of a Microfluidic Magnetic Oscillation Reactor for Enzymes
D. Jussen (2014), xxi, 131 pp
ISBN: 978-3-89336-974-4

Band / Volume 87
Submolecular imaging with single particle atomic force sensors
G. Kichin (2014), 140 pp
ISBN: 978-3-89336-976-8

Band / Volume 88
Multiscale Multimodel Simulation of Micromagnetic Singularities
C. Andreas (2014), xix, 188 pp
ISBN: 978-3-89336-983-6

Band / Volume 89
***Ab initio* description of transverse transport due to impurity scattering in transition-metals**
B. C. Zimmermann (2014), 164 pp
ISBN: 978-3-89336-985-0

Band / Volume 90
Ladungstransport durch Graphenschichten und GaAs-Nanodrähte untersucht mit einem Multispitzen-Rastertunnelmikroskop
S. Korte (2014), 96 pp
ISBN: 978-3-89336-990-4

Band / Volume 91
6th Georgian-German School and Workshop in Basic Science
A. Kacharava (Ed.) (2014), CD
ISBN: 978-3-89336-991-1

Band / Volume 92
Ab initio investigations of π-conjugated-molecule-metal interfaces for molecular electronics and spintronics
M. Callsen (2014), viii, 155 pp
ISBN: 978-3-89336-992-8

Band / Volume 93
Ladungstransportmessungen an Si(111) Oberflächen mit einem Multispitzen-Rastertunnelmikroskop
M. Blab (2014), iv, 132, X pp
ISBN: 978-3-89336-997-3

Band / Volume 94
Functional Soft Matter
Lecture Notes of the 46th IFF Spring School 2015
23 February – 06 March, 2015 Jülich, Germany
ed. by J. Dhont, G. Gompper, G. Meier, D. Richter, G. Vliegenthart, R. Zorn
(2015), ca. 600 pp
ISBN: 978-3-89336-999-7

Band / Volume 95
2-Steps in 1-pot: enzyme cascades for the synthesis of chiral vicinal amino alcohols
T. Sehl (2014), XIV, 167 pp
ISBN: 978-3-95806-001-2

Band / Volume 96
Immunohistochemical and electrophysiological characterization of the mouse model for Retinitis Pigmentosa, *rd10*
S. Biswas (2014), XII, 119 pp
ISBN: 978-3-95806-011-1

Band / Volume 97
Single molecule localization microscopy: Imaging of cellular structures and a new three-dimensional localization technique
X. Fan (2014), XII, 92 pp
ISBN: 978-3-95806-014-2

Band / Volume 98
Cryogenic Break-Junction Characterization of Single Organic Molecules
T. Grellmann (2014), VI, 86 pp
ISBN: 978-3-95806-015-9

Band / Volume 99
Interacting Interactions: A Study on the Interplay of Molecule-Molecule and Molecule-Substrate Interactions at Metal-Organic Interfaces
M. Willenbockel (2014), IX, 245 pp
ISBN: 978-3-95806-018-0

Weitere ***Schriften des Verlags im Forschungszentrum Jülich*** unter
http://wwwzb1.fz-juelich.de/verlagextern1/index.asp

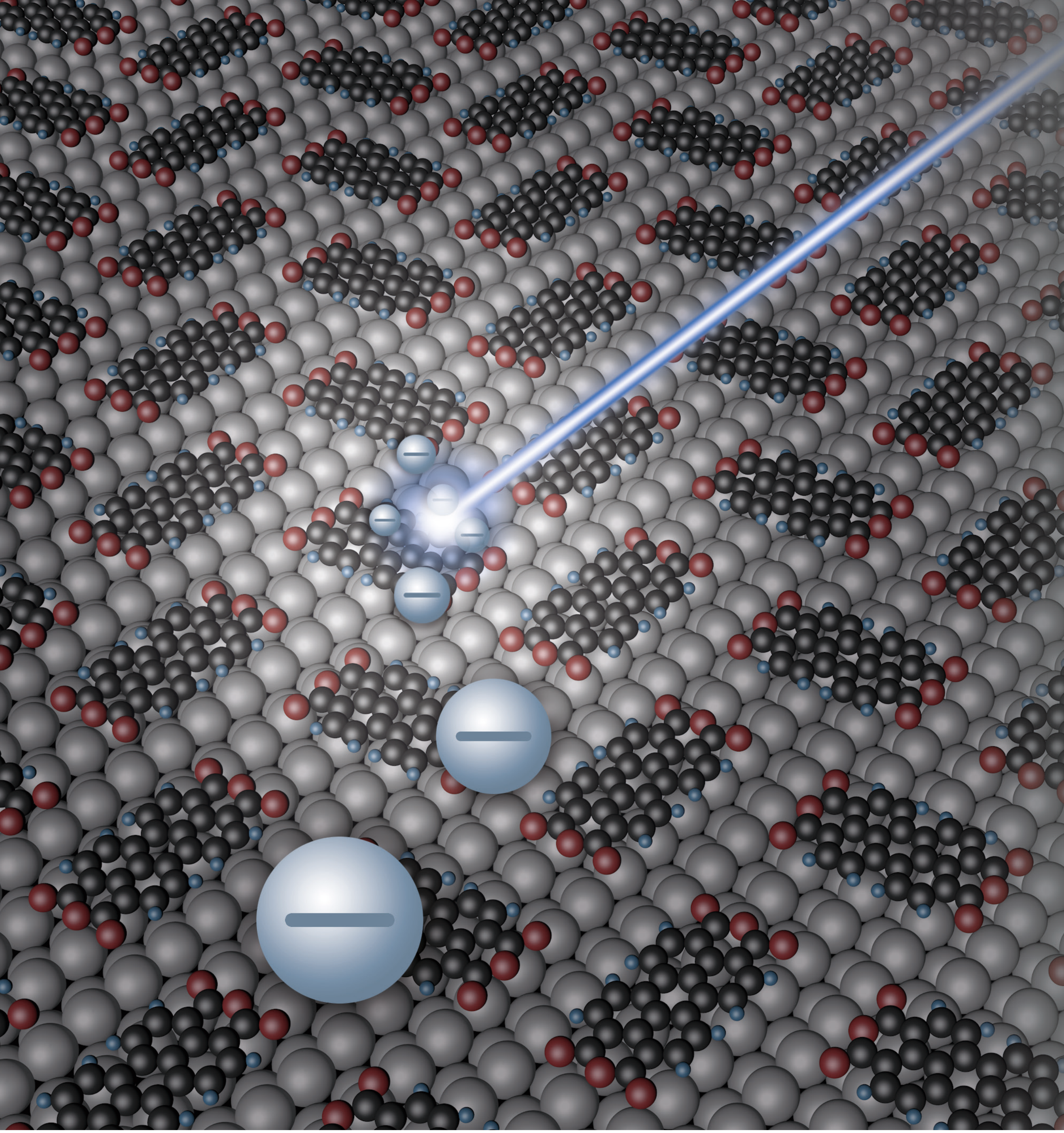

Schlüsseltechnologien / Key Technologies
Band / Volume 99
ISBN 978-3-95806-018-0

JÜLICH
FORSCHUNGSZENTRUM